Internal gravity waves in the Rhine ROFI

Applicability of the KdV model

Hugo Platell

Delft University of Technology

TU Delft

Cover image by NASA Earth Observatory (2007)

Internal gravity waves in the Rhine ROFI

Applicability of the KdV model

by

H. Platell, BSc.

to obtain the degree of

Master of Science Applied Mathematics

and

Master of Science Civil Engineering

at the Delft University of Technology,

to be defended publicly on Monday December 9th, 2019 at 13:30.

Student number:	4292715	
Project duration:	October 29nd, 2018 – December 9th, 2019	
Thesis committee:	Prof. dr. J.D. Pietrzak,	Delft University of Technology
	Dr. H.M. Schuttelaars,	Delft University of Technology
	Dr. A. Geyer,	Delft University of Technology
	Dr. C.A. Katsman,	Delft University of Technology
	Dr. N.L. Jones,	The University of Western Australia
	Prof. dr. K.G. Lamb,	University of Waterloo
	Ir. S. Rijnsburger,	Delft University of Technology

An electronic version of this thesis is available at `http://repository.tudelft.nl/`.

TU Delft

Acknowledgments

This Master Thesis is the final part of the double degree program of the studies Master of Science Applied Mathematics and Civil Engineering at the Delft University of Technology. The problem of internal waves in the Rhine ROFI got my interest after seeing the observations of Rijnsburger et al. (2019a). The complexity of problem showed nicely how Mathematics and Fluid Mechanics can work together to strengthen each other.

From the Applied Mathematics department I would like to thank dr. H.M. Schuttelaars and dr. A. Geyer for providing extensive and constructive feedback on my mathematical derivations and solutions. I would like to thank prof. dr. J.D. Pietrzak and dr. C.A. Katsman from the Civil Engineering department for sharing their knowledge on the Rhine ROFI, internal waves and providing feedback on my report structure. A special thanks to ir. S. Rijnsburger for sharing her knowledge on the observed internal waves events. For developing and validating the initial Delft3D model I would like to thank S. Rijnsburger and F. Zijl. Furthermore, I would like to thank dr. N.L. Jones and prof. dr. K.G. Lamb for providing feedback on the model results and sharing their expertise on the KdV model. Finally, I would like to thank family and friends for the support during my student period and especially during the final bit of my thesis.

Delft, December 2019

Hugo Platell

Abstract

The Rhine Region of Fresh Water Influence (ROFI) is a shallow frictional river plume in front of the Dutch coast. Each tidal cycle a new tidal plume front with fresh-water is released. In the near-field region of a river plume intense mixing is observed (Nash, Kilcher, & Moum, 2009), which is connected to the presence of internal waves for the Columbia river plume, (Pan & Jay, 2009). Internal gravity waves have been observed recently in the Rhine ROFI by Rijnsburger et al. (2019b). This thesis is about the generation and propagation phase of these waves, and how well they are described by the Kortweg-de Vries model (KdV).

To obtain stratification and flow velocity information about the Rhine ROFI a refinement of the Delft3D model by Rijnsburger et al. (2019a) has been created. In the model results, it can be seen that the density differences become smaller, when moving towards the far-field of the Rhine ROFI. Using a Froude number analysis, support for the internal wave generation mechanism by a tidal plume front, as described by Nash and Moum (2005), is found. It is shown, that on averaged neap tides the density stratification is large. This results in a larger area where the internal waves can be released from the tidal plume fronts compared to spring tides.

As the Rhine ROFI is located in shallow water, it is investigated what the effect of bathymetric variations is on internal waves. This is studied by extending the KdV model derivation of Grimshaw, Pelinovsky, and Poloukhina (2002) to account for a variable bed. Therefore, a second (large) length scale, accounting for the bed change, is introduced, while all other properties are scaled by characteristic values for internal waves. The scaling is carried out so that, while making an asymptotic expansion for the unknowns, the most important dynamics are taken into account. From this it is found, that the background flow can be solved independent of the existing wave length scale, which is small compared to the bed scale. The second order equations result in the Taylor-Goldstein equation (TGE) and KdV equation. The solutions of these two equations together predict how internal waves propagate and how steep they are. The variable bed KdV equation is given by

$$\frac{\partial A}{\partial t} + (C_0 + C_h)\frac{\partial A}{\partial x} + \mathrm{A}_1 A \frac{\partial A}{\partial x} + \mathrm{B}_1 \frac{\partial^3 A}{\partial x^3} = 0. \tag{1}$$

In this equation A represents the evolution in time t and space x of a wave; C_0 is the linear propagation speed due to stratification and background flow and C_h is a small correction on this propagation speed due to variable topography; A_1 and B_1 are constants influencing the wave steepness and relating the traveling wave velocity to the amplitude.

Using the solutions of TGE, KdV and variable KdV equation the sensitivity of internal waves to the density stratification and the background flow field is investigated. It is shown, that the variability of the density stratification and the pycnocline depth in the Rhine ROFI have a large influence on the propagation speed. The waves are advected by the background flow and therefore it is shown, that the depth-averaged velocity is an additive term in the linear propagation speed C_0.

The observations of internal waves by Rijnsburger et al. (2019b) have been used to validate the results of the KdV model. It is shown, that the TGE is a good predictor of the vertical velocity amplitude. By developing a TGE fitting procedure, it has been possible to obtain the pycnocline depth and the direction of wave propagation with only limited data available. For this the parameters have been varied and the error between the TGE solution and the vertical velocity measurements has been minimized. By performing a scaling analysis of the observed waves it is found that the relative wave height and relative depth balance for most of the observed events. For these events the wave period and velocity amplitude of the KdV model have been compared to the measurements. The results from the KdV model are well matched with the measurements. This showed that the KdV model may be used for a first estimate of internal waves in the Rhine ROFI.

Contents

List of symbols

Symbol	Description	Unit
A	wave function in the horizontal direction over time	m
a	typical wave height	m
A_1	KdV constant for the quadratic term	s^{-1}
A_1'	KdV constant for the quadratic term, calculated without background flow	s^{-1}
B_1	KdV constant for the linear dispersion	m^3/s
B_1'	KdV constant for the linear dispersion, calculated without background flow	m^3/s
C	traveling wave velocity (from the periodic KdV solution)	m/s
C_0	linear propagation speed	m/s
C_0'	linear propagation speed, calculated without background flow	m/s
C_h	propagation speed due to bathymetric variations	m/s
C_p	(total) propagation speed	m/s
$\Delta\rho$	density difference	kg/m^3
ε	relative wave height, a/h_0	$-$
η	non-dimensional isopycnal displacement in isopycnal coordinates	$-$
δ	relative depth, h_0/λ	$-$
g	gravitation acceleration constant	m/s^2
γ	relative bed change, h_1/h_0	$-$
h_0	undisturbed water depth	m
h_1	typical variation of the bed	m
h'	bed variation	m
l	typical length scale for the bathymetric variation	m
λ	wave length	m
m	wave steepness/shape factor	$-$
μ	wave length relative to the bathymetry change, λ/l	$-$
N	buoyancy frequency	s^{-1}
Φ	modal structure of the vertical velocity	$-$
r_t	relative thickness of the pycnocline	$-$
ρ	density	kg/m^3
ρ_0	undisturbed density profile	kg/m^3
σ	relative density or Boussinesq parameter	$-$
T	wave period, relative to the ground	s
T_U	wave period, relative to mean flow	s
θ	relative depth of the pycnocline	$-$
U	horizontal background flow velocity	m/s
u	(total) horizontal velocity	m/s
u'	horizontal wave induced velocity	m/s
W	vertical background flow velocity	m/s
w	(total) vertical velocity	m/s
w'	vertical wave induced flow velocity	m/s
x	horizontal coordinate	m
x_0	horizontal coordinate, where the flow boundary is prescribed	m
ξ	free surface coordinate	m
y	horizontal coordinate (orthogonal to x)	m
z	vertical coordinate	m
Z	(vertical) isopycnal coordinate	m
ζ	isopycnal displacement	m

List of abbreviations

ADCP	Acoustic Doppler Current Profiler;
Downwelling	Alongshore, northeastern wind direction, which induces downwelling near the coast;
GEP	Generalized eigenvalue problem;
HW	High water;
HW-2	Two hours before high water;
HW+2	Two hours after high water;
KdV	Kortweg-de Vries;
LW	Low water;
M18	Measurement location offshore the Sand-Engine at 18 meters depth;
M12	Measurement location offshore the Sand-Engine at 12 meters depth;
M_2	Lunar semidiurnal tide;
MSE	Mean squared error;
QEP	Quadratic eigenvalue problem;
ROFI	Region of Fresh Water Influence;
S_2	Solar semidiurnal tide;
SEP	Standard eigenvalue problem;
TGE	Taylor-Goldstein equation;
Upwelling	Alongshore, southwestern wind direction, which induces upwelling near the coast.

1 Introduction

River plumes are found along the coast, where a significant amount of fresh-water discharges in the coastal seas, (Horner-Devine, Hetland, & MacDonald, 2015). Following Horner-Devine et al. (2015), each river plume can be divided in three regions: the near-, mid- and far-field, see figure 1.1. In the near-field a phenomena called liftoff is observed, meaning that the water column separates into two-layers, with the fresh-water discharge from the river on top of the saltier water from the sea. This outflow is jet-like and therefore supercritical ($Fr > 1$), which means that the momentum from the river dominates over buoyancy from the fresh-water layer, (Horner-Devine et al., 2015). The acceleration of the upper-layer in this region, results in intense turbulence and mixing. As also observed by Nash et al. (2009), a significant amount of mixing occurs in this near-field region, but the details of this process are still unknown. When the outflow is losing its initial momentum from the river, the mid-field region of the plume is reached. As the momentum is smaller, it allows for Coriolis to take over and to dominate the system. This turns the river-plume in the alongshore direction towards the Northeast. When all momentum present from the river mouth is dissipated, the far-field region is reached. Here, the water is still fresher compared to the surrounding sea water.

In seas with a large tidal range, the near-field is strongly influenced by the tidal flow, (Horner-Devine et al., 2015). This induces the release of individual tidal plume fronts (fresh water lenses). When these tidal plume fronts propagate on a shallow frictional shelf, these river plumes are referred to as a Region of Fresh Water Influence (ROFI), (Simpson et al., 1993). The area of interest for this study is the Rhine ROFI. This river plume is located on a shallow shelf with a water depth of 20 meters. In this area the tidal range is 2 meters, (Luijendijk et al., 2017), which means that the tides have a large influence on the system. At LW the fresh-water is released from the river in offshore direction. When it becomes flood, the tidal Kevin wave advects this fresh water and shifts it in a northeastern direction. After HW due to Coriolis and tidal straining the fresh-water lens is transported onshore. This shows that the surface-current is rotating anti-cyclonically (clockwise), (Visser, Souza, Hessner, & Simpson, 1994; A. Souza & Simpson, 1996; de Boer, Pietrzak, & Winterwerp, 2009). The bottom-current rotates in the opposite direction: cyclonically (anti-clockwise). Horner-Devine et al. (2017) showed that the near-field region of the river plume reaches all the way to the coast, where it potentially impacts the flow, stratification, mixing and sediment dynamics. Rijnsburger, Flores, Pietrzak, Horner-Devine, and Souza (2018) observed that the wind has a large influence on the propagation of the tidal plume front.

In figure 1.2 one sharp tidal plume front (white color) is visible. Ahead of this tidal plume front multiple wave trains (deep black color) are observed, (Rijnsburger et al., 2019b). It is suggested, that these waves are generated by the tidal plume front. Observations of the Columbia river plume by Nash and Moum (2005) showed that internal waves can be generated by a river plume.

This generation mechanism has been associated with the slackening of these tidal plume fronts and consists of three stages: frontal growth, wave fission and free propagation, (Nash & Moum, 2005). During the first stage the difference in horizontal velocity around the plume edge is large: the ambient flow velocity is much smaller compared to the plume flow velocity ($Fr > 1$). This results in a downward

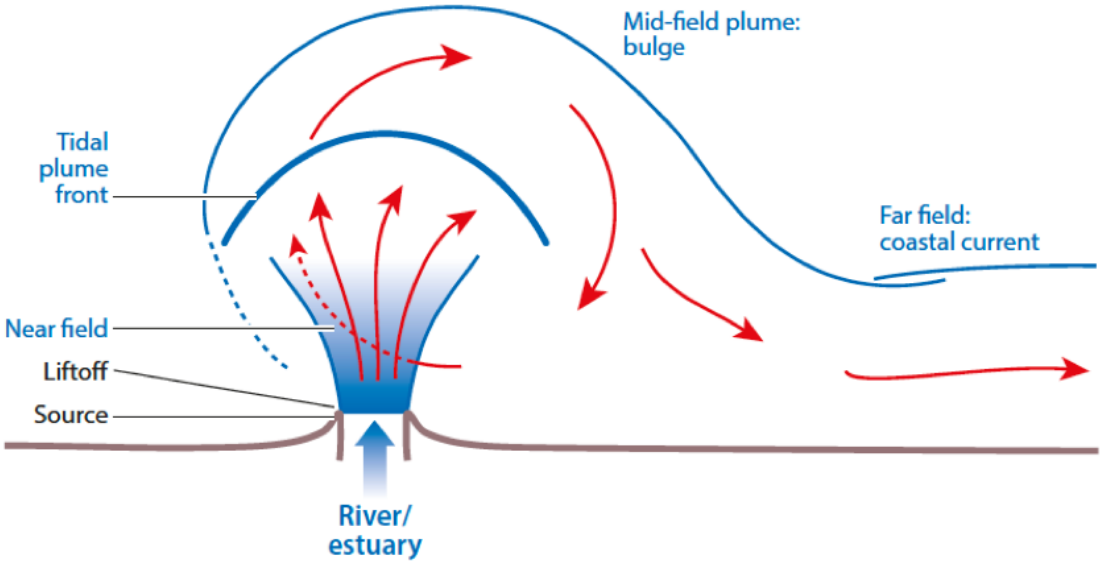

Figure 1.1: Different regions of a river plume, figure by Horner-Devine et al. (2015).

Figure unavailable until publication of Rijnsburger, et al. (2019b)

Figure 1.2: Left: location of the right figure. Right: Satellite image with one tidal plume front (sharp white line) and multiple internal wave trains (deep black) in the Rhine ROFI. Image from Rijnsburger et al. (2019b).

directed velocity, causing the conversion of frontal kinetic energy into potential energy, see figure 1.3 for a sketch of this process. As the frontal velocity is large compared to the ambient internal wave propagation speed, radiation of waves is not possible. The kinetic energy is trapped and no waves can be released in this phase.

After a time the tidal plume front propagates slower (slackens). This means that the frontal speed becomes smaller and the flow becomes subcritical ($Fr < 1$). This allows the potential energy to radiate away and wave fission from the frontal head to occur. The exact moment, that wave fission occurs, is difficult to predict, because the amplitude of the internal wave is related to its propagation speed.

The result of wave fission is, that the internal wave can propagate freely ahead of the tidal plume front: the free propagation stage. During this stage the internal wave speed will be large compared to the frontal speed and therefore: $Fr < 1$. This process generating internal waves can be repeated multiple times by the same tidal plume front.

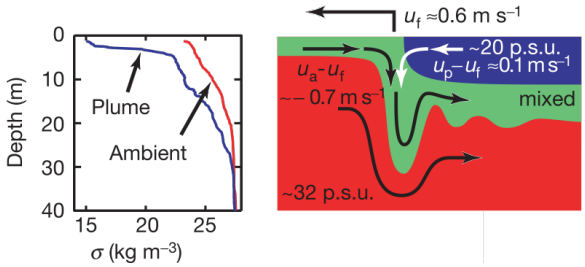

Figure 1.3: Process of frontal growth. Left panel: density stratification profile inside the tidal plume front and ambient. Right panel: flow velocities of the tidal plume front u_p and ambient u_a relative to the propagation speed of the front u_f. Figure by Nash and Moum (2005).

Due to the release of internal waves the tidal plume front can lose up to 70% of its total frontal energy, (Pan & Jay, 2009). This causes an increase of the plume area by a maximum of 20%. Furthermore, these released internal waves are an energy source for mixing and sediment processes in the ambient of the tidal plume front, (Pan & Jay, 2009). To obtain a good estimate of the energy loss and where this energy is transferred towards, it is necessary to have a the propagation speed and direction of internal wave propagation.

Following Pan and Jay (2009), the Taylor-Goldstein equation (TGE) in combination with the Korteweg-de Vries (KdV) equation, by Grimshaw et al. (2002), can be used to estimate energy fluxes induced by internal waves in the Columbia river plume. The TGE is used to calculate the vertical structure and the linear propagation speed C_0. Next, the KdV equation is used to model the shape and propagation of the internal wave in space and time. This KdV model takes the density stratification and non-wave disturbed (background) flow profile as input parameters.

The observations by Nash and Moum (2005) are made in deep water, approximately 60 meters deep. Furthermore, Li, Pawlowicz, and Wang (2018) associated the generation of some internal waves in the Strait of Georgia to the Fraser river plume, with a water-depth of 100 meter. In the meantime, many investigations focused on internal waves within these deep environments, while less is known about internal waves in shallow frictional river plumes, such as the Rhine ROFI. In this thesis the propagation of internal waves in a shallow system is investigated. The KdV model derived by Grimshaw et al. (2002) is valid for a flat bed, and might not be valid for a shallow system, where bathymetric variations have a relative large influence.

More recently, Rijnsburger et al. (2019b) showed the presence of internal waves in this region of the Rhine ROFI. One of the internal waves events observed is presented in figure 1.4 and shows the vertical velocity over a time period of 50 minutes. Between 10:19 and 10:40 alternating up- and downwards directed velocities have the characteristics of a mode-1 internal wave passing the observation point.

As the available density stratification information only provides density informations at four points in the vertical, the depth and thickness of the pycnocline is not measured. It has been shown, that this makes it difficult to obtain the phase velocity of internal waves, which is necessary to calculate the Froude number. Furthermore, the direction of internal wave propagation is not obtained. The wave induced

Figure 1.4: Measurements of vertical velocity on October, 4th at M18, by (Rijnsburger et al., 2019b). Between 10:20 and 10:40 up- and down going velocities due to a mode-1 internal wave can be observed.

horizontal velocities measured by different beams from the Acoustic Doppler Current Profiler (ADCP) should be correlated. As the river plume induces large horizontal shear-velocities, it is not possible to identify the wave induced velocities directly from these measurements. Therefore, Rijnsburger et al. (2019b) concluded based on satellite imagery, figure 1.2, that the internal waves propagate in the same direction as the tidal plume front. This is in the northeastern direction during this phase of the tide.

1.1. Objective

So far the study of Rijnsburger et al. (2019b) is the only one investigating internal waves generated by a tidal plume front on a shallow frictional shelf. As they have focused on explaining their observations, a detailed analysis of how internal waves are impacted by a shallow frictional river plume is missing. The effects of bathymetric variations, density stratification and shear-flow induced by the river plume in a shallow system, still need to be investigated. Continuing on internal waves in the Rhine ROFI, this research estimates the internal wave propagation speed, period and shape using the Korteweg-de Vries (KdV) model. This improves the understanding of internal wave generation and the propagation process. In addition, it is explored how the large tidal range and different wind directions influence the generation and propagation of these waves. This in combination with the from place to place varying flow structure of the Rhine ROFI. This thesis contributes in the ongoing research of the energy redistribution induced by internal waves in the Rhine ROFI. It is investigated, whether the river plume internal wave generation mechanism, as explored by Nash and Moum (2005), operates in the Rhine ROFI. Furthermore it is studied, if the missing pycnocline depth and direction of wave propagation can be estimated using flow velocity measurements for the internal wave events measured by Rijnsburger et al. (2019b).

These problems lead to the following key research question:

> *How does a shallow frictional river plume impact the generation and propagation of internal waves in the near- to mid-field region?*

To answer this main research question, the following sub-questions are posed:

1. How does the density stratification and (background) shear-flow impact the propagation speed of internal waves in a shallow system?
2. How are internal waves in the Rhine ROFI influenced at different locations by tidal stage and wind direction?
3. Are internal waves in the Rhine ROFI generated by the tidal plume front? Is it possible, to show this using a Froude number analysis?
4. How are internal waves influenced by small bathymetric variations of a shallow system?
5. Is it possible to use flow velocity measurements, in order to obtain an estimate of the pycnocline depth and direction of internal wave propagation?

The first research question shows the importance of the pycnocline depth and density difference on the propagation of internal waves in the situation of a shallow frictional river plume. As the tides and winds influence the size and location of the river plume, the second research questions helps to understand how the river plumes varies under these different influences and shows how this variation effects the internal wave generation and propagation. Using a Froude number analysis (third research question) it is searched which effect causes to internal waves to be generated in the Rhine ROFI. The fourth research question is investigated by developing an extension of the theoretical KdV model. This to account for the effect of small bathymetric variations. This model shows the effect of bathymetric variations in a shallow system on the propagation of internal waves. Finally, the answer to the fifth research question helps to estimate the pycnocline and obtain the propagation speed for the measured internal waves. This improves the understanding of the propagation of internal waves inside the Rhine ROFI.

1.2. Outline of this thesis

The research starts by introducing the relevant literature to study internal waves in the Rhine ROFI, (chapter 2). It explains the Rhine ROFI and the important dynamics for internal waves. Next, the models used in this research are introduced, (chapter 3). After the overview, the models are discussed in detail. First, the setup of the Delft3D model is discussed, which is an improved version of the model developed and validated by Rijnsburger et al. (2019a), (chapter 4). This model provides necessary flow and stratification data for the background state of internal waves. Next, in chapter 5 and 6 the variable bed KdV model is derived and solved. This derivation is based on the approach of Grimshaw et al. (2002) for the standard KdV equation, but adjusted to account for variability in topography. The last model to discuss is the TGE fitting procedure, (chapter 7). Here, the approach is discussed for finding the missing data in the measurements using the solution to the TGE.

After a discussion on the different models, the models are validated and the results are discussed. The Delft3D model results are validated using flow observations and are discussed in combination with literature about the Rhine ROFI, (chapter 8). Next, the sensitivity of the KdV model (chapter 9) on a shallow shelf is studied. The relationships obtained from this sensitivity analysis, are used during the validation of the model, which is carried out in chapter 10. After validation, the Delft3D and KdV model are combined to estimate the variation of internal waves at different locations, and to assess the changes due to tide and wind variations, (chapter 11). Using the TGE fitting procedure the pycnocline, direction of wave propagation and phase velocities for the measurements by Rijnsburger et al. (2019b) are obtained. These results are discussed in chapter 12. In chapter 13 the impact of the results is discussed. Finally, with these results it is possible to conclude the research and to answer the research questions, (chapter 14). Furthermore, recommendations for further research are made.

As this Masters thesis is a combination of the Master of Science programs of Applied Mathematics and Civil Engineering each chapter has been considered to be part of the Applied Mathematics or Civil Engineering part. This division is stated on the bottom of each page and an explanation of this division can be found in appendix A.

2

Background

To be able to investigate internal waves in the Rhine ROFI, the relevant literature is introduced step by step. First, the Rhine ROFI including the influences of tide and wind is explained, (section 2.1). Next, the generation, evolution and different types of internal waves is discussed, (section 2.2). Finally, the observation of internal waves in the Rhine ROFI by Rijnsburger et al. (2019b) are discussed in detail, (section 2.3).

2.1. Rhine ROFI

The delta of the Rhine River (and Meuse) is located in the Western part of The Netherlands and is through several branches connected to the North Sea, (de Kok, 1996). See figure 2.1 for the locations. The main discharge goes through the Rotterdam Waterway, which emerges between Hoek van Holland and Maasvlakte. As the river water consists of melt water and rain, it is fresh water which flows into the North Sea at this point. The sea contains salt (more dense) water and therefore the river water forms a layer of fresh (light) water on top of the saltier water. This is called the Rhine Region of Fresh Water Influence (ROFI). This top layer of the Rhine ROFI has a typical thickness of three to five meters, (de Boer et al., 2009), which is 15-25% of the total water depth (20 [m]).

Due to the incoming and outgoing tides from the sea into the river system, each tidal cycle a new fresh water lens is released from the river into the sea, so the fresh water is flowing from the river in offshore direction. Under normal conditions these tidal plume fronts extend 20 [km] offshore, but there are some anomalies observed, where it can extend up to 40 [km], (de Boer, Pietrzak, & Winterwerp, 2006). Depending on the wind conditions, the density stratification induced by these tidal plume fronts is observed 30 [km] southwest of the Haringvliet and in the northeastern direction all the way up to the Wadden Sea, (de Kok, 1996).

Influence of tide on the Rhine ROFI

The North sea is tidally energetic in the region of the Rhine ROFI. The M_2 and S_2 constituent are dominant, (de Boer et al., 2006). The tidal waves behaves like a progressive Kelvin wave with (vertically averaged) velocities between 0.5 and 1.0 [m/s]. At Scheveningen (20 [km] north of the mouth of the Rotterdam Waterway) the tidal range is about $3 - 4$ [m] and the tidal wave shows an asymmetry, (Luijendijk et al., 2017). Here, the falling period is around eight hours (with speeds of 0.5 [m/s]) and the rising period is 4.5 hours (flow speed around 0.7 [m/s]). The location and propagation of the tidal plume fronts can be linked to the phase of the semidiurnal tide, (Hessner et al., 2001).

The different frequencies of M_2 and S_2 induce a spring-neap cycle, with the tidal range large during spring tide and small during neap tide. This difference influences the river plume. During neap tide there mixing is reduced, allowing for a strong stratification. During spring tide the velocities are higher, resulting in more mixing and a reduction of the stratification of the Rhine ROFI, (de Boer et al., 2006).

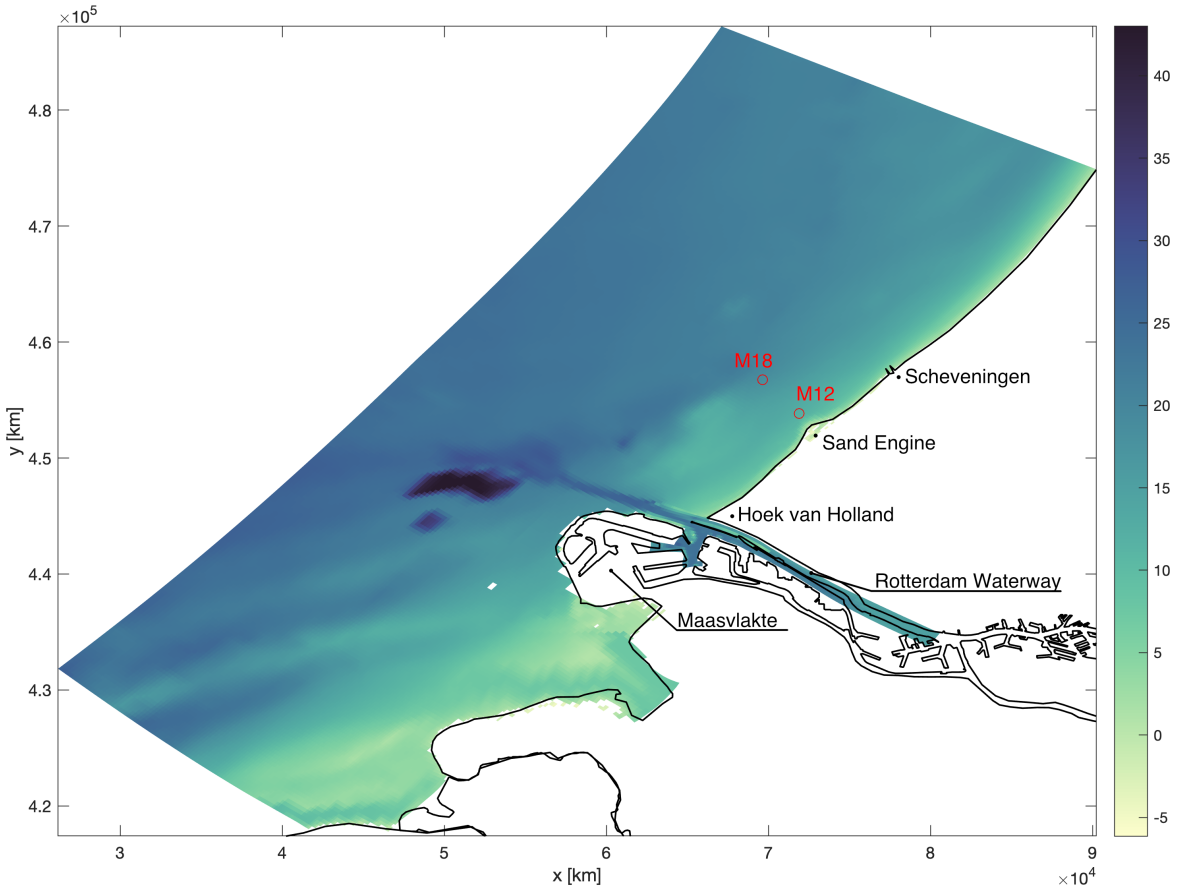

Figure 2.1: Overview of the locations around the Rhine ROFI, with the M18 and M12 measurement locations by Rijnsburger et al. (2018). Colorbar indicates depth in meters.

Tidal straining in the Rhine ROFI

Downstream of the Rhine ROFI, around 30 [km] from the river mouth near Noordwijk, strong cross-shore currents due to tidal straining are observed. On flood tide the main flow is directed alongshore to the north, see figure 2.2. Due to Coriolis, this flow is deflected towards the coast. As the largest flow velocities are observed in the upper layer, the Coriolis force is also largest in the upper layer. This results in a shoreward directed water mass transport in the upper layer. This mechanism is called Ekman transport. As no transport is allowed at the coast, this shorewards directed upper layer transport should be compensated by an offshore directed return flow in the bottom layer. This effect is called downwelling as the water from the upper layer is submerged into the bottom layer.

During the falling tide, the tidal flow is directed southwards and the water in the upper layer is transported offshore due to Coriolis. This should again be compensated by a flow in the bottom layer. In this case, an onshore directed flow. The result is that the surface current rotates anti-cyclonically with the tide while the bottom current moves the other way around (cyclonic behavior), (Visser et al., 1994; A. Souza & Simpson, 1996; de Boer et al., 2009). This process is called tidal straining.

Influence of wind on the Rhine ROFI

Wind has also a large influence on the Rhine ROFI, (de Boer et al., 2009; Rijnsburger et al., 2018). Strong winds induce strong mixing and a reduction of the density stratification, (de Boer et al., 2009). Cross-shore directed winds (perpendicular to the coast) have a direct effect on the plume. With onshore winds the plume is located near the coast, while under offshore wind conditions it is located further offshore.

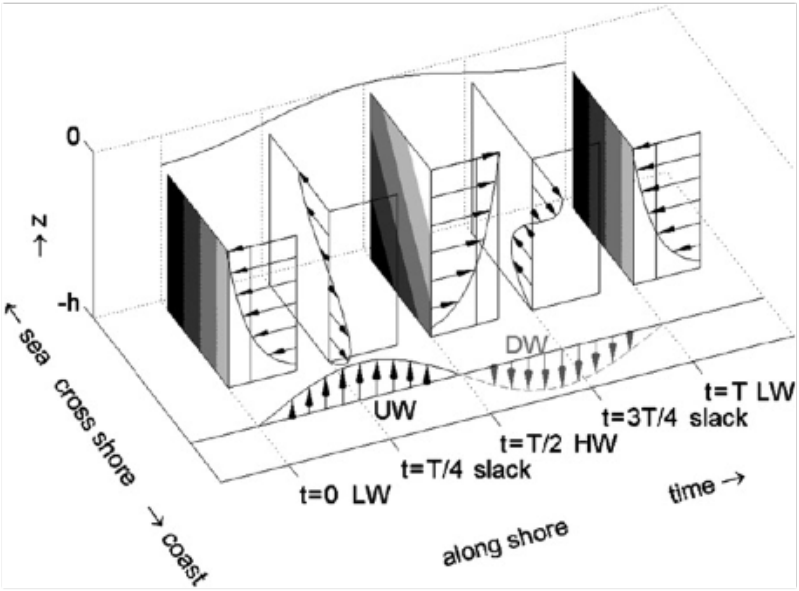

Figure 2.2: Concept of tidal straining. Color shading shows that the stratification is largest during HW; horizontal vectors indicate flow speed and direction; vertical vectors indicate the tidal elevation. UW: Upwelling; DW: Downwelling. Figure by de Boer et al. (2009).

An alongshore north-eastern directed wind leads to a plume close to the coast, as Coriolis induces Ekman transport of the upper layer towards the coast. This also leads to downwelling near the coast, as the transport in the upper layer again needs to be compensated by a return flow in the bottom layer. When the alongshore wind is directed to the south, Ekman transport shifts the plume offshore, which results in upwelling near the coast.

Sand Engine

Along the coast $10\ [\mathrm{km}]$ north of the river mouth, between Hoek van Holland and Scheveningen, a large sand nourishment site is located, called the Sand-Engine, (Luijendijk et al., 2017). For the location see figure 2.1. This nourishment site should protect the coast in a more natural way, as it ensures a constant flow of a sediment. In this area the river plume is transitioning from the near-field to the so-called mid-field region, (Horner-Devine et al., 2015). This means that Coriolis is dominating the system and that the plume is turning towards the coast. According to Rijnsburger et al. (2018) the (anti-)cyclonic circulation by tidal straining can also be observed in this part of the plume.

2.2. Internal waves

The Rhine ROFI consists of two layers with a lighter fluid on top of more dense water. The interface between these layers, where the density gradient is largest is called the pycnocline. An internal wave is an oscillating variation of the location of this interface. This is similar to a surface wave where there is a moving interface between water and air, (Helfrich & Melville, 2006). Most observations of internal waves are made in the ocean, where the water depth is hundreds of meters (or even larger). More recent research by Nash and Moum (2005) has found, that these waves can be generated by a tidal plume front in the coastal ocean. Here, the waves are observed near the fresh water lenses of the Columbia river plume. This is similar to the observations of internal waves in the Rhine ROFI by Rijnsburger et al. (2019b).

Different types of internal waves

There are two types of internal waves, so called mode-1 and mode-2 waves. For mode-1 waves, the particles in the water column move simultaneously up or down, and so also does the pycnocline.

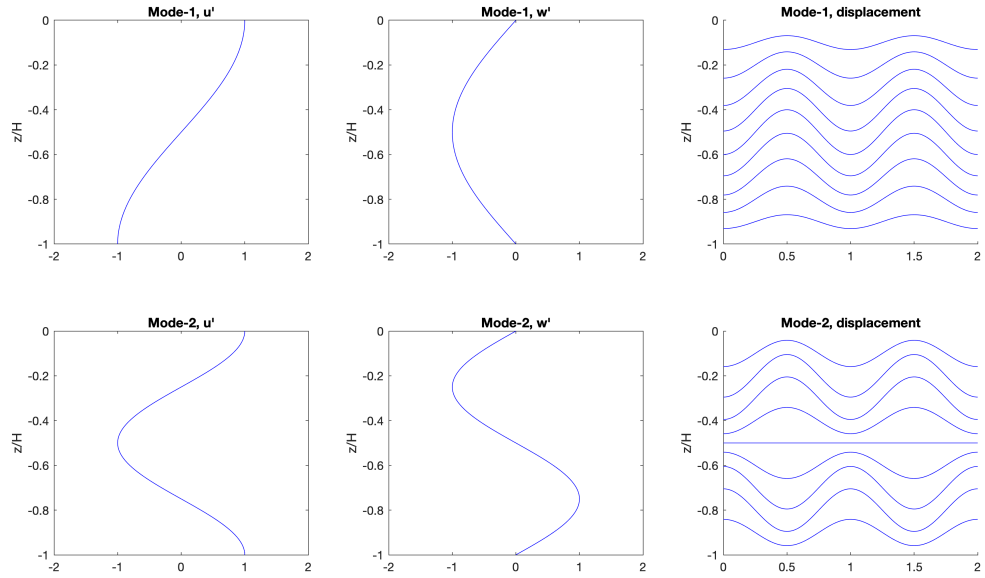

Figure 2.3: Velocity- and particle displacement profiles for mode-1 and mode-2 internal waves. The pycnocline is here located at half depth ($z/H = 0.5$).

The first row of figure 2.3 shows the horizontal and vertical velocity mode, and particle displacement associated with mode-1 waves. Mode-2 waves induce areas of compression and expansion where particles move vertically in the opposite direction above and underneath the pycnocline. The second row of figure 2.3 shows indeed that mode-2 waves induce vertical velocities with a different direction at opposite sides of the pycnocline.

The name of these different wave types can be explained by looking at the vertical structure of the vertical velocity (middle column of figure 2.3). A mode-1 wave is described by $\sin(z\pi/H)$, while a mode-2 wave is described by $\sin(2z\pi/H)$. Here, z is the vertical coordinate and H the total water depth. These are common (eigenmode) solutions to an eigenvalue-eigenfunction problem.

Internal waves in a continuous stratified fluid

The previous discussion assumed a sudden jump in density. However, a fluid can also be continuous stratified, which is the situation observed in the Rhine ROFI. Pietrzak, Kranenburg, and Abraham (1990); Bourgault and Kelley (2004) have shown that the density structure in a continuous stratified fluid can be approximated by an hyperbolic tangent. This approximation can be easily transformed to a two-layer system.

In continuously stratified systems the restoring buoyancy force is of importance. Therefore, following Staquet and Sommeria (2002), the Brunt-Väisäla frequency N (or simply buoyancy frequency) is defined as

$$N(z) = \sqrt{-\frac{g}{\rho}\frac{\partial \rho}{\partial z}}. \tag{2.1}$$

The pycnocline is now defined as the location where the buoyancy frequency reaches its maximum value, this indicating where in the water column internal waves are expected. For a continuous stratified fluid approximated by an hyperbolic tangent this location is the inflection point of the hyperbolic tangent.

Generation of internal waves

An internal wave can be generated in several different ways, (Jackson, da Silva José, & Jeans, 2012). The first generation mechanism for mode-1 waves is the lee wave-mechanism, where a stratified flow

is forced to flow over an obstacle (a sill or a bank). In this mechanism the internal Froude number first changes from subcritical to supercritical, which causes an accumulation of energy near the obstacle. This causes (trapped) waves to form. When the flow slackens and becomes subcritical, these waves can propagate forward from their point of generation.

A second generation mechanism for internal waves is wave fission from the river plume head. This is observed in the Columbia river plume by (Nash & Moum, 2005) and was discussed in chapter 1.

Evolution of internal waves

After its generation, an internal wave evolves in time and propagates in the system. The interesting properties during this phase are the wave amplitude, wave form, period and propagation speed. These properties can be obtained using the Korteweg-de Vries equation, (Korteweg & de Vries, 1895; Bourgault & Kelley, 2004; Helfrich & Melville, 2006). In chapter 5 this equation the derivation of this equation is discussed, and in chapter 6 the solutions corresponding to this KdV model are presented.

2.3. Observations of internal waves in the Rhine ROFI

As discussed in the introduction (chapter 1) Rijnsburger et al. (2019b) has observed internal waves inside the Rhine ROFI. In their measurement campaign instruments were situated on two places offshore from the Sand-Engine: at 12 and 18 meters depth. These locations are called M12 and M18, see figure 2.1 for the exact locations. In table 2.1 the quantities of the observed wave events by are given. In figure 2.4 these quantities are visualized. First, the location relative to the river plume is given; the events of September, 17th 21:16 and 21:29 are observed inside the tidal plume front and therefore behind the frontal head. Next, the frontal propagation direction is given, as indication for the direction of wave propagation. Furthermore, the stratification parameters: upper layer height h_1, lower layer height h_2, mean density $\bar{\rho}$ and density difference $\Delta\rho$, and the depth-averaged flow velocity in alongshore U_a and cross-shore U_c direction are given. Finally, the wave height a and period T are given in combination with the horizontal u' and vertical w' induced velocities. These values are used in chapter 10 to check the validity of the KdV model in the Rhine ROFI.

		Wave events							
		17-09 21:09	17-09 21:16	17-09 21:29	19-09 11:33	04-10 09:27	04-10 09:58	04-10 10:12	04-10 10:24
location									
direction (front)									
h_0	$[\mathrm{m}]$								
h_1	$[\mathrm{m}]$								
h_2	$[\mathrm{m}]$								
$\bar{\rho}$	$[\mathrm{kg/m^3}]$								
$\Delta\rho$	$[\mathrm{kg/m^3}]$								
U_a	$[\mathrm{m/s}]$								
U_c	$[\mathrm{m/s}]$								
a	$[\mathrm{m}]$								
T	$[\mathrm{s}]$								
u'	$[\mathrm{m/s}]$								
w'	$[\mathrm{m/s}]$								

Table 2.1: Parameter values for multiple wave events. Data from the M18 measurement site by Rijnsburger et al. (2019b).

As the Rhine ROFI is located on a shallow frictional shelf, it is suggested that the bathymetry has a relative large influence on the observed wave events. Using data from Rijnsburger et al. (2019a) the depth profiles in the direction of the waves (front), see table 2.1, are found. The resulting profiles are given in figure 2.5. Here it is found, that the slope is at maximum 1.5 $[\mathrm{m}]$ per kilometer.

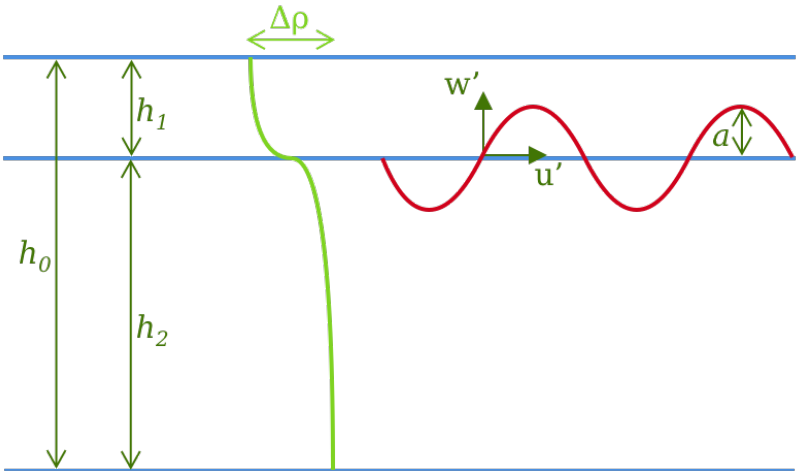

Figure 2.4: Visualization of the internal waves parameters shown in table 2.1.

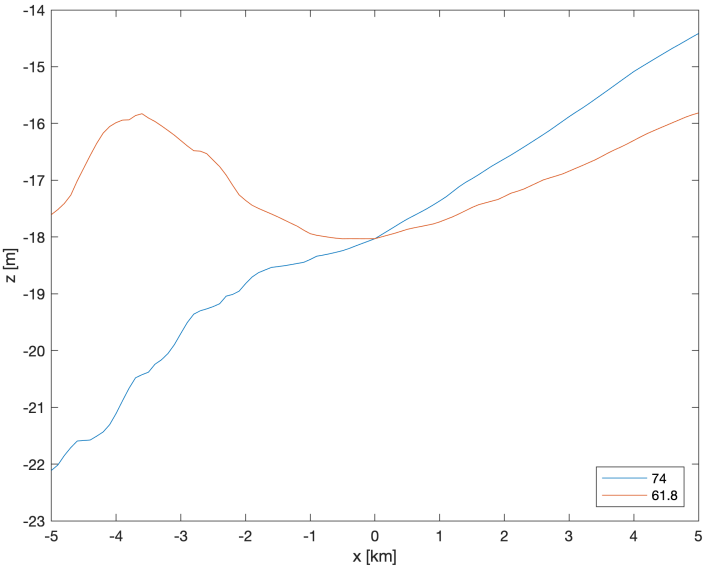

Figure 2.5: Bed profile around M18 in the directions of the waves (legend state angle in degrees from North).

I

Methods and models

3

Introduction to the methods used

To be able to answer the research questions, three different models are applied. A Delft3D model is used to provide information about the flow velocities and the density stratification in the Rhine ROFI, (section 3.1). Secondly, a Korteweg-de Vries (KdV) model is used to obtain the phase velocity and period of internal waves for a given background state, (section 3.2). This KdV model consists of the Taylor-Goldstein equation (TGE), providing the vertical structure and linear propagation speed, and the KdV equation, providing the wave form and propagation in space and time. The KdV model is extended to be able to capture the effect of bathymetric variations. Finally, a TGE fitting procedure is introduced to combine the solution of the TGE with the measurements carried out by Rijnsburger et al. (2019b). This procedure results in the depth of the pycnocline and direction of internal wave propagation, which is essential to get an accurate estimate of the, up to now unknown, phase velocity, (section 3.3). In figure 3.1 the usage of these models and the connections between them is visualized. When referred to information in this figure, it is done as (figure 3.1 - x). Here, x corresponds to the number (data), letter (connection) or Roman Numeral (result) in the figure. The following sections introduce each model one by one and indicate why they are needed. Furthermore, the expected results of these models and the coherence between them is discussed.

3.1. Delft3D model

To answer the research question about the effect of variation of location, tidal stage and wind direction on internal waves, a detailed spatial coverage on the Rhine ROFI is needed. The spatial variation of the main flow and density stratification can be obtained by the use of a hydrostatic Delft3D model. A hydrostatic model can not resolve internal waves, but is used to provide the variation of flow and stratification due to tide and wind. The water motion in the model is forced by temporally varying tidal signals, winds and river discharges and are representative for the year 2014 (figure 3.1 - 2). The model setup, used in this thesis, closely follows the setup of Rijnsburger et al. (2019a). The region, considered in this model, covers the North Sea (from Scotland up to the English Channel); to get a more accurate result near the Rhine ROFI, the grid resolution is increased, by adding multiple refinements. The model results have been verified with the measurements obtained in 2014. The characteristics of the water level, velocity and salinity are captured within this model. The used measurements are from the same campaign, as wherein the internal waves where found by Rijnsburger et al. (2019b).

To be able to use the output of the Delft3D model for usage on internal waves, the model should capture the pycnocline correctly. This is accomplished by increasing the vertical resolution. To do so, the number of vertical sigma-layers is increased compared to the original model by Rijnsburger et al. (2019a).

The new model run needs to be validated (figure 3.1 - I). This is done by comparing the new model results with the results from the original model by Rijnsburger et al. (2019a) and with the flow velocity and salinity measurements from 2014 (figure 3.1 - 1). In addition, the model results are discussed,

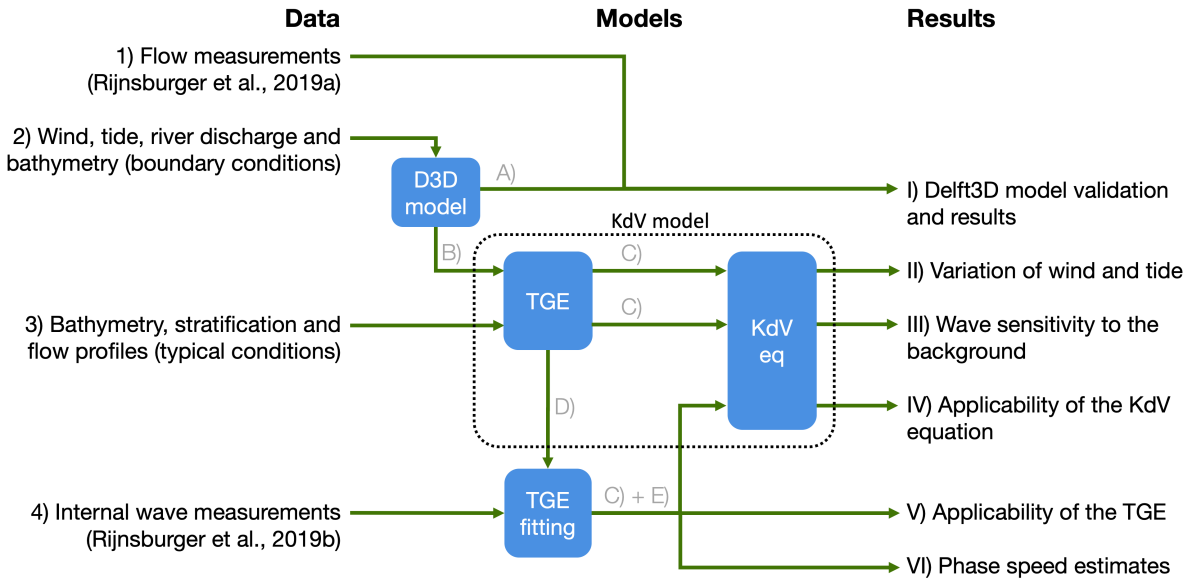

Figure 3.1: Structure and coherence between different models used in this research.
Description of the links between the different models:
A) Calculated flow velocity and salinity in surface- and bottom layer in space and time calculated using Delft3D;
B) Calculated flow velocity and density stratification in space and time calculated using Delft3D;
C) Vertical structure $\Phi(z)$ and propagation speed c_0 calculated using the TGE based on density stratification and flow velocities;
D) Function form of TGE solution and numerical approach to obtain this solution;
E) Pycnocline depth, thickness and direction of wave propagation, for the events observed by Rijnsburger et al. (2019b).

(chapter 8). Here, the behavior of density stratification and typical plume sizes in the Rhine ROFI are discussed and compared with results from literature. As the model contains information about the complete year 2014, different tide and wind conditions are found in this model. To be able to compare the different influences of tide and wind different periods in 2014 will be selected, such that the effect of tide and wind on flow velocities and stratification can be distinguished.

As the model is giving information about flow velocities and stratification, it shows directly its shortcoming. With this model it is not possible to represent internal waves, as the model is set into hydrostatic mode This mode can not produce internal waves, as they occur due to the balance with non-hydrostatic components. The non-hydrostatic mode could be turned on, but as the calculation (clock) time is now already spanning multiple months, an answer to the non-hydrostatic version will not be reached in a reasonable amount of time.

3.2. KdV model

As the Delft3D model can not give any insight on internal waves, an additional model is needed. A model that is typically used to study internal wave dynamics is the Kortweg-de Vries model, introduced by Korteweg and de Vries (1895). This model is typically used to describe internal waves in deeper water (> 60 [m]), but needs to be verified when used in the Rhine ROFI with a depth of approximately 20 meters. The KdV model provides the propagation speed, wave form and wave period and can be solved analytically. Alternative models that could be used, are the Dubriel-Jacotin-Long (DJL) equation or non-hydrostatic numerical models, such as the model described by Bourgault, Galbraith, and Chavanne (2016). The disadvantages of models other than the KdV model are; that the solutions are not explicitly known (Stastna & Lamb, 2002) and therefore it is difficult to distinguish the effect of one specific property, such as the pycnocline depth.

The KdV model is a 2D model, which means that it is defined using the vertical dimension and one horizontal dimension. The model consists of two equations: the Taylor-Goldstein equation (TGE), solving the vertical velocity, and the KdV equation, describing the propagation in time and (horizontal) space. The KdV model takes the water depth, density stratification and background flow as input

parameters. To background flow is referred to as the hydrostatic, non-wave disturbed, flow in the Rhine ROFI, which is the background for internal waves. The Delft3D model provides this data (see connection B in figure 3.1).

Taylor-Goldstein equation

The vertical structure $\Phi(Z)$ of a wave and linear propagation speed C_0 are determined by the Taylor-Goldstein equation (TGE) (Grimshaw et al., 2002), and reads in full-dimensional form

$$\frac{\partial}{\partial Z}\left((U-C_0)^2\frac{\partial \Phi}{\partial Z}\right)-\frac{\partial \rho_0}{\partial Z}\Phi=0. \tag{3.1}$$

This equation is subject to homogenous Dirichlet boundary conditions at the surface and bed. This Taylor-Goldstein equation is an eigenvalue-eigenfunction problem, where C_0 is the eigenvalue and Φ the eigenvalue solution. Furthermore, $U(Z)$ describes the background (shear) velocity and $\rho_0(Z)$ is the density stratification. The TGE is solved analytically for a two-layer system or linear stratification, both without any background flow. When a system with hyperbolic tangent stratification or background flow is considered, an analytical solution is not possible and a numerical approach is required. To obtain this numerical solution the problem is discretized, resulting in a discretized quadratic eigenvalue problem. This problem is linearized, and is solved as standard eigenvalue problem, (section 6.1.2).

KdV equation

The KdV equation (Grimshaw et al., 2002) is given by

$$\frac{\partial A}{\partial t}+C_0\frac{\partial A}{\partial x}+\mathrm{A}_1 A\frac{\partial A}{\partial x}+\mathrm{B}_1\frac{\partial^3 A}{\partial x^3}=0. \tag{3.2}$$

In this equation $A(x,t)$ represents the evolution of the particle displacement in time t and space x of an internal wave. The parameter C_0 is the linear propagation speed obtained from the TGE (figure 3.1 - C). Together with the coefficients A_1 and B_1 the wave form and (small) traveling wave speed are obtained from equation (3.2). The constants A_1 and B_1 are determined based on the solution for the Taylor-Goldstein equation. As the observations of Rijnsburger et al. (2019b) show a periodic signal, an analytical expression for the periodic solution of the KdV equation is given in chapter 6.

From the combination of the solutions for the Taylor-Goldstein and KdV equation the horizontal and vertical flow velocities are determined, (section 6.4). Even more, the vertical isopycnal displacement can be calculated.

Variable bed KdV model

The standard KdV model does not allow variation of the bathymetry. As one of the research questions concerns the effect of bathymetric variations on internal waves, the standard KdV model (3.2) is extended, allowing for bed variation. In chapter 5 the derivation of the variable bed KdV model is treated. The derivation is based on the derivation by Grimshaw et al. (2002) for the standard KdV. The final variable bed KdV equation reads

$$\frac{\partial A}{\partial t}+(C_0+C_h)\frac{\partial A}{\partial x}+\mathrm{A}_1 A\frac{\partial A}{\partial x}+\mathrm{B}_1\frac{\partial^3 A}{\partial x^3}=0, \tag{3.3}$$

where C_h is the propagation speed related to the variability of the bed. When the bathymetry is taken flat in this model, the model will reduce to the standard KdV equation (3.2), as $C_h=0$ in this case. With this new model it is possible to study the sensitivity of internal waves to bathymetric variations.

Different propagation speeds

Throughout this thesis different propagation speeds are used. The total propagation speed C_p consists of three components, for a detailed discussion see chapter 6 and equation (6.48),[1]

$$C_p=C_0+C_h+C. \tag{3.4}$$

[1]Note that C and C_h are small corrections of the propagation speed and therefore $C_p\approx C_0$.

Here, C_0 is the linear propagation speed [2] obtained from the TGE and C_h is referred to as the propagation speed correction for the variability of the bed. C is the traveling wave velocity from the solution to the KdV equation, (section 6.3)[3]. All phase speeds are noted relative to the ground. In the remainder of this thesis, all propagation speeds and KdV constants denoted by a capital letter are dimensional (full-scale) variables, when symbols in lower case are used these represents the non-dimensional (scaled) variables. For example, c_0 is the non-dimensional version of C_0.

Environmental analysis using the Delft3D results

As the KdV model does not account for any variation of tide and wind effects, it is necessary to combine the results from the Delft3D model with the KdV model. This gives the local wave propagation speed and wave period under different tidal and wind conditions (figure 3.1 - I). The variability in the results can be studied to answer the second research question, (chapter 11).

Calculation of the Froude numbers

Nash and Moum (2005) showed that the Froude number can be used to determine, when internal waves can be generated by a river plume. To investigate, if this is also the case in the Rhine ROFI (and answer the third research question) the Froude numbers need to be determined in this situation. From the results of the Delft3D model it is possible to estimate the velocity of the tidal plume front, approximated by the upper layer velocity U_1, and the depth averaged velocity U_m. The KdV model results in a total propagation speed C_p for internal waves. Combining this information allows for the following definition of the Froude number [4]

$$Fr := \frac{U_1}{C_p - U_m}. \tag{3.5}$$

Note that this definition is different to Nash and Moum (2005). They defined two different Froude numbers: $F_a = U_f/C_a$ and $F = U_f/C$[5]. Here, U_f is for both Froude numbers the propagation speed of the tidal plume front; C_a is the calculated linear internal wave propagation speed from the TGE in the ambient (ahead of the tidal plume front) and C is the measured internal wave propagation speed (ahead of the tidal plume front). Nash and Moum (2005) considered F as the most important Froude number, as it takes the relationship between the wave amplitude and its propagation speed into account. In figure 3.2 this definition of the Froude number is shown.

In this research the upper layer velocity U_1 is compared to the internal wave propagation speed relative to the fluid $C_p - U_m$. This analysis is performed both ahead and behind the head of the tidal plume front, see figure 3.2. When the situation behind the frontal head is considered, U_1 is a little bit larger compared to U_f used by Nash and Moum (2005). As the front propagates slower compared to the water inside the plume, this allows the frontal head to grow. $C_p - U_m$ is the internal wave propagation speed relative to the fluid, which is in accordance with the Froude number definition used by Schijf and Schönfled (1953); Pietrzak and Labeur (2004). For the situation ahead, $C_p - U_m$ is close to the C used by Nash and Moum (2005), as this total propagation speed also depends on the wave amplitude. In this case, both C_p and C are obtained ahead of the front. Here, U_1 is not U_f and therefore this Froude number is also slightly different from Nash and Moum (2005). In this research the definition from the Froude number, equation (3.5), is used, as it is difficult to automatically extract the frontal head from the Delft3D model. This makes it difficult to obtain the data needed for the definition used by Nash and Moum (2005).

Sensitivity study of the variable bed KdV model

Using the KdV model, it is possible to relate the background flow and density stratification to the phase velocity and period of internal waves. Therefore the sensitivity of internal waves on these parameters

[2] The linear propagation speed C_0 contains effects of advection.

[3] The definition of C can be found in equation (6.46).

[4] The denominator in this definition of the Froude number is the wave propagation speed relative to the moving fluid. This is similar to the approach of Pietrzak and Labeur (2004).

[5] At this specific point the definition of C in the Froude number is the phase velocity as defined by Nash and Moum (2005) and not the traveling wave velocity from the periodic KdV solution.

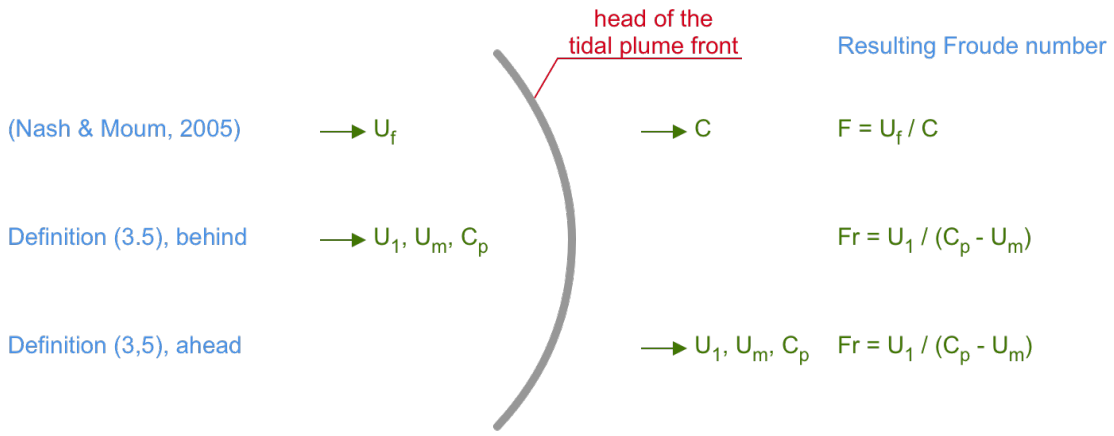

Figure 3.2: Different definitions of the Froude number. Nash and Moum (2005) compared to definition (3.5).

can be studied (figure 3.1 - III), (chapter 9). This answers the first research question. With the variable bed KdV model it is also possible to study the sensitivity of internal waves on changes in the bathymetry, answering research question four.

Applicability of the variable bed KdV model

The applicability of the variable bed KdV model needs to be checked for the Rhine ROFI, as the model and corresponding scaling are typically used for much deeper systems. This is done separately for the TGE and KdV equation. First, the validity of the TGE is considered (figure 3.1 - V). As the measurements are missing detailed information about the pycnocline and wave angle, this is not directly possible. Therefore an extra step is needed, in which the parameters are varied until a good match is obtained: the TGE fitting procedure. The required fitting procedure will be explained in section 3.3.

Next, the KdV equation can be validated (figure 3.1 - IV). The scaling used in the derivation is checked with the magnitudes observed in the Rhine ROFI measurements by Rijnsburger et al. (2019b), to verify that the scaling is in order of magnitude correct. Also the relationship between the relative wave height and relative depth, the KdV balance, is checked. Finally, the velocity measurements are used to check the period and velocity amplitude resulting from the KdV model.

3.3. TGE fitting procedure

Rijnsburger et al. (2019b) shows that it is difficult to estimate the pycnocline and direction of wave propagation from the observations (figure 3.1 - 4). These estimates are needed to obtain the phase speed of internal waves and to check the applicability of the KdV model. To obtain a better estimate, the solution to the TGE is used in the TGE fitting procedure. Therefore, connection D in figure 3.1 shows the relation between the TGE and the TGE fitting procedure.

As the TGE predicts the velocity amplitude over the vertical of an internal wave, this can be compared with the observed vertical flow velocities, (chapter 7). By varying the input to the TGE: pycnocline depth, thickness and direction of wave propagation: the solution is changed. After variation of parameters an optimal match (with minimal error) can be obtained, which gives a prediction of the unknown pycnocline and direction of wave propagation.

Using the predicted pycnocline and wave angle it is possible to check the applicability of the TGE for the observed internal waves (figure 3.1 - V). As the TGE solution results in an estimated phase velocity. These can now be calculated for the observed events by Rijnsburger et al. (2019b). Finally, it is possible to feed the TGE solution into the KdV equation. This to solve for the propagation of internal waves. This makes it possible to reconstruct the internal wave signal and test the validity of the KdV model (figure 3.1 - IV).

4

Setup of the Delft3D model

To provide the local variability of internal waves in the Rhine ROFI and to study the effect of tides and winds a Delft3D is used to provide the density stratification and flow velocity structure. The model developed and validated by Rijnsburger et al. (2019a) is extended. The domain covered by this model consists of the North Sea (from Scotland up to the English Channel) and has a fine horizontal resolution in the area of the Rhine ROFI. To be able to distinguish the effect of the semi-diurnal tide, spring-neap cycle and four different wind directions only, different periods are selected where only one of these processes is changing, while the others are approximately constant. As the conditions for the year 2014 have been applied to the model, the environmental forces of this year will be discussed in section 4.1. The results from this model describe the density stratification and flow velocity structure and are used as input for the KdV model.

To obtain a good resolution of the pycnocline, the setup of the model by Rijnsburger et al. (2019a) should be checked. This to make sure that the model can provide qualitative results, which can be used as input for the KdV model (figure 3.1 - B). The different options are discussed in section 4.2.

4.1. Environmental state

To determine the typical conditions for internal wave to occur in, the density stratification and flow speeds in the Rhine ROFI under different tide and wind conditions is investigated. The model has been forced by the environmental conditions of the year 2014. In figure 4.1 the wind and discharge conditions for this year are shown. To assess the effect of tides, a time interval is selected during which the wind and discharge are constant, such that tidal variation is distinguished from other influences. The same is done for the wind direction; four periods with different wind directions are chosen in which the wind speed and discharge are approximately constant. As these conditions have been applied to the Delft3D model, the outcome for the selected periods can be used to assess the effect of tidal variation and different wind directions on internal waves.

First, a period is selected to investigate the effect of tidal variation. As M_2 and S_2 are the dominant constituents in the area (de Boer et al., 2006), the ROFI moves north and south along the coast due to the tides. The slightly different frequencies of these modes induce a spring-neap cycle, where the tidal range is larger during spring tide and smaller during neap tide. This variation induces a different amount of mixing between salt and fresh water and is therefore investigated. To address this effect the period from July, 10th till August, 8th (red part of figure 4.1) is used. This period is long enough to capture two complete spring-neap cycles. In this period no storm passed the area and the wind was more or less constantly directed onshore with an averaged speed around $5\ [\mathrm{m/s}]$. Furthermore, the discharge of the Rhine is constant (see red part of bottom plot in figure 4.1), implying that the spring-neap variation was the main variation in this period.

The other temporally varying forcing of interest is the wind. Wind has two main properties: direction and speed. In 2014 a few storms passed over the area. However, the spring-neap phase, river dis-

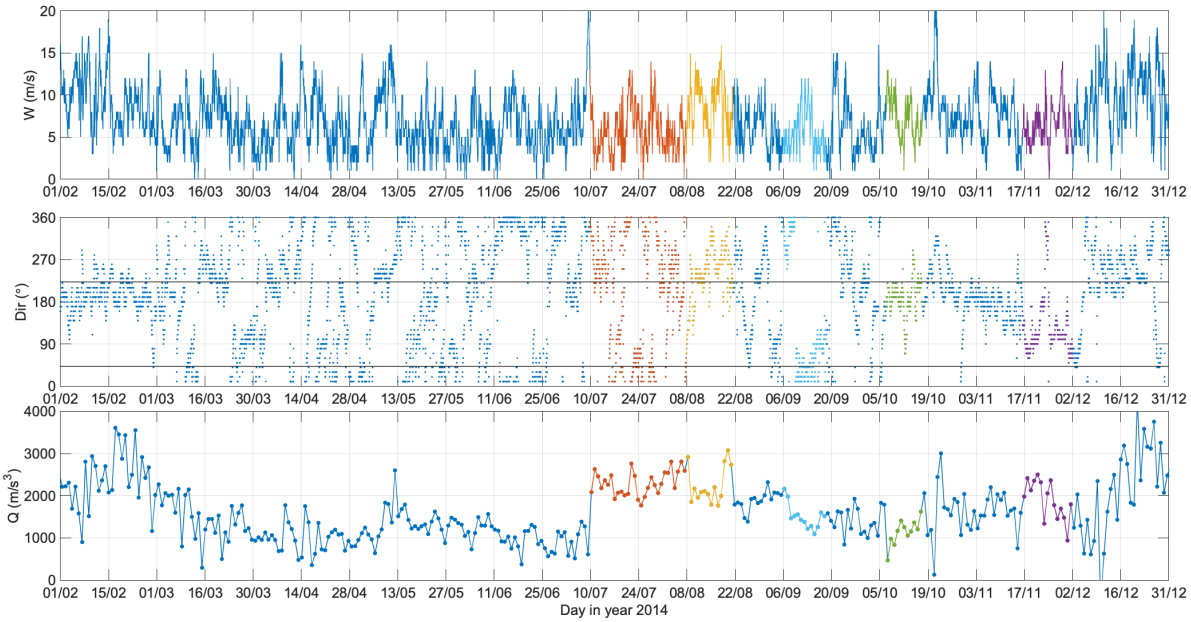

Figure 4.1: Meteorological conditions for the year 2014, data from Rijnsburger et al. (2018).
Top figure: wind speed. Middle figure: wind direction, where the grey lines indicate the orientation of the coast. Bottom figure: river discharge.
Red: July, 10th - August, 8th (tidal variation). Yellow: August, 8th - August, 22nd (onshore wind). Light blue: September, 6th - September, 19th (upwelling wind). Green: October, 7th - October, 18th (downwelling wind). Purple: November, 17th - December, 2nd (offshore wind).

charge and wind direction, were not similar during these events, a comparison for the wind speed can not be made. Therefore only the wind directions are investigated. The wind directions are grouped in four classes: offshore, onshore and two alongshore directed classes. The alongshore winds are divided in downwelling and upwelling favoring winds. The downwelling winds have a southwestern direction (from the southwest directed to the northeast) and due to Ekman transport, these events result in downwelling, (Rijnsburger et al., 2018). Upwelling winds are coming from the northeast and have (due to Ekman transport) the opposite effect: upwelling. Figure 4.1 shows that the wind speed and river discharge are approximately constant for the chosen periods: onshore (yellow), offshore (purple), alongshore downwelling (green), alongshore upwelling (light blue). The corresponding periods for these directions are August, 8th till August, 22nd (onshore); November, 17th till December, 2nd (offshore); October, 7th - October, 18th (alongshore downwelling) and September, 6th - September, 19th (alongshore upwelling). In figure 4.2 wind roses for these four periods are given.

4.2. Delft3D model settings

To be able to model internal waves, a good estimate of the pycnocline should be made. This depends on the vertical resolution and therefore increasing the vertical resolution results probably in a better estimate. The vertical resolution will be discussed first. The horizontal resolution and time-step should be reviewed after setting the vertical resolution. This to limit the computation time.

4.2.1. Vertical resolution

The model by Rijnsburger et al. (2019a) consists of 20 non-equidistant layers, see second column in figure 4.3. As sigma-layers are used in this model, the number of layers is equal on each location. Rijnsburger et al. (2019a) have considered five different options for the vertical grids, which are already partly tested (with three horizontal grids). The layout of all these grids is shown in figure 4.3.

For a good resolution of the frontal head, it is necessary to have a small grid size near the surface and near the bottom, (Rijnsburger et al., 2019a). The pycnocline is located in the upper half of the water

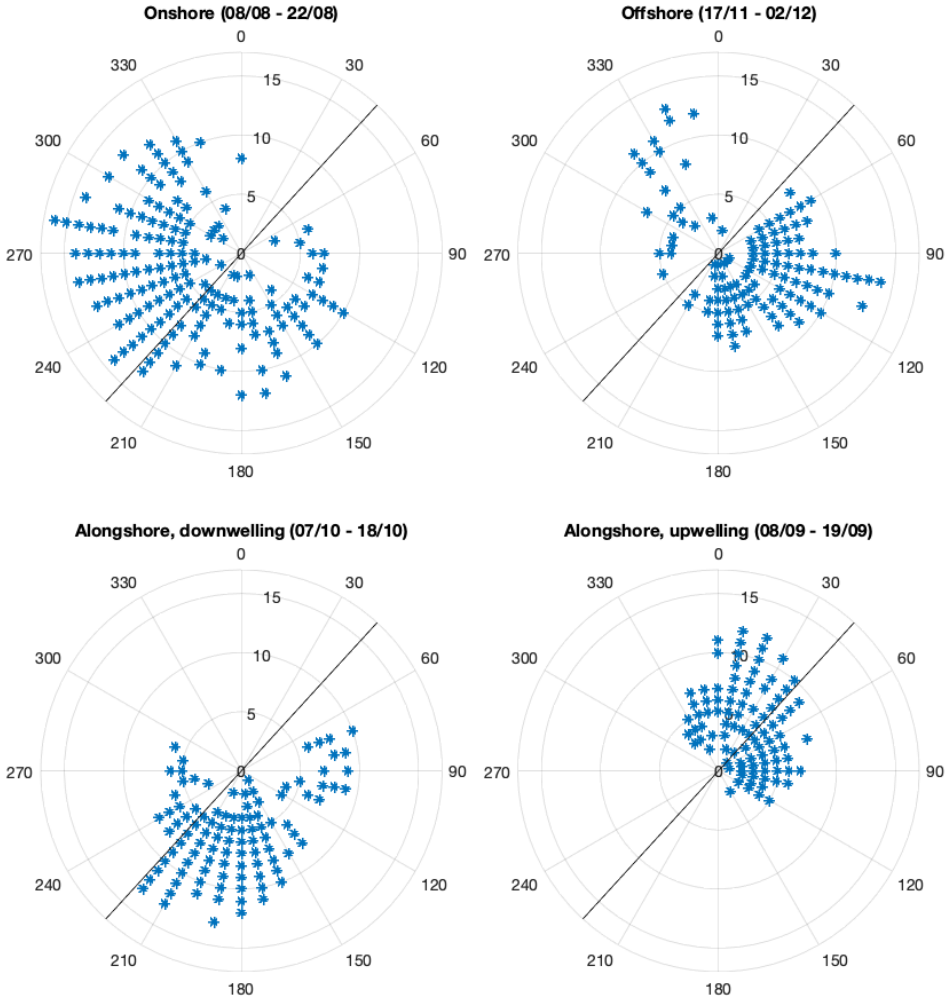

Figure 4.2: Wind speed (in $\mathrm{m/s}$) and direction (in degree from north), presented in wind roses, for the four periods with different wind directions. The grey lines indicate the orientation of the coast.

column, but not necessary in the upper 10%. Therefore a good resolved pycnocline also requires a finer grid in the center of the water column. Since both the frontal head and the location of the pycnocline have to be resolved as accurate as possible, the best option of the available grids shown in figure 4.3 is the 48-eq grid. The grid size near the surface and bed is of the same order as used by Rijnsburger et al. (2019a), but it also has a high resolution in the middle part of the water column. Therefore, the 48-eq grid is as extension to the original model by Rijnsburger et al. (2019a).

4.2.2. Horizontal resolution

The domain of the model is split, such that it is covered by four different (connected) grids. These grids are coupled such that the complete North Sea is covered and that the refinements provide a higher resolution near the Rhine ROFI. A choice is made between two different setups: four grids (figure 4.4) as in the model by Rijnsburger et al. (2019a) or three grids (figure 4.5). The third grid is extended in the area of the fourth grid, but the mesh size is kept equal. The (averaged) grid size of each grid is given in table 4.1.

Preferably the four grid model will be chosen, as Rijnsburger et al. (2019a) showed that it significantly improves the behavior of the tidal plume fronts. As a four grid model requires more time to compute relative to a three grid model (one month compared to three months), the model was first adjusted to use three refined grids. After that run was successful the model was adjusted to work with four grids.

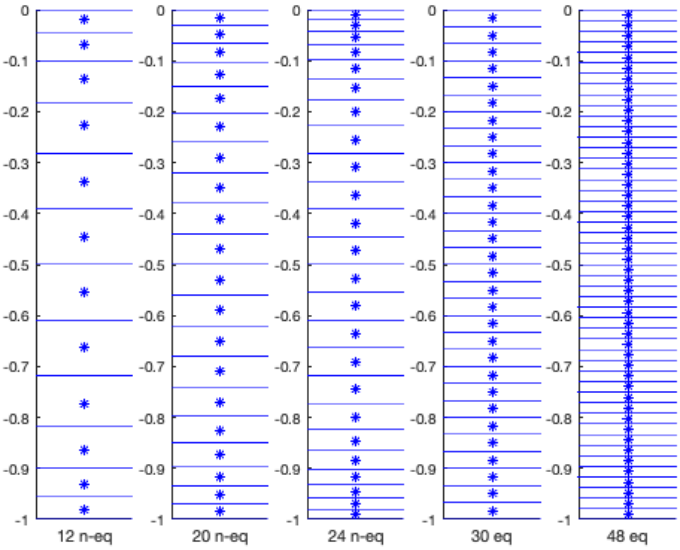

Figure 4.3: Options for vertical resolution (eq = equidistant, n-eq = non-equidistant)

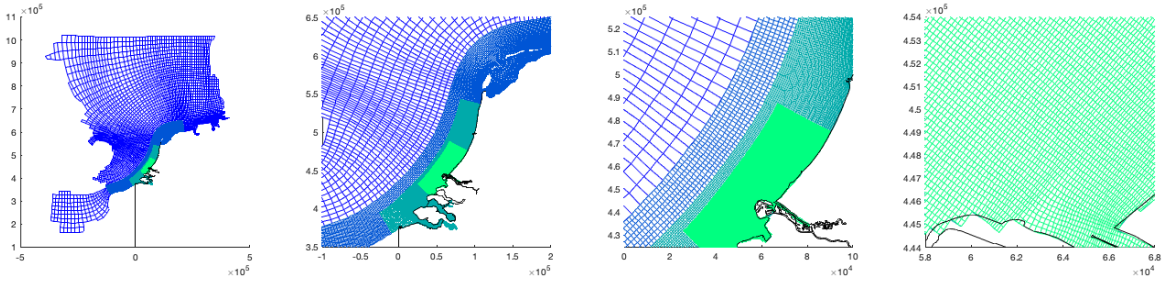

Figure 4.4: Setup with four grids

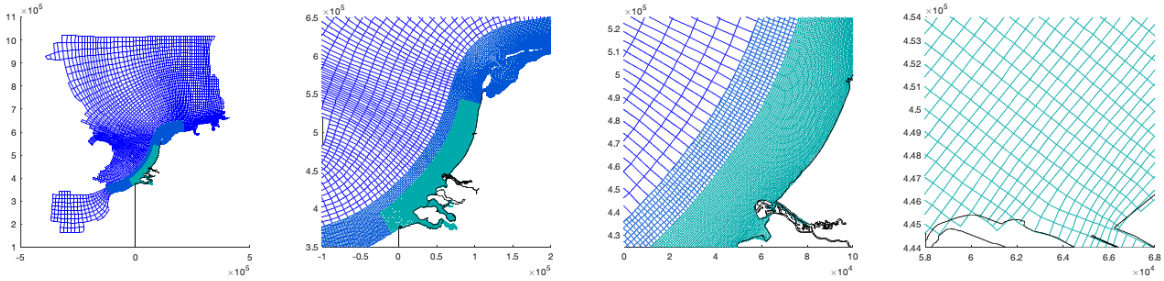

Figure 4.5: Setup with three grids

Grid	Δx, Δy
1	9.8 [km]
2	1.5 [km]
3	0.75 [km]
4	0.24 [km]

Table 4.1: Mesh sizes for different grids

Model	Number of layers	Equidistant	Number of horizontal grids	Time step
Reference	20	No	4 grids	0.8 [min]
48-3g	48	Yes	3 grids	4 [min]
48-4g-2	48	Yes	4 grids	2 [min]
48-4g-0.8	48	Yes	4 grids	0.8 [min]

Table 4.2: Specifications of the models and the reference (original) model by Rijnsburger et al. (2019a).

4.2.3. Time step

To perform the model calculation a time step needs to be chosen. In a previous model setup with three grids by Rijnsburger et al. (2019a) a time step of 4 [min] was used. Their choice was based on the CFL-condition. In the current setup this time step was also used as a first try. As no stability warnings occurred, this was a reasonable choice.

For the four grid model a smaller time step is required (accordingly to the CFL-condition), as with a time step of 4 [min] the model is unstable. With a time step of 2 [min] the model showed only some accidental warnings, while with a time step of 0.8 [min] no stability warnings occurred at all. The results of the setup with a time step 0.8 [min] are discussed in chapter 8. Here, a comparison between the results from the three different model setups will also be given.

The specifications of the different models runs as discussed are given in table 4.2.

5

Derivation of the variable bed KdV model

In this chapter, the derivation of the KdV model for internal waves on a variable bed is discussed. This is done by modification of the derivation by Grimshaw et al. (2002) for the internal wave KdV. The steps in the derivation are ordered similar to the derivation of the KdV equation for surface waves by Johnson (1997). The parameter scaling used, is mainly based on Lee and Beardsley (1974). As an addition to Grimshaw et al. (2002) a second horizontal large length scale for the variability of the bed is introduced. In contrast to the KdV equation presented by Helfrich and Melville (2006) a two-layer model is not required; a continuous density stratification profile can be accommodated. Furthermore, the Boussinesq approximation and rigid-lid assumption are not made a priori, but are made based on scaling arguments.

As a first step in deriving the KdV equation, the incompressible Euler equations are introduced, (section 5.1), allowing for a prescribed density stratification profile and a variable bed profile. In section 5.2 the equations are scaled to a non-dimensional equivalent. In section 5.3 an isopycnal coordinate system is introduced. In this new coordinate system an asymptotic expansion of the unknown physical variables is made in a small parameter ε, that is the ratio of the wave height and water depth, (section 5.4). The remaining set of equations is split in a background only (time-independent) part and a wave dependent part (influenced by the background state). The background part is solved by evaluating the time-independent equations at different orders of ε, (section 5.5). The resulting background solution is used to find a solution for the leading order wave quantities. This motivates the use of a moving reference frame, (section 5.6). At first order the long-wave limit is obtained, resulting in the Taylor-Goldstein equation, (section 5.7). At the second order, a compatibility condition is derived (section 5.8). That will be used to derive the variable bed KdV equation. Finally, in section 5.9, the dimensional variable bed KdV equation is given.

The main steps for the derivation of the variable bed KdV model are given here, detailed calculations can be found in appendix B.

5.1. Governing equations

To describe (internal) waves, the fluid can be assumed to be incompressible and inviscid, (Grimshaw et al., 2002). Therefore, the incompressible Euler equations are used. A sketch of the fluid domain is given in figure 5.1. The equation of mass conservation, which is also referred to as the continuity equation, reads (Johnson, 1997)

$$\frac{\partial \rho}{\partial t} + \frac{\partial}{\partial x}(\rho u) + \frac{\partial}{\partial z}(\rho w) = 0. \tag{5.1}$$

Here, x, z and t are the spatial and time coordinates, ρ is the density field, and u and w are respectively the horizontal and vertical velocities. For incompressible flows, the following condition can be satisfied,

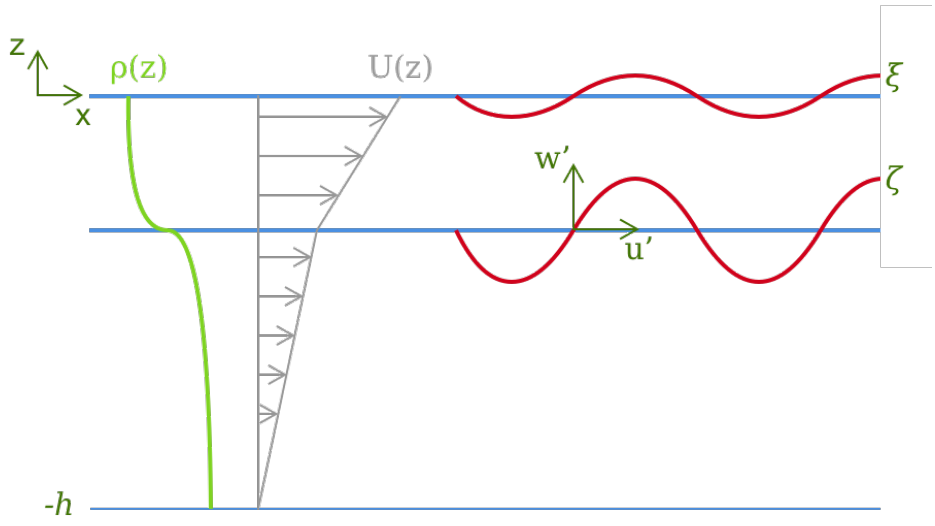

Figure 5.1: Sketch of the fluid domain. x and z horizontal- and vertical coordinates; $\rho(z)$ density stratification; $U(z)$ background flow profile; u' and w' horizontal and vertical wave induced flow velocities; ζ and ξ wave induced isopycnal displacement.

(Johnson, 1997),

$$\frac{d\rho}{dt} = \frac{\partial\rho}{\partial t} + u\frac{\partial\rho}{\partial x} + w\frac{\partial\rho}{\partial z} = 0. \tag{5.2}$$

This condition implies that the density is constant for each volume element. As also noted by Johnson (1997), the continuity equation than simplifies to

$$\frac{\partial u}{\partial x} + \frac{\partial w}{\partial z} = 0. \tag{5.3}$$

A detailed discussion can be found in appendix B, equations (B.1)-(B.3). For the horizontal and vertical momentum balances the Euler equations are used. The horizontal balance reads (Johnson, 1997)

$$\rho\left(\frac{\partial u}{\partial t} + u\frac{\partial u}{\partial x} + w\frac{\partial u}{\partial z}\right) = -\frac{\partial p}{\partial x}, \tag{5.4}$$

and the vertical balance is given by

$$\rho\left(\frac{\partial w}{\partial t} + u\frac{\partial w}{\partial x} + w\frac{\partial w}{\partial z}\right) = -\frac{\partial p}{\partial z} - g\rho. \tag{5.5}$$

Here, p is the pressure field and g is the gravitation acceleration constant.

The above equations have to be complemented by two boundary conditions. At the free-surface a kinematic and dynamic condition are prescribed, (Johnson, 1997). The kinematic condition is given by

$$w = \frac{\partial\xi}{\partial t} + u\frac{\partial\xi}{\partial x}\bigg|_{z=\xi(x,t)}, \tag{5.6}$$

where ξ is the location of the free surface and the dynamic condition is given by

$$p = p_a|_{z=\xi(x,t)}, \tag{5.7}$$

where p_a is a prescribed atmospheric pressure, which is assumed to be zero.

The location of the bed are described by a function $-h(x)$, which means that local depth can vary in space. The bottom boundary condition follows from the kinematic boundary condition and reads

$$w = -\frac{dh}{dt} = -u\frac{\partial h}{\partial x}\bigg|_{z=-h(x)}. \tag{5.8}$$

When h is assumed to be constant, this condition reduces to the flat bed boundary conditions used by Grimshaw et al. (2002), which reads

$$w = 0|_{z=-h}. \tag{5.9}$$

Usually a vertical boundary condition and initial condition are required as well. However for the derivation of the KdV equation, these are not essential and therefore left out.

5.1.1. Transformation for internal waves

The physical variables are decomposed into background and wave dependent properties, the resulting background problem is time-independent; the wave properties are allowed to vary in time. Since the background flow is assumed time-independent the decomposition can be solved independently of the wave. The wave-flow interactions only appear in the wave-dependent equations.

Isopycnal displacement

To simplify the analysis, a special vertical coordinate is used: the isopycnal coordinate. An isopycnal is a line of constant density. The isopycnals are assumed to be continuous along the x direction, such that the vertical displacement, denoted by $\zeta(x,z,t)$, is continuous in all coordinates. Note, that this vertical displacement still depends on x. This displacement has been split in a time-independent background and wave part that can consists of both a time-dependent and a time-independent part. The time-averaged displacement, denoted by $\bar{\zeta}(x,z)$, represents the change of the isopycnal lines due to the background flow and large scale bathymetry variability, while the wave part, denoted by $\zeta'(x,z,t)$, is the induced displacement by internal waves and the interaction with the background flow.

Hence the vertical displacement reads

$$\zeta(x,z,t) = \bar{\zeta}(x,z) + \zeta'(x,z,t). \tag{5.10}$$

Without loss of generality the background displacement can be chosen zero at one specific horizontal location x_0

$$\bar{\zeta}(x_0,z) = 0. \tag{5.11}$$

The isopycnal coordinate Z is defined as

$$Z := z - \zeta(x,z,t). \tag{5.12}$$

The density is constant in the (x,Z) space, implying that in the (x,z) space $Z(x,z,t)$ describes a material surface, see also section 5.3.

At any time the density may be described by the initial density profile $\rho_0(Z)$ in combination with the particle displacement ζ. The density can be split in two parts: a depth-mean density $\bar{\rho}$ and a vertical variation ρ_0, defined in terms of the isopycnal coordinate Z.

$$\rho = \bar{\rho} + \rho_0(Z), \tag{5.13}$$

This automatically satisfies the incompressibility condition, see appendix B, equations (B.4)-(B.8).

As the free surface ξ is also an isopycnal line, a similar decomposition as in (5.10) is made, resulting in

$$\xi(x,t) = \bar{\xi}(x) + \xi'(x,t). \tag{5.14}$$

Velocity decomposition

The velocity is also decomposed in a time-independent part U and the wave related part u'. The time-independent velocity U is defined in terms of the isopycnal coordinate Z, resulting in The horizontal velocity is now described as

$$u = U(x, Z) + u'(x, z, t). \tag{5.15}$$

A similar decomposition of the velocity was used by Johnson (1997); Grimshaw et al. (2002). The vertical velocity is decomposed similarly and reads

$$w = W(x, Z) + w'(x, z, t) \tag{5.16}$$

Note that in the case of a flat bed there is no contribution of the background flow to the vertical velocity field and w' could be used directly, see Grimshaw et al. (2002).

To be able to solve the background velocity field the horizontal velocity has to be prescribed at x_0, reading

$$U(x_0, Z) = U_0(Z), \tag{5.17}$$

Pressure decomposition

The decomposition of the pressure results in a part representing the hydrostatic pressure and a non-hydrostatic part:

$$p(x, z, t) = \underbrace{\int_z^{\xi(x,t)} g\rho(x, z', t)dz'}_{\text{hydrostatic pressure}} + \underbrace{Q(x, z, t)}_{\text{non-hydrostatic pressure}}. \tag{5.18}$$

Introducing the isopycnal coordinate as the a new integration variable defined by $z^* = z' - \zeta(x, z', t)$, this equation is transformed to

$$p(x, z, t) = \int_{z-\zeta(x,z,t)}^{\xi(x,t)-\zeta(x,\xi(x,t),t)} (g\bar{\rho} + g\rho_0(z^*)) \frac{1}{1 - \frac{\partial \zeta}{\partial z'}} dz^* + Q(x, z, t), \tag{5.19}$$

where the decomposition of the density ρ, equation (5.13), is used. Note that for the upper limit the free surface ξ is equal to the the displacement ζ at that point, giving

$$p(x, z, t) = \int_{z-\zeta(x,z,t)}^{0} (g\bar{\rho} + g\rho_0(z^*)) \frac{1}{1 - \frac{\partial \zeta}{\partial z'}} dz^* + Q(x, z, t). \tag{5.20}$$

The Jacobian $\frac{1}{1-\frac{\partial \zeta}{\partial z'}}$ can be rewritten using a geometric series. Requiring that $\left|\frac{\partial \zeta}{\partial z'}\right| < 1$, this results in

$$p(x, z, t) = \int_{z-\zeta(x,z,t)}^{0} g\bar{\rho} + g\rho_0(z^*)dz^* + \int_{z-\zeta(x,z,t)}^{0} (g\bar{\rho} + g\rho_0(z^*)) \sum_{k=1}^{\infty} \left(\frac{\partial \zeta}{\partial z'}\right)^k dz^* + Q(x, z, t). \tag{5.21}$$

By defining the varying pressure as

$$q(x, z, t) := Q(x, z, t) + \int_{z-\zeta(x,z,t)}^{z} g\bar{\rho} + g\rho_0(z^*)dz^* + \int_{z-\zeta(x,z,t)}^{0} (g\bar{\rho} + g\rho_0(z^*)) \sum_{k=1}^{\infty} \left(\frac{\partial \zeta}{\partial z'}\right)^k dz^*. \tag{5.22}$$

the pressure relationship (5.21), results in

$$p(x, z, t) = \underbrace{\int_z^0 g\bar{\rho} + g\rho_0(z^*)dz^*}_{\text{time-averaged hydrostatic pressure}} + \underbrace{q(x, z, t)}_{\text{varying pressure}}. \tag{5.23}$$

By calculating the first contribution of the integral on the right-handside, which is the time-averaged hydrostatic pressure resulting from the mean density, is calculated. This results in

$$p(x,z,t) = -g\bar{\rho}z + g\int_z^0 \rho_0(z^*)dz^* + q(x,z,t). \tag{5.24}$$

This expression was also used by Johnson (1997); Grimshaw et al. (2002).

Topography

Finally, the bed profile is decomposed into the mean depth and a correction due to the variable topography

$$h(x) = h_0 + h'(x). \tag{5.25}$$

The location of x_0 can now be chosen such that

$$h'(x_0) = 0. \tag{5.26}$$

These decompositions, together with the coordinate transformation, are applied to the set of equations. First, an appropriate scaling is introduced.

5.2. Scaling

To assess the order of magnitude of the various terms in the system of equations, the variables in the equations need to be made dimensionless, by using typical scales of the internal waves. A summary of all used scaling is presented in equations (5.42)-(5.59).

Scaling of the coordinate system

When modeling internal waves with respect to a spatially varying bed, there are two typical horizontal length scales. The first typical horizontal scale is associated with the internal wave variation, which is denoted by the internal wave length λ. The second scale, the horizontal scale for the variation of the bed, is denoted by l. It is assumed that the bed variations are much larger compared to the internal wave length, which means that: $l \gg \lambda$. Later on the length scale l is linked to the actual bathymetric variations in the Rhine ROFI. Since there are two distinct horizontal length scales, the method of multiple scales can be used (Holmes, 1995), resulting in two horizontal variables:

$$\hat{x} := \frac{1}{\lambda}x, \tag{5.27}$$

$$\hat{X} := \frac{1}{l}x = \frac{\lambda}{l}\frac{1}{\lambda}x, \tag{5.28}$$

The dimensionless variables are denoted with a hat. That are considered to be independent. Horizontal derivatives can now be expressed in terms of the new coordinates

$$\frac{\partial}{\partial x} = \frac{1}{\lambda}\frac{\partial}{\partial \hat{x}} + \frac{1}{l}\frac{\partial}{\partial \hat{X}}. \tag{5.29}$$

All variables now dependent on both $\hat{x}$ and $\hat{X}$.

As characteristic vertical scale the undisturbed water depth h_0 is taken, which results in the vertical scaling

$$\hat{z} = \frac{1}{h_0}z. \tag{5.30}$$

Before introducing a characteristic time scale and propagation speed, some parameters need to be introduced. First, the top to bottom density difference is denoted by $\Delta\rho$. Now the relative density, also called the Boussinesq parameter, is defined as

$$\sigma := \frac{\Delta\rho}{\bar{\rho}}, \tag{5.31}$$

where the mean density $\bar{\rho}$ is equal to the one introduced in the previous section. The characteristic (horizontal) propagation speed of an internal wave is proportional to (Sutherland, 2010)

$$\sqrt{\sigma g h_0}. \tag{5.32}$$

Using the propagation speed in combination with the characteristic horizontal length scale, a typical time scale of the phenomena of interest is obtained

$$\frac{\lambda}{\sqrt{\sigma g h_0}}, \tag{5.33}$$

which is the time needed to travel one wave length given the characteristic propagation speed. Using this characteristic time scale the dimensionless time coordinate $\hat{t}$ is defined as

$$\hat{t} = \frac{\sqrt{\sigma g h_0}}{\lambda} t. \tag{5.34}$$

Scaling of the isopycnal coordinate

The vertical displacement ζ is decomposed into a time-independent and wave-induced (time-dependent) part. Since different physical processes are associated with these different parts, a different scaling is used for these two parts. The wave-induced variation is scaled by the typical wave height a. The background isopycnal displacement $\bar{\zeta}$ is independent of time. As the isopycnal at the bottom follows the bed profile, the change of $\bar{\zeta}$ is proportional to the typical bathymetric variation h_1. Therefore, the background displacement $\bar{\zeta}$ can be scaled by h_1; it is expected that the maximum background displacement occurs at the bed.

Scaling the total displacement by the wave height a, the scaling reads

$$\hat{\zeta} = \frac{1}{a}\zeta. \tag{5.35}$$

Using this scaling it is found that

$$\hat{\zeta} = \frac{h_1}{a}\hat{\bar{\zeta}} + \hat{\zeta}'. \tag{5.36}$$

The isopycnal coordinate Z is scaled with the undisturbed water depth h_0, resulting in

$$\hat{Z} = \hat{z} - \frac{a}{h_0}\hat{\zeta}(\hat{x}, \hat{X}, \hat{z}, \hat{t}). \tag{5.37}$$

Scaling of flow velocities

To scale the velocity, the wave induced disturbance velocities are considered first. The disturbance flow u' is scaled by the characteristic propagation speed multiplied by the relative wave height, which is the wave height divided by the water depth. As the horizontal movement of a water particle is proportional to the relative wave height, this is a reasonable choice. The vertical disturbance velocity w' is scaled similar to u', except now the relative depth h_0/λ is taken into account. In order to keep the balance in the continuity equation (5.3) valid. The background shear flow is scaled with characteristic propagation speed (5.32), even though physically this scaling can not be related to the background flow. However, the assumption is made that the background velocity is of the same order as the wave speed, such that the derived equations are still valid for cases without shear flow. The scale of the vertical background velocity W is related to U, by considering the continuity equation. As the background velocities are expected to be influenced only by the bathymetric variation and not by the waves, this variation is depending on the large length scale only, the background flow is also only depending on the large length scale. The scaling for W reads

$$\hat{W} = \frac{1}{\sqrt{\sigma g h_0}} \frac{l}{h_0} W. \tag{5.38}$$

The scalings for the velocities are similar to what was presented by Lee and Beardsley (1974); Grimshaw et al. (2002).

Scaling of the density

Following Lee and Beardsley (1974) the density variation has a typical value of the top to bottom density difference $\Delta\rho$, therefore ρ_0 is scaled with this value. This means that the full dimensional density equals

$$\rho = \bar{\rho}(1 + \sigma\hat{\rho}_0). \tag{5.39}$$

The scaling for the varying pressure q is taken similar to the hydrostatic pressure, resulting in a reduction of the number of scalars in the equations.

Scaling of the boundary conditions

The typical bathymetric variations are associated to scale with h_1. The bed varies it is assumed to vary on the the large length scale only, which is similar to the slowly varying coefficients used by Holmes (1995). This means that the bed variation can be written as

$$h'(x) = h_1\hat{h}'(\hat{X}). \tag{5.40}$$

The typical slope of the bathymetry is given by h_1/l.

The locations of the free surface and bottom boundaries are scaled similar to the corresponding vertical displacement. Therefore, the time averaged free-surface $\bar{\xi}$ is scaled by h_1 and temporal variation ξ' by the wave height a.

The composed quantity is scaled with a and reads

$$\hat{\xi} = \frac{h_1}{a}\hat{\bar{\xi}} + \hat{\xi}'. \tag{5.41}$$

The complete scaling is given by

$$x = \lambda\hat{x}, \tag{5.42}$$
$$x = l\hat{X}, \tag{5.43}$$
$$z = h_0\hat{z}, \tag{5.44}$$
$$t = \frac{\lambda}{\sqrt{\sigma g h_0}}\hat{t}, \tag{5.45}$$
$$\bar{\zeta}(x,z) = h_1\hat{\bar{\zeta}}(\hat{x},\hat{z}), \tag{5.46}$$
$$\zeta'(x,z,t) = a\hat{\zeta}'(\hat{x},\hat{z},\hat{t}), \tag{5.47}$$
$$\zeta(x,z,t) = a\hat{\zeta}(\hat{x},\hat{z},\hat{t}), \tag{5.48}$$
$$Z(x,z,t) = h_0\hat{Z}(\hat{x},\hat{X},\hat{z},\hat{t}), \tag{5.49}$$
$$U(x,Z) = \sqrt{\sigma g h_0}\hat{U}(\hat{x},\hat{X},\hat{Z}), \tag{5.50}$$
$$u'(x,z,t) = \sqrt{\sigma g h_0}\frac{a}{h_0}\hat{u}'(\hat{x},\hat{X},\hat{z},\hat{t}), \tag{5.51}$$
$$W(x,Z) = \sqrt{\sigma g h_0}\frac{h_0}{l}\hat{W}(\hat{x},\hat{X},\hat{Z}), \tag{5.52}$$
$$w'(x,z,t) = \sqrt{\sigma g h_0}\frac{a}{h_0}\frac{h_0}{\lambda}\hat{w}'(\hat{x},\hat{X},\hat{z},\hat{t}), \tag{5.53}$$
$$\rho_0(Z) = \bar{\rho}\sigma\hat{\rho}_0(\hat{Z}), \tag{5.54}$$
$$q(x,z,t) = ag\Delta\rho\hat{q}(\hat{x},\hat{X},\hat{z},\hat{t}), \tag{5.55}$$
$$h'(x) = h_1\hat{h}'(\hat{X}), \tag{5.56}$$
$$\bar{\xi}(x) = h_1\hat{\bar{\xi}}(\hat{x}), \tag{5.57}$$
$$\xi'(x,t) = a\hat{\xi}'(\hat{x},\hat{t}), \tag{5.58}$$
$$\xi(x,t) = a\hat{\xi}(\hat{x},\hat{t}). \tag{5.59}$$

Here, all variables with a hat on top denote the dimensionless variables.

The governing equations are now transformed using all transformations of the previous section. Furthermore, the scaling is carried out. Detailed calculations can be found in appendix B (equation (B.9) to (B.21)). Four small parameters are defined: the relative wave height, given by

$$\varepsilon = \frac{a}{h_0}, \tag{5.60}$$

the relative depth

$$\delta = \frac{h_0}{\lambda}, \tag{5.61}$$

the wave length relative to the bathymetric variations

$$\mu = \frac{\lambda}{l}, \tag{5.62}$$

and the relative bed change

$$\gamma = \frac{h_1}{h_0}. \tag{5.63}$$

Using these parameters, the transformed equations are

$$(1+\sigma\hat{\rho}_0)\left[\left(\frac{\partial\hat{U}}{\partial\hat{t}}+\varepsilon\frac{\partial\hat{u}'}{\partial\hat{t}}\right)+\left(\hat{U}+\varepsilon\hat{u}'\right)\left(\frac{\partial\hat{U}}{\partial\hat{x}}+\varepsilon\frac{\partial\hat{u}'}{\partial\hat{x}}+\mu\frac{\partial\hat{U}}{\partial\hat{X}}+\mu\varepsilon\frac{\partial\hat{u}'}{\partial\hat{X}}\right)+\left(\mu\hat{W}+\varepsilon\hat{w}'\right)\left(\frac{\partial\hat{U}}{\partial\hat{z}}+\varepsilon\frac{\partial\hat{u}'}{\partial\hat{z}}\right)\right]+\varepsilon\frac{\partial\hat{q}}{\partial\hat{x}}+\varepsilon\mu\frac{\partial\hat{q}}{\partial\hat{X}}=0, \tag{5.64}$$

$$\delta^2(1+\sigma\hat{\rho}_0)\left[\left(\mu\frac{\partial\hat{W}}{\partial\hat{t}}+\varepsilon\frac{\partial\hat{w}'}{\partial\hat{t}}\right)+\left(\hat{U}+\varepsilon\hat{u}'\right)\left(\mu\frac{\partial\hat{W}}{\partial\hat{x}}+\varepsilon\frac{\partial\hat{w}'}{\partial\hat{x}}+\mu^2\frac{\partial\hat{W}}{\partial\hat{X}}+\varepsilon\mu\frac{\partial\hat{w}'}{\partial\hat{X}}\right)+\left(\mu\hat{W}+\varepsilon\hat{w}'\right)\left(\mu\frac{\partial\hat{W}}{\partial\hat{z}}+\varepsilon\frac{\partial\hat{w}'}{\partial\hat{z}}\right)\right]+\varepsilon\frac{\partial\hat{q}}{\partial\hat{z}}-\hat{\rho}_0(\hat{z})+\hat{\rho}_0(\hat{Z})=0, \tag{5.65}$$

$$\left(\frac{\partial\hat{U}}{\partial\hat{x}}+\varepsilon\frac{\partial\hat{u}'}{\partial\hat{x}}+\mu\frac{\partial\hat{U}}{\partial\hat{X}}+\varepsilon\mu\frac{\partial\hat{u}'}{\partial\hat{X}}\right)+\mu\frac{\partial\hat{W}}{\partial\hat{z}}+\varepsilon\frac{\partial\hat{w}'}{\partial\hat{z}}=0, \tag{5.66}$$

$$-\gamma\mu\left(\hat{U}+\varepsilon\hat{u}'\right)\frac{\partial\hat{h}'}{\partial\hat{X}}=\mu\hat{W}+\varepsilon\hat{w}'\big|_{\hat{z}=-1-\gamma\hat{h}'}, \tag{5.67}$$

$$\varepsilon\hat{\xi}-\sigma\int_{\varepsilon\hat{\xi}}^{0}\hat{\rho}_0(z')dz'=\varepsilon\sigma\hat{q}|_{\hat{z}=\varepsilon\hat{\xi}}, \tag{5.68}$$

$$\varepsilon\frac{\partial\hat{\xi}}{\partial\hat{t}}+\left(\hat{U}+\varepsilon\hat{u}'\right)\left(\varepsilon\frac{\partial\hat{\xi}}{\partial\hat{x}}+\varepsilon\mu\frac{\partial\hat{\xi}}{\partial\hat{X}}\right)=\mu\hat{W}+\varepsilon\hat{w}'\big|_{\hat{z}=\varepsilon\hat{\xi}}. \tag{5.69}$$

Note, that in these equations (unless noted otherwise) $\hat{\rho}_0$ and $\hat{U}$ are functions of $\hat{Z}$ and not of $\hat{z}$. For simplicity the hats on top of the variables are dropped from now on.

5.2.1. Relating the relative wave height to the relative depth

Four small parameters ε, δ, μ and γ are left in the current equations. Lee and Beardsley (1974); Lamb and Yan (1996); Grimshaw et al. (2002) relate these two parameters by using the substitution: $\varepsilon = \delta^2$. Johnson (1997) showed, while deriving the KdV equation for surface waves, that by introducing an addition scaling step, δ can be removed without using this assumption explicitly. When required that

the quantities before and after this second scaling are both of order one, still the assumption $\varepsilon = \mathcal{O}\left(\delta^2\right)$ needs to be adopted, but this second scaling allows small changes between these two parameters. The final result is exactly the same, as when the substitution $\varepsilon = \delta^2$ is used directly. To show that this also works for internal waves, the approach of Johnson (1997) is used and extended for internal waves and variable topography, resulting in

$$x = \frac{\delta}{\sqrt{\varepsilon}} x^*, \tag{5.70}$$

$$X = \frac{\delta}{\sqrt{\varepsilon}} X^*, \tag{5.71}$$

$$t = \frac{\delta}{\sqrt{\varepsilon}} t^*, \tag{5.72}$$

$$w' = \frac{\sqrt{\varepsilon}}{\delta} w'^*, \tag{5.73}$$

$$W = \frac{\sqrt{\varepsilon}}{\delta} W^*. \tag{5.74}$$

No other variables are rescaled. The explicit rescaling is performed in equation (B.22)-(B.33) and results in

$$\begin{aligned}(1+\sigma\rho_0^*)\left[\left(\frac{\partial U^*}{\partial \hat{t}} + \varepsilon\frac{\partial u'^*}{\partial t^*}\right) + (U^*+\varepsilon u'^*)\left(\frac{\partial U^*}{\partial x^*} + \varepsilon\frac{\partial u^*}{\partial x^*} + \mu\frac{\partial U^*}{\partial X^*} + \mu\varepsilon\frac{\partial u'^*}{\partial X^*}\right)\right.\\ \left. + (\mu W^* + \varepsilon w'^*)\left(\frac{\partial U^*}{\partial z^*} + \varepsilon\frac{\partial u'^*}{\partial z^*}\right)\right] + \varepsilon\frac{\partial q^*}{\partial x^*} + \varepsilon\mu\frac{\partial q^*}{\partial X^*} = 0,\end{aligned} \tag{5.75}$$

$$\begin{aligned}\varepsilon(1+\sigma\rho_0^*)\left[\left(\mu\frac{\partial W^*}{\partial t^*} + \varepsilon\frac{\partial w'^*}{\partial t^*}\right) + (U^*+\varepsilon u'^*)\left(\mu\frac{\partial W^*}{\partial x^*} + \varepsilon\frac{\partial w'^*}{\partial x^*} + \mu^2\frac{\partial W^*}{\partial X^*} + \varepsilon\mu\frac{\partial w'^*}{\partial X^*}\right)\right.\\ \left. + (\mu W^* + \varepsilon w'^*)\left(\mu\frac{\partial W^*}{\partial z^*} + \varepsilon\frac{\partial w'^*}{\partial z^*}\right)\right] + \varepsilon\frac{\partial q^*}{\partial z^*} - \rho_0^*(z^*) + \rho_0^*(Z^*) = 0,\end{aligned} \tag{5.76}$$

$$\left(\frac{\partial U^*}{\partial x^*} + \varepsilon\frac{\partial u'^*}{\partial x^*} + \mu\frac{\partial U^*}{\partial X^*} + \varepsilon\mu\frac{\partial u'^*}{\partial X^*}\right) + \mu\frac{\partial W^*}{\partial z^*} + \varepsilon\frac{\partial w'^*}{\partial z^*} = 0, \tag{5.77}$$

$$-\gamma\mu\,(U^*+\varepsilon u'^*)\,\frac{\partial h'^*}{\partial X^*} = \mu W^* + \varepsilon w'^*|_{z^*=-1-\gamma h'^*}, \tag{5.78}$$

$$\varepsilon\xi^* - \sigma\int_{\varepsilon\xi^*}^{0}\rho_0^*(z')dz' = \varepsilon\sigma q^*|_{z^*=\varepsilon\xi^*}, \tag{5.79}$$

$$\varepsilon\frac{\partial\xi^*}{\partial t^*} + (U^*+\varepsilon u'^*)\left(\varepsilon\frac{\partial\xi^*}{\partial x^*} + \varepsilon\mu\frac{\partial\xi^*}{\partial X^*}\right) = \mu W^* + \varepsilon w'^*|_{z^*=\varepsilon\xi^*}. \tag{5.80}$$

Comparing these equations with (5.64)-(5.69), it is observed that only δ^2 is replaced by ε. From now on the asterisks on top of the variables are dropped to improve readability.

5.3. Isopycnal coordinate system

In section 5.2 the vertical displacement field ζ and corresponding isopycnal coordinate Z were introduced. To be able to solve the system of equations, the system is now completely transformed to this new coordinate. First, the coordinate system is introduced and the transformation will be compared to the theory of Generalized Lagrangian Mean flow. Finally, the coordinate transformation is applied to the system of equations.

Previously, it has already been shown that the incompressibility condition is satisfied when using equation (5.12), $Z = z - \zeta(x,z,t)$, in combination with

$$w = \frac{d\zeta}{dt} = \frac{\partial\zeta}{\partial t} + u\frac{\partial\zeta}{\partial x} + w\frac{\partial\zeta}{\partial z}, \tag{5.81}$$

in the dimensional coordinate system. This showed, that the density may be written as a function of the short hand Z only. Using the new scaled coordinates equation (5.81) reads

$$\mu W + \varepsilon w' = \varepsilon \frac{d\zeta}{dt} = \varepsilon \left[\frac{\partial \zeta}{\partial t} + (U + \varepsilon u') \left(\frac{\partial \zeta}{\partial x} + \mu \frac{\partial \zeta}{\partial X} \right) + (\mu W + \varepsilon w') \frac{\partial \zeta}{\partial z} \right]. \tag{5.82}$$

Next, introduce the new set of coordinates, where the isopycnal coordinate $\tilde{Z}$ is used:

$$\tilde{x} = x, \tag{5.83}$$
$$\tilde{X} = X, \tag{5.84}$$
$$\tilde{Z} = z - \varepsilon \zeta(x, z, t), \tag{5.85}$$
$$\tilde{t} = t. \tag{5.86}$$

Note, that all coordinates and quantities in the new coordinate system are noted by a tilde and that the displacement is written as $\tilde{\eta}$, such that

$$\zeta(x, X, z, t) = \tilde{\eta}(x, X, z - \varepsilon \zeta(x, X, z, t), t) \equiv \tilde{\eta}(\tilde{x}, \tilde{X}, \tilde{Z}, \tilde{t}). \tag{5.87}$$

In equations (B.38)-(B.57) all necessary transformations for the derivatives are calculated. Using the relationship from (B.49) equation (5.82) reads

$$\mu \tilde{W} + \varepsilon \tilde{w}' = \varepsilon \frac{\partial \tilde{\eta}}{\partial \tilde{t}} + \varepsilon (\tilde{U} + \varepsilon \tilde{u}') \left(\frac{\partial \tilde{\eta}}{\partial \tilde{x}} + \mu \frac{\partial \tilde{\eta}}{\partial \tilde{X}} \right). \tag{5.88}$$

Another way to look at an isopycnal is using the fact, that it is a material surface. The kinematic condition holds for all material surfaces. Consider a specific surface $\zeta_Z(x, t)$ at an arbitrary initial level $Z \in [-h, 0]$, then is obtained in dimensional coordinates

$$w = \frac{\partial \zeta_Z}{\partial t} + u \frac{\partial \zeta_Z}{\partial x}, \text{ at } (x, Z, t). \tag{5.89}$$

After scaling and transformation to the new scaled coordinate system, this relationship reads

$$\mu \tilde{W} + \varepsilon \tilde{w}' = \varepsilon \frac{\partial \tilde{\eta}_Z}{\partial \tilde{t}} + \varepsilon (\tilde{U} + \varepsilon \tilde{u}') \left(\frac{\partial \tilde{\eta}_Z}{\partial \tilde{x}} + \mu \frac{\partial \tilde{\eta}_Z}{\partial \tilde{X}} \right), \text{ at } (\tilde{x}, \tilde{X}, \tilde{t}). \tag{5.90}$$

This is equivalent to the condition provided in equation (5.88) as $\tilde{\eta}_Z$ exists for all values of $\tilde{Z}$.

The way of describing water flows in moving coordinates is also covered in the theory of Generalized Lagrangian Mean Flow, (Andrews & Mcintyre, 1978). Here, a similar, but two-dimensional, displacement field is created following the movement of particles due to waves. Assume that the mapping induced by the displacement field is invertible. This makes sense as each individual particle is tracked in the mapping, and for each particle there is a one to one relationship (between different times). Required by the Generalized Lagrangian Mean Flow is that time average of ζ is zero, which implies that ζ is a disturbance quantity. Next, Lagrangian disturbance velocities corresponding to the displacement field can be obtained, which are u' for the horizontal velocity and w' for the vertical velocity. Required is that the Eulerian averaged value of these velocity fields also equal zero. The definition of the Lagrangian disturbance velocity, as introduced by Andrews and Mcintyre (1978), implies that the flow can be decomposed in a main (background shear) flow and an (internal) wave disturbance field, which is similar to what was presented in (5.15). Finally, Andrews and Mcintyre (1978) also came up with the relationship in equation (5.82).

The previous set of equations (5.75)-(5.80) is transformed to use the new coordinate Z, using the transformations from (B.38)-(B.57). As stated earlier all new coordinate and variables are denoted by

a tilde. The resulting system of equations reads, see (B.58)-(B.74) for the details of the transformation,

$$(1+\sigma\tilde{\rho}_0)\left[\varepsilon\frac{\partial\tilde{u}'}{\partial\tilde{t}}+(\tilde{U}+\varepsilon\tilde{u}')\left(\frac{\partial\tilde{U}}{\partial\tilde{x}}+\varepsilon\frac{\partial\tilde{u}'}{\partial\tilde{x}}+\mu\frac{\partial\tilde{U}}{\partial\tilde{X}}+\mu\varepsilon\frac{\partial\tilde{u}'}{\partial\tilde{X}}\right)\right]$$
$$+\varepsilon\left(\frac{\partial\tilde{q}}{\partial\tilde{x}}+\mu\frac{\partial\tilde{q}}{\partial\tilde{X}}\right)-\varepsilon^2\frac{\partial\tilde{q}}{\partial\tilde{Z}}\frac{\frac{\partial\tilde{\eta}}{\partial\tilde{x}}+\mu\frac{\partial\tilde{\eta}}{\partial\tilde{X}}}{1+\varepsilon\frac{\partial\tilde{\eta}}{\partial\tilde{z}}}=0, \tag{5.91}$$

$$\varepsilon(1+\sigma\tilde{\rho}_0)\left[\mu\frac{\partial\tilde{W}}{\partial\tilde{t}}+\varepsilon\frac{\partial\tilde{w}'}{\partial\tilde{t}}+(\tilde{U}+\varepsilon\tilde{u}')\left(\mu\frac{\partial\tilde{W}}{\partial\tilde{x}}+\varepsilon\frac{\partial\tilde{w}'}{\partial\tilde{x}}+\mu^2\frac{\partial\tilde{W}}{\partial\tilde{X}}+\varepsilon\mu\frac{\partial\tilde{w}'}{\partial\tilde{X}}\right)\right]$$
$$+\varepsilon\frac{\partial\tilde{q}}{\partial\tilde{Z}}\frac{1}{1+\varepsilon\frac{\partial\tilde{\eta}}{\partial\tilde{z}}}+\tilde{\rho}_0(\tilde{Z})-\tilde{\rho}_0(\tilde{Z}+\varepsilon\tilde{\eta})=0, \tag{5.92}$$

$$\frac{\partial\tilde{U}}{\partial\tilde{x}}+\varepsilon\frac{\partial\tilde{u}'}{\partial\tilde{x}}+\mu\frac{\partial\tilde{U}}{\partial\tilde{X}}+\varepsilon\mu\frac{\partial\tilde{u}'}{\partial\tilde{X}}+\mu\frac{\partial\tilde{W}}{\partial\tilde{Z}}+\varepsilon\frac{\partial\tilde{w}'}{\partial\tilde{Z}}$$
$$-\frac{\varepsilon}{1+\varepsilon\frac{\partial\tilde{\eta}}{\partial\tilde{z}}}\left[\left(\frac{\partial\tilde{U}}{\partial\tilde{Z}}+\varepsilon\frac{\partial\tilde{u}'}{\partial\tilde{Z}}\right)\left(\frac{\partial\tilde{\eta}}{\partial\tilde{x}}+\mu\frac{\partial\tilde{\eta}}{\partial\tilde{X}}\right)+\left(\mu\frac{\partial\tilde{W}}{\partial\tilde{Z}}+\varepsilon\frac{\partial\tilde{w}'}{\partial\tilde{Z}}\right)\frac{\partial\tilde{\eta}}{\partial\tilde{Z}}\right]=0, \tag{5.93}$$

$$\mu\tilde{W}+\varepsilon\tilde{w}'=\varepsilon\frac{\partial\tilde{\eta}}{\partial\tilde{t}}+\varepsilon(\tilde{U}+\varepsilon\tilde{u}')\left(\frac{\partial\tilde{\eta}}{\partial\tilde{x}}+\mu\frac{\partial\tilde{\eta}}{\partial\tilde{X}}\right), \tag{5.94}$$

$$\varepsilon\tilde{\eta}=-\gamma\tilde{h}'\big|_{\tilde{Z}=-1}, \tag{5.95}$$

$$\varepsilon\tilde{\eta}+\sigma\int_0^{\varepsilon\tilde{\eta}}\tilde{\rho}_0(z')dz'=\varepsilon\sigma\tilde{q}|_{\tilde{Z}=0}. \tag{5.96}$$

From now on the tilde on top of the variables is dropped.

5.4. Asymptotic expansion

The solution to the final system of equations, is obtained using an asymptotic expansion of the physical variables. Before this expansion is made, the number of equations and variables is reduced. By substitution of the four governing equations, W, w' and q can be expressed in terms of the other physical variables, see equations (B.75)-(B.90) in appendix B for the details. Therefore, they are removed from the system of equations. Also, the number of equations valid inside the domain is now lowered from four to only two. The resulting set of equations for U, u' and η reads

$$\frac{\partial}{\partial Z}\left\{(1+\sigma\rho_0)\left[\varepsilon\frac{\partial u'}{\partial t}+(U+\varepsilon u')\left(\frac{\partial U}{\partial x}+\varepsilon\frac{\partial u'}{\partial x}+\mu\frac{\partial U}{\partial X}+\varepsilon\mu\frac{\partial u'}{\partial X}\right)\right]\right\}$$
$$-\left(\frac{\partial}{\partial x}+\mu\frac{\partial}{\partial X}\right)\left\{\varepsilon^2(1+\sigma\rho_0)\left[\frac{\partial}{\partial t}+(U+\varepsilon u')\left(\frac{\partial}{\partial x}+\mu\frac{\partial}{\partial X}\right)\right]^2\eta\right\}\left[1+\varepsilon\frac{\partial\eta}{\partial Z}\right]$$
$$+\frac{\partial}{\partial Z}\left\{\varepsilon^3(1+\sigma\rho_0)\left[\frac{\partial}{\partial t}+(U+\varepsilon u')\left(\frac{\partial}{\partial x}+\mu\frac{\partial}{\partial X}\right)\right]^2\eta\right\}\left(\frac{\partial\eta}{\partial x}+\mu\frac{\partial\eta}{\partial X}\right)+\varepsilon\frac{\partial\rho_0}{\partial Z}\left(\frac{\partial\eta}{\partial x}+\mu\frac{\partial\eta}{\partial X}\right)=0. \tag{5.97}$$

$$\left[1+\varepsilon\frac{\partial\eta}{\partial Z}\right]\left(\frac{\partial U}{\partial x}+\varepsilon\frac{\partial u'}{\partial x}+\mu\frac{\partial U}{\partial X}+\varepsilon\mu\frac{\partial u'}{\partial X}\right)+\varepsilon\left[\frac{\partial}{\partial t}+(U+\varepsilon u')\left(\frac{\partial}{\partial x}+\mu\frac{\partial}{\partial X}\right)\right]\frac{\partial\eta}{\partial Z}=0. \tag{5.98}$$

$$\varepsilon\eta=-\gamma h'|_{Z=-1} \tag{5.99}$$

$$\varepsilon\left(\frac{\partial\eta}{\partial x}+\mu\frac{\partial\eta}{\partial X}\right)=-\sigma\left[\varepsilon\frac{\partial u'}{\partial t}+(U+\varepsilon u')\left(\frac{\partial U}{\partial x}+\varepsilon\frac{\partial u'}{\partial x}+\mu\frac{\partial U}{\partial X}+\mu\varepsilon\frac{\partial u'}{\partial X}\right)\right]$$
$$-\varepsilon^3\sigma\left\{\left[\frac{\partial}{\partial t}+(U+\varepsilon u')\left(\frac{\partial}{\partial x}+\mu\frac{\partial}{\partial X}\right)\right]^2\eta\right\}\left(\frac{\partial\eta}{\partial x}+\mu\frac{\partial\eta}{\partial X}\right)\Bigg|_{Z=0} \tag{5.100}$$

In section 5.1.1 a decomposition was introduced for the isopycnal displacement ζ. This decomposition of η, using equations (5.36) and (5.87) reads

$$\eta(x,X,Z,t) = \frac{h_1}{a}\bar{\eta}(x,X,Z) + \eta'(x,X,Z,t), \tag{5.101}$$

or, using the definitions of the small parameters ε and γ,

$$\eta(x,X,Z,t) = \frac{\gamma}{\varepsilon}\bar{\eta}(x,X,Z) + \eta'(x,X,Z,t). \tag{5.102}$$

Introducing this decomposition the system of equations, yields

$$\begin{aligned}
&\frac{\partial}{\partial Z}\left\{(1+\sigma\rho_0)\left[\varepsilon\frac{\partial u'}{\partial t} + (U+\varepsilon u')\left(\frac{\partial U}{\partial x} + \varepsilon\frac{\partial u'}{\partial x} + \mu\frac{\partial U}{\partial X} + \varepsilon\mu\frac{\partial u'}{\partial X}\right)\right]\right\} \\
&-\left(\frac{\partial}{\partial x} + \mu\frac{\partial}{\partial X}\right)\left\{\varepsilon(1+\sigma\rho_0)\left[\frac{\partial}{\partial t} + (U+\varepsilon u')\left(\frac{\partial}{\partial x} + \mu\frac{\partial}{\partial X}\right)\right]^2(\gamma\bar{\eta} + \varepsilon\eta')\right\}\left[1 + \gamma\frac{\partial\bar{\eta}}{\partial Z} + \varepsilon\frac{\partial\eta'}{\partial Z}\right] \\
&+\frac{\partial}{\partial Z}\left\{\varepsilon(1+\sigma\rho_0)\left[\frac{\partial}{\partial t} + (U+\varepsilon u')\left(\frac{\partial}{\partial x} + \mu\frac{\partial}{\partial X}\right)\right]^2(\gamma\bar{\eta} + \varepsilon\eta')\right\}\left(\gamma\frac{\partial\bar{\eta}}{\partial x} + \varepsilon\frac{\partial\eta'}{\partial x} + \mu\gamma\frac{\partial\bar{\eta}}{\partial X} + \mu\varepsilon\frac{\partial\eta'}{\partial X}\right) \\
&+\frac{\partial\rho_0}{\partial Z}\left(\gamma\frac{\partial\bar{\eta}}{\partial x} + \varepsilon\frac{\partial\eta'}{\partial x} + \mu\gamma\frac{\partial\bar{\eta}}{\partial X} + \mu\varepsilon\frac{\partial\eta'}{\partial X}\right) = 0,
\end{aligned} \tag{5.103}$$

$$\begin{aligned}
&\left[1 + \gamma\frac{\partial\bar{\eta}}{\partial Z} + \varepsilon\frac{\partial\eta'}{\partial Z}\right]\left(\frac{\partial U}{\partial x} + \varepsilon\frac{\partial u'}{\partial x} + \mu\frac{\partial U}{\partial X} + \varepsilon\mu\frac{\partial u'}{\partial X}\right) \\
&+\left[\frac{\partial}{\partial t} + (U+\varepsilon u')\left(\frac{\partial}{\partial x} + \mu\frac{\partial}{\partial X}\right)\right]\left(\gamma\frac{\partial\bar{\eta}}{\partial Z} + \varepsilon\frac{\partial\eta'}{\partial Z}\right) = 0.
\end{aligned} \tag{5.104}$$

$$\gamma\bar{\eta} + \varepsilon\eta' = -\gamma h'|_{Z=-1} \tag{5.105}$$

$$\begin{aligned}
\gamma\frac{\partial\bar{\eta}}{\partial x} + \varepsilon\frac{\partial\eta'}{\partial x} + \mu\gamma\frac{\partial\bar{\eta}}{\partial X} + \mu\varepsilon\frac{\partial\eta'}{\partial X} &= -\sigma\left[\varepsilon\frac{\partial u'}{\partial t} + (U+\varepsilon u')\left(\frac{\partial U}{\partial x} + \varepsilon\frac{\partial u'}{\partial x} + \mu\frac{\partial U}{\partial X} + \mu\varepsilon\frac{\partial u'}{\partial X}\right)\right] \\
&-\varepsilon\sigma\left\{\left[\frac{\partial}{\partial t} + (U+\varepsilon u')\left(\frac{\partial}{\partial x} + \mu\frac{\partial}{\partial X}\right)\right]^2(\gamma\bar{\eta} + \varepsilon\eta')\right\} \\
&\cdot\left(\gamma\frac{\partial\bar{\eta}}{\partial x} + \varepsilon\frac{\partial\eta'}{\partial x} + \mu\gamma\frac{\partial\bar{\eta}}{\partial X} + \mu\varepsilon\frac{\partial\eta'}{\partial X}\right)\Big|_{Z=0}
\end{aligned} \tag{5.106}$$

The unknown physical variables $\bar{\eta}$, η', U and u' are expanded in the small parameter ε as

$$\bar{\eta}(x,X,Z) = \sum_{i=0}^{\infty}\varepsilon^i\bar{\eta}^{(i)}(x,X,Z), \tag{5.107}$$

$$\eta'(x,X,Z,t) = \sum_{i=0}^{\infty}\varepsilon^i\eta'^{(i)}(x,X,Z,t), \tag{5.108}$$

$$U(x,X,Z) = \sum_{i=0}^{\infty}\varepsilon^i U^{(i)}(x,X,Z), \tag{5.109}$$

$$u'(x,X,Z,t) = \sum_{i=0}^{\infty}\varepsilon^i u'^{(i)}(x,X,Z,t). \tag{5.110}$$

To order the system of equations in terms of ε, the other small parameters have to be linked to ε. This is done by by using their typical order of magnitude compared to ε. This results in

$$\sigma = \varepsilon^2 \hat{\sigma}, \tag{5.111}$$
$$\gamma = \varepsilon \hat{\gamma}, \tag{5.112}$$
$$\mu = \varepsilon^2 \hat{\mu}, \tag{5.113}$$

with $\hat{\sigma}$, $\hat{\gamma}$ and $\hat{\mu}$ order 1 quantities. These scalings hold for the observations of the Rhine ROFI. In section 10.2 this is checked.

5.5. Time-independent problem

To solve for background flow, the wave quantities are set to zero, resulting in a system of equations where the only unknowns are the background flow U and time-averaged displacement $\bar{\eta}$. This system of equations reads

$$\begin{aligned}
&\frac{\partial}{\partial Z}\left\{(1+\varepsilon^2\hat{\sigma}\rho_0)\left[U\left(\frac{\partial U}{\partial x}+\varepsilon^2\hat{\mu}\frac{\partial U}{\partial X}\right)\right]\right\}\\
-\varepsilon^2\hat{\gamma}\left(\frac{\partial}{\partial x}+\varepsilon^2\hat{\mu}\frac{\partial}{\partial X}\right)&\left\{(1+\varepsilon^2\hat{\sigma}\rho_0)\left[U\left(\frac{\partial}{\partial x}+\varepsilon^2\hat{\mu}\frac{\partial}{\partial X}\right)\right]^2\bar{\eta}\right\}\left[1+\varepsilon\hat{\gamma}\frac{\partial\bar{\eta}}{\partial Z}\right]\\
+\varepsilon^3\hat{\gamma}^2\frac{\partial}{\partial Z}&\left\{(1+\varepsilon^2\hat{\sigma}\rho_0)\left[U\left(\frac{\partial}{\partial x}+\varepsilon^2\hat{\mu}\frac{\partial}{\partial X}\right)\right]^2\bar{\eta}\right\}\left(\frac{\partial\bar{\eta}}{\partial x}+\varepsilon^2\hat{\mu}\frac{\partial\bar{\eta}}{\partial X}\right)\\
&+\varepsilon\hat{\gamma}\frac{\partial\rho_0}{\partial Z}\left(\frac{\partial\bar{\eta}}{\partial x}+\varepsilon^2\hat{\mu}\frac{\partial\bar{\eta}}{\partial X}\right)=0,
\end{aligned} \tag{5.114}$$

$$\left[1+\varepsilon\hat{\gamma}\frac{\partial\bar{\eta}}{\partial Z}\right]\left(\frac{\partial U}{\partial x}+\varepsilon^2\hat{\mu}\frac{\partial U}{\partial X}\right)+\varepsilon\hat{\gamma}\left[U\left(\frac{\partial}{\partial x}+\varepsilon^2\hat{\mu}\frac{\partial}{\partial X}\right)\right]\frac{\partial\bar{\eta}}{\partial Z}=0, \tag{5.115}$$

$$\bar{\eta} = -h'|_{Z=-1}, \tag{5.116}$$

$$\hat{\gamma}\frac{\partial\bar{\eta}}{\partial x}+\varepsilon^2\hat{\mu}\hat{\gamma}\frac{\partial\bar{\eta}}{\partial X} = -\varepsilon\hat{\sigma}\left[U\left(\frac{\partial U}{\partial x}+\varepsilon^2\hat{\mu}\frac{\partial U}{\partial X}\right)\right] - \varepsilon^4\hat{\gamma}^2\hat{\sigma}\left\{\left[U\left(\frac{\partial}{\partial x}+\varepsilon^2\hat{\mu}\frac{\partial}{\partial X}\right)\right]^2\bar{\eta}\right\}\left(\frac{\partial\bar{\eta}}{\partial x}+\varepsilon^2\hat{\mu}\frac{\partial\bar{\eta}}{\partial X}\right)\Bigg|_{Z=0}, \tag{5.117}$$

where U and $\bar{\eta}$ can be expanded using expressions (5.107) and (5.109). This to make the equations more compact.

The boundary condition at x_0, equation (5.17), for the different orders of $U^{(i)}$ reads

$$U^{(0)}(0,0,Z) = U_0(Z), \tag{5.118}$$
$$U^{(i)}(0,0,Z) = 0, \qquad \text{for } i \geq 1. \tag{5.119}$$

At x_0 resulting in a zero isopycnal displacement and bed disturbance, see (5.11) and (5.26), resulting in

$$\bar{\eta}^{(i)}(0,0,Z) = 0, \qquad \text{for } i \geq 0, \tag{5.120}$$
$$h'(0) = 0. \tag{5.121}$$

Below, the leading and first order are used to show that $U^{(0)}$, $U^{(1)}$ and $\bar{\eta}^{(0)}$ are independent of x. These results are used at the second order to obtain, that $U^{(0)}$ is also independent of X and therefore only depends on Z. Furthermore, it is shown that $U^{(2)}$ is independent of x. At the next order, a solution for $\bar{\eta}^{(0)}$ and $U^{(1)}$ is found.

Leading order

The leading order reads

$$\frac{\partial}{\partial Z}\left(U^{(0)}\frac{\partial U^{(0)}}{\partial x}\right)=0, \tag{5.122}$$

$$\frac{\partial U^{(0)}}{\partial x}=0, \tag{5.123}$$

$$\bar{\eta}^{(0)}=-h', \qquad \text{at } Z=-1, \tag{5.124}$$

$$\hat{\gamma}\frac{\partial \bar{\eta}^{(0)}}{\partial x}=0, \qquad \text{at } Z=0. \tag{5.125}$$

From these equations no solution can be obtained, as the differential equations do not give information about $U^{(0)}$ in the X, Z and t coordinates. However, based on equation (5.123) it is concluded, that $U^{(0)}$ is independent of x.

First order

At $\mathcal{O}(\varepsilon)$ the equations read

$$\frac{\partial}{\partial Z}\left(U^{(0)}\frac{\partial U^{(1)}}{\partial x}+U^{(1)}\frac{\partial U^{(0)}}{\partial x}\right)+\hat{\gamma}\frac{\partial \rho_0}{\partial Z}\frac{\partial \bar{\eta}^{(0)}}{\partial x}=0, \tag{5.126}$$

$$\frac{\partial U^{(1)}}{\partial x}+\hat{\gamma}\frac{\partial \bar{\eta}^{(0)}}{\partial Z}\frac{\partial U^{(0)}}{\partial x}+\hat{\gamma}U^{(0)}\frac{\partial^2 \bar{\eta}^{(0)}}{\partial x\partial Z}=0, \tag{5.127}$$

$$\bar{\eta}^{(1)}=0, \qquad \text{at } Z=-1, \tag{5.128}$$

$$\hat{\gamma}\frac{\partial \bar{\eta}^{(1)}}{\partial x}=-\hat{\sigma}U^{(0)}\frac{\partial U^{(0)}}{\partial x}, \qquad \text{at } Z=0. \tag{5.129}$$

Using the result obtained from the previous order, $U^{(0)}$ is independent of x, this set of equations reduces to

$$\frac{\partial}{\partial Z}\left(U^{(0)}\frac{\partial U^{(1)}}{\partial x}\right)+\hat{\gamma}\frac{\partial \rho_0}{\partial Z}\frac{\partial \bar{\eta}^{(0)}}{\partial x}=0, \tag{5.130}$$

$$\frac{\partial U^{(1)}}{\partial x}+\hat{\gamma}U^{(0)}\frac{\partial^2 \bar{\eta}^{(0)}}{\partial x\partial Z}=0, \tag{5.131}$$

$$\bar{\eta}^{(1)}=0, \qquad \text{at } Z=-1, \tag{5.132}$$

$$\frac{\partial \bar{\eta}^{(1)}}{\partial x}=0, \qquad \text{at } Z=0. \tag{5.133}$$

The first two equations of this system can be written as one equation, containing only $\bar{\eta}^{(0)}$. Combined with the boundary conditions (5.124), (5.125) and (5.120) for $i=0$, $\bar{\eta}^{(0)}$ follows from

$$\frac{\partial}{\partial Z}\left(\left(U^{(0)}\right)^2\frac{\partial^2 \bar{\eta}^{(0)}}{\partial x\partial Z}\right)-\frac{\partial \rho_0}{\partial Z}\frac{\partial \bar{\eta}^{(0)}}{\partial x}=0, \tag{5.134}$$

$$\bar{\eta}^{(0)}=-h', \qquad \text{at } Z=-1, \tag{5.135}$$

$$\frac{\partial \bar{\eta}^{(0)}}{\partial x}=0, \qquad \text{at } Z=0, \tag{5.136}$$

$$\bar{\eta}^{(0)}(0,0,Z)=0. \tag{5.137}$$

Assuming that $\bar{\eta}^{(0)}$ can be written as a product of two functions

$$\bar{\eta}^{(0)}(x,X,Z)=B_1(x,X)B_2(X,Z), \tag{5.138}$$

the governing equation is now written as

$$\left[\frac{\partial}{\partial Z}\left(\left(\hat{U}^{(0)}\right)^2\frac{\partial B_2}{\partial Z}\right)-\frac{\partial \rho_0}{\partial Z}B_2\right]\frac{\partial B_1}{\partial x}=0, \tag{5.139}$$

with the bottom boundary condition

$$B_1(x,X)B_2(X,-1) = h'(X). \tag{5.140}$$

From this boundary condition it follows that $B_1(x,X)$ has to be independent of x. Using this observation it immediately follows, that equation (5.139) and the other two boundary conditions of the problem for $\bar{\eta}^{(0)}$ are satisfied as well. This means that $\bar{\eta}^{(0)}$ is a function independent of x. and combing with (5.131) it follows that

$$\frac{\partial U^{(1)}}{\partial x} = 0, \tag{5.141}$$

which means that $U^{(1)}$ is also independent of x.

The results at this order are, that $\bar{\eta}^{(0)}$ and $U^{(1)}$ are independent of x. This is used to simplify the equations in the next orders.

Second order

Equations (5.114)-(5.117) evaluated at $\mathcal{O}\left(\varepsilon^2\right)$ are given by

$$\begin{aligned}\frac{\partial}{\partial Z}\left(U^{(0)}\left(\frac{\partial U^{(2)}}{\partial x}+\hat{\mu}\frac{\partial U^{(0)}}{\partial X}\right)+U^{(1)}\frac{\partial U^{(1)}}{\partial x}+U^{(2)}\frac{\partial U^{(0)}}{\partial x}+\hat{\sigma}\rho_0 U^{(0)}\frac{\partial U^{(0)}}{\partial x}\right)\\ -\hat{\gamma}\frac{\partial}{\partial x}\left(\left(U^{(0)}\frac{\partial}{\partial x}\right)^2\bar{\eta}^{(0)}\right)\frac{\partial\bar{\eta}^{(0)}}{\partial x}+\hat{\gamma}\frac{\partial\rho_0}{\partial Z}\frac{\partial\bar{\eta}^{(1)}}{\partial x}=0,\end{aligned} \tag{5.142}$$

$$\begin{aligned}\frac{\partial U^{(2)}}{\partial x}+\hat{\mu}\frac{\partial U^{(0)}}{\partial X}+\hat{\gamma}\frac{\partial\bar{\eta}^{(0)}}{\partial Z}\frac{\partial U^{(1)}}{\partial x}+\hat{\gamma}\frac{\partial\bar{\eta}^{(1)}}{\partial Z}\frac{\partial U^{(0)}}{\partial x}\\ +\hat{\gamma}U^{(0)}\frac{\partial^2\bar{\eta}^{(1)}}{\partial x\partial Z}+\hat{\gamma}U^{(1)}\frac{\partial^2\bar{\eta}^{(0)}}{\partial x\partial Z}=0,\end{aligned} \tag{5.143}$$

$$\bar{\eta}^{(2)} = 0, \qquad \text{at } Z=-1, \tag{5.144}$$

$$\hat{\gamma}\frac{\partial\bar{\eta}^{(2)}}{\partial x}+\hat{\mu}\hat{\gamma}\frac{\partial\bar{\eta}^{(0)}}{\partial X}=-\hat{\sigma}\left(U^{(0)}\frac{\partial U^{(1)}}{\partial x}+U^{(1)}\frac{\partial U^{(0)}}{\partial x}\right), \qquad \text{at } Z=0. \tag{5.145}$$

Use the results from previous orders, where it was concluded that $U^{(0)}$, $U^{(1)}$ and $\bar{\eta}^{(0)}$ are independent of x, this set of equations simplifies to

$$\frac{\partial}{\partial Z}\left(U^{(0)}\left(\frac{\partial U^{(2)}}{\partial x}+\hat{\mu}\frac{\partial U^{(0)}}{\partial X}\right)\right)+\hat{\gamma}\frac{\partial\rho_0}{\partial Z}\frac{\partial\bar{\eta}^{(1)}}{\partial x}=0, \tag{5.146}$$

$$\frac{\partial U^{(2)}}{\partial x}+\hat{\mu}\frac{\partial U^{(0)}}{\partial X}+\hat{\gamma}U^{(0)}\frac{\partial^2\bar{\eta}^{(1)}}{\partial x\partial Z}=0, \tag{5.147}$$

$$\bar{\eta}^{(2)} = 0, \qquad \text{at } Z=-1, \tag{5.148}$$

$$\hat{\gamma}\frac{\partial\bar{\eta}^{(2)}}{\partial x}+\hat{\mu}\hat{\gamma}\frac{\partial\bar{\eta}^{(0)}}{\partial X}=0, \qquad \text{at } Z=0. \tag{5.149}$$

Similar to the first order equations (5.146) and (5.147) can be combined, resulting in an equation containing only $\bar{\eta}^{(1)}$. Combining this equation with the boundary conditions: (5.120), (5.132) and (5.133), the resulting equation and boundary conditions read

$$\frac{\partial}{\partial Z}\left(\left(U^{(0)}\right)^2\frac{\partial^2\bar{\eta}^{(1)}}{\partial x\partial Z}\right)-\frac{\partial\rho_0}{\partial Z}\frac{\partial\bar{\eta}^{(1)}}{\partial x}=0, \tag{5.150}$$

$$\bar{\eta}^{(1)} = 0, \qquad \text{at } Z=-1, \tag{5.151}$$

$$\frac{\partial\bar{\eta}^{(1)}}{\partial x} = 0, \qquad \text{at } Z=0, \tag{5.152}$$

$$\bar{\eta}^{(1)}(0,0,Z) = 0. \tag{5.153}$$

The unknown $\bar{\eta}^{(1)}$ is written as a product of two functions

$$\bar{\eta}^{(1)}(x, X, Z) = B_3(x, X)B_4(X, Z). \tag{5.154}$$

The remaining governing equation reads

$$\left[\frac{\partial}{\partial Z}\left(\left(\hat{U}^{(0)}\right)^2 \frac{\partial B_4}{\partial Z}\right) - \frac{\partial \rho_0}{\partial Z} B_4\right] \frac{\partial B_3}{\partial x} = 0, \tag{5.155}$$

and a bottom boundary condition is given by

$$B_3(x, X)B_4(X, -1) = 0. \tag{5.156}$$

A solution is found when $\frac{\partial B_3}{\partial x} = 0$, as the governing equations and boundary conditions are satisfied with this choice. In the case that $\frac{\partial B_3}{\partial x} \neq 0$, the following system needs to be solved

$$\left[\frac{\partial}{\partial Z}\left(\left(U^{(0)}\right)^2 \frac{\partial B_4}{\partial Z}\right) - \frac{\partial \rho_0}{\partial Z} B_4\right] = 0, \tag{5.157}$$

$$B_4 = 0, \qquad \text{at } Z = -1, \tag{5.158}$$

$$B_4 = 0, \qquad \text{at } Z = 0. \tag{5.159}$$

This problem is similar to the Taylor-Goldstein equation (3.1), where the eigenvalue C_0 equals zero. Next, it is shown that the trivial solution is the only possible solution for this system, start using (5.157)

$$\int_{-1}^{0} B_4 \left[\frac{\partial}{\partial Z}\left(\left(U^{(0)}\right)^2 \frac{\partial B_4}{\partial Z}\right) - \frac{\partial \rho_0}{\partial Z} B_4\right] dZ = 0, \tag{5.160}$$

using integration by parts, this yields

$$\left[B_4 \left(U^{(0)}\right)^2 \frac{\partial B_4}{\partial Z}\right]_{-1}^{0} - \int_{-1}^{0} \left(U^{(0)}\right)^2 \left(\frac{\partial B_4}{\partial Z}\right)^2 + \frac{\partial \rho_0}{\partial Z} B_4^2 \, dZ = 0, \tag{5.161}$$

using the boundary conditions, the equation simplifies to

$$\int_{-1}^{0} \left(U^{(0)}\right)^2 \left(\frac{\partial B_4}{\partial Z}\right)^2 + \frac{\partial \rho_0}{\partial Z} B_4^2 \, dZ = 0. \tag{5.162}$$

For a stable stratified fluid holds

$$\frac{\partial \rho_0}{\partial Z} \geq 0, \tag{5.163}$$

which means that in combination with equation (5.162) should be concluded that

$$\frac{\partial B_4}{\partial Z} = 0. \tag{5.164}$$

In combination with the boundary conditions, the trivial solution is obtained

$$B_4 = 0, \tag{5.165}$$

and using equation (5.154) this yields

$$\bar{\eta}^{(1)} = 0. \tag{5.166}$$

Therefore, in both cases the solution satisfies

$$\frac{\partial \bar{\eta}^{(1)}}{\partial x} = 0. \tag{5.167}$$

With this result equation (5.147) reduces to

$$\frac{\partial U^{(2)}}{\partial x} = -\hat{\mu}\frac{\partial \hat{U}^{(0)}}{\partial X}. \tag{5.168}$$

As the right-hand side of this equation is independent of x, $U^{(2)}$ is linear in x and can be written as

$$U^{(2)} = C_1(X,Z)x + C_2(X,Z), \tag{5.169}$$

with the slope C_1 given by

$$C_1(X,Z) = -\hat{\mu}\frac{\partial U^{(0)}}{\partial X}. \tag{5.170}$$

and $C_2(X,Z)$ an integration constant.

Based on the asymptotic expansion, it is required that

$$\varepsilon U^{(2)} \ll U^{(1)}. \tag{5.171}$$

For x large enough, $C_1(X,Z)x \geq 1/\varepsilon$, it is found that

$$U^{(2)} \geq \mathcal{O}\left(1/\varepsilon\right). \tag{5.172}$$

This means, that the condition of (5.171) is not satisfied anymore, unless $C_1(X,Z) = 0$. This means, that $U^{(2)}$ is independent of x and does not grow for larger values of x. This observation combined with equation (5.168), shows that

$$\frac{\partial U^{(0)}}{\partial X} = 0, \tag{5.173}$$

and, combined with the boundary condition (5.118), it follows that $U^{(0)}$ can be written as

$$U^{(0)} = U_0(Z). \tag{5.174}$$

This means that the leading order background velocity $U^{(0)}$ is only dependent on Z.

Third order

At the third order the equations (5.114)-(5.117) are given by

$$\begin{aligned}
&\frac{\partial}{\partial Z}\left(U^{(0)}\left(\frac{\partial U^{(3)}}{\partial x} + \hat{\mu}\frac{\partial U^{(1)}}{\partial X}\right) + U^{(1)}\left(\frac{\partial U^{(2)}}{\partial x} + \hat{\mu}\frac{\partial U^{(0)}}{\partial X}\right) + U^{(2)}\frac{\partial U^{(1)}}{\partial x} + U^{(3)}\frac{\partial U^{(0)}}{\partial x}\right.\\
&\left.+\hat{\sigma}\rho_0\left(U^{(0)}\frac{\partial U^{(1)}}{\partial x} + U^{(1)}\frac{\partial U^{(0)}}{\partial x}\right)\right) - \hat{\gamma}\frac{\partial}{\partial x}\left(\left(U^{(0)}\frac{\partial}{\partial x}\right)^2\bar{\eta}^{(1)} + \left(U^{(0)}\frac{\partial}{\partial x}U^{(1)} + U^{(1)}\frac{\partial}{\partial x}U^{(0)}\right)\bar{\eta}^{(0)}\right)\\
&-\hat{\gamma}^2\left(\frac{\partial}{\partial x}\left(U^{(0)}\frac{\partial}{\partial x}\right)^2\bar{\eta}^{(0)}\right)\frac{\partial\bar{\eta}^{(0)}}{\partial Z} + \hat{\gamma}^2\frac{\partial}{\partial Z}\left(\left(U^{(0)}\frac{\partial}{\partial x}\right)^2\bar{\eta}^{(0)}\right)\frac{\partial\bar{\eta}^{(0)}}{\partial x} + \hat{\gamma}\frac{\partial\rho_0}{\partial Z}\left(\frac{\partial\bar{\eta}^{(2)}}{\partial x} + \hat{\mu}\frac{\partial\bar{\eta}^{(0)}}{\partial X}\right) = 0,
\end{aligned} \tag{5.175}$$

$$\begin{aligned}
&\frac{\partial U^{(3)}}{\partial x} + \hat{\mu}\frac{\partial U^{(1)}}{\partial X} + \hat{\gamma}\frac{\partial\bar{\eta}^{(0)}}{\partial Z}\left(\frac{\partial U^{(2)}}{\partial x} + \hat{\mu}\frac{\partial U^{(0)}}{\partial X}\right) + \hat{\gamma}\frac{\partial\bar{\eta}^{(1)}}{\partial Z}\frac{\partial U^{(1)}}{\partial x} + \hat{\gamma}\frac{\partial\bar{\eta}^{(2)}}{\partial Z}\frac{\partial U^{(0)}}{\partial x}\\
&+\hat{\gamma}U^{(0)}\frac{\partial}{\partial x}\frac{\partial\bar{\eta}^{(2)}}{\partial Z} + \hat{\gamma}U^{(1)}\frac{\partial}{\partial x}\frac{\partial\bar{\eta}^{(1)}}{\partial Z} + \hat{\gamma}\left(U^{(2)}\frac{\partial}{\partial x} + \hat{\mu}U^{(0)}\frac{\partial}{\partial X}\right)\frac{\partial\bar{\eta}^{(0)}}{\partial Z} = 0,
\end{aligned} \tag{5.176}$$

$$\bar{\eta}^{(3)} = 0, \qquad \text{at } Z = -1, \tag{5.177}$$

$$\hat{\gamma}\frac{\partial\bar{\eta}^{(3)}}{\partial x} + \hat{\mu}\hat{\gamma}\frac{\partial\bar{\eta}^{(1)}}{\partial X} = -\hat{\sigma}\left[U^{(0)}\left(\frac{\partial U^{(2)}}{\partial x} + \hat{\mu}\frac{\partial U^{(0)}}{\partial X}\right) + U^{(1)}\frac{\partial U^{(1)}}{\partial x} + U^{(2)}\frac{\partial U^{(0)}}{\partial x}\right], \qquad \text{at } Z = 0. \tag{5.178}$$

Using the results from all previous orders, this problem reduces to

$$\frac{\partial}{\partial Z}\left(U_0\left(\frac{\partial U^{(3)}}{\partial x}+\hat{\mu}\frac{\partial U^{(1)}}{\partial X}\right)\right)+\hat{\gamma}\frac{\partial \rho_0}{\partial Z}\left(\frac{\partial \bar{\eta}^{(2)}}{\partial x}+\hat{\mu}\frac{\partial \bar{\eta}^{(0)}}{\partial X}\right)=0, \tag{5.179}$$

$$\frac{\partial U^{(3)}}{\partial x}+\hat{\mu}\frac{\partial U^{(1)}}{\partial X}+\hat{\gamma}U_0\left(\frac{\partial}{\partial x}\frac{\partial \bar{\eta}^{(2)}}{\partial Z}+\hat{\mu}\frac{\partial}{\partial X}\frac{\partial \bar{\eta}^{(0)}}{\partial Z}\right)=0, \tag{5.180}$$

$$\bar{\eta}^{(3)}=0, \qquad \text{at } Z=-1, \tag{5.181}$$

$$\hat{\gamma}\frac{\partial \bar{\eta}^{(3)}}{\partial x}+\hat{\mu}\hat{\gamma}\frac{\partial \bar{\eta}^{(1)}}{\partial X}=0, \qquad \text{at } Z=0. \tag{5.182}$$

The first two equations are combined and written as

$$\left[\frac{\partial}{\partial Z}\left(U_0^2\frac{\partial}{\partial Z}\right)-\frac{\partial \rho_0}{\partial Z}\right]\left(\frac{\partial \bar{\eta}^{(2)}}{\partial x}+\hat{\mu}\frac{\partial \bar{\eta}^{(0)}}{\partial X}\right)=0. \tag{5.183}$$

Taking the x-derivative from this equation, results in

$$\left[\frac{\partial}{\partial Z}\left(U_0^2\frac{\partial}{\partial Z}\right)-\frac{\partial \rho_0}{\partial Z}\right]\frac{\partial^2 \bar{\eta}^{(2)}}{\partial x^2}=0. \tag{5.184}$$

As $\bar{\eta}^{(2)}$ is the only unknown in this equation, the corresponding boundary conditions are collected from previous orders to close this problem. From equation (5.148)

$$\bar{\eta}^{(2)}=0, \qquad \text{at } Z=-1, \tag{5.185}$$

and after taking the derivative with respect to x of (5.149), it is found

$$\frac{\partial^2 \bar{\eta}^{(2)}}{\partial x^2}=0, \qquad \text{at } Z=0, \tag{5.186}$$

Equation (5.120) requires

$$\bar{\eta}^{(2)}(0,0,Z)=0. \tag{5.187}$$

This system is similar to (5.150)-(5.153), except that each first order derivative to x is replaced by a second order derivative. Therefore, the same reasoning is followed to finally conclude that

$$\frac{\partial \bar{\eta}^{(2)}}{\partial x}=0. \tag{5.188}$$

This tells that $\bar{\eta}^{(2)}$ is linear in x. Therefore, similar to the reasoning for $U^{(2)}$ in (5.169)-(5.172) it may be concluded that $\bar{\eta}^{(2)}$ is independent of x. This result applied to (5.183), yields

$$\left[\frac{\partial}{\partial Z}\left(U_0^2\frac{\partial}{\partial Z}\right)-\frac{\partial \rho_0}{\partial Z}\right]\frac{\partial \bar{\eta}^{(0)}}{\partial X}=0. \tag{5.189}$$

The corresponding boundary conditions for this equation are given by (5.135), (5.149) and (5.137):

$$\bar{\eta}^{(0)}=-h', \qquad \text{at } Z=-1, \tag{5.190}$$

$$\frac{\partial \bar{\eta}^{(0)}}{\partial X}=0, \qquad \text{at } Z=0, \tag{5.191}$$

$$\bar{\eta}^{(0)}(0,Z)=0. \tag{5.192}$$

Assuming that $\bar{\eta}^{(0)}$ can be written as a product of two functions:

$$\bar{\eta}^{(0)}(X,Z)=f(X)g(Z). \tag{5.193}$$

Equation (5.189) can be rewritten as

$$\left[\frac{\partial}{\partial Z}\left(U_0^2(Z)\frac{\partial g(Z)}{\partial Z}\right)-\frac{\partial \rho_0(Z)}{\partial Z}g(Z)\right]\frac{\partial f(X)}{\partial X}=0, \tag{5.194}$$

$$f(X)g(-1)=-h'(X), \tag{5.195}$$

$$\frac{\partial f(X)}{\partial X}g(0)=0, \tag{5.196}$$

$$f(0)g(Z)=0. \tag{5.197}$$

Without loss of generality it can be assumed that $g(-1)=1$, because $\bar{\eta}^{(0)}(X,Z)$ depends on the product of f and g. The bottom boundary condition directly gives the solution of $f(X)$

$$f(X)=-h'(X). \tag{5.198}$$

The boundary condition (5.197) at $X=0$ is now directly satisfied as $h'(0)=0$, see (5.26). The function $g(Z)$ now follows from

$$\left[\frac{\partial}{\partial Z}\left(U_0^2(Z)\frac{\partial g(Z)}{\partial Z}\right)-\frac{\partial \rho_0(Z)}{\partial Z}g(Z)\right]=0, \tag{5.199}$$

$$g(0)=0, \tag{5.200}$$

$$g(-1)=1. \tag{5.201}$$

This problem is very similar to the Taylor-Goldstein equation, and can only be solved analytically in some easy cases; numerical in any other situation. This is explored in section 6.2.

To obtain an expression for $U^{(1)}$, the fact that $\bar{\eta}^{(2)}$ is independent of x is used. Employing this fact in equation (5.180), it follows

$$\hat{\mu}\frac{\partial U^{(1)}}{\partial X}+\hat{\gamma}\hat{\mu}U_0\frac{\partial^2\bar{\eta}^{(0)}}{\partial X\partial Z}=-\frac{\partial U^{(3)}}{\partial x}. \tag{5.202}$$

Following a similar analysis as for $U^{(2)}$, see equations (5.168)-(5.172), it can be concluded that $U^{(3)}$ is independent of x. This means, that this equation can be simplified to

$$\frac{\partial U^{(1)}}{\partial X}=-\hat{\gamma}U_0\frac{\partial^2\bar{\eta}^{(0)}}{\partial X\partial Z}, \tag{5.203}$$

resulting in the solution for $U^{(1)}$, given by

$$U^{(1)}(X,Z)=\hat{\gamma}U_0h'(X)\frac{\partial g(Z)}{\partial Z}+C_2(Z), \tag{5.204}$$

where equation (5.193) has been substituted and $C_2(Z)$ is an integration constant. This integration constant is zero using that $h'(X)=0$, from (5.26), and $U^{(1)}(0,Z)=0$, from (5.119).

Solution of the time-independent problem

Summarized the solution of the time-independent problem is given as:

$$U^{(0)}(x,X,Z)=U_0(Z), \tag{5.205}$$

$$U^{(1)}(x,X,Z)=\hat{\gamma}U_0h'(X)\frac{\partial g(Z)}{\partial Z}, \tag{5.206}$$

$$\bar{\eta}^{(0)}(x,X,Z)=-h'(X)g(Z), \tag{5.207}$$

where g satisfies the set of equations described in (5.199)-(5.201). Furthermore, it is found that $U^{(2)}$, $U^{(3)}$, $\bar{\eta}^{(1)}$ and $\bar{\eta}^{(2)}$ are independent of x.

5.6. Moving reference frame

The solution of the time-independent problem is used to solve the time-dependent problem. Consider the first order of the system of equations (5.103)-(5.106)

$$\frac{\partial}{\partial Z}\left\{\left[\frac{\partial u'^{(0)}}{\partial t}+(U^{(1)}+u'^{(0)})\frac{\partial U^{(0)}}{\partial x}+U^{(0)}\left(\frac{\partial U^{(1)}}{\partial x}+\frac{\partial u'^{(0)}}{\partial x}\right)\right]\right\}+\frac{\partial \rho_0}{\partial Z}\left(\hat{\gamma}\frac{\partial \bar{\eta}^{(0)}}{\partial x}+\frac{\partial \eta'^{(0)}}{\partial x}\right)=0, \quad (5.208)$$

$$\frac{\partial U^{(1)}}{\partial x}+\frac{\partial u'^{(0)}}{\partial x}+\left[\hat{\gamma}\frac{\partial \bar{\eta}^{(0)}}{\partial Z}+\frac{\partial \eta'^{(0)}}{\partial Z}\right]\frac{\partial U^{(0)}}{\partial x}+\left[\frac{\partial}{\partial t}+U^{(0)}\frac{\partial}{\partial x}\right]\left(\hat{\gamma}\frac{\partial \bar{\eta}^{(0)}}{\partial Z}+\frac{\partial \eta'^{(0)}}{\partial Z}\right)=0, \quad (5.209)$$

$$\hat{\gamma}\bar{\eta}^{(0)}+\eta'^{(0)}=-\hat{\gamma}h'|_{Z=-1}, \quad (5.210)$$

$$\hat{\gamma}\frac{\partial \bar{\eta}^{(0)}}{\partial x}+\frac{\partial \eta'^{(0)}}{\partial x}=0|_{Z=0}. \quad (5.211)$$

Using (5.124), (5.125), (5.130) and (5.131) and the solution of the time-independent problem, these equations simplify to

$$\frac{\partial}{\partial Z}\left\{\left[\frac{\partial u'^{(0)}}{\partial t}+U_0\frac{\partial u'^{(0)}}{\partial x}\right]\right\}+\frac{\partial \rho_0}{\partial Z}\frac{\partial \eta'^{(0)}}{\partial x}=0, \quad (5.212)$$

$$\frac{\partial u'^{(0)}}{\partial x}+\left[\frac{\partial}{\partial t}+U_0\frac{\partial}{\partial x}\right]\frac{\partial \eta'^{(0)}}{\partial Z}=0, \quad (5.213)$$

$$\eta'^{(0)}=0|_{Z=-1}, \quad (5.214)$$

$$\frac{\partial \eta'^{(0)}}{\partial x}=0|_{Z=0}. \quad (5.215)$$

Note, that U_0 and ρ_0 are independent of X, therefore the solution of $\eta'^{(0)}$ and $u'^{(0)}$ is not forced in X. Therefore, the solution of these two physical quantities do not change with X and can be found independent of X. The first two equations of this system are simplified to one equation containing $\eta'^{(0)}$ only (see (B.91)-(B.95))

$$\frac{\partial}{\partial Z}\left(\frac{\partial^3 \eta'^{(0)}}{\partial t^2 \partial Z}+2U_0\frac{\partial^3 \eta'^{(0)}}{\partial t \partial x \partial Z}+U_0^2\frac{\partial^3 \eta'^{(0)}}{\partial x^2 \partial Z}\right)-\frac{\partial \rho_0}{\partial Z}\frac{\partial^2 \eta'^{(0)}}{\partial x^2}=0, \quad (5.216)$$

with the boundary conditions (5.214) and (5.215).

This equation is solved using separation of variables. The solution is therefore written as

$$\eta'^{(0)}(x,Z,t)=A(x,t)\Phi(Z), \quad (5.217)$$

see appendix B, equations (B.96)-(B.104) for the case without shear-flow and equations (B.105)-(B.119) where shear is considered. For the time dependent horizontal structure the linear wave equation with speed c_0 is obtained. The solution for $A(x,t)$ should follow from this equation (B.112)

$$\frac{\partial^2 A}{\partial t^2}-c_0^2\frac{\partial^2 A}{\partial x^2}=0, \quad (5.218)$$

which results in a solution given by two traveling waves

$$A(x,X,t)=f(x+c_0t)+g(x-c_0t). \quad (5.219)$$

For simplicity only the right going waves are considered from now on.

To obtain information about the evolution of the waves while propagating the system is investigated in a moving reference frame with speed c_0. This to see the change of internal wave form, the corresponding coordinate is given by

$$\xi=x-c_0t. \quad (5.220)$$

The solution in the current time frame is not valid for $t \to \infty$. It is only valid for $t = \mathcal{O}(1)$ and not for longer time scales like $\varepsilon t = \mathcal{O}(1)$. To be able to investigate waves in a longer period $t = \mathcal{O}(1/\varepsilon)$, a new slow timescale needs to be introduced, following Johnson (1997),

$$\tau = \varepsilon t. \tag{5.221}$$

In this time frame the evolution of a wave can be followed over a longer timerange, up to $t = \mathcal{O}(1/\varepsilon)$.

This transformation is applied to the system of equations, see (B.120)-(B.132) and reads

$$\frac{\partial}{\partial Z}\left[(U+\varepsilon u')\frac{\partial U}{\partial \xi} + \varepsilon(U-c_0)\frac{\partial u'}{\partial \xi}\right] + \varepsilon\frac{\partial \rho_0}{\partial Z}\left(\hat{\gamma}\frac{\partial \bar{\eta}}{\partial \xi} + \frac{\partial \eta'}{\partial \xi}\right) = F, \tag{5.222}$$

$$\left[1 + \hat{\gamma}\varepsilon\frac{\partial \bar{\eta}}{\partial Z} + \varepsilon\frac{\partial \eta'}{\partial Z}\right]\frac{\partial U}{\partial \xi} + \varepsilon\frac{\partial u'}{\partial \xi} + \varepsilon(U-c_0)\left(\frac{\partial^2(\hat{\gamma}\bar{\eta}+\eta')}{\partial \xi \partial Z}\right) = G, \tag{5.223}$$

$$-\varepsilon^2\hat{\gamma}\hat{\mu}\frac{\partial \bar{\eta}}{\partial X} - \varepsilon^2\hat{\mu}\frac{\partial \eta'}{\partial X} - \varepsilon\hat{\sigma}(U+\varepsilon u')\frac{\partial U}{\partial \xi} - \varepsilon^2\hat{\sigma}(U-c_0)\frac{\partial u'}{\partial \xi} + \varepsilon\hat{\sigma}H_1 = \hat{\gamma}\frac{\partial \bar{\eta}}{\partial \xi} + \frac{\partial \eta'}{\partial \xi}\bigg|_{Z=0}, \tag{5.224}$$

$$\hat{\gamma}\bar{\eta} + \eta' = -\hat{\gamma}h'|_{Z=-1}. \tag{5.225}$$

Here F, G and H_1 are defined as in (B.124), (B.128) and (B.131).

5.7. First order solution

The time-dependent system in the moving reference frame (5.222)-(5.225) is evaluated at the first order of ε. This system of equations at this order is given

$$\frac{\partial}{\partial Z}\left[U^{(0)}\frac{\partial U^{(1)}}{\partial \xi} + (U^{(1)}+u'^{(0)})\frac{\partial U^{(0)}}{\partial \xi} + (U^{(0)}-c_0)\frac{\partial u'^{(0)}}{\partial \xi}\right] + \frac{\partial \rho_0}{\partial Z}\left(\hat{\gamma}\frac{\partial \bar{\eta}^{(0)}}{\partial \xi} + \frac{\partial \eta'^{(0)}}{\partial \xi}\right) = 0, \tag{5.226}$$

$$\frac{\partial U^{(1)}}{\partial \xi} + \left[\hat{\gamma}\frac{\partial \bar{\eta}^{(0)}}{\partial Z} + \frac{\partial \eta'^{(0)}}{\partial Z}\right]\frac{\partial U^{(0)}}{\partial \xi} + \frac{\partial u'^{(0)}}{\partial \xi} + (U^{(0)}-c_0)\frac{\partial^2(\hat{\gamma}\bar{\eta}^{(0)}+\eta'^{(0)})}{\partial \xi \partial Z} = 0, \tag{5.227}$$

with boundary conditions

$$\hat{\gamma}\frac{\partial \bar{\eta}^{(0)}}{\partial \xi} + \frac{\partial \eta'^{(0)}}{\partial \xi} = 0|_{Z=0}, \tag{5.228}$$

$$\hat{\gamma}\bar{\eta}^{(0)} + \eta'^{(0)} = -\hat{\gamma}h'|_{Z=-1}. \tag{5.229}$$

The solution to the time-independent problem has shown that $U^{(0)}$, $U^{(1)}$ and $\bar{\eta}^{(0)}$ are independent of x. Based on the transformation to the moving reference frame, these variables are therefore also independent of ξ. Using this with the boundary condition for $\bar{\eta}^{(0)}$ (5.124) and the solution of $U^{(0)}$ (5.174), the system is simplified to

$$\frac{\partial}{\partial Z}\left[(U_0-c_0)\frac{\partial u'^{(0)}}{\partial \xi}\right] + \frac{\partial \rho_0}{\partial Z}\frac{\partial \eta'^{(0)}}{\partial \xi} = 0, \tag{5.230}$$

$$\frac{\partial u'^{(0)}}{\partial \xi} + (U_0-c_0)\frac{\partial^2 \eta'^{(0)}}{\partial \xi \partial Z} = 0, \tag{5.231}$$

$$\frac{\partial \eta'^{(0)}}{\partial \xi} = 0|_{Z=0}, \tag{5.232}$$

$$\eta'^{(0)} = 0|_{Z=-1}. \tag{5.233}$$

From equations (B.133)-(B.136) it is seen, that the displacement can be separated as

$$\eta'^{(0)}(\xi, Z, \tau) = A(\xi, \tau)\Phi(Z). \tag{5.234}$$

Both terms are assumed to be of the same order: as $\eta^{(0)}$ is the leading order, $A(x,t)$ and $\Phi(Z)$ is assumed to be $\mathcal{O}(1)$. This leads to the following equations for $\Phi(Z)$ describing the vertical velocity

$$\frac{\partial}{\partial Z}\left((U_0 - c_0)^2 \frac{\partial \Phi}{\partial Z}\right) - \frac{\partial \rho_0}{\partial Z}\Phi = 0, \tag{5.235}$$

$$\Phi = 0|_{Z=0}, \tag{5.236}$$

$$\Phi = 0|_{Z=-1}. \tag{5.237}$$

This is the Taylor-Goldstein equation in the long-wave limit under the Boussinesq approximation with shear flow included (Stastna & Lamb, 2002), subject to homogenous boundary conditions. Note that, this is a Sturm-Liouville eigenvalue problem, with eigenvalue c_0, where the solution can be written as a sum of eigenfunctions. Each eigenfunction is normalized to satisfy the condition $\Phi(Z) = \mathcal{O}(1)$. This is accomplished by requiring

$$\max_{-h \le Z \le 0} \Phi(Z) = 1. \tag{5.238}$$

From this solution in combination with (5.231) the leading order perturbation velocity can be expressed in terms of $\Phi(Z)$ and the unknown amplitude $A(\xi,\tau)$, see (B.139)

$$u'^{(0)} = -A(U_0 - c_0)\frac{d\Phi}{dZ}. \tag{5.239}$$

5.8. Compatibility condition

The system (5.222)-(5.225) evaluated at the second order is used to solve for the unknown leading order wave amplitude $A(\xi,\tau)$ and reads

$$\begin{aligned}
&\frac{\partial}{\partial Z}\left[U^{(0)}\frac{\partial U^{(2)}}{\partial \xi} + (U^{(1)} + u'^{(0)})\frac{\partial U^{(1)}}{\partial \xi} + (U^{(2)} + u'^{(1)})\frac{\partial U^{(0)}}{\partial \xi}\right.\\
&\left.+(U^{(0)} - c_0)\frac{\partial u'^{(1)}}{\partial \xi} + U^{(1)}\frac{\partial u'^{(0)}}{\partial \xi}\right] + \frac{\partial \rho_0}{\partial Z}\left(\hat{\gamma}\frac{\partial \bar{\eta}^{(1)}}{\partial \xi} + \frac{\partial \eta'^{(1)}}{\partial \xi}\right) = -\frac{\partial}{\partial Z}\left\{\frac{\partial u'^{(0)}}{\partial \tau} + u'^{(0)}\frac{\partial u'^{(0)}}{\partial \xi}\right.\\
&\qquad\left.+\hat{\mu}U^{(0)}\frac{\partial U^{(0)}}{\partial X} - \hat{\sigma}\rho_0 U^{(0)}\frac{\partial U^{(0)}}{\partial \xi}\right\}\\
&\qquad + \frac{\partial}{\partial \xi}\left[(U^{(0)} - c_0)\frac{\partial}{\partial \xi}\right]^2(\hat{\gamma}\bar{\eta}^{(0)} + \eta'^{(0)}),
\end{aligned} \tag{5.240}$$

$$\begin{aligned}
&\frac{\partial U^{(2)}}{\partial \xi} + \left[\hat{\gamma}\frac{\partial \bar{\eta}^{(0)}}{\partial Z} + \frac{\partial \eta'^{(0)}}{\partial Z}\right]\frac{\partial U^{(1)}}{\partial \xi} + \left[\hat{\gamma}\frac{\partial \bar{\eta}^{(1)}}{\partial Z} + \frac{\partial \eta'^{(1)}}{\partial Z}\right]\frac{\partial U^{(0)}}{\partial \xi}\\
&+\frac{\partial u'^{(1)}}{\partial \xi} + (U^{(0)} - c_0)\frac{\partial^2(\hat{\gamma}\bar{\eta}^{(1)} + \eta'^{(1)})}{\partial \xi \partial Z} + U^{(1)}\frac{\partial^2(\hat{\gamma}\bar{\eta}^{(0)} + \eta'^{(0)})}{\partial \xi \partial Z} = -\hat{\mu}\frac{\partial U^{(0)}}{\partial X} - \frac{\partial}{\partial \xi}\left(u'^{(0)}\frac{\partial(\hat{\gamma}\bar{\eta}^{(0)} + \eta'^{(0)})}{\partial Z}\right)\\
&\qquad - \frac{\partial^2(\hat{\gamma}\bar{\eta}^{(0)} + \eta'^{(0)})}{\partial \tau \partial Z},
\end{aligned} \tag{5.241}$$

with the relevant boundary conditions

$$\hat{\gamma}\frac{\partial \bar{\eta}^{(1)}}{\partial \xi} + \frac{\partial \eta'^{(1)}}{\partial \xi} = -\hat{\sigma}U^{(0)}\frac{\partial U^{(0)}}{\partial \xi}\bigg|_{Z=0}, \tag{5.242}$$

$$\hat{\gamma}\bar{\eta}^{(1)} + \eta'^{(1)} = 0|_{Z=-1}. \tag{5.243}$$

Using the results from the time-independent problem, the solution for $U^{(0)}$ (5.174), the bottom boundary condition of $\bar{\eta}^{(1)}$ (5.132) and that $U^{(1)}$, $U^{(2)}$ and $\bar{\eta}^{(1)}$ are independent of x and therefore also ξ, so the

problem simplifies to

$$\frac{\partial}{\partial Z}\left[(U_0-c_0)\frac{\partial u'^{(1)}}{\partial \xi}+U^{(1)}\frac{\partial u'^{(0)}}{\partial \xi}\right]+\frac{\partial \rho_0}{\partial Z}\frac{\partial \eta'^{(1)}}{\partial \xi}=-\frac{\partial}{\partial Z}\left\{\frac{\partial u'^{(0)}}{\partial \tau}+u'^{(0)}\frac{\partial u'^{(0)}}{\partial \xi}\right\}+\frac{\partial}{\partial \xi}\left[(U_0-c_0)\frac{\partial}{\partial \xi}\right]^2\eta'^{(0)}, \tag{5.244}$$

$$\frac{\partial u'^{(1)}}{\partial \xi}+(U_0-c_0)\frac{\partial^2 \eta'^{(1)}}{\partial \xi \partial Z}+U^{(1)}\frac{\partial^2 \eta'^{(0)}}{\partial \xi \partial Z}=-\frac{\partial}{\partial \xi}\left(u'^{(0)}\frac{\partial \eta'^{(0)}}{\partial Z}\right)-\hat{\gamma}\frac{\partial u'^{(0)}}{\partial \xi}\frac{\partial \bar{\eta}^{(0)}}{\partial Z}-\frac{\partial^2 \eta'^{(0)}}{\partial \tau \partial Z}, \tag{5.245}$$

$$\frac{\partial \eta'^{(1)}}{\partial \xi}=0|_{Z=0}, \tag{5.246}$$

$$\eta'^{(1)}=0|_{Z=-1}. \tag{5.247}$$

When the first two equations are combined and the relationship from (5.231) is used, the combined equation reads

$$\begin{aligned}\frac{\partial}{\partial Z}\left[(U_0-c_0)^2\frac{\partial \eta'^{(1)}}{\partial \xi \partial Z}\right]-\frac{\partial \rho_0}{\partial Z}\frac{\partial \eta'^{(1)}}{\partial \xi}=&\frac{\partial}{\partial Z}\left\{\frac{\partial u'^{(0)}}{\partial \tau}+u'^{(0)}\frac{\partial u'^{(0)}}{\partial \xi}\right\}-\frac{\partial}{\partial \xi}\left[(U_0-c_0)\frac{\partial}{\partial \xi}\right]^2\eta'^{(0)}\\&-\frac{\partial}{\partial Z}\left[(U_0-c_0)\left(\frac{\partial}{\partial \xi}\left(u'^{(0)}\frac{\partial \eta'^{(0)}}{\partial Z}\right)+\hat{\gamma}\frac{\partial u'^{(0)}}{\partial \xi}\frac{\partial \bar{\eta}^{(0)}}{\partial Z}+\frac{\partial^2 \eta'^{(0)}}{\partial \tau \partial Z}\right)\right].\end{aligned} \tag{5.248}$$

This equation is subject to boundary conditions (5.246) and (5.247).

Next, define the linear operator L as

$$L:=\frac{\partial}{\partial Z}\left((U_0-c_0)^2\frac{\partial}{\partial Z}\right)-\frac{\partial \rho_0}{\partial Z}, \tag{5.249}$$

and the operator M as

$$\begin{aligned}M:=&\frac{\partial}{\partial Z}\left\{\frac{\partial u'^{(0)}}{\partial \tau}+u'^{(0)}\frac{\partial u'^{(0)}}{\partial \xi}\right\}-\frac{\partial}{\partial \xi}\left[(U_0-c_0)\frac{\partial}{\partial \xi}\right]^2\eta'^{(0)}\\&-\frac{\partial}{\partial Z}\left[(U_0-c_0)\left(\frac{\partial}{\partial \xi}\left(u'^{(0)}\frac{\partial \eta'^{(0)}}{\partial Z}\right)+\hat{\gamma}\frac{\partial u'^{(0)}}{\partial \xi}\frac{\partial \bar{\eta}^{(0)}}{\partial Z}+\frac{\partial^2 \eta'^{(0)}}{\partial \tau \partial Z}\right)\right].\end{aligned} \tag{5.250}$$

Using these definitions, equation (5.248) is written as

$$L\frac{\partial \eta'^{(1)}}{\partial \xi}=M. \tag{5.251}$$

Note that equation (5.235) reduces to

$$L\Phi=0, \tag{5.252}$$

with the definition of L given in (5.249). Based on (B.140)-(B.147), Green's formula (Haberman, 2014) and the homogenous boundary conditions it is found that

$$\int_{-1}^{0}\left(L\frac{\partial \eta'^{(1)}}{\partial \xi}\right)\Phi-(L\Phi)\frac{\partial \eta'^{(1)}}{\partial \xi}dZ=0, \tag{5.253}$$

for Φ satisfying (5.252). This implies that

$$\int_{-1}^{0}M\Phi\,dZ=0, \tag{5.254}$$

the so-called compatibility condition. In (B.148)-(B.164) an explicit expression is obtained, resulting in an equation amplitude A has to satisfy;

$$\frac{\partial A}{\partial \tau}+c_h\frac{\partial A}{\partial \xi}+\alpha_1 A\frac{\partial A}{\partial \xi}+\beta_1\frac{\partial^3 A}{\partial \xi^3}=0, \tag{5.255}$$

This equation is the variable bed KdV equation, with the relevant constants given by

$$c_h = \frac{\hat{\gamma}}{2}\frac{\int_{-1}^{0}(c_0-U_0)^2\left(\frac{\partial\Phi}{\partial Z}\right)^2\frac{\partial\bar{\eta}^{(0)}}{\partial Z}\,dZ}{\int_{-1}^{0}(c_0-U_0)\left(\frac{\partial\Phi}{\partial Z}\right)^2\,dZ}, \tag{5.256}$$

$$\alpha_1 = \frac{3}{2}\frac{\int_{-1}^{0}(c_0-U_0)^2\left(\frac{\partial\Phi}{\partial Z}\right)^3\,dZ}{\int_{-1}^{0}(c_0-U_0)\left(\frac{\partial\Phi}{\partial Z}\right)^2\,dZ}, \tag{5.257}$$

$$\beta_1 = \frac{1}{2}\frac{\int_{-1}^{0}(c_0-U_0)^2\Phi^2\,dZ}{\int_{-1}^{0}(c_0-U_0)\left(\frac{\partial\Phi}{\partial Z}\right)^2\,dZ}. \tag{5.258}$$

This equation differs from the standard KdV equations (3.2), as it has an extra propagation speed induced by the bathymetric variations.

5.9. Full-dimensional equation

To obtain the dimensional variable KdV equation, the coordinate transformations of (5.220) and (5.221).

$$\frac{1}{\varepsilon}\frac{\partial A}{\partial t} + \frac{c_0}{\varepsilon}\frac{\partial A}{\partial x} + c_h\frac{\partial A}{\partial x} + \alpha_1 A\frac{\partial A}{\partial x} + \beta_1\frac{\partial^3 A}{\partial x^3} = 0. \tag{5.259}$$

Next, the equation is multiplied with ε, yielding

$$\Rightarrow \frac{\partial A}{\partial t} + (c_0+\varepsilon c_h)\frac{\partial A}{\partial x} + \varepsilon\alpha_1 A\frac{\partial A}{\partial x} + \varepsilon\beta_1\frac{\partial^3 A}{\partial x^3} = 0. \tag{5.260}$$

Since A is independent of Z, reversing the transformation to the isopycnal coordinates does not change the considered equation. Next, the coordinate transformation where the relative wave height and relative depth are related is reversed. The relevant transformations are given in (5.70) and (5.72). This leads to

$$\frac{\delta}{\sqrt{\varepsilon}}\frac{\partial A}{\partial t} + (c_0+\varepsilon c_h)\frac{\delta}{\sqrt{\varepsilon}}\frac{\partial A}{\partial x} + \varepsilon\alpha_1\frac{\delta}{\sqrt{\varepsilon}}A\frac{\partial A}{\partial x} + \varepsilon\beta_1\left(\frac{\delta}{\sqrt{\varepsilon}}\right)^3\frac{\partial^3 A}{\partial x^3} = 0, \tag{5.261}$$

multiplying this by $\sqrt{\varepsilon}$ and dividing by δ will give

$$\Rightarrow \frac{\partial A}{\partial t} + (c_0+\varepsilon c_h)\frac{\partial A}{\partial x} + \varepsilon\alpha_1 A\frac{\partial A}{\partial x} + \delta^2\beta_1\frac{\partial^3 A}{\partial x^3} = 0. \tag{5.262}$$

Finally, the scaling of section 5.2 is reversed, using (5.42), (5.45) and (5.48), this gives

$$\frac{\lambda}{a\sqrt{\sigma g h_0}}\frac{\partial A}{\partial t} + (c_0+\varepsilon c_h)\frac{\lambda}{a}\frac{\partial A}{\partial x} + \varepsilon\alpha_1\frac{\lambda}{a^2}A\frac{\partial A}{\partial x} + \delta^2\beta_1\frac{\lambda^3}{a}\frac{\partial^3 A}{\partial x^3} = 0, \tag{5.263}$$

multiply this expression with $\frac{a\sqrt{\sigma g h_0}}{\lambda}$ and using the definition of ε and δ

$$\Rightarrow \frac{\partial A}{\partial t} + (C_0+C_h)\frac{\partial A}{\partial x} + \mathrm{A}_1 A\frac{\partial A}{\partial x} + \mathrm{B}_1\frac{\partial^3 A}{\partial x^3} = 0. \tag{5.264}$$

Here, the full dimensional constants are given by

$$C_0 = \sqrt{\sigma g h_0}c_0, \tag{5.265}$$

$$C_h = \sqrt{\sigma g h_0}\frac{a}{h_0}c_h, \tag{5.266}$$

$$\mathrm{A}_1 = \frac{\sqrt{\sigma g h_0}}{h_0}\alpha_1, \tag{5.267}$$

$$\mathrm{B}_1 = \sqrt{\sigma g h_0}h_0^2\beta_1. \tag{5.268}$$

The KdV equation is known in full-scale (dimensional) variables, which means that the system can be solved, (chapter 6). When the Taylor-Goldstein problem is solved the linear propagation speed and velocity amplitude over the vertical are obtained. Next, these results are combined with the solution of the background, such that the KdV constants can be determined. Finally, the solution to the variable bed KdV equation will help to obtain information about the time evolution and propagation of the waves.

6

Solutions to the variable bed KdV model

To obtain solutions of the variable bed KdV model for internal waves, as derived in chapter 5, three systems need to be solved. As the Taylor-Goldstein equation is independent of the background, the vertical structure and scaled KdV constants c_0, α_1 and β_1 are determined first, using this equation, (section 6.1). This is done based on a linearized numerical quadratic eigenvalue problem. Next, the background system is solved using a similar numerical approach, (section 6.2). This results in a value for c_h. The variable bed KdV equation is solved, resulting in the wave propagation and shape of the waves, (section 6.3). Finally, the pycnocline displacement and flow velocities are determined, (section 6.4).

The Taylor-Goldstein equation (from (5.235)-(5.238)), for the vertical structure in non-dimensional version, is given by

$$\frac{\partial}{\partial Z}\left((U_0 - c_0)^2 \frac{\partial \Phi}{\partial Z}\right) - \frac{\partial \rho_0}{\partial Z}\Phi = 0, \tag{6.1}$$

with corresponding boundary conditions

$$\Phi = 0|_{Z=0}, \tag{6.2}$$
$$\Phi = 0|_{Z=-1}. \tag{6.3}$$

In this problem c_0 is the eigenvalue, which needs to be determined together with the solution. This means that the problem can be seen as a eigenvalue-eigenfunction problem. The eigenfunctions are normalized, by requiring that

$$\max_{-h \le Z \le 0} \Phi(Z) = 1. \tag{6.4}$$

Next, the background system can be solved. Here $g(Z)$ describes the vertical variation of the isopycnal displacement due to the changes in bathymetry. This system is given in equation (5.199)-(5.201) and reads

$$\left[\frac{\partial}{\partial Z}\left(U_0^2(Z)\frac{\partial g(Z)}{\partial Z}\right) - \frac{\partial \rho_0(Z)}{\partial Z} g(Z)\right] = 0, \tag{6.5}$$
$$g(0) = 0, \tag{6.6}$$
$$g(-1) = 1. \tag{6.7}$$

After obtaining the solution for $g(Z)$, the values for $U^{(1)}$ and $\bar{\eta}^{(0)}$ can be determined. From equation (5.206) and (5.207), these relationships are given by

$$U^{(1)}(x, X, Z) = \hat{\gamma} U_0 h'(X) \frac{\partial g(Z)}{\partial Z}, \tag{6.8}$$
$$\bar{\eta}^{(0)}(x, X, Z) = -h'(X) g(Z). \tag{6.9}$$

With the solution of c_0, Φ and the background, the constants in the KdV equation can be determined. These are given by, see equations (5.256)-(5.258):

$$c_h = \frac{\hat{\gamma}}{2} \frac{\int_{-1}^{0} (c_0 - U_0)^2 \left(\frac{\partial \Phi}{\partial Z}\right)^2 \frac{\partial \bar{\eta}^{(0)}}{\partial Z} \, dZ}{\int_{-1}^{0} (c_0 - U_0) \left(\frac{\partial \Phi}{\partial Z}\right)^2 \, dZ}, \tag{6.10}$$

$$\alpha_1 = \frac{3}{2} \frac{\int_{-1}^{0} (c_0 - U_0)^2 \left(\frac{\partial \Phi}{\partial Z}\right)^3 \, dZ}{\int_{-1}^{0} (c_0 - U_0) \left(\frac{\partial \Phi}{\partial Z}\right)^2 \, dZ}, \tag{6.11}$$

$$\beta_1 = \frac{1}{2} \frac{\int_{-1}^{0} (c_0 - U_0)^2 \Phi^2 \, dZ}{\int_{-1}^{0} (c_0 - U_0) \left(\frac{\partial \Phi}{\partial Z}\right)^2 \, dZ}. \tag{6.12}$$

The variable bed KdV equation is solved on an infinite domain without an initial condition. The non-dimensional version of this equation is given by, from (5.255),

$$\frac{\partial A}{\partial \tau} + c_h \frac{\partial A}{\partial \xi} + \alpha_1 A \frac{\partial A}{\partial \xi} + \beta_1 \frac{\partial^3 A}{\partial \xi^3} = 0. \tag{6.13}$$

Appendix C contains the detailed calculations relevant for this chapter. This chapter will just give an overview of the necessary steps to arrive at these solutions.

6.1. Solutions to the Taylor-Goldstein equation

For two simplified cases the solution of Φ is determined using an analytical approach. In other cases this becomes more complicated and the solution needs to be found numerically. This is done using an approach based on a quadratic eigenvalue problem and is discussed in section 6.1.2. Here, this method is compared to the shooting method as used by (Stastna & Lamb, 2002).

6.1.1. Analytical solutions to the Taylor-Goldstein equation

In the case of a two-layer system and a linear stratified fluid it is possible to find an analytical solution. In both cases the background-flow is assumed constant, so

$$\frac{\partial U_0}{\partial Z} = 0. \tag{6.14}$$

Two-layer system without shear flow

In this case a two-layer system is investigated. That means, that the water column can be divided in two layers with different densities. The upper layer has a height of h_1 with density ρ_1, while the bottom layer is defined with a height h_2 and density ρ_2. The sum of these two layer heights is equal to the total water depth h_0.

The solution for the problem is derived in (C.1)-(C.27). The only eigenfunction solution for this situation reads

$$\Phi = \begin{cases} -\frac{h_0}{h_1} Z & \text{for } -\frac{h_1}{h_0} \leq Z \leq 0, \\ \frac{h_0}{h_2}(Z+1) & \text{for } -1 \leq Z \leq -\frac{h_1}{h_0}. \end{cases} \tag{6.15}$$

The solution of the eigenfunction is plotted in figure 6.1 and is piecewise linear.

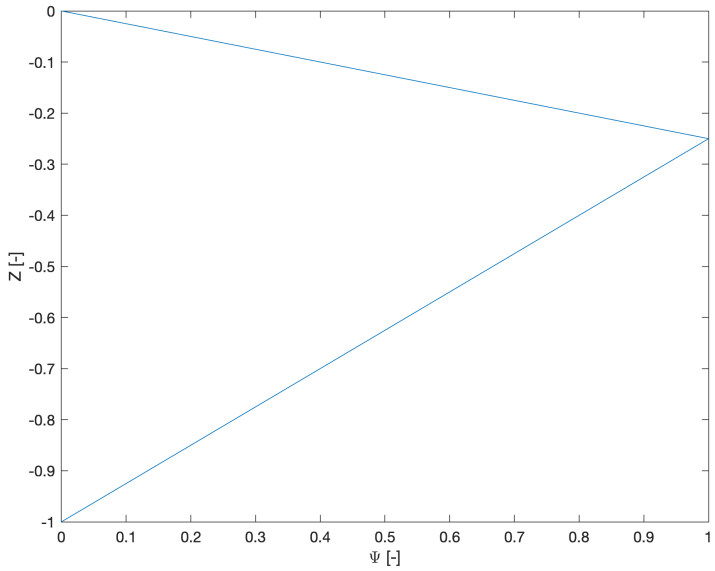

Figure 6.1: Solution to the Taylor-Goldstein equation for a two-layer system, with $h_1/h_0 = 0.25$

According to (5.265)-(5.268) the constants for the KdV equation in full dimensional state, are given by

$$C_0 = \sqrt{\frac{\sigma g h_1 h_2}{h_0}}, \tag{6.16}$$

$$\mathrm{A}_1 = \frac{3}{2} C_0 \frac{h_1 - h_2}{h_1 h_2}, \tag{6.17}$$

$$\mathrm{B}_1 = \frac{1}{6} C_0 h_1 h_2. \tag{6.18}$$

The expressions of these constants are equal to the ones given by Helfrich and Melville (2006).

In the case that a constant background flow is present in the system, the velocity in dimensional form is prescribed by

$$U_0(Z) = U_c, \tag{6.19}$$

and the solutions for c_0 (the eigenvalue) are now all shifted by the amount U_c and equals

$$C_0 = U_c + \sqrt{\frac{\sigma g h_1 h_2}{h_0}}. \tag{6.20}$$

This shift will not change the corresponding eigenfunction.

Linear stratification without shear flow

In this system the density is described by a linear function and no background flow is present in the system. The density varies from ρ_1 at the surface to ρ_2 at the bottom.

Following the calculations in (C.54)-(C.64), this definition for the density results in the following set of solutions for the Taylor-Goldstein eigenfunction-eigenvalue problem (for $n \in \mathbb{N}$)

$$\Phi^{(n)} = -\sin(n\pi Z) \tag{6.21}$$

In figure 6.2 the eigenfunction is plotted for the first three modes of the vertical velocity Φ. The first two modes correspond to the discussion in chapter 2 about figure 2.3.

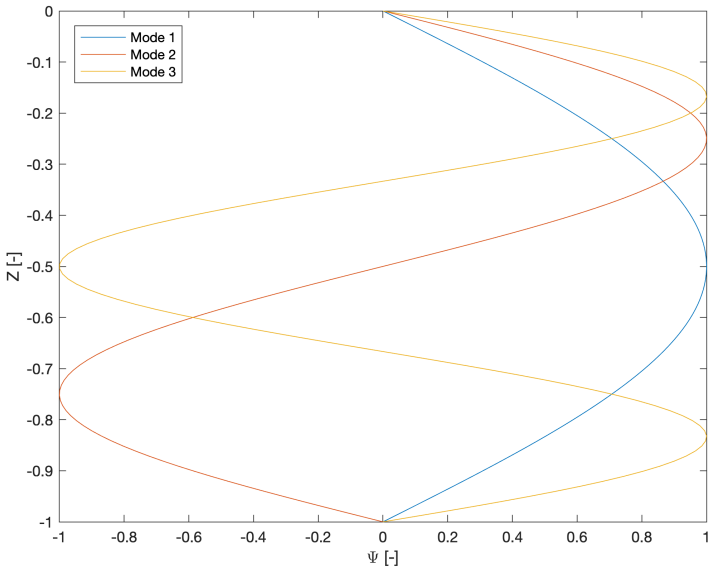

Figure 6.2: Solution to the Taylor-Goldstein equation for linear stratification

Finally, the scaling is applied such that the full dimensional constants are obtained

$$C_0^{(n)} = \frac{\sqrt{\sigma g h_0}}{n\pi}, \tag{6.22}$$

$$\mathrm{A}_1^{(n)} = 0, \tag{6.23}$$

$$\mathrm{B}_1^{(n)} = \frac{1}{2}\frac{h_0}{\sigma g}\left(C_0^{(n)}\right)^3. \tag{6.24}$$

Note that, if in this situation a constant background flow was assumed, as in equation (6.19), the eigenvalues had to be shifted by the same amount, resulting in

$$C_0^{(n)} = U_c + \frac{\sqrt{\sigma g h_0}}{n\pi}. \tag{6.25}$$

This result is similar to the result for a two-layer system with a constant background flow.

6.1.2. Numerical solutions to the Taylor-Goldstein equation

In cases with a more complicated density stratification or a background shear-flow, it is not possible to solve the Taylor-Goldstein equation analytically. Therefore, a numerical approach is required. Two approaches are compared to solve this problem. First, a new approach is introduced where the problem is first written as a quadratic eigenvalue problem (QEP), which can be linearized to obtain a general eigenvalue problem (GEP). The second approach is the shooting method, which is used more often. Finally, these two approaches are compared and one is chosen.

Solving as quadratic eigenvalue problem

It is first shown that the problem can be written as a numerical quadratic eigenvalue problem. To account for the cases where U_0 equals zero somewhere in the vertical, U_{min} will be introduced. This value is equal to the minimal velocity in the vertical, such that

$$U_0 - U_{min} \geq 0. \tag{6.26}$$

Let the eigenvalue be equal to

$$\lambda = c_0 - U_{min}. \tag{6.27}$$

Furthermore, define Φ' as the discrete vector representing the function Φ. Following equations (C.79)-(C.100), the Taylor-Goldstein equation (6.1) can be discretized using central differences. By concentrating the powers of the eigenvalue λ, the equation can be written as a QEP, which reads

$$\left(\lambda^2 M + \lambda C + K\right)\Phi' = 0, \tag{6.28}$$

see appendix C for the exact definitions of M, C and K. By introducing a new eigenvector Ψ' this QEP can be linearized and written as a GEP, (Tisseur & Meerbergen, 2001). This new eigenvector is given by

$$\Psi' = \begin{bmatrix} \lambda\Phi' \\ \Phi' \end{bmatrix}. \tag{6.29}$$

The corresponding GEP is than given by

$$\begin{bmatrix} -C & -K \\ I & 0 \end{bmatrix}\Psi' = \lambda \begin{bmatrix} M & 0 \\ 0 & I \end{bmatrix}\Psi', \tag{6.30}$$

with I the identity matrix.

Finally, this can also be written as a standard eigenvalue problem (SEP), (Tisseur & Meerbergen, 2001),

$$\begin{bmatrix} -M^{-1}C & -M^{-1}K \\ I & 0 \end{bmatrix}\Psi' = \lambda\Psi'. \tag{6.31}$$

This SEP can be solved by using `eigs` in Matlab. From the resulting eigenvector the second part is normalized and reported as the eigenfunction of the original problem. Modes with a positive value for λ are classified as positive (and have right-going waves). Finally, these results are used to determine the KdV constants. For this step the approach is discussed in equations (C.101)-(C.109).

Note, that `eigs` is not the most efficient solver when solving a system for only one eigenvalue. Therefore, this solution method can be improved by implementing a more efficient procedure. This limits the calculation time.

Solving with the shooting method

A different approach solving problem (6.1) is using a shooting method. This approach is based on the solution to the long-wave Taylor-Goldstein equation for internal waves by Stastna and Lamb (2002). c_0 is used as a shooting parameter. For a given c_0 the value of Φ at the surface is determined. If this value matches the surface boundary condition (6.2), it was a correct guess and the solution is stored.

To determine the solution along the water column and obtain the surface value, the governing equation needs to be integrated. Therefore, the equation is written as a linear system

$$\frac{\partial}{\partial Z}\begin{bmatrix} \Phi \\ \Phi_Z \end{bmatrix} = \begin{bmatrix} 0 & 1 \\ \frac{\frac{\partial \rho_0}{\partial Z}}{(U_0 - c_0)^2} & -2\frac{\frac{\partial U_0}{\partial Z}}{U_0 - c_0} \end{bmatrix}\begin{bmatrix} \Phi \\ \Phi_Z \end{bmatrix}. \tag{6.32}$$

This system can easily integrated using the Runge-Kutta integration method. Therefore, the initial value at the bottom needs to be set. For Φ is it clear that this should be zero, since it is the boundary condition (6.3). As non-zero eigenfunctions are searched Φ_Z should be set non-zero. The exact value does not matter, as each eigenfunction is normalized in a later stage.

Choosing guesses is performed in two stages. First 10 points between $U_M + 0.5$ and $U_M + 0.005$ are chosen, where U_M is the maximum value of $U_0 - U_{min}$. 0.5 is the maximum value for a two-layer system (without background flow) and 0.05 is just 10% of this value. The choice of shifting the domain by U_M makes sure that the singularity around $(U_0 - U_{min}) - c_0 = 0$ is avoided. From the surface values of Φ corresponding to this guesses two consecutive values with a different sign are selected. The correct value of c_0 should be in between, as the value searched for is zero. Here it is assumed, that $\Phi_0(c_0)$ is continuous. In the second phase the interval between these two points is reduced in multiple steps, by calculating a value in between and checking the sign. Until a certain required accuracy is reached.

Comparison and performance of the quadratic eigenvalue problem and shooting method

The performance of the QEP and shooting method without background flow are tested. The time to solve the problem and calculate all KdV constants is measured for both methods for three different grid sizes: $N = 10$, $N = 100$ and $N = 1000$ (all equidistant grids). This analysis is performed for two different cases: a two-layer and a linear stratified fluid. As the analytical solution is known for these two cases the error can be calculated, such that the accuracy can be checked. The results are given in table 6.1 and 6.2. In both tables can be found that the calculation time of the shooting method is largest, certainly when asked to calculate five eigenvalues instead of one. The error for the two-layer system (table 6.1) is becoming smaller when the number of grid points increases from ten to hundred. When the number of grid points increases even more, to a thousand, the error remains around the same value. This has to do with the approximation of the two-layer system in the numerical case. The derivative of the density is in this case given by a delta-function. This delta-function is approximated by an exponential function

$$\delta(Z) \approx \frac{1}{|a|\sqrt{\pi}} e^{-((Z-Z_0)/a)^2}, \tag{6.33}$$

where in the limit $a \to 0$ the relationship is exactly equal. As the applied function is an approximation, an offset from the exact value occurs always and the numerical error does not decrease when the approximation of the delta-function is not improved.

The error of c_0 in the linear stratified case is also decreasing when the number of grid points rises. The shooting method has the same error for hundred and thousand points. This has to do with the method, as it is asked to find a value for c_0 within a required accuracy. Which also explains, why the shooting method outperforms the other methods at ten grid points. For α_1 the error is almost zero after the calculations of the QEP method. The analytical value also equals zero in this case. The shooting method shows a much larger error. The error of β_1 has also been estimated, which does not show large differences between the two methods.

Finally, one of the numerical methods should be chosen to use in further analysis. As the QEP solver is faster and has smaller errors than the shooting method, this solver is preferred and used from now on to calculate the necessary vertical velocity amplitude Φ and KdV constants.

6.2. Solutions to the background system

The background problem (6.5)-(6.7) contains similar differentials as the TGE (6.1). Therefore the numerical approximations can be made, using the same central differences. First, observe that equation (6.5) is equivalent to

$$U_0 \frac{\partial^2 g}{\partial Z^2} + 2U_0 \frac{\partial U_0}{\partial Z}\frac{\partial g}{\partial Z} - \frac{\partial \rho_0}{\partial Z} g = 0. \tag{6.34}$$

Next, discretize this equation similar to the TGE. Write g' as the discrete version of g. The discrete version of the problem is given by

$$(K_1 A_2 + K_2 A_1 + K_3) g' = \begin{bmatrix} -(K_1)_{(1,1)}\mu_{1,2} + (K_2)_{(1,1)}\nu_1 \\ 0 \\ \vdots \end{bmatrix}, \tag{6.35}$$

where A_1, A_2, K_1, K_2, K_3, $\mu_{1,2}$ and ν_1 are equal to the definitions in appendix C.2 for the numerical approximation of the TGE. As this system is a simple matrix-vector problem, this system is easily solved by calculating the inverse of the matrix. This results in a solution for g'.

Combined with (6.8) and (6.9) the velocities can be determined. Note, that if the bed is flat, $h' = 0$, the system results in that both $U^{(1)}$ and $\bar{\eta}^{(0)}$ are equal to zero.

Finally, the KdV constant c_h are determined. Therefore, numerical approximations (C.109) and (C.112) are used.

Solution method	QEP			Shooting		
N	10	10^2	10^3	10	10^2	10^3
Calculation time [s]	0.0029	0.0216	0.1898	0.0079	0.0565	0.5002
Error c_0	$3.5 \cdot 10^{-1}$	$1.3 \cdot 10^{-2}$	$1.3 \cdot 10^{-2}$	$3.6 \cdot 10^{-1}$	$1.3 \cdot 10^{-2}$	$1.3 \cdot 10^{-2}$
Error α_1	$5.8 \cdot 10^{-2}$	$2.4 \cdot 10^{-3}$	$2.5 \cdot 10^{-3}$	$7.3 \cdot 10^{-2}$	$2.5 \cdot 10^{-3}$	$2.5 \cdot 10^{-3}$
Error β_1	$4.7 \cdot 10^{0}$	$5.4 \cdot 10^{-2}$	$5.1 \cdot 10^{-2}$	$4.5 \cdot 10^{0}$	$4.1 \cdot 10^{-2}$	$5.0 \cdot 10^{-2}$

Table 6.1: Calculation time and errors for a two-layer system without shear flow (N is the number of grid points).

	Solution method	QEP			Shooting		
	N	10	10^2	10^3	10	10^2	10^3
One eigenvalue	Calculation time [s]	0.0196	0.0142	0.1367	0.0161	0.0415	0.3291
	Error c_0	$1.1 \cdot 10^{-3}$	$1.3 \cdot 10^{-5}$	$1.3 \cdot 10^{-7}$	$1.8 \cdot 10^{-5}$	$5.3 \cdot 10^{-7}$	$5.3 \cdot 10^{-7}$
	Error α_1	$2.8 \cdot 10^{-15}$	$3.6 \cdot 10^{-14}$	$8.2 \cdot 10^{-12}$	$2.8 \cdot 10^{-5}$	$5.0 \cdot 10^{-6}$	$5.0 \cdot 10^{-6}$
	Error β_1	$1.7 \cdot 10^{-4}$	$2.0 \cdot 10^{-6}$	$2.0 \cdot 10^{-8}$	$1.1 \cdot 10^{-4}$	$1.2 \cdot 10^{-6}$	$1.2 \cdot 10^{-7}$
Five eigenvalues	Calculation time [s]	0.0159	0.0165	0.2261	0.0448	0.3151	2.9753
	Error c_0	$5.7 \cdot 10^{-3}$	$6.4 \cdot 10^{-5}$	$6.5 \cdot 10^{-7}$	$8.5 \cdot 10^{-4}$	$3.1 \cdot 10^{-7}$	$3.1 \cdot 10^{-7}$
	Error α_1	$4.9 \cdot 10^{-15}$	$7.6 \cdot 10^{-14}$	$8.2 \cdot 10^{-12}$	$6.5 \cdot 10^{-3}$	$5.9 \cdot 10^{-6}$	$5.9 \cdot 10^{-6}$
	Error β_1	$1.7 \cdot 10^{-4}$	$2.0 \cdot 10^{-6}$	$2.0 \cdot 10^{-8}$	$1.1 \cdot 10^{-4}$	$1.3 \cdot 10^{-6}$	$2.6 \cdot 10^{-8}$

Table 6.2: Calculation time and errors for linear stratification without shear flow (N is the number of grid points).

6.3. Periodic solution to the KdV equation

For the KdV equation (6.13) periodic solutions are investigated, as the observations by Rijnsburger et al. (2019b) behave like periodic waves, see figure 1.4. These solutions are already explored in literature for the standard KdV equation. The standard KdV equation does not contain a propagation speed, only a derivative to time and terms for α_1 and β_1. To be able to solve the variable bed KdV equation, it is possible to make a coordinate transformation such that it results in the standard KdV equation. Introducing the following coordinate transformation

$$\xi' := \xi - c_h \tau, \tag{6.36}$$

$$\tau' := \tau. \tag{6.37}$$

The partial derivatives for this transformation read

$$\frac{\partial}{\partial \xi} = \frac{\partial}{\partial \xi'}, \tag{6.38}$$

$$\frac{\partial}{\partial \tau} = \frac{\partial}{\partial \tau'} - c_h \frac{\partial}{\partial \xi'}. \tag{6.39}$$

Equation (6.13) in the new coordinate system is given by

$$\frac{\partial A}{\partial \tau'} + \alpha_1 A \frac{\partial A}{\partial \xi'} + \beta_1 \frac{\partial^3 A}{\partial \xi'^3} = 0, \tag{6.40}$$

which is the standard KdV equation. Based on Drazin and Johnson (1989) the solution for this equation reads

$$A(\xi', \tau') = a_t + \mathrm{cn}^2(2K(m)(\xi' - c\tau')|m), \tag{6.41}$$

Here $\mathrm{cn}^2(\cdot|m)$ is an Jacobi elliptic function with a period of $2K(m)$, where $K(m)$ is the complete elliptic integral of the first kind, (Drazin & Johnson, 1989). The constants in the solution are determined, by using for the shape factor m (elliptic modulus)

$$K(m) = \sqrt{\frac{\alpha_1}{48\beta_1}} \frac{1}{m}, \tag{6.42}$$

a_t can be determined using

$$a_t = -\int_0^1 \mathrm{cn}^2(2K(m)\chi|m) d\chi, \tag{6.43}$$

and c can be found by

$$c = \alpha_1 \left(a_t + \frac{2}{3} - \frac{1}{3m^2} \right). \tag{6.44}$$

Reversing the transformations to the original framework, yields to the final solution

$$A(x, X, t) = A_t + a\,\mathrm{cn}^2 \left(2K(m) \frac{\sqrt{a}}{h_0 \sqrt{h_0}} (x - (C_0 + C_h(X) + C)t) \middle| m \right), \tag{6.45}$$

where

$$C = \frac{a}{h_0} \sqrt{\sigma g h_0} c, \tag{6.46}$$

$$A_t = a a_t. \tag{6.47}$$

Note that, this solutions breaks down when $\alpha_1/\beta_1 < 0$, as the square root of a negative number is not a real number. This situation is handled by changing the sign of α_1 and A in equation (6.13). After this

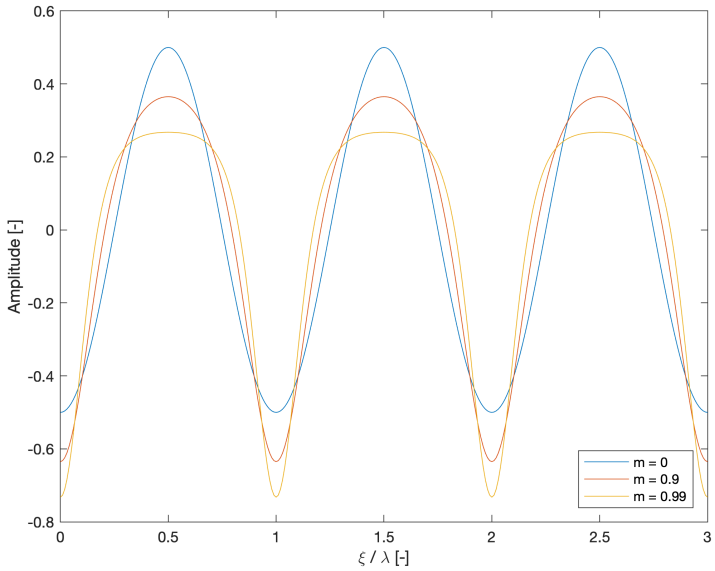

Figure 6.3: Periodic solution to the KdV for multiple values of m

substitution the original equation is again obtained and α_1 and β_1 have the same sign and a solution can be obtained. For three different values of m the solution has been plotted in figure 6.3. For $m = 0$ the signal is just a sinusoid and for larger values of m the waves become steeper (more asymmetric).

The wave properties of this solution can be obtained, by using the periodicity of the elliptic function. The total propagation speed is given by

$$C_p := C_0 + C_h + C. \tag{6.48}$$

The wave length is calculated by

$$\lambda = h_0 \sqrt{\frac{h_0}{a}}. \tag{6.49}$$

Note that this follows directly from the relationship $\varepsilon = \delta^2$. Finally the wave period is equal to

$$T = \frac{\lambda}{C_p} = \frac{h_0\sqrt{h_0}}{\sqrt{a}(C_0 + C_h + C)}. \tag{6.50}$$

6.4. Calculation method for total displacement and flow velocities

In the previous sections the solution to the Taylor-Goldstein, KdV equation and background have been discussed. With these solutions in hand the isopycnal displacement, and horizontal- and vertical velocity can be determined. From the decompositions and the asymptotic expansions the total displacement in full dimensional variables equals

$$\eta(x, X, Z, t) = -h'(X)g(Z) + A(x, X, t)\Phi(Z) + \mathcal{O}(\varepsilon). \tag{6.51}$$

The total horizontal velocity is given by

$$u(x, X, Z, t) = U_0(Z)\left(1 + h'(X)\frac{\partial g}{\partial Z}\right) - A(x, X, t)(U_0(Z) - C_0)\frac{\partial \Phi(Z)}{\partial Z} + \mathcal{O}\left(\varepsilon^2\right). \tag{6.52}$$

Equation (5.94) evaluated at the first order results in an expression for the time-dependent vertical velocity

$$w'(x,Z,t) = \left(\frac{\partial A}{\partial t} + U\frac{\partial A}{\partial x}\right)\Phi + \mathcal{O}(\varepsilon). \tag{6.53}$$

As $\eta(x,Z,t)$ is now known, the value of z can be determined for each Z. This means that the transformation to the isopycnal coordinate can be reversed to a normal Eulerian coordinate system. After that the reversed scaling transformations can be applied, to obtain the result at full scale.

Finally, the solution for all three systems as stated in the beginning of this chapter are solved. The solution for the TGE is used next in the development of the TGE fitting procedure, (chapter 7). Using the solutions to the variable KdV model, the sensitivity of internal waves is studied, (chapter 9). Furthermore, the applicability of this KdV model is tested (chapter 10) and the typical properties of the observed internal wave events are estimated, (chapter 12).

7

TGE fitting procedure

The Taylor-Goldstein equation can be solved by providing the density stratification and background flow. The observations of Rijnsburger et al. (2019b) contain only four density measurement points in the vertical at: -1, -2.5, -10, -15 $[\mathrm{m}]$. Through these data points an hyperbolic tangent can be fitted, but the location and thickness of the pycnocline is unsure, as the pycnocline is usually located somewhere between -2.5 and -10 $[\mathrm{m}]$. In this range there is no density data available. Furthermore, the direction of wave propagation can not be determined clearly from the velocity measurement data. As the TGE and KdV equation are defined in a 2DV domain, it is not possible to get a good estimate of the background flow without this direction of propagation.

To find the missing information on stratification and direction of wave propagation, the TGE solution is fitted on the measurement data. To obtain the missing data a procedure is developed, wherein the unknowns are varied such that a minimal error between the TGE solution and measured velocity amplitude is obtained. First, the construction and scoring of a TGE solution fit is explained, (section 7.1). Next, the approach to minimize the error is discussed, (section 7.2). Finally, the limitations of this procedure are investigated, (section 7.3).

7.1. Constructing and scoring of TGE solution fit

To be able to solve the TGE it is necessary, that the density stratification and background flow profile are given. To obtain the density stratification profile, the four density observations are used. For each wave event in table 2.1 the data is averaged over a timeframe of 5 to 15 minutes wherein the waves are visible. This is giving for each wave event a representation of the non-wave-disturbed density at these points. By fitting an hyperbolic tangent through these points, a density profile is obtained. This hyperbolic tangent does not necessarily have the correct depth and thickness of the pycnocline, as there is no information about the density close to the pycnocline. However, this profile can be used to construct a solution for the TGE.

To obtain the background flow profile a propagation direction is required. As this value is not clearly obtained from the research of Rijnsburger et al. (2019b), the direction of the upper layer is used as a first guess, which is used to obtain the flow profile in the 2DV domain. This flow profiles is determined by averaging the data over an interval of 5 to 15 minutes. Note that, this flow profile is obtained for every 25 $[\mathrm{cm}]$. Therefore, the flow profile is known over the complete water column.

With these two profiles the TGE (6.1) can be solved. This is done using the QEP approach discussed in section 6.1.2. Next, the TGE solution depending on the isopycnal coordinate Z is obtained. Based on the solution for w' the TGE solution Φ can be compared with the velocity measurements. As Φ is the only vertical depending value in equation (6.53), it is concluded that any non-zero vertical velocity profile should be proportional to Φ.

The vertical velocities are measured by the Acoustic Doppler Current Profiler (ADCP) with a resolution

of 25 [cm], (Rijnsburger et al., 2019b). From each layer the minimum velocity (negative) is subtracted from the maximum velocity and the result is divided by two. This results in velocity amplitude profile in the Eulerian coordinate z. In the timeframe of 5-15 minutes the waves look periodic, therefore it is assumed that these can be described by the periodic KdV solution (6.45). Furthermore, the assumption is made that the wave is symmetric, $m = 0$ in the periodic KdV solution. This implies that the wave can be described by a cosine. Meaning that the maximum vertical velocity is located at the midpoint (equilibrium level), and that the vertical amplitude profile in Eulerian coordinates is the same as the profile in isopycnal coordinates, which implies that this profile can be compared directly to the TGE solution. Finally, the resulting amplitude profile is normalized such that the maximum value equals one.

As the TGE solution and the velocity amplitude profile are in the same coordinate system, these two can be compared. By interpolation of the TGE solution to the measurement data an error for each measured velocity amplitude can be obtained. Interpolation is necessary, as the TGE solution is in this case solved on an equidistant grid with 100 points, and the ADCP measurements are not necessary on these grid points. With the errors per observation point, the mean squared error (MSE) is calculated. This is the score for the quality of the constructed fit.

7.2. Error minimization procedure

As it is now known, how the TGE fit can be constructed and scored, the error minimization procedure is explained. This is done in three different steps: first the pycnocline depth is fitted, next the pycnocline thickness and finally the direction of wave propagation are handled.

Step 1: Fit pycnocline depth

The depth of the pycnocline is unsure, therefore this is used as a free variable to optimize the match of the TGE solution. First, the effect of the pycnocline depth is studied. In figure 7.1 the location of the pycnocline is varied while all other variables are kept the same. It is clear that the location of the pycnocline determines the location of the peak in the eigenmode solution. This is logical, when looking at the analytical solution for a two-layer system, equation (6.15), as there the location of the pycnocline determines where the top of the function is located.

Next, the optimization of the pycnocline can be performed. The objective of this optimization process is to minimize the mean squared error (MSE) between the solution and the measurements. This is done by varying one variable: the depth of the pycnocline. The constraints on this variable are that the optimum should be found between -2 and -10 [m], as otherwise the data can not be matched.

Step 2: Fit pycnocline thickness

After optimizing the depth there is only one unknown left for the pycnocline: the thickness. When the pycnocline depth is fixed, the effect of the thickness is visible in figure 7.2. From this can be seen that when the pycnocline thickness is larger, the peak is also shifted towards the water surface. Note that this effect is much smaller compared to the variation of the pycnocline depth. Furthermore, it is seen that for larger thicknesses the function values are also larger in the area around the pycnocline. This effect is best visible above the pycnocline, but can also be found underneath. Next, the thickness can be optimized, with the objective to again obtain a minimum MSE.

Step 3: Fit direction of wave propagation

As the variables for the pycnocline are now optimized, the unknown value left is the wave angle. Remember that this wave angle influences the TGE solution, because it determines the background flow. The effect of the wave angle is studied in figure 7.3. Here, it can be seen that the velocity keeps the location of the peak (nearly) unchanged. It influences mainly the curvature of the obtained function.

The optimization is performed over a range of propagation directions, which are bounded by ± 90 degrees around the direction of the flow in the upper layer, which is the initial guess based on Rijnsburger

Figure unavailable until publication of Rijnsburger et al. (2019b)

Figure 7.1: Effect of the pycnocline depth on the solution of the Taylor-Goldstein equation. Wave event October, 4th 10:24, measurement data from Rijnsburger et al. (2019b).

et al. (2019b). During this optimization the pycnocline height and thickness are kept equal. The objective of the optimization is also here to obtain the minimum MSE.

This three step procedure results in an estimate for the pycnocline (depth and thickness) and the direction of wave propagation. With this estimate it is also possible to obtain the linear phase velocity of the internal wave as the TGE provides this as solution.

7.3. Limitations to the TGE fitting procedure

There are some limitations to this procedure. The assumption is made, that the maximum vertical velocity of a wave occurs at its equilibrium level. This is true for symmetric waves with $m = 0$ for the periodic KdV solution, but if the waves become steeper or can not be described by the periodic KdV solution this assumption does not hold. In these cases a transformation from Eulerian to isopycnal coordinates should be made to eliminate the error. As the waves observed in the Rhine ROFI are not steep and not of large amplitude the error made is small. For periodic waves, the wave height should be over 1 [m] and the steepness should be large $m > 0.9$, to have an error larger than the vertical ADCP resolution of 25 [cm].

In this procedure the three free variables are varied one by one and not combined at once. This to limit the computation time and to keep this procedure simple. The order of the minimization steps is fixed. This may be a limitation, as it is not sure if the pycnocline thickness has a larger influence on the vertical structure Φ compared to the direction of wave propagation.

Finally, this procedure does only take the leading order solution of the vertical velocity w' into account. The data may be influenced by smaller effects, which are now not taken into account.

Figure 7.2: Effect of the pycnocline thickness on the solution of the Taylor-Goldstein equation. Wave event October, 4th 10:24, measurement data from Rijnsburger et al. (2019b).

Figure 7.3: Effect of the wave angle on the solution of the Taylor-Goldstein equation. Legend states the angle, relative to the flow in the upper layer. Wave event October, 4th 10:24, measurement data from Rijnsburger et al. (2019b).

II

Validations and results

8

Delft3D model results

The Delft3D model developed by Rijnsburger et al. (2019a) has been refined to get a better estimate of the pycnocline, (chapter 4). The new model runs have been compared to the reference model and measurements from 2014 in the Rhine ROFI. This analysis can be found in appendix D and corresponds to result I in figure 3.1. Concluded is, that the 48 layers refinement resolves the horizontal velocities better compared to the reference run, with 20 layers and that the refined model performs at least as good for the salinity measurements as the reference run.

The results from the new refined model run are used to assess the effect of tide and wind on the stratification. To perform this analysis two quantities for the pycnocline are defined. The relative layer depth is defined as

$$\theta = \frac{h_1}{h_1 + h_2}, \tag{8.1}$$

where h_1 and h_2 are the depths of the upper and lower layer respectively. This quantity is also referred to as the non-dimensional upper layer depth or the relative location of the pycnocline (as in section 9.1). The density difference is defined as

$$\Delta\rho = \rho_2 - \rho_1, \tag{8.2}$$

where ρ_1 and ρ_2 are the densities of the upper and lower layer. This quantity is chosen, such that a strong front gives a larger and positive difference compared to a weak front. These two properties are used to study the stratification in the Rhine ROFI.

The behavior of stratification under different tidal and wind conditions in the Delft3D model is verified with literature on the Rhine ROFI. In section 8.1 the effect of semi-diurnal tide and the spring-neap cycle on the density stratification is assessed. Next, in section 8.2, the effect of different wind directions is investigated.

8.1. Tidal effects on the stratification

First, the effect of the semi-diurnal tide (M_2) on the density stratification is investigated. Figure 8.1 shows the water level, relative layer depth and density difference at M18 for a consecutive period of ten days. This figure demonstrates that the relative layer depth (middle panel) varies between 0.1 and 0.5. The peaks of this signal do not give a clear correlation with the tidal elevation (top panel). The density difference in the bottom panel varies between 0 and 6.5 $[\mathrm{kg/m^3}]$ and has typically a peak around HW+2 (see top panel for the tidal elevation). This corresponds to the finding of de Boer, Pietrzak, and Winterwerp (2008); Rijnsburger et al. (2018) where the passage of the front at this location was observed around HW+2.

Next, the effect of the tidal variation due to the semi-diurnal tidal cycle is studied more quantitative. Therefore, the relative layer depth and density differences are collected at four different tidal phases:

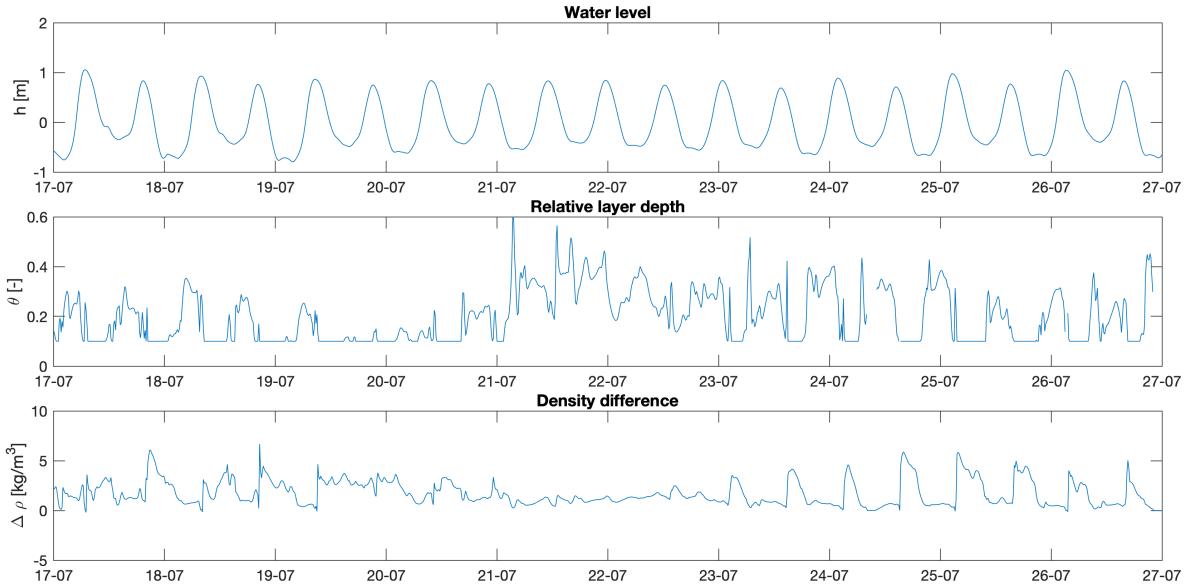

Figure 8.1: Water level, relative layer depth and density difference at M18 (September, 17th - September, 27th).

HW-2, HW, HW+2 and LW during the period from July, 10th till August, 8th (which is the period selected in section 4.1). These phases are chosen as the moments where the tidal elevation has extreme values (HW and LW), when the front passes the observation points (HW+2), following de Boer et al. (2008), and the moment when the ROFI is located south of the river mouth (HW-2). Note, that the choice of HW+2 is valid for averaged conditions and that the exact arrival at the observation points differs between spring and neap tides.

The statistics for M18 are presented in the form of a box-plot (figure 8.2). Here is observed, that the upper layer is thinnest during the HW+2 phase and thickest during HW-2. As the fresh water plume has a thin upper layer, this corresponds with the expected arrival of the front at this location, (de Boer et al., 2008). The density differences appears to be largest during HW+2.

In figure 8.4 the surface density and velocity vectors for the averaged spring and neap tide conditions is given. During LW the flow is directed to the southeast and the fresh-water is released from the river mouth. During HW-2 the flow velocity is nearly zero and the tide is turning, this moves the fresh-water in the northeastern direction as can be seen during HW. Here, the flow is directed to the northeast and has a large magnitude. This finally results in the HW+2 stage, where the fresh-water reaches the Sand-Engine and where the velocities are partially turned towards the coast due to tidal straining. At HW+2 the magnitude of the flow is smaller compared to HW, which shows that tide starts to turn. From the comparison between spring and neap tide, it is seen that the fresh water spreads further during neap tides. The $1020\ [\mathrm{kg/m^3}]$ contour is much further offshore during all phases of the semi-diurnal tide.

The local variation of the four tidal stages is given in figure 8.5; the density difference averaged over the complete spring-neap cycle is given in figure E.1, here the mean value is presented of a specific phase over all tidal cycles in the given period. In the figures for relative layer depth and density difference it can be seen that the latest released tidal plume front of the ROFI is located in the south (near Maasvlakte) during LW and HW-2, and more north around HW and HW+2. At HW+2 the upper layer is thin over a large area, while at the other phases of the tide the thinnest parts of the front are equally thick but the area where this occurs is much smaller. So on average the river plume is thinnest around HW+2. The area where the upper layer is thin, correlates with the locations of large density differences. The maximum density difference is equal over all tidal phases, but the area where the density difference is half of the maximum is much larger just after the release of the front (during HW and HW+2) compared to the other phases. Note that the density is relatively constant in the lower layer, which implies that the density difference is mainly a measure for the density in the upper (surface) layer. From figure 8.6 can now be concluded that the surface layer rotates anti-cyclonic (clockwise). This is the expected

behavior based on tidal straining, (A. J. Souza & Simpson, 1997; Visser et al., 1994). It is observed that the fresh water lens passes the observation point indeed at HW+2 and that this is the key moment of interest. Around this moment the largest density differences occur at the observation points.

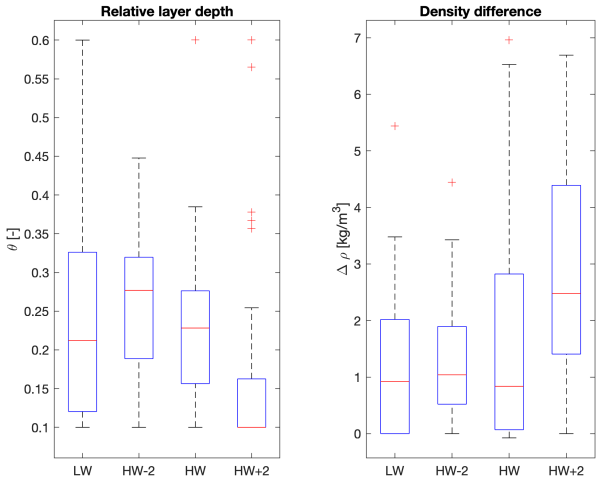

Figure 8.2: Statistics of relative layer depth and density difference for multiple M_2 tidal stages at M18 (July, 10th - August, 8th).

Using the same data the effect of the spring-neap cycle on the stratification is assessed, as it is expected that due to spring tide the water column would be more mixed than during neap tide. In figure 8.3 the statistics for the different tidal phases during spring and neap tide are given. The relative depth shows that during neap tide the front is clearly thinnest around HW+2. During spring tide the median of the relative depth is approximately equal for HW, HW+2 and LW. At HW+2 a large variation is shown from 0.1 up to 0.6. More interesting are the density differences, where it is clearly visible that the median and variation are much larger during neap, than during spring tide. Visser et al. (1994) showed that the Rhine ROFI is well-mixed during spring tide and stratified during neap tides. This clearly matches the obtained model data (see figure 8.3). In figure 8.5 the local variability of the relative layer depth is visualized. In the areas where no data is displayed, the water column is always well mixed and the two-layer approach can not be used. The areas with large density differences have a relative small relative layer depth and therefore a shallow pycnocline. It is observed that the relative layer depth is smaller during neap tides. The maximum density difference (figure 8.6) is approximately the same during neap as during spring tide. The figure shows that during neap tides the newly released tidal plume front extends further from the river mouth (area where density differences are over $4\ [\mathrm{kg/m^3}]$ is much larger), this compared to spring tide. This confirms the expectation that the stratification is more visible during neap tides and that the mixing is stronger during spring tides.

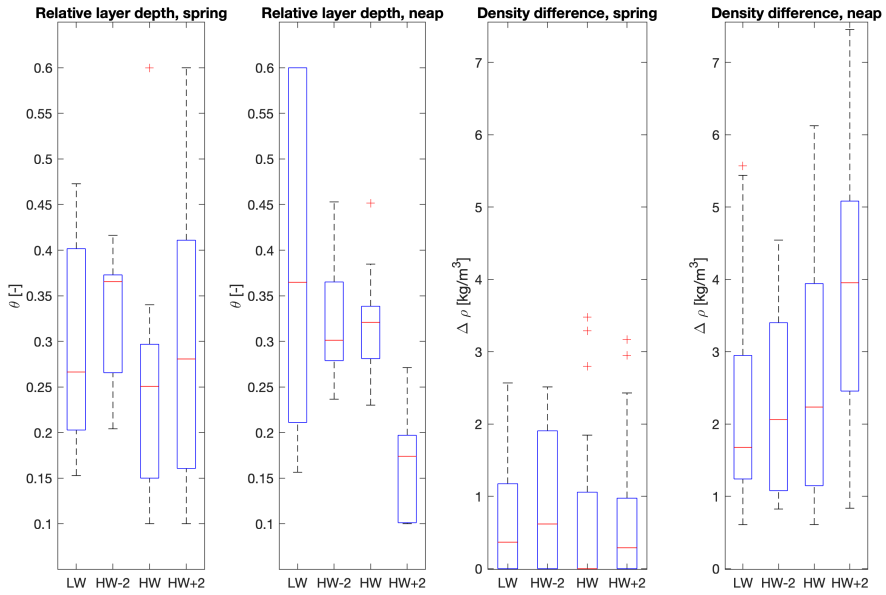

Figure 8.3: Statistics of relative layer depth and density difference for multiple M_2 tidal stages during spring and neap tide at M18 (July, 10th - August, 8th).

Figure unavailable until publication of Rijnsburger et al. (2019a)

Figure 8.4: Mean value of the upper layer density and velocity vectors indicating the flow for multiple M_2 tidal stages during spring and neap tide (July, 10th - August, 8th).

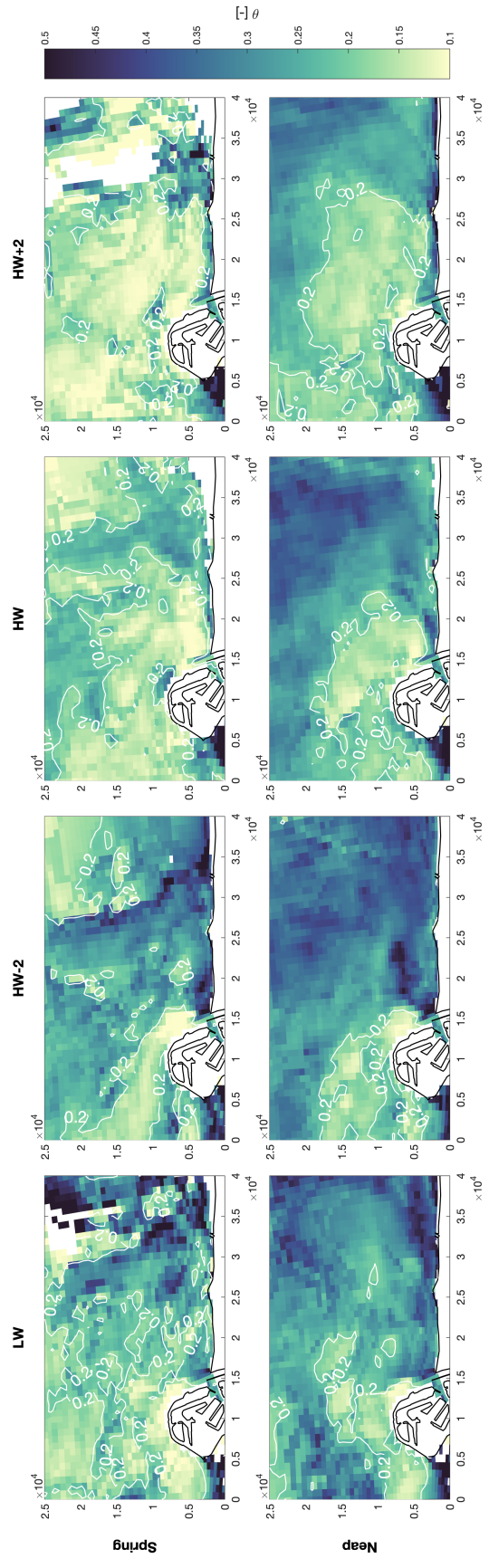

Figure 8.5: Mean value of relative layer depth for multiple M_2 tidal stages during spring and neap tide (July, 10th - August, 8th).

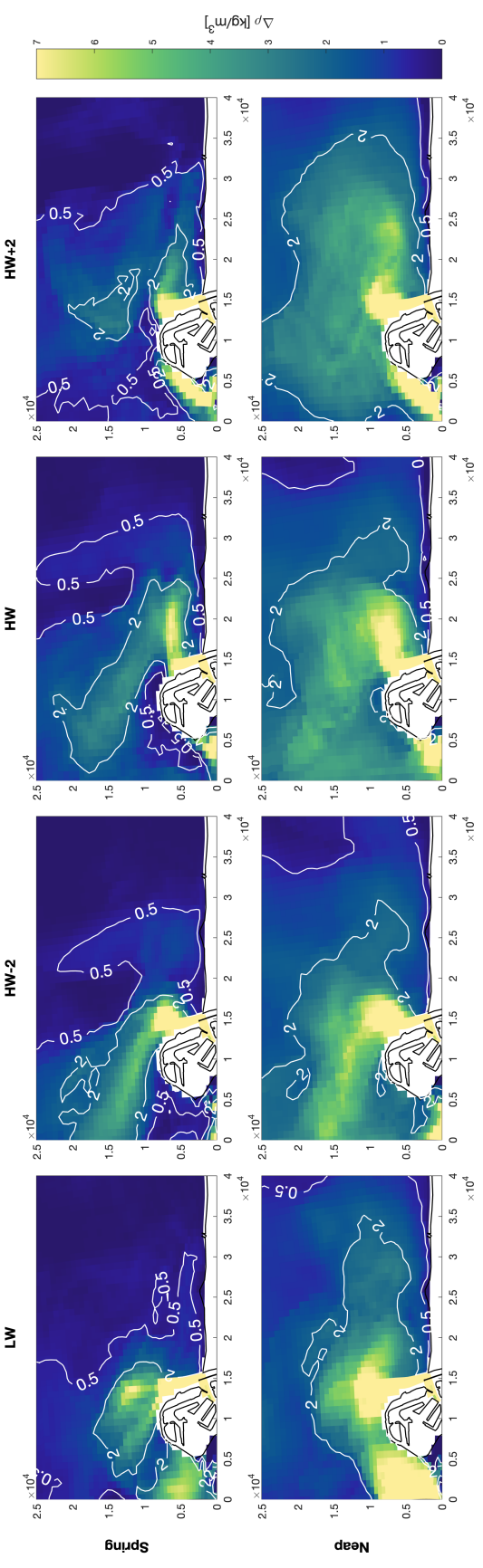

Figure 8.6: Mean value of density difference for multiple M_2 tidal stages during spring and neap tide (July, 10th - August, 8th).

8.2. Wind effects on the stratification

The statistics of the relative depth for the four different wind directions, as seen in figure 4.1, are given in figure 8.7. The periods used for this analysis are discussed in section 4.1. The relative depth is much larger during onshore and downwelling winds, when compared to offshore and upwelling wind conditions. Also the bandwidth of the relative depth is wider under onshore and downwelling winds, compared to the other two directions. The similarity between upwelling and offshore winds can be explained by the direction of the frictional and Ekman transport components, (Fong & Geyer, 2001). Upwelling winds are alongshore directed to the southeast, such that the frictional component is also directed to the southeast. Here the Ekman component is directed to the northeast, which is the same direction as the offshore frictional component. The similarity between downwelling winds and onshore winds can be argued in the same way, according to Rijnsburger et al. (2018).

The density difference (figure 8.8) shows that the density differences during onshore and downwelling winds are less variable over the tidal phases, when compared to offshore and upwelling winds. At HW+2 the density differences are larger under offshore and upwelling conditions and smaller under downwelling and onshore winds. This corresponds to the results of A. J. Souza and Simpson (1997). Under offshore and upwelling conditions the other phases of M_2 are well-mixed.

In figure 8.9 the surface density and surface flow velocities are presented. During HW the different locations of the river plume induced by the different wind directions are clearly visible. With onshore winds the fresh water is located near the coast, while under offshore wind it is located further offshore. With downwelling winds the fresh water is also located near the coast, while under upwelling conditions the river plume is located offshore. These two displacements are due to the Ekman transport induced by the wind.

When the local variation of the relative layer depth is considered (figure E.2), it is obtained that the pycnocline is located deeper for onshore and downwelling winds, this compared to offshore and upwelling winds. The pycnocline is located deepest for downwelling winds, which was also concluded by Rijnsburger et al. (2018). It is obtained that the upper layer is thinnest under the forcing of an upwelling wind. Also the density difference is reported (figure E.3). Here, can be seen that the maximum density difference for all wind directions equals approximately $10\ [\mathrm{kg/m^3}]$. Under offshore and upwelling winds the ROFI is more spread and moved further from the coast, while during onshore and downwelling conditions it is located nearshore. The fact that downwelling leads to a river plume close to the coast, is already observed by Fong and Geyer (2001).

For the background stratification has now found that the largest density differences occur during HW+2 at M18 and during neap tides. Onshore and downwelling winds also lead to relative large density differences.

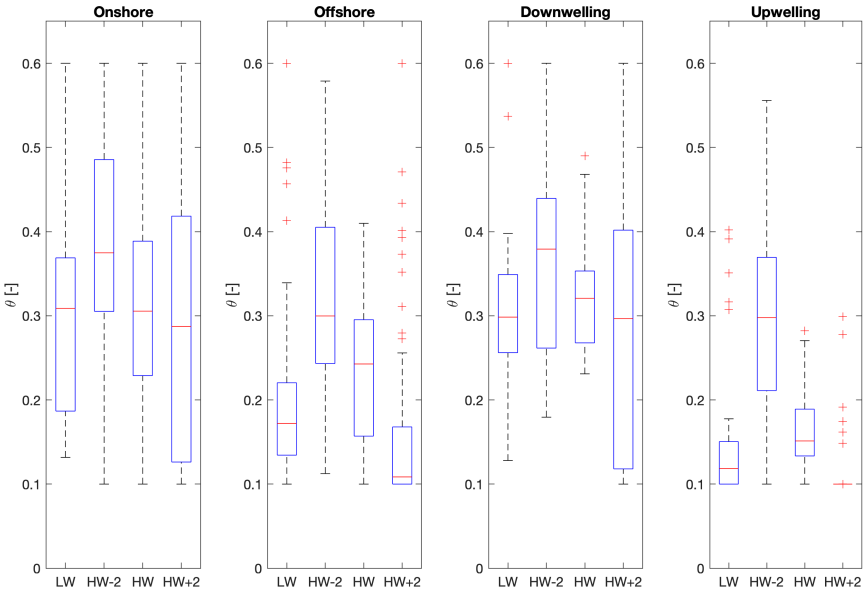

Figure 8.7: Statistics of relative layer depth for multiple M_2 tidal stages for multiple wind directions at M18.

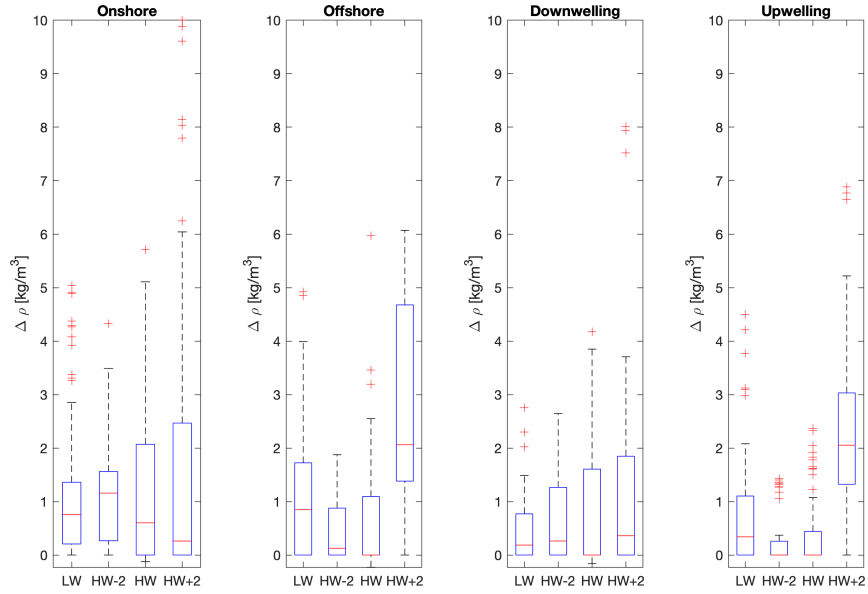

Figure 8.8: Statistics of density difference for multiple M_2 tidal stages for multiple wind directions at M18.

Figure unavailable until publication of Rijnsburger et al. (2019a)

Figure 8.9: Mean value of the upper layer density and velocity vectors indicating the flow for multiple M_2 tidal stages for multiple wind directions.

9

Sensitivity of the variable bed KdV model

Internal waves are influenced by the bathymetry, stratification and background flow. This influence is studied by varying the background state and observing the changes of the periodic KdV solution for internal waves, which is result III in figure 3.1. First, the influence of the background velocity and density stratification on the dimensional KdV constants (C_0, C_h, A_1 and B_1) is studied, (section 9.1). This shows, that the depth of the pycnocline is an important factor for the linear propagation speed C_0 and that this depth determines if waves of elevation or depression are present in the system. Furthermore, it is shown that the amount of shear in the system has a positive correlation with the linear propagation speed C_0. Thereafter, the periodic wave solution is studied, (section 9.2).

9.1. Sensitivity of the KdV constants to the background state

In this section, the influence of the background state on the dimensional KdV constants is studied. This analysis is divided in three parts. First, bathymetric variations are studied, followed by a discussion on the effects of stratification. Finally, the effect of the background (shear) flow is investigated.

While varying the parameters of the bathymetry and stratification, a vertical uniform background flow-profile, velocity U_0, is used. Therefore, the propagation speed is studied by assessing $C_0 - U_0$. A_1 and B_1 do not change under different constant flow profiles and can therefore be studied directly. The coefficient C_h is influenced by the value of U_0. In the first analysis this is neglected. This to study the effect on the constant C_h by bathymetry and stratification only. When the effect of flow variation is studied, the bathymetry and stratification are kept constant. If not mentioned otherwise, the standard setup from table 9.1 is used to perform the necessary calculations.

9.1.1. Effect of bathymetry on the KdV constants

If the undisturbed (mean) water depth h_0 is changed, and the density structure is scaled, such that the pycnocline remains at a constant relative depth, the scaled (non-dimensional) problems of the TGE and KdV equation are not effected. As the scaled system of equations is untouched for changes in the

Physical quantity		Value
Water depth	h_0	$20\ [\mathrm{m}]$
Bathymetric variation	h'	$1\ [\mathrm{m}]$
Relative density	σ	$0.0049\ [-]$
Relative pycnocline depth	θ	$0.2\ [-]$
Relative pycnocline thickness	r_t	$0.18\ [-]$
Relative wave height	ε	$0.05\ [-]$

Table 9.1: Default values used to perform the calculations for the sensitivity analysis.

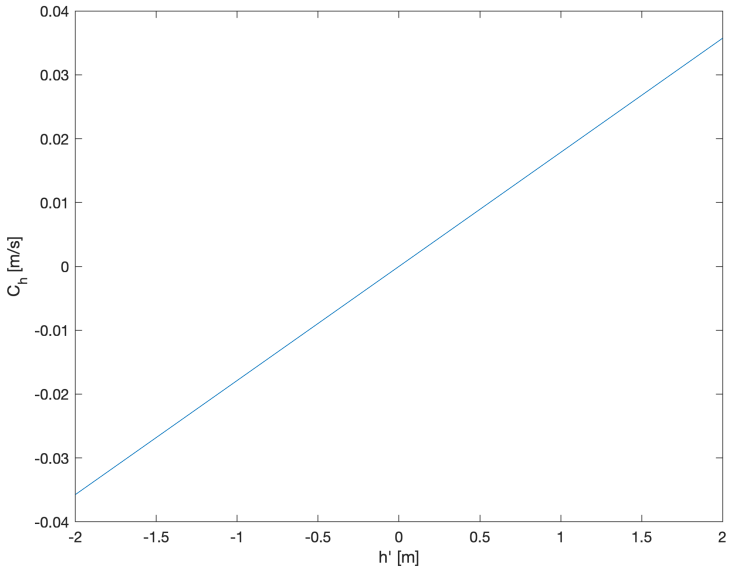

Figure 9.1: Propagation speed due to bathymetry changes C_h $[\mathrm{m/s}]$ relative to the bathymetry change h'.

water depth, the scaled KdV constants are also untouched. In the expressions for the dimensional KdV constants (5.265)-(5.268) the water depth is found, which tells that the long wave internal wave speed C_0 is proportional to the square root of the water depth. The relationships for all four dimensional KdV constants to the depth are stated in table 9.2, second column.

Next, the bed profile is perturbed by introducing a value for the perturbation h'. By the definition of the KdV constants (5.265)-(5.268) is concluded, that only C_h is influenced by this change. From the solution for the background-flow problem and the definition of C_h can be concluded that the propagation speed due to bathymetry changes is linearly dependent on the variation h'. Figure 9.1 shows, that this is indeed the case. For deeper waters h' is larger and that results in faster propagating waves. This is similar to the influence by h_0 on C_0.

As the dependence of C_h on h' is linear, the slope of this line is only important for further analysis of the sensitivity. Therefore, C_h is calculated for $h' = 1$ $[\mathrm{m}]$ in the coming sections. Other bathymetric variations scale proportional to these outcomes.

	h_0	σ	θ
C_0	$h_0^{1/2}$	$\sigma^{1/2}$	$(\theta(1-\theta))^{1/2}$
C_h	$h_0^{1/2}$	$\sigma^{1/2}$	No expression
A_1	$h_0^{-1/2}$	$\sigma^{1/2}$	$(2\theta-1)(\theta(1-\theta))^{-1/2}$
B_1	$h_0^{5/2}$	$\sigma^{1/2}$	$(\theta(1-\theta))^{3/2}$

Table 9.2: Proportionality between the background state (with a constant background flow) and the KdV constants.

9.1.2. Effect of stratification on the KdV constants

When the density difference $\Delta\rho$ and mean density $\bar{\rho}$ are varied, there are two options: these two constants are changed such that σ is not changed or σ is changed. When the value of σ is not changed, the scaled density profile ρ_0 is also not changed. So in this case the scaled KdV constants remain the same, and as σ has not changed the scaling of the KdV constants is also untouched. This implies, that the dimensional KdV constants are not changed. In the case that σ is changed, the scaled system of equations and KdV constants do also not change. The dimensional KdV constants changes change now proportional to the square root of σ, following from the relationships in (5.265)-(5.268). These

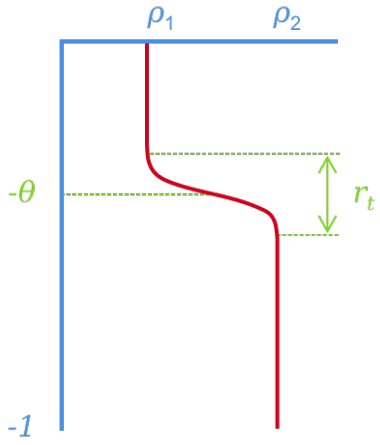

Figure 9.2: Visualization of the definition of the relative location of the pycnocline θ and the relative thickness r_t.

relationships are also obtained in the analytical solutions obtained for the two-layer system and linear stratified system, see equations (6.16)-(6.18) and (6.22)-(6.24).

Subsequently, investigate the effect of the location of the pycnocline. Therefore, the relative location of the pycnocline θ is used, which is defined as the depth of the pycnocline divided by the (total) water depth, see equation (8.1). For a stratification profile, described by a hyperbolic tangent, the location of the pycnocline is given by the location of the inflection point. An example of this definition is given in figure 9.2. Figure 9.3 shows the influence on the KdV constants. These relations are similar to the

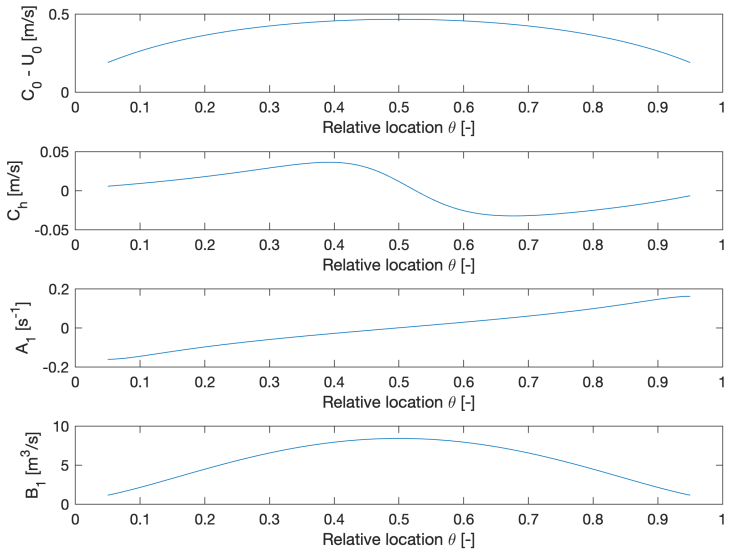

Figure 9.3: Dimensional KdV constants as function of the relative location of the pycnocline.

behavior of the constants of the two-layer model, which means that the long wave speed is proportional to (based on equation (6.16))

$$\sqrt{\theta(1-\theta)}. \tag{9.1}$$

Using equation (6.17) it is found, that the constant A_1 is proportional to

$$\frac{2\theta-1}{\sqrt{\theta(1-\theta)}}. \tag{9.2}$$

Finally, following (6.18), B_1 is proportional to

$$(\theta(1-\theta))^{3/2}. \tag{9.3}$$

Note that, the scaling of the KdV constants is not changed and therefore these relationships hold for the scaled and dimensional constants. From figure 9.3 and the relationships can be found that the problem is symmetric around the midpoint ($\theta = 0.5$). Comparing the first and second panel of figure 9.3, it is found that C_h is small compared to $C_0 - U_0$. Based on the second panel, it can be concluded that the propagation speed due to bathymetry changes is the largest, if the pycnocline is close to mid-depth, but not exactly at mid-depth. The sign of A_1 is different at both sides of the midpoint, which means that when the pycnocline is located in the upper half of the water column waves of depression can be found, but when it is located deeper waves of elevation are present.

Finally, the density structure can also change by varying the thickness of the pycnocline. The relative thickness of the pycnocline r_t is determined for a hyperbolic tangent by the height where 95% of the change in density is taking place divided by the water depth. A sketch of this definition is given in figure 9.2. For multiple thicknesses the KdV constants have been calculated, see figure 9.4. The relationship between these constants and the relative thickness is not as clear as for the relative depth. It can be obtained that C_0, C_h and A_1 decrease in magnitude, when the relative thickness becomes larger, while B_1 remains approximately constant.

The values of the KdV constants are influenced by the combination of θ and r_t, therefore figure 9.5 shows the value of the KdV constants based on these two parameters. It can be seen, that the influence of the relative depth is much larger than the influence of the relative thickness. From figure 9.5b it is found, that when the relative thickness is large, the depth where C_h changes sign is also larger. In these cases the pycnocline is located at a deeper level.

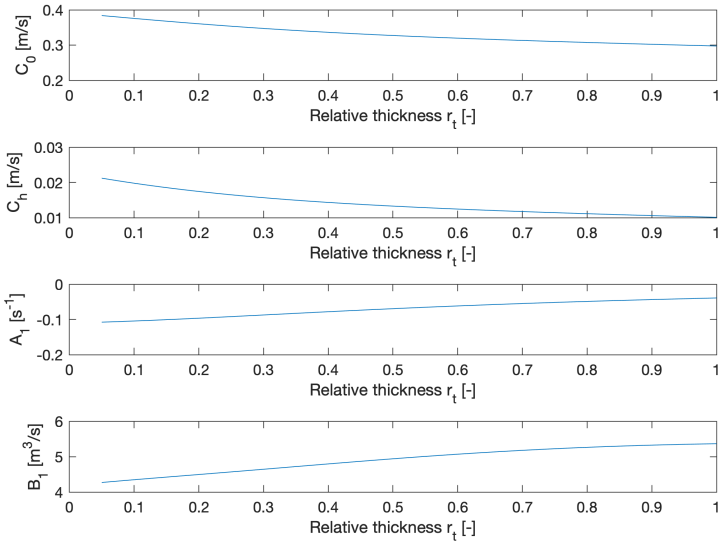

Figure 9.4: Dimensional KdV constants as function of the relative layer thickness of the pycnocline, $\theta = 0.2$ [−].

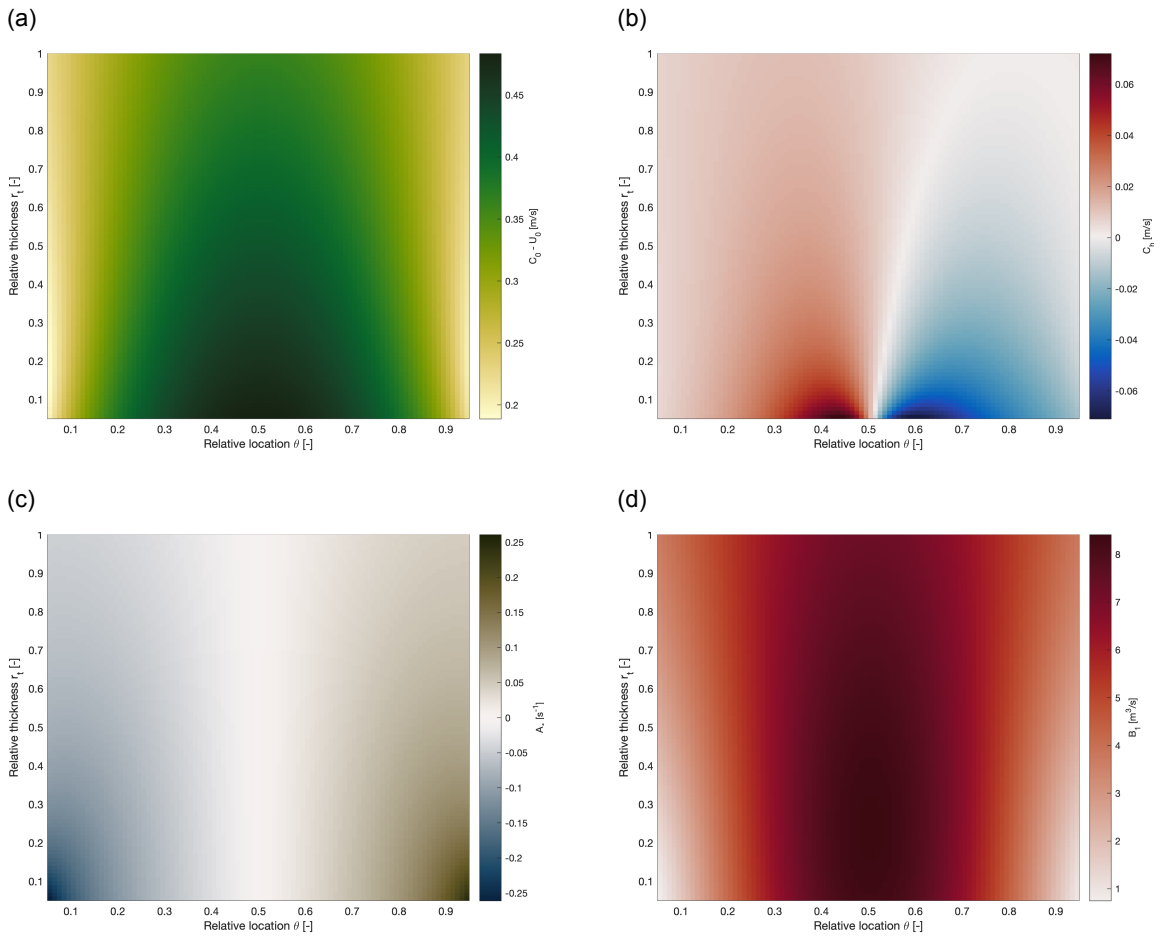

Figure 9.5: KdV constants against relative location and thickness of the pycnocline. (a) $C_0 - U_0$ [m/s]; (b) C_h [m/s]; (c) A_1 [s^{-1}]; (d) B_1 [m^3/s].

9.1.3. Effect of background flow on the KdV constants

The influence of the background shear flow is investigated for two different flow profiles. First, a linear flow-profile with a zero depth-averaged velocity is considered, such that the effect of shear on the constants C_0, A_1 and B_1 can be assessed. This implies, that the flow at the bottom equals the flow at the surface in magnitude. The value of C_h is not discussed, as the situation where the flow velocity is maximum at the bottom is not physical realistic. The second profile is a two-directional flow profile with zero velocity near the bed and a depth-averaged velocity of zero. An example of this flow profile is given in figure 9.7.

Consider the linear flow profile. Here, the flow velocity at the bottom has the same magnitude as the surface velocity, but in opposite direction, such that the depth-averaged flow velocity is zero. This makes sure that the depth-averaged advection does not contribute to the linear internal wave propagation speed C_0. In figure 9.6 the KdV constants are plotted against the maximum flow velocity scaled by the typical internal wave speed, (using equation (5.50)). The constants are more or less piecewise linear, it can be seen that for stronger shear flows the long wave speed increases and that A_1 changes sign. Note that the behavior in the figure is not symmetric around zero velocity, as only the first positive eigenvalue (right going wave) is shown. B_1 is zero at both ends and has a positive value in the area between -0.25 and 1.00. When B_1 is zero, the eigenfunctions have only one narrow peak, which physically means that internal waves can not occur in these cases.

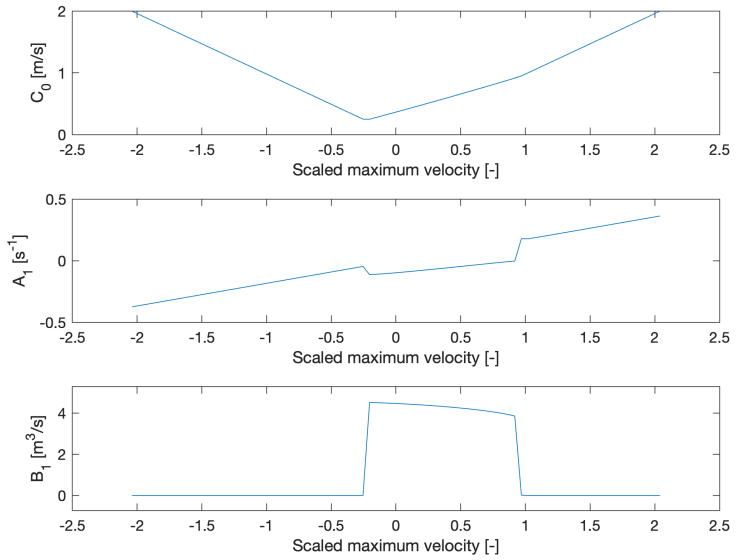

Figure 9.6: Dimensional KdV constants against maximum flow velocity for a linear flow profile.

Finally, a more realistic, reversing or return, flow profile is considered. The velocity at the bed of this profile is zero. Furthermore, the flow changes direction at a relative depth of 20%, which is also the location of the pycnocline. Also, for this profile it is required that the depth averaged velocity is zero. This means that the maximum velocity can be found at the surface. An example flow profile is given in figure 9.7. In figure 9.8 the KdV constants are plotted against the maximum velocity.

Again, a positive relationship is obtained between the maximum velocity and long wave speed. Multiple ranges are found where B_1 is zero, which shows that for scaled maximum velocities over $0.8\ [-]$, internal waves are suppressed by the background flow. The behavior of C_h is similar to B_1 and increases between a maximum velocity between $-0.8\ [-]$ and $0.8\ [-]$.

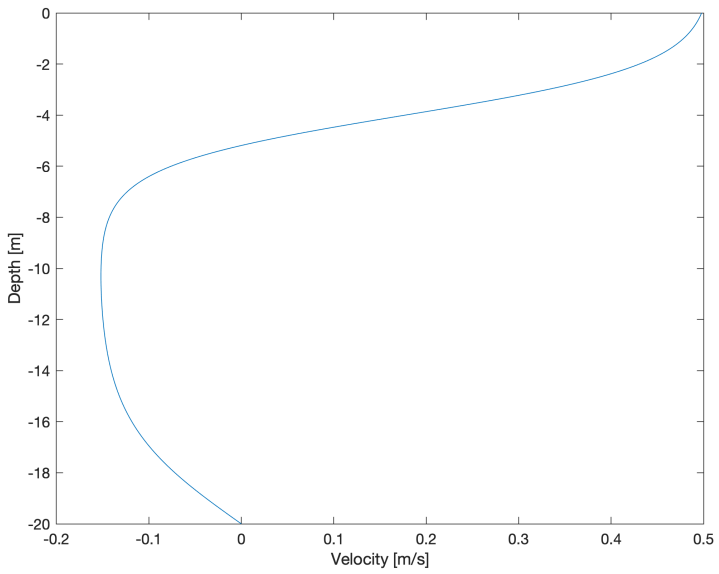

Figure 9.7: Example return flow profile with a maximum velocity of $0.5\ [\mathrm{m/s}]$.

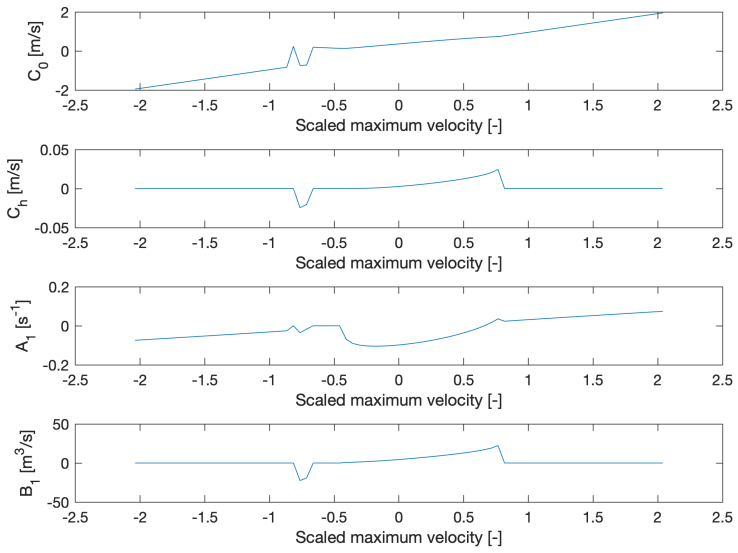

Figure 9.8: Dimensional KdV constants against maximum flow velocity for a return flow profile.

9.2. Sensitivity of the periodic KdV solution to the background state

To investigate the influence of the KdV constants on internal waves the periodic KdV solution, equation (6.45), is used. To calculate the solution, first the shape factor m (elliptic modulus) and traveling wave speed C (6.46), arising from the periodic KdV solution, are determined. In figure 9.9a the shape factor is plotted against the ratio of β_1 and α_1 (note that these are scaled KdV constants). For larger ratios the shape factor is small. This means that in these cases waves look more or less like a sinusoid, remember figure 6.3 indicating a relation between the shape factor and the wave form. For smaller values of this ratio the waves become more asymmetric with smaller crests and wider troughs. From figure 9.9b it could be concluded that the traveling wave speed divided by α_1 is directly proportional to the ratio β_1 and α_1, which means that the traveling wave speed is only sensitive to changes in β_1. This relationships tells, that for a larger value of β_1 the magnitude of c increases as well, which implies that in this case internal waves travel with a lower propagation speed.

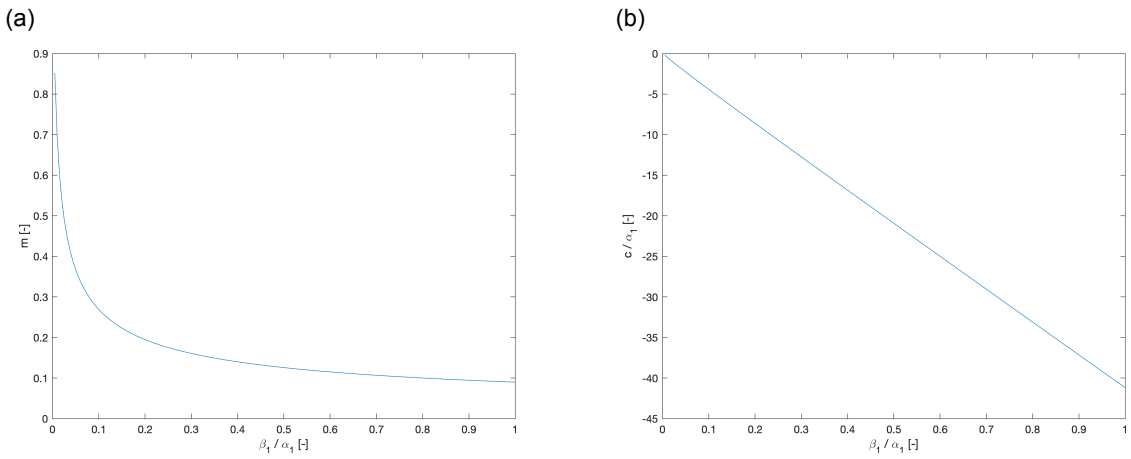

Figure 9.9: Relationships between the KdV constants and the periodic solution constants. (a) Shape factor m plotted against β_1/α_1; (b) Non-dimensional traveling wave speed c/α_1 plotted against β_1/α_1.

9.2.1. Effect of bathymetry and stratification on the periodic KdV solution

When changing the undisturbed water depth h_0, the scaled KdV constants do not change. This implies, that the values of m and the non-dimensional traveling wave velocity c are also not changed. With the extra assumption that ε remains constant, is the ratio between the internal wave amplitude a and the water depth, it could be found that the dimensional traveling wave velocity C is proportional to the square root of h_0 (according to (6.46)). As C_p is defined as the sum of C_0, C_h and C, it can be found that C_p is proportional to the square root of h_0, see table 9.3. The scaled problem is untouched when the value of σ is changed, see section 9.1. This provides that all three propagation speeds C_0, C and C_p are proportional to the square root of σ. Furthermore it is obtained, that the wave period is proportional to $1/\sqrt{h_0}$.

	h_0	σ
C	$h_0^{1/2}$	$\sigma^{1/2}$
C_p	$h_0^{1/2}$	$\sigma^{1/2}$
T	$h_0^{-1/2}$	$\sigma^{-1/2}$

Table 9.3: Relationships between the background state (without shear flow), propagation speed and wave period.

Next, the location of the pycnocline is considered (figure 9.10). The shape factor is symmetric around $\theta = 0.5$. When the pycnocline is located close to this mid-depth, the waves behave like a sinusoid (as m is near zero). In contrast, when the pycnocline is near the surface (or bed) the waves have

sharper crests and wider troughs. As the KdV constants were (point) symmetric around the midpoint, so is also the traveling wave velocity C. The magnitude of the traveling wave velocity C with $\varepsilon = 0.05$ is approximately ten times smaller as the linear wave speed C_0 and has therefore added a small correction to the total propagation speed C_p. As C_h is also in the order of ε this adds another small correction to the total propagation speed. It is seen that the speed is largest when the pycnocline is closely located to the midpoint of the water column. This is the point where the period is smaller, as faster propagating waves have a shorter period.

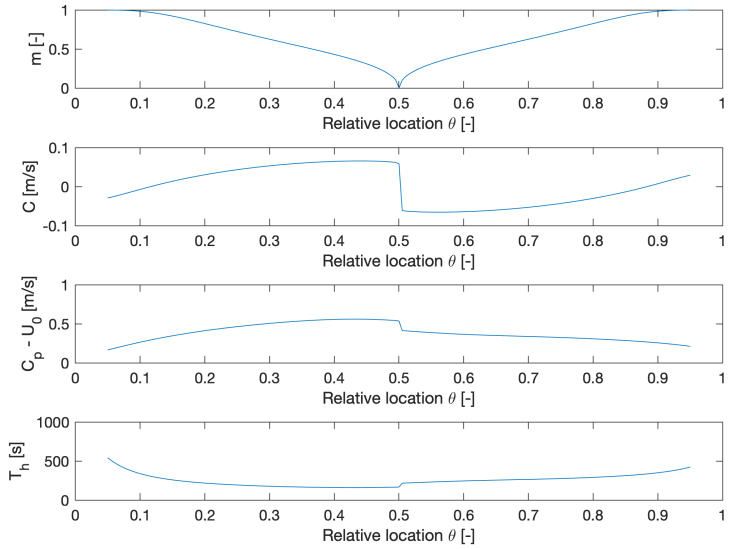

Figure 9.10: Shape factor m, traveling wave velocity C, propagation speed C_p and wave period T as function of the relative location of the pycnocline, with $\varepsilon = 0.05$ $[-]$.

The shape factor m is also plotted against the relative thickness, figure 9.11. From this it can be concluded that a sharper pycnocline (small relative thickness) induces steeper waves with small crests. C shows a similar behavior to B_1, which is logical as these two variables are directly proportional to each other. Also, in this case C is a small correction on C_0. It can be observed that for sharper pycnoclines (small relative thicknesses) the propagation speed is largest. The propagation speed and wave period are influenced by the combination of the depth and thickness of the pycnocline, the combined effect is shown in figure 9.12. It can be seen that the relative location is much more important than the relative thickness, which was already the case for the KdV constants, (section 9.1.1).

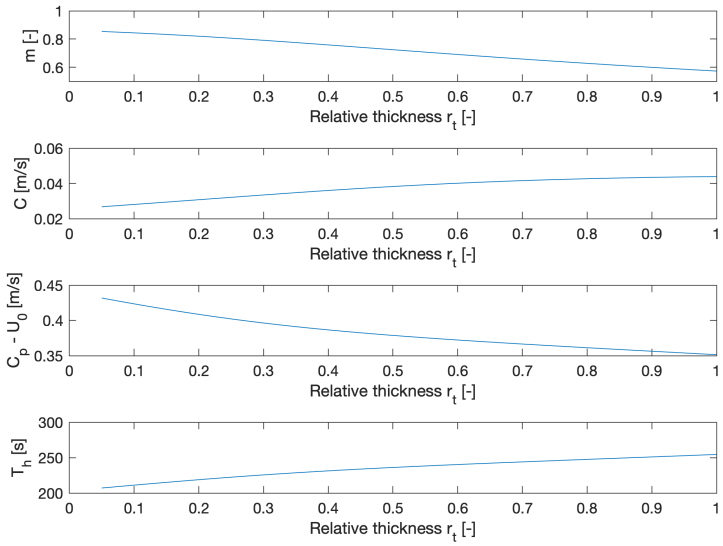

Figure 9.11: Shape factor m, traveling wave velocity C, propagation speed C_p and wave period T as function of the relative layer thickness of the pycnocline, with $\varepsilon = 0.05$ $[-]$ and $\theta = 0.2$ $[-]$.

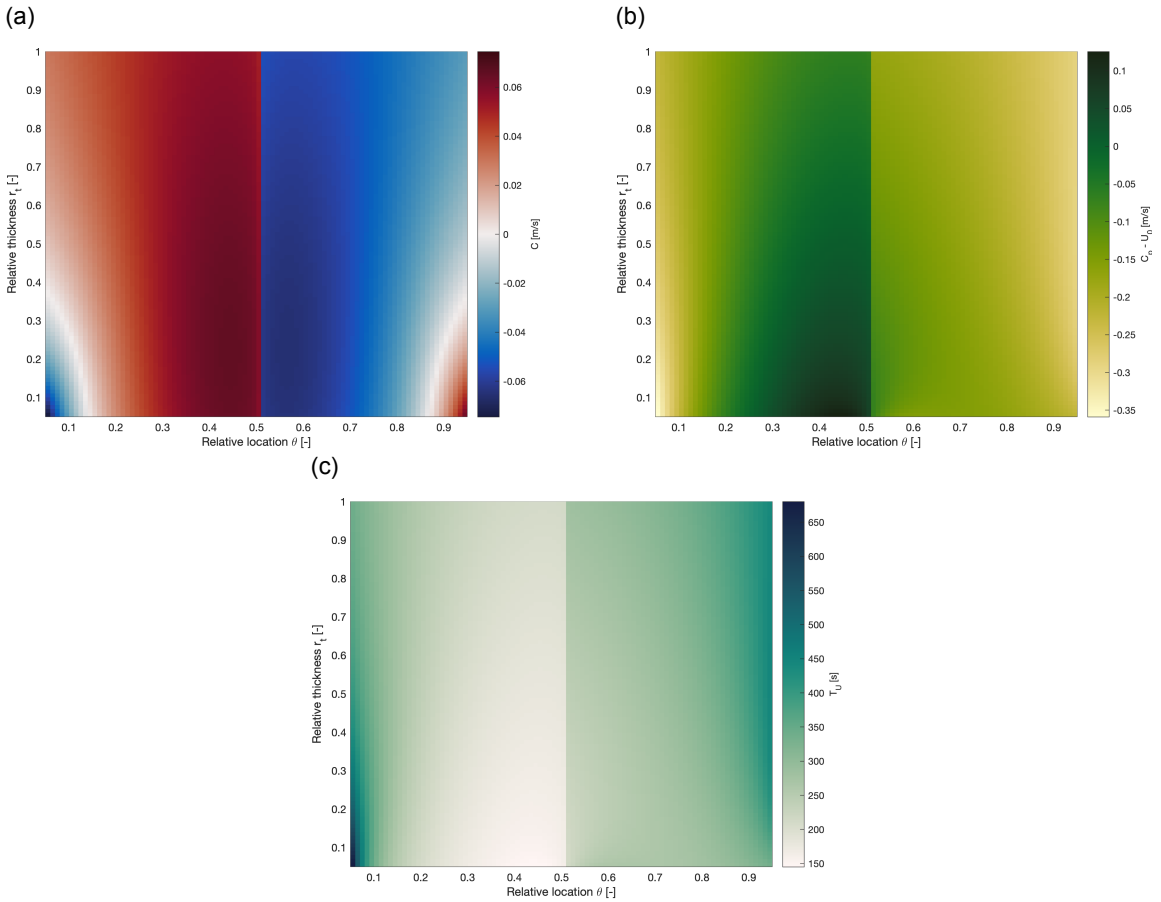

Figure 9.12: Wave properties against relative location and thickness of the pycnocline, with $\varepsilon = 0.05$ $[-]$. (a) C $[\mathrm{m/s}]$; (b) C_p $[\mathrm{m/s}]$; (c) T $[\mathrm{s}]$.

9.2.2. Effect of background flow on the periodic KdV solution

The wave properties under a linear flow profile are given in figure 9.13. As B_1 is zero for a large part of the domain (figure 9.6), the properties have only been determined after a certain threshold. This is because for very small values of B_1 internal waves can not exist. For stronger shear flows (with a larger scaled maximum velocity) m is small, which means that in these cases waves behave more or less like a sinusoid. It can be seen that C is relatively small and that the correction does not change the behavior of C_0 in the value of C_p. C_p shows a linear trend with the maximum velocity.

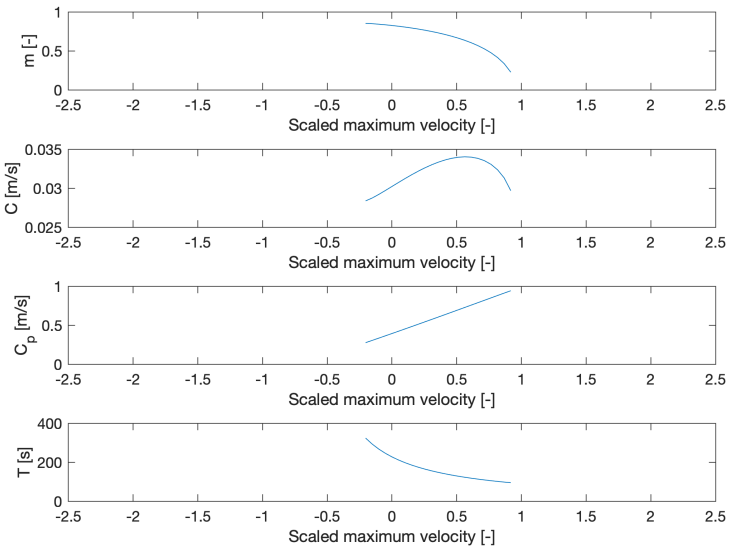

Figure 9.13: Shape factor m, traveling wave velocity C, propagation speed C_p and wave period T against maximum flow velocity for a linear flow profile, with $\varepsilon = 0.05$ $[-]$.

Finally, a return flow profile is considered, see figure 9.7 for an example profile. Figure 9.14 shows that all wave parameters have a sudden change when the scaled maximum velocity equals 0.7. This is also the point where B_1 jumps to zero (figure 9.8). The shape factor is also near zero at this point, while for other scaled maximum velocities the waves is steeper. The traveling wave velocity is now larger compared to the case with a linear flow profile. Near the end of the domain where B_1 is large enough, A_1 switches sign. This also means that the traveling wave velocity switches sign and has therefore a strong gradient. This results into the behavior that C_p first increases for larger maximum velocities and finally stays at a constant level.

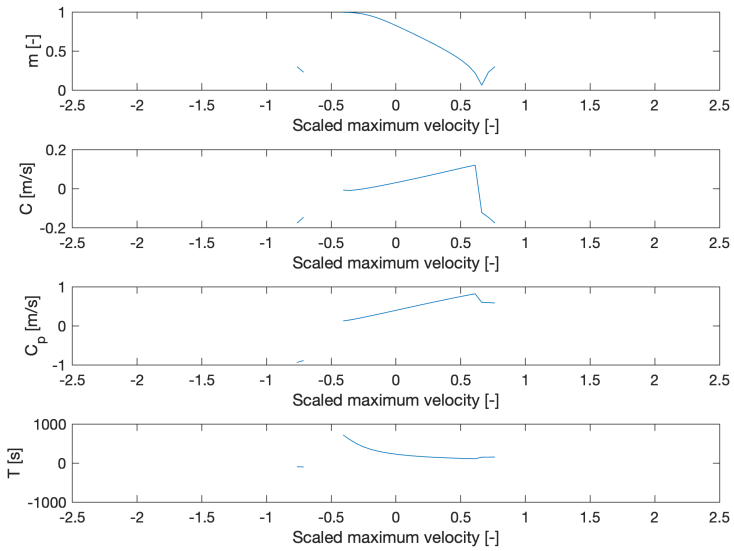

Figure 9.14: Shape factor m, traveling wave velocity C, propagation speed C_p and wave period T against maximum flow velocity for a return flow profile, with $\varepsilon = 0.05$ $[-]$.

10

Applicability of the KdV model in the Rhine ROFI

After the derivation of the variable bed KdV model and studying the sensitivity of the model, the applicability of the model needs to be checked. First, the results from the Taylor-Goldstein equation in combination with the TGE fitting procedure are checked using the measurements by Rijnsburger et al. (2019b) (figure 3.1 - V), (section 10.1). From this analysis new estimates for the propagation speed follow, which are used to estimate the typical wave properties. These wave properties are used to check the scaling used to derive the variable bed KdV model, (section 10.2). This is done by discussing the bulk order of the important variables. Finally, the results are used to check the applicability of the KdV equation (figure 3.1 - IV), (section 10.3). As the measurements are performed at two points, not capturing the same waves, the bathymetric variation of the variable bed KdV equation can not be checked. This means that this validation is limited to the case where the effect of bathymetric variation is neglected.

10.1. Validity of the Taylor-Goldstein equation

The validity of the Taylor-Goldstein equation (TGE) is checked in two steps, first the performance of the TGE fitting procedure is discussed. This to obtain a good estimate of the pycnocline and direction of wave propagation. Next, this information is used, to check the validity of the TGE in the Rhine ROFI.

10.1.1. Performance of the TGE fitting procedure

Using the TGE solution from chapter 6 and the fitting procedure from chapter 7 a good fit for the TGE can be found. These results are tested against the measurements by Rijnsburger et al. (2019b). From this measurement data, it is first necessary to calculate the normalized velocity amplitude. This as following equation (6.53) this should (theoretically) be equal to the velocity amplitude Φ. This is obtained by first extracting the amplitude from the vertical velocity for each layer of $25\ [\mathrm{cm}]$. Next, the amplitudes are normalized such that the maximum over the vertical equals one.

The optimization is performed for all wave events stated in table 2.1. The mean squared error (MSE) after each optimization step is given in table 10.1. Next, the performance of each step is discussed separately.

From the first optimization step, where the pycnocline depth is fitted, it can be obtained that this helps to reduce the errors in most cases. In the cases where the error was not reduced significantly, the first estimate (without optimization) already fitted the peak of the vertical velocity, see figure 10.2a. In figure 10.2b the fit is presented after this optimization step. In the cases where there is a clear peak visible in the measurements, this is also recognized by the fit.

After optimization	17-09 21:09	17-09 21:16	17-09 21:29	19-09 11:33	04-10 09:27	04-10 09:58	04-10 10:12	04-10 10:24
None								
Pycnocline depth								
Pycnocline thickness								
Wave direction								

Table 10.1: Mean squared error of the solution from the Taylor-Goldstein equation after each optimization step.

The second optimization step, for the pycnocline thickness, is performed. This shows that the MSE has again been reduced. Note, that this effect is smaller compared to the first step, which is logical as in the sensitivity analysis (chapter 9) was concluded that the location of the pycnocline has a larger influence compared to thickness. Figure 10.2c shows the fits after this step. Here can be seen, that these new fits follow the sharpness of the peak more closely.

Finally, the minimum MSE is searched by varying the wave direction. The optimized (minimum) MSE is given in the last row of table 10.1. The MSE has in most cases not much improved compared to the previous step, this has to do with the relatively good guess of the wave direction.

In figure 10.1 the MSE is plotted against the wave direction for the considered wave events. From this can be seen that in most cases a clear minimum value can be found, but for the cases of September 17th, 21:09 and October 4th, 10:12 the minimum is too wide, which means that the wave direction has a small influence on Φ. This means that for these events no clear direction can be obtained. The final fit of the Taylor-Goldstein solution is given in figure 10.2d, in which can be seen that the form of the solution is now following the measurements more closely compared to the previous optimization step.

Figure unavailable until publication of Rijnsburger, et al. (2019b)

Figure 10.1: Mean squared error of the Taylor-Goldstein equation over the direction of wave propagation for multiple wave events. Direction relative to the direction of the upper layer velocity.

It is shown that TGE fitting procedure works to obtain a better fit for the TGE on the measurement data. In each step the error is reduced and a better estimate is obtained. Based on the sensitivity analysis (chapter 9) it is logical to start to find the the pycnocline depth as this property has the largest influence. The pycnocline thickness and direction of wave propagation have a smaller effect and follow logically after. The direction of wave propagation can be clearly obtained in a number of cases, but in some cases the effect of the direction and different background flow is so small that no best direction can be found.

	17-09 21:09	17-09 21:16	17-09 21:29	19-09 11:33	04-10 09:27	04-10 09:58	04-10 10:12	04-10 10:24
C_0 m/s								

Table 10.2: Values for the linear propagation speed, resulting from the TGE solution and the TGE fitting procedure.

	17-09 21:09	17-09 21:16	17-09 21:29	19-09 11:33	04-10 09:27	04-10 09:58	04-10 10:12	04-10 10:24
ε								
δ^2								
σ								

Table 10.3: Parameter values for multiple wave events, based on data from table 2.1 and 10.2.

From this TGE fitting procedure values for the linear propagation speed are obtained. These are stated in table 10.2 and are used in section 10.2 to validate the scaling.

10.1.2. Match of the Taylor-Goldstein equation

The final results of the TGE fitting procedure are shown in figure 10.2d. These results show a good match between the measurements and the predicted vertical velocity by the TGE. The peak, located around the pycnocline, is captured in all fits. Also, the data points around this peak are good predicted by the TGE. Most notable offset is that for all events the measured data of the vertical velocity near the bottom is becoming smaller but is not going to zero. This while the theory predicts that it should go to zero. This may have to do that the measurements errors are more relevant here. Another possibility is that the boundary layer effects are not captured by the KdV model. As the predicted vertical velocity amplitude Φ is close to the measurements and that the MSE is small, the conclusion is drawn that the TGE is indeed capable of describing this vertical velocity amplitude.

10.2. Validity of the KdV scaling in the Rhine ROFI

The scaling used in the derivation of the variable KdV model is verified in three steps. The first step is to estimate the small parameters and check the scaling relative to each other. Next, the bulk parameter scaling is checked by comparing the used scaling factor and the observed quantity. Finally, the assumed slope is compared to the slope observed in the bathymetry of the Rhine ROFI.

Validity of the small parameters

Based on the observations of internal waves as described in section 2.3 and the propagation speed from table 10.2, three small parameters, ε, δ^2 and σ, are calculated. From these values given in table 10.3, is obtained these parameters are indeed small ($\mathcal{O}\left(10^{-1}\right)$ or smaller). In the case of October, 4th 09:58 the relative depth is very small ($\delta^2 < 0.1$), which means that the advection terms of the vertical momentum equation are less important, compared to the other wave events. While deriving the KdV equation $\varepsilon = \mathcal{O}\left(\delta^2\right)$ is assumed (see section 5.2.1). In the cases of September, 17th; September, 19th and October, 4th 10:12 this condition is clearly satisfied. For the last event on October, 4th (10:24) the balance is not perfect but can still be seen as valid. For the event October, 4th at 09:27 and 09:58 this assumption breaks down, as the wave length is too long. This means that for these events the KdV model is not applicable.

Validity of the bulk parameter scaling

In table 10.4 the scaling of the parameters is checked. For each quantity the measured values are given in the first row and next the active scaling factor for the quantity is calculated. Since the scaled variable is assumed to be order one, the measured value and scaling factor should be of the same order. The direction of the waves is not exactly known. Therefore, it is not directly clear whether the

		17-09 21:09	17-09 21:16	17-09 21:29	19-09 11:33	04-10 09:27	04-10 09:58	04-10 10:12	04-10 10:24
U_a	m/s								
U_c	m/s								
$\sqrt{\sigma g h_0}$	m/s								
T	s								
$\frac{\lambda}{\sqrt{\sigma g h_0}}$	s								
u'	m/s								
$\sqrt{\sigma g h_0}\frac{a}{h_0}$	m/s								
w'	m/s								
$\sqrt{\sigma g h_0}\frac{a}{h_0}\frac{h_0}{\lambda}$	m/s								

Table 10.4: Comparison between scaling and measured values for multiple wave events, based on data from table 2.1.

alongshore (U_a) or cross-shore (U_c) velocity should be used for validation of the scaling. Hence, both velocities are given in the table for comparison. The alongshore velocities are matching (in order of ε) the typical wave velocities. This is in contrast to the cross-shore velocities which are an order of magnitude smaller compared to the typical propagation speed. This means that for a wave directed perpendicular to the coast the effect of the shear flow is smaller. As mentioned earlier (section 5.2) the characteristic scale for the shear flow is a maximum and the scaling does not brake down when the values are smaller.

The observed period of the internal waves matches the typical period in the same order of ε. The match for the waves observed on October, 4th is relatively good, but still the match for the other events is good enough. Considering the observed value for u' and the typical horizontal perturbation velocity, it can be seen that in all cases these values are of the same order. Therefore, the scaling of u' seems to work under all events. For the vertical perturbation velocity w' the typical and measured values are also close to each other, so here the assumed scaling also seems to be valid. Beside these four properties, there are more properties scaled in section 5.2 (wave induced displacement, depth and density). These scalings are directly based on the measured property itself and are therefore always the correct scaling.

Validity of the bathymetric variation

In the derivation of the variable KdV model an order of ε was assumed for the small parameters related to the bathymetry changes, (section 5.4). To test if these scalings are correct the slope has to be calculated. Using definitions (5.61), (5.62) and (5.63). The slope is estimated by

$$\frac{h_1}{l} = \delta\mu\gamma = \mathcal{O}\left(\varepsilon^{7/2}\right). \tag{10.1}$$

As ε varies between 0.03 and 0.11 the expected slope varies between $0.005 - 0.44$ meter per kilometer. In section 2.3 was stated that the average slope in the Rhine ROFI is 1.5 [m] per kilometer. This means that for the larger amplitude waves (large value of ε) the scaling of the slope is in the correct order of ε. For smaller waves, $\varepsilon = 0.03$ or $\varepsilon = 0.04$, the variable bed KdV equation may not be applied as the bathymetry is too steep (or the wave amplitude is too small).

10.3. Validity of the KdV equation

The optimum fit of the TGE is used to reconstruct the solution to the KdV equation. Therefore one new parameter should be chosen, which is the wave amplitude. The wave amplitudes influences the vertical velocities in two ways: for larger wave amplitudes the velocity amplitude is also larger. This as the particles have to travel further. A larger wave amplitude results also in a larger contribution to the traveling wave propagation speed C, which influences the wave period. This also means that there are two measures for scoring the KdV equation fit, the difference from both the velocity amplitude and wave

period can be investigated. The first option is to fit the wave amplitude using the velocity amplitude as a measure. As this match results in agreement of the velocity amplitude, the period is used as final score to check if this fit makes sense or not.

In table 10.5 the expected and calculated period (using the velocity amplitude fit) are given for multiple wave events. The events of September, 17th 21:16, 21:29; 19th 11:33 and October, 4th 10:12 show a good agreement (difference of less than 25%). The wave event of October, 4th 10:24 shows a less strong agreement. For the other three events (September, 17th 21:09 and October, 4th 09:27 and 09:58) the periods do not match all. In section 10.2 was concluded that for some events the KdV balance does not hold. It is now obtained that for these events the period does also not match, which was expected. The events wherefore the KdV model turns out to be valid, show also a good agreement for the period, except the first event of September, 17th (21:09). Here the KdV balance is valid, but the periods differ a factor two.

Next, the period is matched and in this case the velocity amplitude is used as scoring mechanism. The results are stated in the two last rows of table 10.5. The fits for September, 17th 21:15, 21:29; 19th at 11:33 and October, 4th 10:12 show again good agreement. Which is logical as when the solution is close in one situation, it is also close in the other situation.

		17-09 21:09	17-09 21:16	17-09 21:29	19-09 11:33	04-10 09:27	04-10 09:58	04-10 10:12	04-10 10:24
Expected period	s								
Calculated period	s								
Expected velocity amp.	$\mathrm{m/s}$								
Calculated velocity amp.	$\mathrm{m/s}$								

Table 10.5: Expected and fitted value for the wave period and velocity amplitude.

To discuss the results in more detail one event is chosen. This is the event of September, 17th 21:16. In figure 10.3 the vertical velocity over time is plotted for multiple depths. The waves are approximately following the data points. The timing of the first peak is not as good as the others, this as the first wave in the measurements has a shorter period compared to the others. Also, the amplitude for the first wave is not well matched, while the KdV model predicted the correct amplitude for the peak around 21:19. This variability can not be captured in the periodic KdV solution, as in this solution the period and amplitude for all waves are equal. In field data this is not the case. Using this solution for the KdV equation the complete vertical and horizontal velocity can be constructed. The result is given in figure 10.4, where the measured data is given in the plots on the left, while the model outcomes are visualized on the right. The agreement of the vertical velocity is quite good. Also, the reconstructed horizontal velocity looks like the measured velocities, which has mainly to do with the exact matching of the background flow field. In the horizontal velocity field from the model it can be clearly found that the waves are giving an opposite directed contribution above and underneath the pycnocline. For example at 21:17 can be seen that the horizontal velocity underneath the pycnocline is larger than averaged, while above the pycnocline it is less than averaged.

It can be concluded that the KdV model matches the measurements reasonably well. In a number of cases the velocity amplitude and period are very close to the observed data. This means that in cases that the KdV balance $\varepsilon = \mathcal{O}\left(\delta^2\right)$ holds, the KdV model can be used to get a first estimate of internal waves in the environment of the Rhine ROFI.

(a)

(b)

(c)

(d)

Figure 10.2: Fit of the Taylor-Goldstein equations after multiple optimization steps. (a) No optimization; (b) Fit after optimization of the pycnocline depth; (c) Fit after optimization of the pycnocline thickness; (d) Fit after optimization of the wave direction.

Figure 10.3: Vertical velocity from the measurements and the KdV model at multiple depths after amplitude optimization. Event of September, 17th 21:16. Legend states the depth in meters.

Figure 10.4: Reconstruction of the internal wave measured on September, 17th 21:16. On the left the measured horizontal and vertical velocities; on the right the model outcomes.

11

Environmental variation of internal waves

In the Delft3D model validation (chapter 8) the effects on the density stratification have been studied under different tidal and wind conditions. Here, these results are summarized and combined with the KdV model. This to see, how the propagation of internal waves differs under tidal and wind variation. First, the tidal influence is assessed, (section 11.1). Thereafter, the effect of different wind conditions is investigated, (section 11.2).

11.1. Effect of tidal variation on internal waves

The combination is made between the Delft3D and KdV models. This is done by first restating the behavior of the Rhine ROFI for different tidal stages, which is based on the findings in chapter 8. Next, the QEP numerical solution of the TGE from chapter 6 is used to calculate the KdV constants using the Delft3D density stratification and background flow data. In this analysis each point in space is treated separately and therefore the bathymetric variations are zero. This means that the effect of C_h can be neglected. Next, the results of the KdV constants are discussed. Using these constants the total propagation speed C_p and wave period T resulting from the periodic KdV solution are determined. Finally, these results are combined to obtain the Froude numbers. This to determine if the flow is sub- or supercritical for internal waves.

Effect of tidal variation on stratification and flow

During each tidal cycle, induced by the semi-diurnal M_2 tide, a new tidal plume front with fresh water is formed and released. When it becomes LW (ebb tide), this water is released from the Rotterdam Waterway and is moved offshore. During the flooding process up to HW+2 this water bulge is moved alongshore in northeastern direction. This means that the fresh water is passing the observation points M12 and M18 around HW+2 and that at this moment the density differences are largest at these two points. When moving in downstream direction of the Rhine ROFI, from the near- to mid-field and even further to the far-field, the water column gets more mixed and the vertical density stratification fade away.

Next to the semi-diurnal tidal variation, the tidal range is large during spring tide compared to neap tides. The typical state for the Rhine ROFI during HW+2 is visualized in figure 11.1a for spring tide and in figure 11.1b for neap tide. It is seen that the tidal plume fronts reach much further offshore during neap tide. This is because the tidal range is small and that there is less energy available to mix the water column. As the tide induced flow velocities are much larger during spring tides, the effect of Coriolis is also much stronger. This means that the plume is more rotational advected, which results in a plume close to the coast, (figure 11.1a). As the mixing is less strong during neap tides, the pycnocline

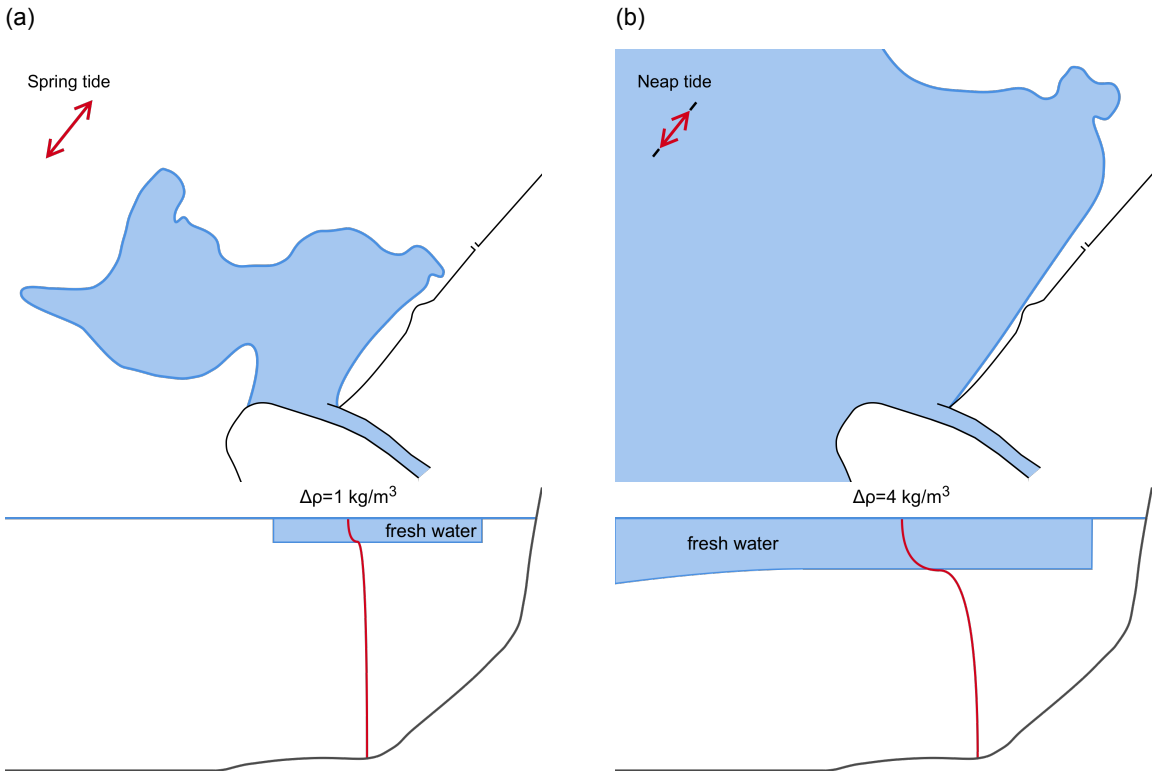

Figure 11.1: Visualization of the size and location of the river plume during different spring-neap phases. Top panel: location and size of the river plume; Bottom panel: typical thickness, size and density stratification of the river plume. (a) Spring tide; (b) Neap tide.

			Spring tide	Neap tide
Density difference	$\Delta\rho$	$[\mathrm{kg/m^3}]$	1.0	4.0
Relative depth of the pycnocline	θ	$[-]$	0.10	0.25
Linear propagation speed without shear-flow	C_0'	$[\mathrm{m/s}]$	0.1	0.2
Linear propagation speed with shear-flow	C_0	$[\mathrm{m/s}]$	0.9	0.7
Total propagation speed	C_p	$[\mathrm{m/s}]$	0.9	0.7
Froude number	Fr	$[-]$	1.5	0.9

Table 11.1: Typical stratification parameters, propagation speeds and Froude numbers for spring- and neap tides at HW+2.

is located deeper and larger density differences are found under this condition. The typical values of the density difference $\Delta\rho$ and the pycnocline depth θ for spring and neap tides are given in table 11.1.

Effect of tidal variation on KdV constants

In figure 11.2 the statistics for M18 of the KdV constants without any background flow are given. The statistics are again reported along the four phases of the M_2 tide. The median and range of C_0' are approximately equal along the different tidal phases. This in comparison to the input parameters, the relative layer depth and density difference, which differ along these stages, see figure 8.2. As discussed in the sensitivity analysis (chapter 9) a smaller relative layer depth and smaller density difference result both in a smaller value for the linear wave speed C_0'. At HW+2 a small relative layer depth and large density difference are found. This compared to the other phases of the tide. This resulted in approximately the same value for the linear propagation speed C_0'. A_1' has the largest magnitude during HW+2, which is logical as a small relative layer depth induces a large value for A_1' (based on table 9.2). The value of B_1' is in the same order for all phases but during HW+2 the variation is small.

Next, these results can be compared to the KdV constants where shear-flow is included, (figure 11.3).

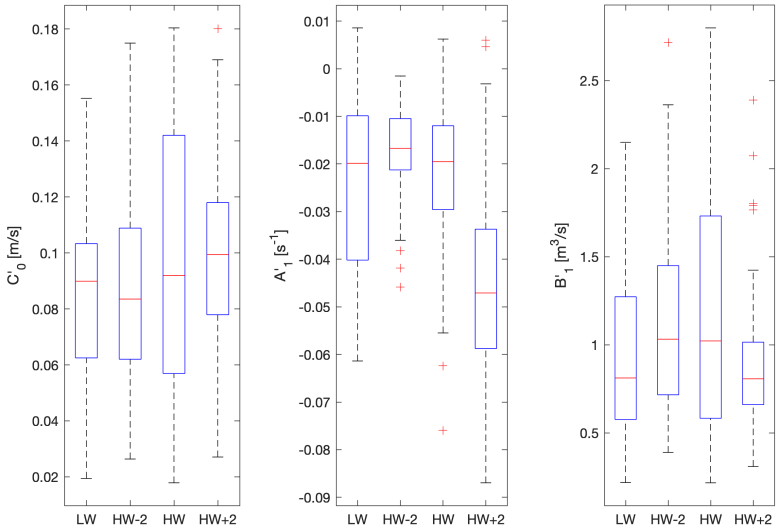

Figure 11.2: Statistics of the KdV constants without shear-flow for multiple M_2 tidal stages at M18 (July, 10th - August, 8th).

The value of C_0 is now a factor 10 larger and there is a large difference between the tidal phases. This as the background flow is advecting the waves and that the depth-averaged flow velocity is an additive term in the linear propagation speed C_0. The propagation speed is largest around HW and LW, while it is small during the HW+2 and HW-2 phases. This is due to the effect that the background flow is largest during these phases of the tide, (de Boer et al., 2006). Most values for A_1 and B_1 (figure 11.3) are more or less in the same range as earlier, but the outliers are now significantly larger.

In figure 11.4 the averaged value of the propagation speed without shear flow C_0' is plotted during spring and neap tide. It can be seen that the propagation speed has the largest values of approximately $0.2\ [\mathrm{m/s}]$ during neap, as stated in table 11.1. As it is concluded that the density differences and pycnocline depth are larger during neap. Both effects lead towards a larger value for C_0' based on the sensitivity analysis, (chapter 9). Furthermore, the area, with a propagation speed larger than $0.1\ [\mathrm{m/s}]$, is much larger during neap. As the tidal plume front is much larger during neap compared to spring, figure 11.1b compared to figure 11.1a. In figure 11.5 the effect of shear flow is included. As the tidal range is larger during spring tide, the tidal induced flow velocity is also larger. This results in a larger linear propagation speed during spring tide compared to neap tide by advection, which is most clearly visible when comparing the two figures for HW. When comparing the values with and without shear-flow, C_0 and C_0', in table 11.1, it is found that this conclusion is different compared to C_0' without shear-flow. This means, that the background flow has a larger contribution in the value of the linear propagation speed C_0 than the density stratification.

Also, the other two KdV constants A_1 and B_1 are considered. The relevant figures therefore are given in the appendix. The stratification during neap tide shows large density differences and a deeper located pycnocline compared to spring tide. In the sensitivity analysis it is seen, that these two effects have an opposite contribution: a larger density difference induces a larger value for A_1 and a deeper located pycnocline induces a smaller value (provided that the pycnocline is in the upper half of the water column). From this it is expected that values for A_1' are similar for spring and neap tide. Figure E.4 shows that this is indeed the case. The advection does not contributes to the value of A_1 with shear flow. Only the shear (velocity difference) over the vertical contributes to this value. If shear flow is included in the calculations (figure E.5), the data shows that the maximum (of the mean) value in the area is approximately three times larger. While the largest part of the area of interest is approximately zero.

Based on the stratification only (figure E.6), the value of B_1' can be studied under spring and neap tide conditions. It is found that for neap tides large values appear in a much wider area. The tidal plume

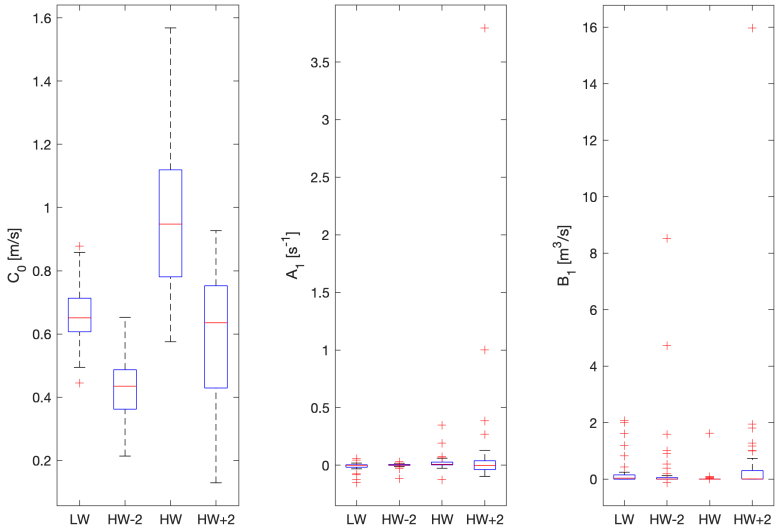

Figure 11.3: Statistics of the KdV constants with shear-flow in the flow direction of the upper layer for multiple M_2 tidal stages at M18 (July, 10th - August, 8th).

fronts are much larger in this case and the combination of a larger density difference and a deeper located pycnocline induces a larger value for B_1'. When for the KdV constant B_1 the effect of shear flow is included, the value is small, $\mathrm{B}_1 < 0.5\ [\mathrm{m}^3/\mathrm{s}]$, in the largest part of the domain. At LW during neap tide B_1 is significantly larger compared to the spring tide counterpart. When the comparison is made for other tidal stages less difference can be obtained, but B_1 is largest during neap tides.

Effect of tidal variation on wave properties

Using the periodic KdV solution the total propagation speed C_p and wave period T can be obtained. As C_p consists of the linear propagation speed C_0 and a small correction from the traveling wave velocity C the behavior of C_p is similar to C_0, see equation (6.48). In this calculation $\varepsilon = 0.05$ is used for the relative wave height, which is approximately the value obtained for the observed waves in table 10.3.

From figure E.8 can be obtained, that the influence of the traveling wave velocity C is in the order of ε (as expected). Due to the large value of B_1 during neap tides the de largest value of C is also found during neap tides. This based on the relationship as obtained from figure 9.9b. These values of the traveling wave velocity are used to calculate the total propagation speed C_p. The behavior of this total propagation speed (figure E.9) is basically the same as the linear propagation speed C_0. The largest speeds are obtained during spring tide, which is caused by the influence of advection.

In figure 11.6 the wave period T corresponding to the total propagation speed C_p is given. As the the wave period is inversely related to the propagation speed, the areas with fast propagating waves have waves with a short period. It is visible that moving towards the far-field (the North) the period becomes longer, as the total propagation speed is smaller. This is due to the less strong density stratification. Therefore, it is logical to conclude that periods are shortest during the HW and HW+2 phase of the M_2 tide. When spring and neap tides are compared, it is concluded that waves with the shortest periods can be found during spring tide. Again, this is caused by the relative large advection during spring tide.

Effect of tidal variation on Froude number

The velocity of the upper layer relative to the internal wave phase velocity determines if internal waves can propagate ahead of a tidal plume front. Therefore, the Froude number has been calculated, (figure 11.7). The largest Froude numbers are obtained during HW and LW, as the tidal induced velocities are

largest at these moments. Around HW-2 and HW+2 the lowest Froude numbers are found. These moments are close to tidal slack, which is defined as the moments where the depth-averaged alongshore velocities are zero, (de Boer et al., 2009). During HW the flow is supercritical ($Fr > 1$) and therefore the frontal head is allowed to grow. Around HW+2 the tidal plume front moves onshore, and subcritical flow ($Fr < 1$) is obtained inside the river plume, which means that wave fission may occur. Note, that the definition of the Froude number Fr, equation (3.5), is different to the definition F_a used by Nash and Moum (2005). As the propagation speed of the tidal plume front U_f is smaller compared to the upper layer velocity U_1, it can be concluded that $F_a < Fr < 1$ and that the Froude number used by Nash and Moum (2005) is subcritical for the Rhine ROFI at HW+2. As the magnitude of U_f is close to U_1, it holds that $2U_f > U_1$ and as Froude numbers larger than two are obtained at HW (figure 11.7), it is concluded that: $F_a > \frac{1}{2}Fr > 1$ and that the Froude number by Nash and Moum (2005) is also supercritical for the Rhine ROFI at HW. This combination of super- and subcritical flow shows that waves in the Rhine ROFI can be generated by a tidal plume front.

Comparing spring to neap in figure 11.7 it is shown, that the Froude number is smaller during neap. This is also stated in the bottom row of table 11.1. This is induced by a lower tidal range, inducing less strong tidal velocities (smaller U_1) and stronger stratification, leading to larger $C_p - U_m$. The area with $Fr < 1$ during HW+2 is much wider during neap. This implies that internal wave generation may occur more often during neap. This matches the observations of Rijnsburger et al. (2019b) of more wave events during neap than during spring.

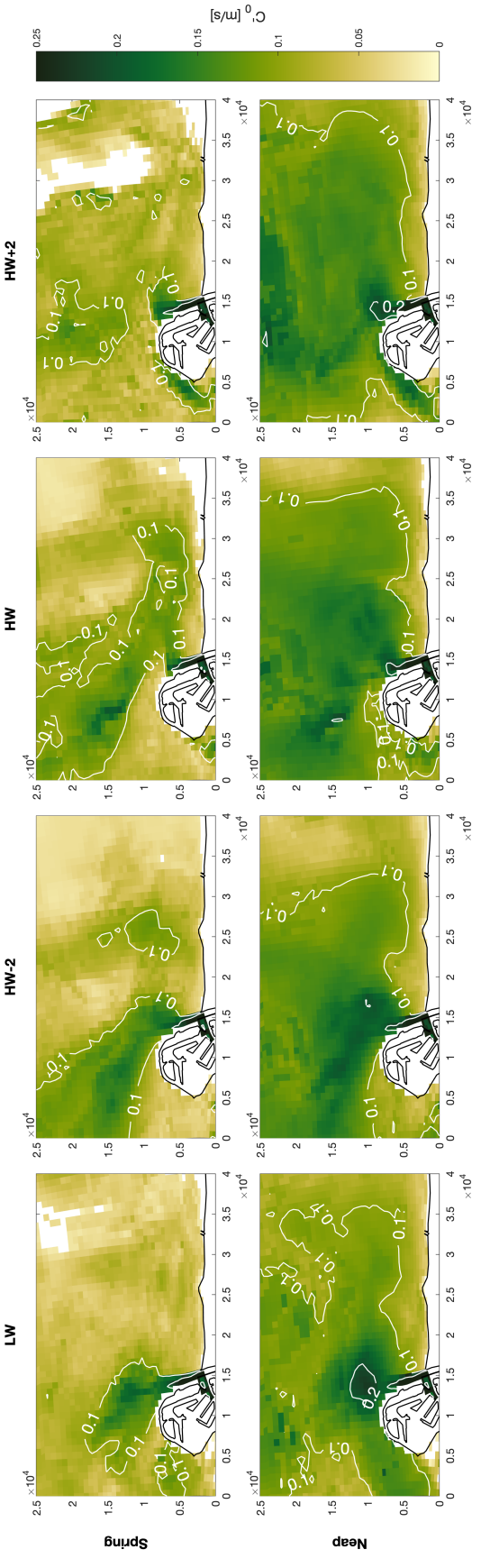

Figure 11.4: Mean value of C_0' without shear-flow for multiple M_2 tidal stages during spring and neap tide.

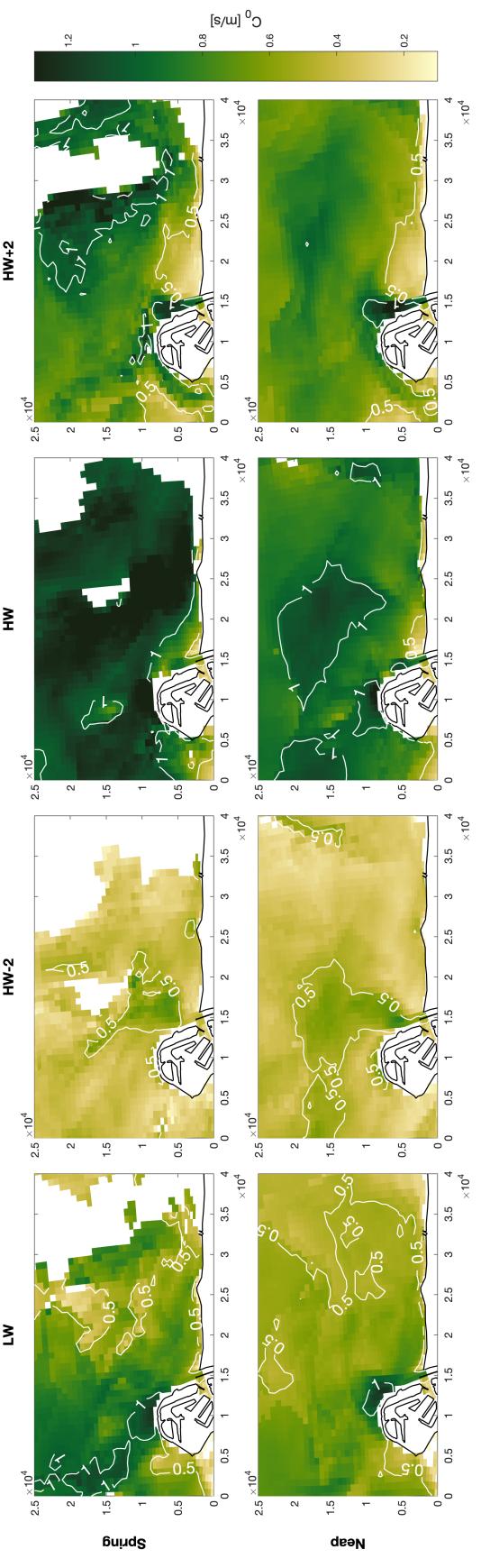

Figure 11.5: Mean value of C_0 with shear-flow in the flow direction of the upper layer for multiple M_2 tidal stages during spring and neap tide.

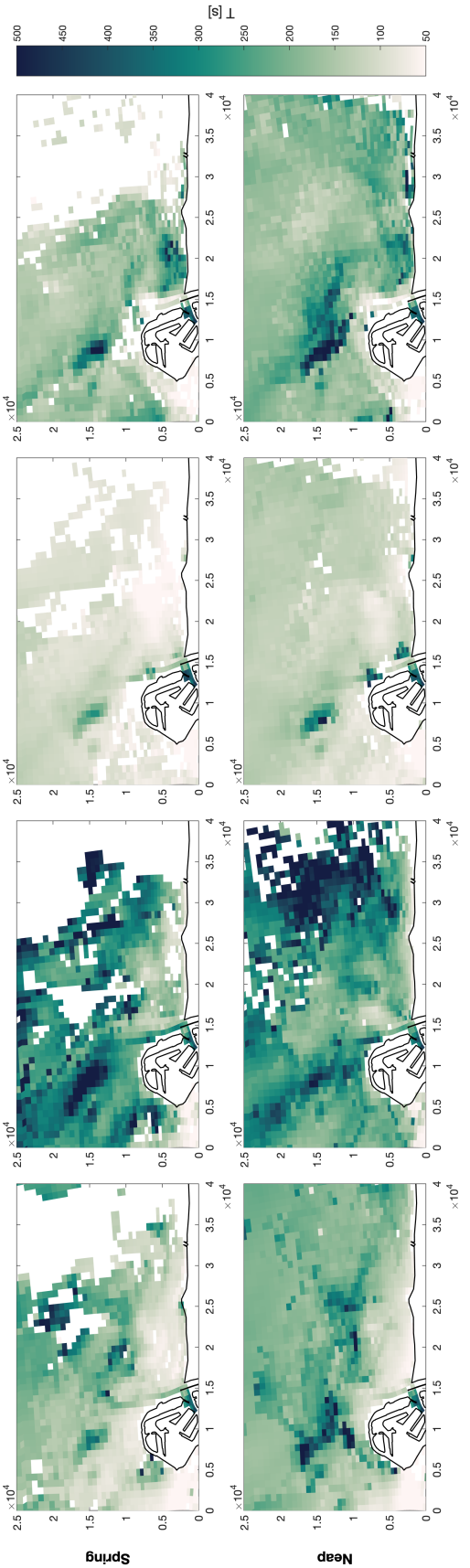

Figure 11.6: Mean value of the wave period with shear-flow in the flow direction of the upper layer for multiple M_2 tidal stages during spring and neap tide.

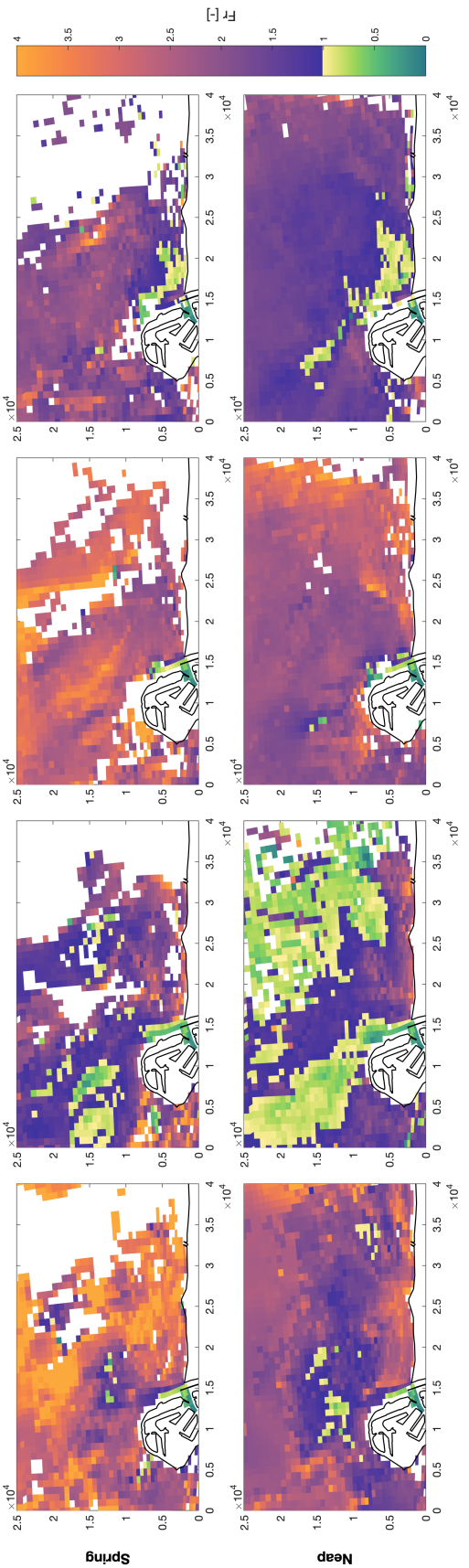

Figure 11.7: Mean value of the Froude number (with shear-flow) in the flow direction of the upper layer for multiple M_2 tidal stages during spring and neap tide.

11.2. Effect of different wind directions on internal waves

The data from the different wind directions from the Delft3D model is used to assess the influence on the propagation of internal waves. This is done similar to the tidal variation. So first, the effect on the stratification based on the results from section 8.2 are discussed. Next, the KdV constants are calculated and discussed. Finally, the wave properties and Froude numbers are discussed.

Effect of different wind directions on stratification

Four different wind conditions are considered: onshore, offshore, downwelling and upwelling. An onshore directed wind leads to a plume located close to the coast, (figure 11.8a). This by the direct contribution of the wind current. Furthermore, the plume is located in the south near Maasvlakte. This is due to the southeastern directed contribution of Ekman transport. An offshore directed wind leads to a plume located further offshore, (figure 11.8b). Due to Ekman transport the plume is also located more to the north. Downwelling winds (figure 11.8c) from the southwest result in a movement of the Rhine ROFI towards the northeast, and towards the coast due to the southeast directed Ekman transport. Upwelling winds (figure 11.8d) are coming from the opposite direction: the northeast, and result in a movement to the south and offshore, respectively due to the direct contribution of the wind speed and the upwelling winds.

Next, consider the stratification. Onshore and downwelling winds lead to more mixing in the river plume, as the the water is pushed towards the coast where it is stopped by the coastal wall. This results in a small density difference over the vertical, as can be seen in figures 11.8a and 11.8c. This also causes the pycnocline to be located deeper in these cases. For an overview of the typical values for the density difference and pycnocline depth see table 11.2. When offshore and upwelling conditions with the same wind speed are considered, it is seen that the water column is less mixed, which implies a stronger density stratification. Also the fresh water is located over a large area, which induces a shallow located pycnocline.

Effect of different wind directions on KdV constants

Each wind direction has one of the following properties: a large density stratification or a deep located pycnocline. Both properties result in a larger value for the linear propagation speed without background flow C_0'. Therefore, it is expected that under all wind directions the propagation speed has the same maximum value, only the places where it occurs is different. Figure 11.8 shows the location of the river plume under the different wind conditions. Next, figure E.10 confirms that the propagation speed has indeed the same maximum value, which occurs in places according to figure 11.8. This result is also stated in table 11.2. A slightly larger value for C_0' is obtained during HW+2 with an onshore wind. The same behavior is expected for the linear propagation speed with shear flow included C_0. As the wind speed is approximately equal for the four cases, the effect is comparable. Figure 11.9 shows that the magnitude of C_0 is approximately equal under the four different wind directions. During the HW and HW+2 phases larger propagation speeds are found in a more onshore region under downwelling and onshore winds, this in contrast to offshore and upwelling winds. As the propagation speed is proportional to squared value of the water depth h_0, the dimensionless propagation speed should be larger for onshore and downwelling winds.

			Wind direction			
			Onshore	Offshore	Down.	Up.
Density difference	$\Delta\rho$	$[\mathrm{kg/m^3}]$	4.0	3.5	1.0	3.0
Relative depth of the pycnocline	θ	$[-]$	0.25	0.15	0.30	0.10
Linear prop. speed without shear-flow	C_0'	$[\mathrm{m/s}]$	0.1	0.1	0.1	0.1
Linear prop. speed with shear-flow	C_0	$[\mathrm{m/s}]$	0.8	0.8	0.8	0.8
Total propagation speed	C_p	$[\mathrm{m/s}]$	0.8	0.8	0.8	0.8
Froude number	Fr	$[-]$	1.1	1.1	1.1	1.1

Table 11.2: Typical stratification parameters, propagation speeds and Froude numbers for different wind conditions at HW+2. Down. stands for downwelling winds; Up. stands for upwelling winds.

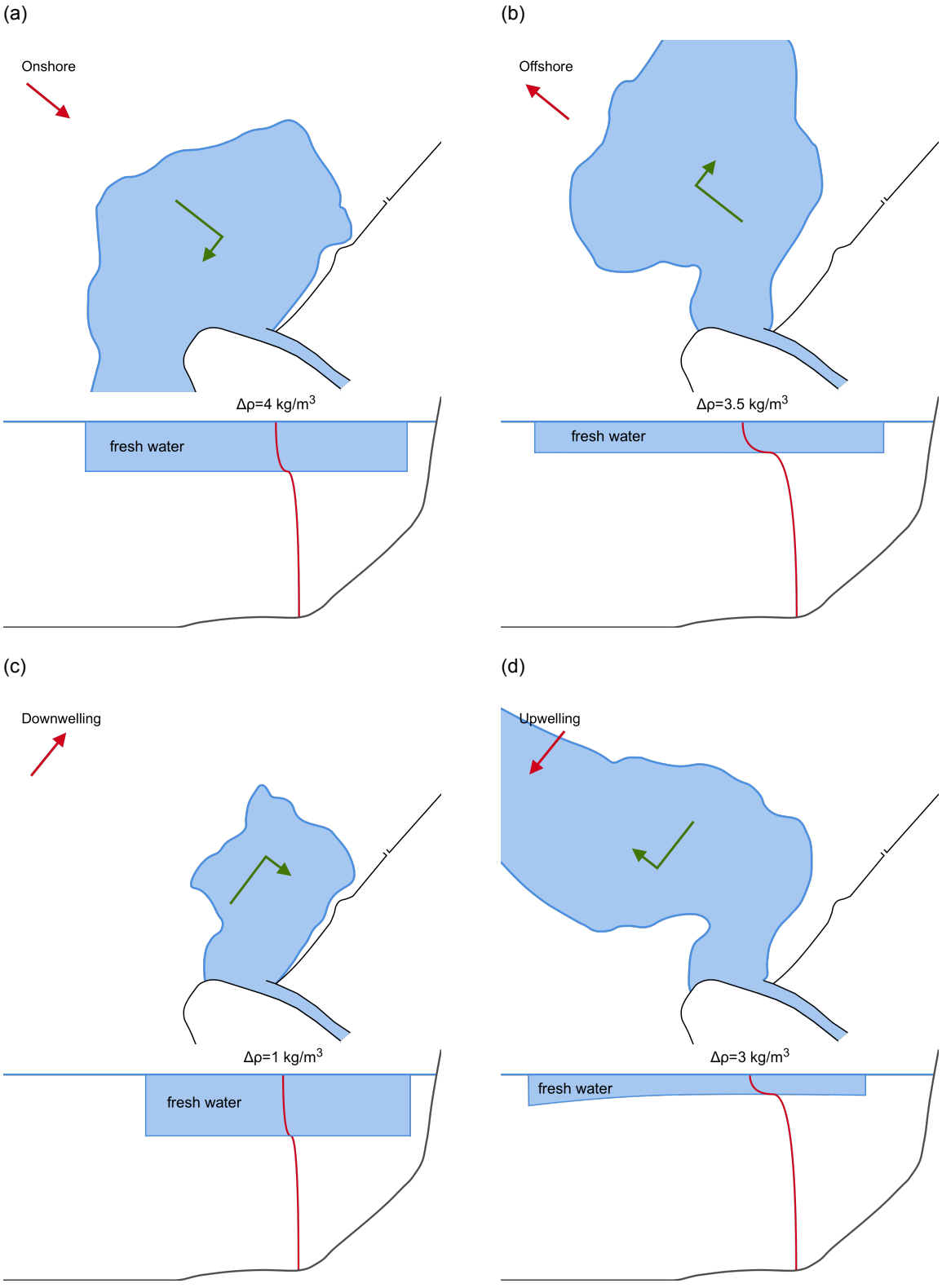

Figure 11.8: Visualization of the size and location of the river plume under different wind directions. Top panel: location and size of the river plume; Bottom panel: typical thickness, size and density stratification of the river plume. (a) Onshore; (b) Offshore (c) Downwelling; (d) Upwelling.

From figure E.13 can be obtained that the stratification induces the largest values for B_1 under onshore winds, which corresponds to the large density difference in figure 11.8a. This is also the case when shear flow is included (figure E.14), but the difference is smaller compared to the other wind conditions.

Effect of different wind directions on wave properties

Based on the constants of KdV equation the total propagation speed C_p and wave period T can be determined, using the periodic KdV solution. Again $\varepsilon = 0.05$ is used to scale the traveling wave velocity C an to calculate the total propagation speed C_p.

As expected the traveling wave velocity C is now also order ε. The strongest decrease in propagation speed (figure E.15) is found during HW-2 with an onshore directed wind, while the largest increase is found with upwelling winds at LW. This corresponds to the earlier observed result for B_1.

The result of the traveling wave velocity C is combined with the total propagation speed C_p. This shows that the behavior of C_p is mainly influenced by C_0 and that the magnitude is equal under the four different wind directions, but that the location differs, see figure E.16. This also implies that the values of C_0 and C_p are equal in table 11.2. In figure 11.10 the wave period is given. It can be observed that the magnitude is equal under four different wind directions during the HW and HW+2 tidal phase. This is, as the magnitude of the total propagation speed is also the same for the four directions during these phases. At HW-2 under onshore and downwelling winds larger wave periods have been found, as the river plume area is small compared to offshore and upwelling winds.

Effect of different wind directions on Froude number

Finally, the Froude numbers have been calculated for these four different wind directions. The Froude number is influenced by the total propagation speed C_p and the background flow. During HW and HW+2 the magnitude of the total propagation speed is considered constant under the four different wind conditions, see table 11.2. As the wind speed is kept equal over the four directions, this influence does not change the Froude number. This means, that the Froude number is not changed by the wind directions during the HW and HW+2 tidal phase. This is supported by figure 11.11. Under all four wind directions supercritical is found at HW. Furthermore, subcritical flow is found for all four wind directions near the river mouth during HW+2. This means that it is possible for waves to be generated under all wind directions. Not having a preferred wind directions corresponds with the finding of internal waves under all wind directions by Rijnsburger et al. (2019b).

In has been seen, that the river plumes passes the observation points around HW+2 and that the stratification is strongest at these points and during this moment of the semi-diurnal tide. During spring tide the water column is mixed so the stratification is less compared to neap tide. As the advection is strong during spring due to the large tidal range; fast propagating waves with short periods can be found. Waves get damped downstream in the Rhine ROFI, while moving from the near- to mid-field region, as here the waves are propagation slower and have a longer period. This is induced by the stratification, which gets less when moving away from the river mouth. Wind directed onshore and alongshore downwelling (from the southwest to the northeast) advects the Rhine ROFI to the coast. This means that a deep pycnocline is obtained and that internal waves propagate fast in more shallow water. This compared to the other two wind directions. Finally, the Froude number has been considered, concluded is that the supercritical flow is found during HW and subcritical flow during HW+2, which means that waves can be generated by the river plume head.

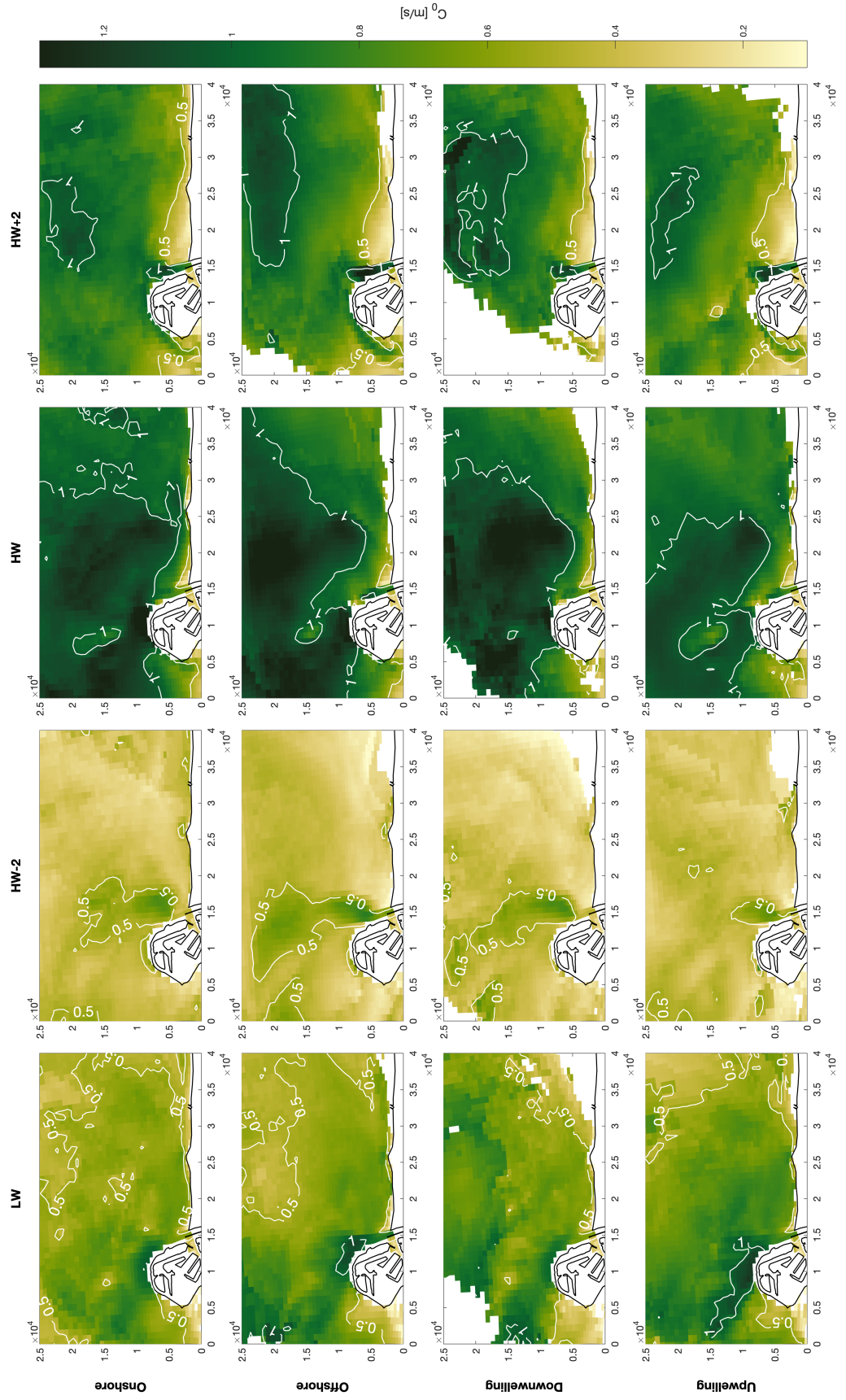

Figure 11.9: Mean value of C_0 with shear-flow in the flow direction of the upper layer for multiple M_2 tidal stages for multiple wind directions.

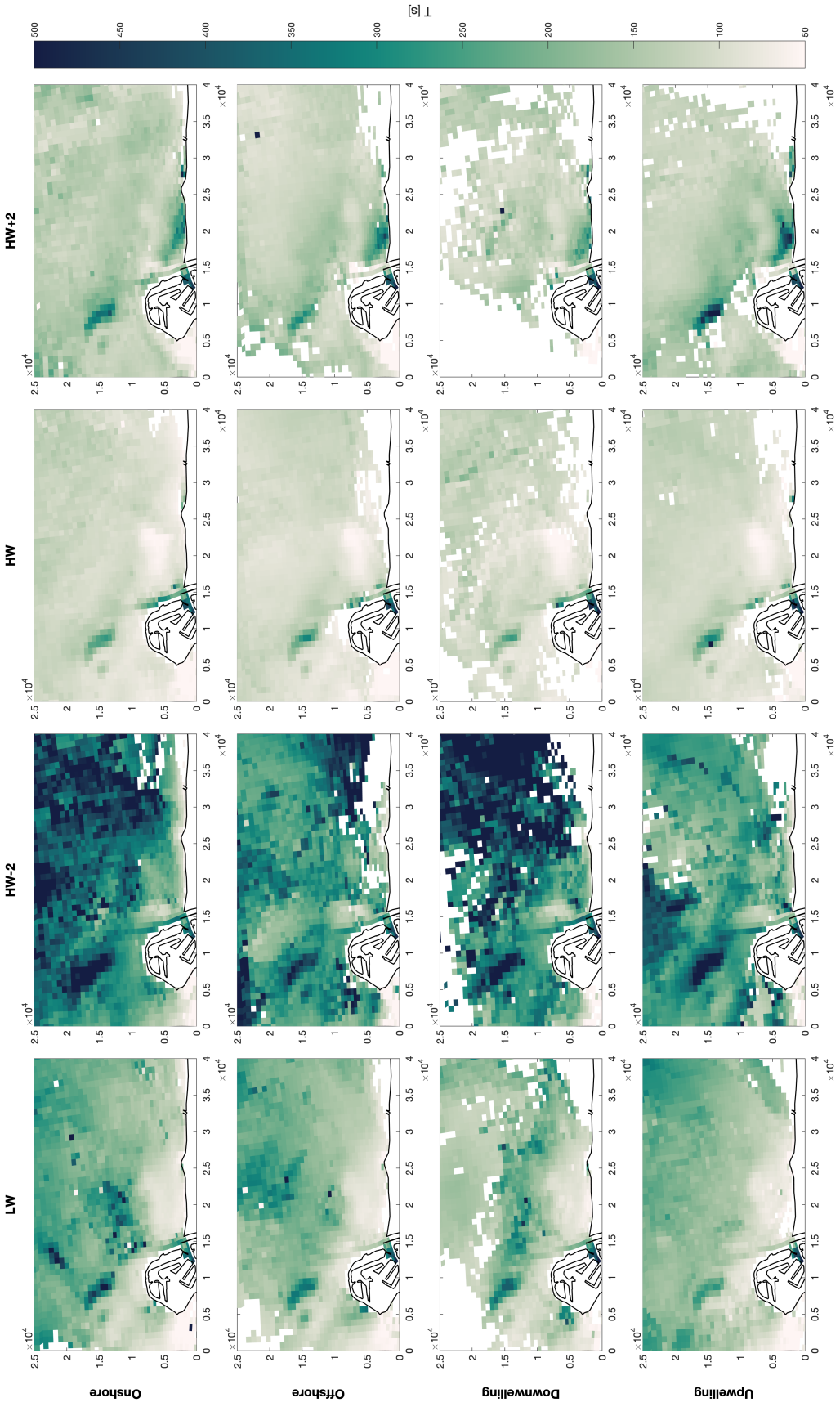

Figure 11.10: Mean value of the wave period with shear-flow in the flow direction of the upper layer for multiple M_2 tidal stages for multiple wind directions.

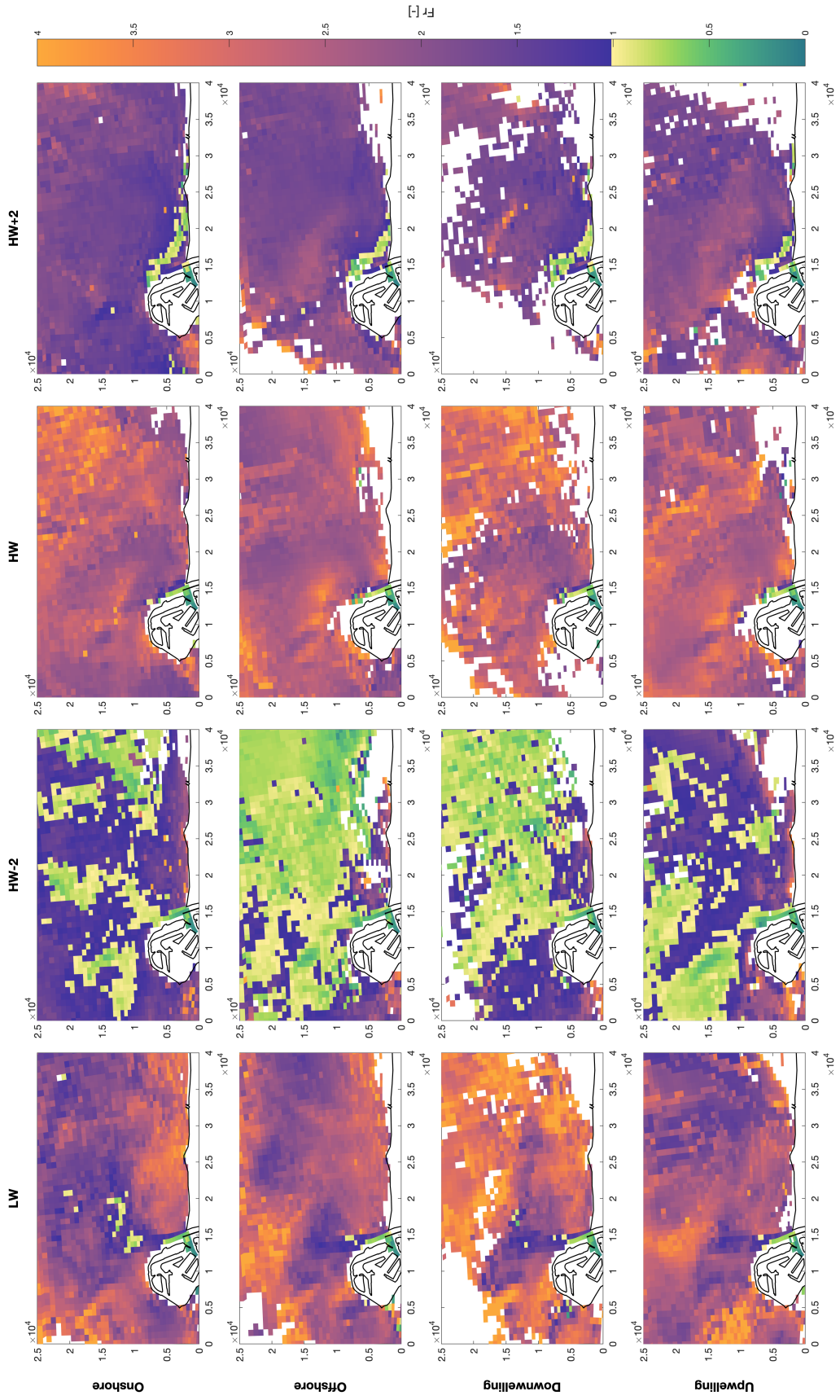

Figure 11.11: Mean value of the Froude number (with shear-flow) in the flow direction of the upper layer for multiple M_2 tidal stages for multiple wind directions.

12

Results for observed wave events

Using the TGE fitting procedure (chapter 7) new information about the background for the wave measurements by Rijnsburger et al. (2019b) can be found. Section 10.1 has gone through this procedure in order to check the validity of the procedure and the TGE. Next, the results of this fitting procedure are discussed (figure 3.1 - VI), (section 12.1). Using these results and the bathymetry the variable bed KdV model are used to obtain the propagation speed and period in space for the observed internal waves, (section 12.2).

12.1. Results of the TGE fitting procedure

While performing the TGE fitting procedure estimates have been obtained for the pycnocline depth, thickness and wave angle. These values for the wave events are presented in 12.1.

First, the results for the pycnocline are discussed. For all events the resulting stratification profiles, figure 12.1, are close to the measured density values at the four different depths. For the events of September, 17th 21:29 and October, 4th 09:27 the measurement point at -2.5 [m] is not matched by the stratification profile. The predict depth of the pycnocline is half a meter off. On average the pycnocline is located around 3 meters depth, which matches the typical thickness of the upper layer of three to five meters observed by de Boer et al. (2009). Note that, the pycnocline depth determined by the TGE fitting procedure is the averaged depth of the pycnocline when a wave is passing by (timeframe of 5-15 minutes). As the solution is assumed to be periodic. For a number of events the pycnocline has a small relative thickness (sharp pycnocline), while for the first two and the last event the thickness is much larger. As there are no measurements made for the sharpness of the pycnocline, it is not clear if these thicknesses are realistic (or not).

Next, in table 12.1 the direction of the upper layer and the fitted wave angle are given. In most cases it was possible to obtain the fitted angle, but as already stated in section 10.1 the method does not work for the events of September, 17th 21:09 and October, 4th 10:12. For most of the other events the upper layer direction is close to the fitted wave angle (difference of 15°or less). Only the event September, 19th has a large difference of 50°. This supports the conclusion by Rijnsburger et al. (2019b) that the waves are more or less in the same directions as the tidal plume fronts.

Corresponding to the solution of the TGE, figure 10.2d, the TGE fitting procedure also predicts a linear propagation speed C_0. This propagation speed is given in the last two rows of table 12.1 and have already been used to validate the scaling, (section 10.2). These values match the propagation speeds calculated by Rijnsburger et al. (2019b) using the DJL equation. The propagation speed corrected for the mean background flow $C_0 - \tilde{U}$ is in the same order as the propagation speed by Pietrzak and Labeur (2004). This means that the regime of the propagation speed prediction is correct.

		17-09 21:09	17-09 21:16	17-09 21:29	19-09 11:33	04-10 09:27	04-10 09:58	04-10 10:12	04-10 10:24
Pycnocline depth	m								
Pycnocline thickness	m								
Upper layer direction									
Fitted wave angle									
C_0	$\mathrm{m/s}$								
$C_0 - \bar{U}$	$\mathrm{m/s}$								

Table 12.1: Data obtained from the TGE fitting procedure for observed wave events by Rijnsburger et al. (2019a).

Figure unavailable until publication of Rijnsburger, et al. (2019b)

Figure 12.1: Stratification profiles after performing TGE fitting procedure.

12.2. Results of the variable bed KdV model

From the TGE fitting procedure a direction of wave propagation was obtained for each wave event. Next, for each of the events where the KdV balance is valid (see section 10.2), the bed profile in that direction is found. This is done by using the bathymetry data from the Delft3D model by Rijnsburger et al. (2019a). The resulting bed profiles are given in the first panel of figure 12.2. On a length of $5\ [\mathrm{km}]$ the maximum offset from the depth at the observation point (M18) is $5\ [\mathrm{m}]$ for the event of October, 4th 10:12.

All these bathymetry profiles are used to model internal waves with the derived variable bed KdV equation, (chapter 5). This results in a linear propagation speed C_0 as in table 12.1 and a variable bed propagation speed C_h. This phase velocity is given in the second panel of figure 12.2. The influence of the variable bed is small, less than 10% of C_0. For the event of September, 19th 11:33 the variation is largest. This while the bathymetric variation is not the largest for this event. This has to do with the solution of the background where the strong background flow near the bottom results in a larger contribution of a bed level change.

With these two phase velocities, C_0 and C_h, and the traveling wave velocity from the periodic KdV solution the total propagation speed C_p has been determined. Using this value it is also possible to calculate the period T. The results for C_p and T are given in the bottom two panels of figure 12.2. On these two wave quantities the small impact of the bathymetric variation is indeed visible. The lines in the figures are more or less of constant value, which means that the order of magnitude is not changed by the influence of the bed changes.

Figure 12.3 and 12.4 show the isopycnal displacement, horizontal- and vertical wave induced velocity for the wave events of September, 19th 11:33 and October, 4th 10:24 respectively. Here, the waves are shown $250\ [\mathrm{m}]$ before and behind the observation point. For both events the absolute bathymetry changes are small on this short distance. Therefore the level change of the isopycnals is mainly due to the presence of internal waves (see top panel of both figures). From these isopycnals can be seen that the waves for the event of September, 19th have a larger amplitude and are steeper compared to event of October, 4th. In the wave induced horizontal velocity of the event of September, 19th a sudden change in flow direction around the pycnocline can be observed (see middle panel figure 12.3). This

Figure 12.2: Effect on bathymetric variation for the wave events with valid KdV balance.

is the case, as the estimated pycnocline thickness is small for this event. For the event of October, 4th the thickness is larger and therefore also the change of flow direction is less sharp. Comparing the middle panel and bottom panel of figures 12.3 and 12.4 shows that the maximum vertical velocity is approximately three times smaller than the maximum horizontal velocity.

This variable KdV model has shown that the bathymetric variation only delivers a small change of the propagation speed of internal waves. This means that the influence of the bathymetry on wave refraction is small at this point. In chapter 11 was shown that the internal wave propagation speed differs more from place to place. This means that this variable KdV model is missing information about the density stratification and background flow changes due to the variability inside the Rhine ROFI and that a 2DV approximation is too simplistic.

Figure unavailable until publication of Rijnsburger, et al. (2019b)

Figure 12.3: Isopycnal displacement, horizontal- and vertical wave induced velocities. For the observed wave event of September, 19th 11:33.

Figure unavailable until publication of Rijnsburger, et al. (2019b)

Figure 12.4: Isopycnal displacement, horizontal- and vertical wave induced velocities. For the observed wave event of October, 4th 10:24.

III

Discussions and conclusions

13

Discussion

This research investigated the generation and propagation of internal waves on a shallow frictional shelf, in particular to the Rhine ROFI. Rijnsburger et al. (2019b) have shown the presence of internal waves in this system. Using three different models (see figure 3.1) and measurement data the generation mechanism and propagation speed of internal waves have been investigated. This chapter gives an overview of the implications obtained from this research.

Dynamics of the Rhine ROFI

The Rhine ROFI is a river plume exposed to a large tidal range, which induces the release of tidal plume fronts in each tidal cycle. It is shown, that the propagation of these tidal plume fronts are captured in the Delft3D model developed by Rijnsburger et al. (2019a). During LW the fresh-water is released, and when the initial momentum is dissipated, Coriolis turns the plume in alongshore direction to the Northeast, see figure 1.1, (Horner-Devine et al., 2015). In the Rhine ROFI tidal straining is observed, (Visser et al., 1994; A. Souza & Simpson, 1996; de Boer et al., 2009). These effects are also captured by the Delft3D model, including the anti-cyclonic rotation of the surface layer and the cyclonic rotation of the bottom layer.

The stratification induced by the Rhine ROFI determines the propagation speed and shape of the internal waves possible in the environment. To study this effect the density stratification and hydrostatic flow profiles from the Delft3D model have been used, this to calculate the propagation speed using the KdV model. To capture the pycnocline correctly the number of sigma-layers in the Delft3D model has been increased compared to Rijnsburger et al. (2019a). The results from this model give a better estimate of the location of the pycnocline, also the horizontal velocities are in better agreement with the measurement data. The density stratification profiles, resulting from Delft3D, have been approximated by a hyperbolic tangent profile, similar to Pietrzak et al. (1990) in the Rotterdam Waterway. As observed by Rijnsburger et al. (2019a) this is a reasonable choice, but not valid at all times and locations in the Rhine ROFI. Next, the propagation speed was combined with the flow velocities to determine Froude numbers. This analysis was performed at four key moments in the semi-diurnal tidal cycle: LW, HW-2, HW and HW+2.

From the KdV model it is determined, that both a deeper located pycnocline and stronger density stratification result in fast propagating waves. Beside, the pycnocline depth determines if waves of elevation or depression could be present in the system. The depth-averaged background flow, contributes to the linear propagation speed C_0 as additive term by advection. Furthermore, an increase of shear in the background flow (velocity difference over the vertical) results in a larger propagation speed.

Influence of tides on the generation and propagation of internal waves

In the Rhine ROFI the tidal range is large during spring tides and small during neap tides. This induces a different stratification in these situations. The small tidal range during neap tides, leads to less mixing

(Visser et al., 1994), and therefore to a strong density stratification of $\Delta\rho = 4\ [\mathrm{kg/m^3}]$. Furthermore, the pycnocline is located deeper during neap tides (relative to spring tides), see figure 11.1b. This has resulted in a larger linear propagation speed without advection C_0'. Therefore, the observed Froude numbers are lower during spring tides than during neap tides. As the Froude numbers are lower during neap tides, this phase is considered favourable for the generation of internal waves. This corresponds with the observation of more wave events during neap tide than during spring tide by Rijnsburger et al. (2019b).

The Froude number analysis showed, that the flow in the Rhine ROFI is always supercritical during HW and LW for internal waves. At HW-2 and HW+2, around tidal slack, subcritical flow is found inside the river plume. As the flow is first supercritical during HW, and becomes subcritical during HW+2, the frontal growth and free propagation stages are found. As the change occurs around tidal slack, the generation of internal waves has been associated with the slackening of the tidal plume fronts. This matches the observations of internal wave generation by Nash and Moum (2005) in the Columbia river plume. The definition of the Froude number used in this research is different to Nash and Moum (2005), (section 3.2), as the upper layer velocity U_1 is used instead of the tidal plume front propagation speed U_f. Based on the observations that $U_1 \approx 1.1U_f$, the Froude number is large during HW $Fr > 2$, and small during HW+2 $Fr < 1$, it is concluded that the Froude number used by Nash and Moum (2005) also changes from super- to subcritical in the Rhine ROFI.

Influence of wind on the generation and propagation of internal waves

Different wind directions result in density stratification at a different location, (Rijnsburger et al., 2019a). Onshore and downwelling winds force the river plume to be attached to the coast, see figure 11.8a and 11.8c. This leads to more mixing and therefore a deeper located pycnocline with a weaker density stratification compared to offshore and upwelling winds. As a weaker density stratification leads to a smaller propagation speed, and a deeper located pycnocline to a larger propagation speed, the maximum propagation speed is equal for the four considered wind directions. This also implies that the behavior of the Froude number is equal for the different wind directions. This matches to the observations of Rijnsburger et al. (2019b), that there is no clear favourable wind direction for internal waves.

Propagation speed estimations based on field data

As the missing pycnocline depth and direction of propagation have a large influence on the propagation of internal waves, a TGE fitting procedure has been been developed, (chapter 7). This procedure links the vertical velocity measurements with the point stratification measures using the TGE equation. The obtained results are in agreement with the range for the pycnocline depth of three to five meters by de Boer et al. (2009), and the direction of internal wave propagation is close to the direction of the tidal plume front observed by Rijnsburger et al. (2019b). This resulted in an estimate between $0.57 - 0.99\ [\mathrm{m/s}]$ for the linear propagation speed C_0 for the observed wave events by Rijnsburger et al. (2019b). These results are in the same order as the linear propagation speeds estimated by Rijnsburger et al. (2019b) using the DJL equation. Furthermore, the direction of wave propagation has been estimated. The obtained direction is close towards the direction of the tidal plume front and is consistent with the predicted direction by Rijnsburger et al. (2019b).

Variable bed KdV model

As the Rhine ROFI is located on a shallow frictional shelf the importance of bathymetric variations (bed profile) for internal waves is investigated. Therefore, the standard KdV model derived by Grimshaw et al. (2002) is extended. In the presented derivation (chapter 5) a small variation of the bed is allowed, which is representative for the Rhine ROFI. The variation is taken into account by introducing a (large) length scale for this variation next to the existing (short) length scale for the wave variation. This has resulted in two flow problems: one for the background (non-wave related) flow, exposed to the bathymetric variations, and one for the wave induced flow, influenced by the large scale motions.

It appears that the background flow problem can be solved separately from the internal waves using one ordinary differential equation. The problem for internal waves resulted in two differential equations:

the Taylor-Goldstein equation, determining the vertical structure and linear propagation speed; and the variable bed KdV equation, which accounts for horizontal time-dependent wave propagation and is influenced by a small parameter accounting for the bathymetric variation. It is shown that the Taylor-Goldstein problem can be solved by writing it as numerical quadratic eigenvalue problem (QEP) and next it can be solved as a standard eigenvalue problem (SEP). In this approach the singularity of no-flow is avoided by shifting the flow, which is mathematically allowed. However, the physical aspects of this critical layers are not considered. This QEP numerical approach can be solved faster and more accurate compared to the shooting method as presented by Stastna and Lamb (2002). Using a transformation it is shown that the variable bed KdV equation can be written as the standard KdV equation. This made it possible to use the existing knowledge on the KdV equation. Therefore, the periodic solution of the KdV equation can be used.

Influence of bathymetric variations on internal waves

In the Rhine ROFI bathymetric variations h' in the direction of internal wave propagation are small. It is shown, that the bathymetric variations h' deliver a small linear contribution in the total propagation speed C_p. The influence behaves similar to the undisturbed water depth h_0: shallower water induces slower propagating waves.

Applicability of the KdV model

As the Rhine ROFI is shallow and different to the regions where the KdV for internal waves is normally to applied. Using the observations of internal waves by Rijnsburger et al. (2019b) the parameter scaling and assumptions necessary for the KdV have been checked. It is seen, that the KdV balance $\varepsilon = \mathcal{O}\left(\delta^2\right)$ holds for most of the observed events. For the events of October, 4th at 09:27 and 09:58 this balance does not hold, as in these cases δ is smaller, the advection terms of the vertical momentum equation contribute less. It is a limitation of the KdV model, that it can not be applied to these cases. For the events where the balance holds the KdV model results are in agreement with the measured vertical velocities. This means that the KdV model can be used for a first estimate of internal waves in the Rhine ROFI.

In contribution to the ongoing research on energy redistribution by internal waves in the Rhine ROFI, it is now possible to apply the KdV model and to estimate the energy flux. This in accordance with Pan and Jay (2009), where the KdV model was applied to the Columbia river plume to estimate the energy flux. After obtaining the energy flux, it will be possible to estimate the contribution of internal waves to the plume area, mixing processes and sediment fluxes in the Rhine ROFI.

14

Conclusions and recommendations

This research has studied the internal waves in a shallow frictional river plume, the Rhine ROFI. By the combination of a Delft3D model with a variable bed KdV model, it was possible to estimate the internal wave propagation speed under different tidal and wind conditions. Furthermore, an estimate of the missing field data was obtained by the development of the TGE fitting procedure. First, the research questions are answered, (section 14.1). After that, recommendations for future research are made, (section 14.2).

14.1. Conclusions

Based on the different models and results it is possible to draw conclusions and to answer the research questions. This is done, by first answering the sub-questions. Next, the main question is answered.

1. How does the density stratification and (background) shear-flow impact the propagation speed of internal waves in a shallow system?

The pycnocline depth in the Rhine ROFI varies from three to five meters, (de Boer et al., 2009). The sensitivity analysis showed that this variation has a large influence on the propagation speed of internal waves, as the water depth in the region is only 20 meters. While the influence of the pycnocline depth is large, the contribution of the pycnocline thickness is small.

The tidal flow in the Rhine ROFI has a large amplitude, as the tidal range is large. This flow advects the internal waves, which leads to an additive term in the linear propagation speed C_0. In addition, larger shear (velocity differences) in the water column results in an increase of the propagation speed. However, when this shear becomes too large the waves are suppressed.

2. How are internal waves in the Rhine ROFI influenced at different locations by tidal stage and wind direction?

It is observed that the propagation speed is large, in the areas where the density differences are also large. So while moving downstream the Rhine ROFI from the near-field to mid-field region the waves propagate slower and have a longer period. In the near-field the tidal velocity and density difference are largest around HW+2. This has resulted in the largest propagation speeds during this phase of the tide. HW+2 is also the moment that the internal waves are observed by Rijnsburger et al. (2019b). Over the spring-neap cycle the amount of mixing in the near-field changes, this has as effect that the Rhine ROFI is more stratified during neap tides, compared to spring tides. This leads to fast propagating waves. However, the internal wave advection during spring tides is larger than during neap tides, and therefore the largest propagation speed are found during spring tides.

The tidal plume fronts are attached to the coast, when the wind is directed in onshore or downwelling direction. In these situations the effect of a less strong density difference is cancelled by a deeper

located pycnocline, resulting in a propagation speed of the same magnitude as during offshore and upwelling winds. The different wind directions do not control the propagation speed of the internal waves, but only the location where the waves occur.

3. Are internal waves in the Rhine ROFI generated by the tidal plume front? Is it possible, to show this using a Froude number analysis?

From the analysis of the Froude number it is concluded, that supercritical flow is found at HW and LW. During HW-2 and HW+2 the tidal induced flow velocities are small, which results in subcritical flow. Note that these moments are close to tidal slack. As seen mainly during neap tide, the flow inside the river plume changes from supercritical during HW ($Fr > 1$) to subcritical ($Fr < 1$) during HW+2. This is around the time, that the internal waves are observed by Rijnsburger et al. (2019b). This analysis shows that internal waves in the Rhine ROFI can be generated by the tidal plume front mechanism, as explained by Nash and Moum (2005).

4. How are internal waves influenced by small bathymetric variations of a shallow system?

In the observed direction of internal wave propagation the bathymetric variation in the Rhine ROFI is small. Using the variable bed KdV model it can be concluded, that the bathymetry changes in this case contribute to small adjustments of the propagation speed (and therefore also of the period). This adjustment C_h is in the same order of magnitude as the traveling wave velocity C, but an order ε smaller compared to the linear propagation speed C_0. The contribution of C_h is linear in the depth variation h', and for shallower water it is seen that the propagation speed becomes smaller.

5. Is it possible to use flow velocity measurements, in order to obtain an estimate of the pycnocline depth and direction of internal wave propagation?

As the measurements of Rijnsburger et al. (2019b) do not give a clear indication of the pycnocline location, thickness and direction of wave propagation the TGE fitting procedure is developed. This procedure takes the solution of the TGE and the vertical velocity measurements. Next, it searches for the best stratification profile and direction of wave propagation suited. By the use of this procedure the missing information of the pycnocline depth, thickness and direction of internal wave propagation has been estimated. When these results are combined with the KdV model, it is obtained that the results are in agreement with the measurements performed by Rijnsburger et al. (2019b). The results of this procedure match the expectations of the pycnocline depth as obtained from earlier research by de Boer et al. (2009).

Main question: How does a shallow frictional river plume impact the generation and propagation of internal waves in the near- to mid-field region?

Internal waves in a shallow system are sensitive to the amount of density stratification and the pycnocline depth. Also the background flow delivers a large contribution to the propagation speed of internal waves, as the depth-averaged velocity adds directly to the propagation speed. The influence of a large amount of shear in the water column is, that the waves have a larger propagation speed.

As the Rhine ROFI, a shallow frictional river plume, depends on tidal stage and wind direction, the waves are influenced by these changes. This is caused by the differences in density stratification and background flow. It has been found that spring tides result in fast propagating waves (large value of C_p). Finally, it is found that the bathymetric variations in the Rhine ROFI are small. This is shown by the small contribution of the propagation speed due to bathymetric variations C_h in the total propagation speed C_p of internal waves.

Using a Froude number analysis the generation mechanism of internal waves by tidal plume fronts is supported in the Rhine ROFI. It has been seen, that the flow changes from supercritical at HW to subcritical at HW+2 inside the river plume. This allows the release of free propagating waves from the tidal plume head. As the tidal velocities are small and the density stratification is large during neap tides, these neap tides are considered as favourable for internal wave generation.

14.2. Recommendations

This research has answered questions about the propagation phase of internal waves internal waves. On the assumptions made remarks can be made, which can be investigated in more detail in future research.

The results of the Delft3D model has shown a constant bias in the salinity values near the bottom. This is due to the model spin-up of the model and has influenced the analysis of tidal and wind variation, (chapter 11). It is advised to improve this model setup, such that this bias can be removed from the results. This will hopefully give better insight in the background for the waves.

Showing that internal waves are generated by the tidal plume front, a Froude number analysis have been used in this research. The definition of this froude number is slightly different to Nash and Moum (2005). So is the recommended to improve the analysis by using the same definition. Therefore, the location of the tidal plume front needs to be found in a high resolution Delft3D output. It has been found, that this is difficult to obtain. This will help to estimate the tidal plume front propagation speed U_f and can connect in to the internal wave speed relative to the fluid $C_p - U_m$ in the ambient. Furthermore, it would be an improvement to consider a complete tidal cycle from LW all the way up to HW+2, as it is expected that this will show where and when the internal waves are exactly generated.

Based on the environmental analysis internal waves are more likely to occur during neap tides, as the propagation speed relative to the fluid is larger in this case. Therefore it is recommended, to setup new measurement campaigns during neap tides. Beside, this condition can be used, when searching for evidence of internal waves in satellite imagery.

The validation of the TGE showed that there is an offset between the measurements and theory near the bottom. It would be interesting to investigate if boundary processes have caused this difference or that this is a measurement error from the instruments. The limitation of the KdV equation is that the KdV balance needs to be assumed, and that the results do not hold for all observed wave events. It is recommended to look further into the derivation, to see what happens when $\delta = \mathcal{O}(\varepsilon)$ is assumed, instead of $\delta = \mathcal{O}\left(\sqrt{\varepsilon}\right)$. For waves approaching the coast in the Rhine ROFI the currently used slope in the variable bed KdV derivation is too gentle. Therefore the derivation should be changed, such that a steeper bed is allowed. The KdV has now been derived for the leading order of the wave perturbation. Including the next order would be interesting, as Lamb and Yan (1996) have shown that this may change the predicted wave amplitude by $10-25\%$. Furthermore, the model does not account for waves in very shallow water and the effects of breaking and reflection near the coast. This can be studied in future research by the use of numerical models.

The developed TGE fitting procedure has been tested on the limited data available. It is recommended to test this approach on more accurate field data, or to validate it using tests from the laboratory. Furthermore, for this procedure it is assumed that the waves are periodic and symmetric. This has allowed to neglect the difference between Eulerian and isopycnal coordinates for the maximum vertical velocity. By keeping track of the isopycnals and making the correction between the two different coordinates this assumption will be unnecessary.

This research has focussed on the propagation of internal waves. The effect of energy transfer from the tidal plume front to the ambient as suggested by Pan and Jay (2009) is not studied. As Pan and Jay (2009) used the KdV model to estimate the energy flux and this research has checked the applicability of the KdV model, the next step can be taken by calculating the energy flux in the Rhine ROFI using the KdV model. This contributes in the research to the energy redistribution by internal waves in the Rhine ROFI. This will be interesting, as it contributes in the understanding of the intense mixing in the near-field region of the river plume, (Horner-Devine et al., 2017).

References

Andrews, D. G., & Mcintyre, M. E. (1978, dec). An exact theory of nonlinear waves on a Lagrangian-mean flow. *Journal of Fluid Mechanics*, *89*(04), 609. doi: 10.1017/S0022112078002773

Bourgault, D., Galbraith, P. S., & Chavanne, C. (2016, dec). Generation of internal solitary waves by frontally forced intrusions in geophysical flows. *Nature Communications*, *7*, 13606. doi: 10.1038/ncomms13606

Bourgault, D., & Kelley, D. E. (2004, dec). A Laterally Averaged Nonhydrostatic Ocean Model. *Journal of Atmospheric and Oceanic Technology*, *21*(12), 1910–1924. doi: 10.1175/JTECH-1674.1

de Boer, G. J., Pietrzak, J. D., & Winterwerp, J. C. (2006, jul). On the vertical structure of the Rhine region of freshwater influence. *Ocean Dynamics*, *56*(3-4), 198–216. doi: 10.1007/s10236-005-0042-1

de Boer, G. J., Pietrzak, J. D., & Winterwerp, J. C. (2008, jan). Using the potential energy anomaly equation to investigate tidal straining and advection of stratification in a region of freshwater influence. *Ocean Modelling*, *22*(1-2), 1–11. doi: 10.1016/J.OCEMOD.2007.12.003

de Boer, G. J., Pietrzak, J. D., & Winterwerp, J. C. (2009, jan). SST observations of upwelling induced by tidal straining in the Rhine ROFI. *Continental Shelf Research*, *29*(1), 263–277. doi: 10.1016/J.CSR.2007.06.011

de Kok, J. (1996, sep). A two-layer model of the Rhine plume. *Journal of Marine Systems*, *8*(3-4), 269–284. doi: 10.1016/0924-7963(96)00010-3

Drazin, P. G., & Johnson, R. S. (1989). *Solitons: an introduction*. Cambridge: Cambridge University Press.

Fong, D. A., & Geyer, W. R. (2001, jan). Response of a river plume during an upwelling favorable wind event. *Journal of Geophysical Research: Oceans*, *106*(C1), 1067–1084. doi: 10.1029/2000JC900134

Grimshaw, R., Pelinovsky, E., & Poloukhina, O. (2002). Higher-order Korteweg-de Vries models for internal solitary waves in a stratified shear flow with a free surface. *Nonlinear Processes in Geophysics*, *9*(3/4), 221–235. doi: 10.5194/npg-9-221-2002

Haberman, R. (2014). *App;ied Partial Differential Equations with Fourier Series and Boundary Value Problems* (5th Editio ed.). Pearson Education Limited.

Helfrich, K. R., & Melville, W. K. (2006, jan). LONG NONLINEAR INTERNAL WAVES. *Annual Review of Fluid Mechanics*, *38*(1), 395–425. doi: 10.1146/annurev.fluid.38.050304.092129

Hessner, K., Rubino, A., Brandt, P., Alpers, W., Hessner, K., Rubino, A., … Alpers, W. (2001, oct). The Rhine Outflow Plume Studied by the Analysis of Synthetic Aperture Radar Data and Numerical Simulations. *Journal of Physical Oceanography*, *31*(10), 3030–3044. doi: 10.1175/1520-0485(2001)031<3030:TROPSB>2.0.CO;2

Holmes, M. H. (1995). *Introduction to Perturbation Methods* (Vol. 20). New York, NY: Springer New York. doi: 10.1007/978-1-4614-5477-9

Horner-Devine, A. R., Hetland, R. D., & MacDonald, D. G. (2015, jan). Mixing and Transport in Coastal River Plumes. *Annual Review of Fluid Mechanics*, *47*(1), 569–594. doi: 10.1146/annurev-fluid-010313-141408

Horner-Devine, A. R., Pietrzak, J. D., Souza, A. J., McKeon, M. A., Meirelles, S., Henriquez, M., … Rijnsburger, S. (2017, jun). Cross-shore transport of nearshore sediment by river plume frontal pumping. *Geophysical Research Letters*, *44*(12), 6343–6351. doi: 10.1002/2017GL073378

Jackson, C. R., da Silva José, C., & Jeans, G. (2012). The generation of nonlinear internal waves. *Oceanography*, *25*(2), 108–123. doi: 10.5670/oceanog.2012.46

Johnson, R. S. (1997). *A Modern Introduction to the Mathematical Theory of Water Waves*. Cambridge University Press.

Korteweg, D. J., & de Vries, G. (1895, may). On the change of form of long waves advancing in a rectangular canal, and on a new type of long stationary waves. *The London, Edin-*

burgh, and Dublin Philosophical Magazine and Journal of Science, *39*(240), 422–443. doi: 10.1080/14786449508620739

Lamb, K. G., & Yan, L. (1996, dec). The Evolution of Internal Wave Undular Bores: Comparisons of a Fully Nonlinear Numerical Model with Weakly Nonlinear Theory. *Journal of Physical Oceanography*, *26*(12), 2712–2734. doi: 10.1175/1520-0485(1996)026<2712:TEOIWU>2.0.CO;2

Lee, C.-Y., & Beardsley, R. C. (1974, jan). The generation of long nonlinear internal waves in a weakly stratified shear flow. *Journal of Geophysical Research*, *79*(3), 453–462. doi: 10.1029/JC079i003p00453

Li, L., Pawlowicz, R., & Wang, C. (2018, aug). Seasonal Variability and Generation Mechanisms of Nonlinear Internal Waves in the Strait of Georgia. *Journal of Geophysical Research: Oceans*, *123*(8), 5706–5726. doi: 10.1029/2017JC013563

Luijendijk, A. P., Ranasinghe, R., de Schipper, M. A., Huisman, B. A., Swinkels, C. M., Walstra, D. J., & Stive, M. J. (2017, jan). The initial morphological response of the Sand Engine: A process-based modelling study. *Coastal Engineering*, *119*, 1–14. doi: 10.1016/J.COASTALENG.2016.09.005

NASA Earth Observatory. (2007, mar). *Thames River Plume in the North Sea.* NASA Earth Observatory. Retrieved from [2019-10-09]https://earthobservatory.nasa.gov/images/18169

Nash, J. D., Kilcher, L. F., & Moum, J. N. (2009, feb). Structure and composition of a strongly stratified, tidally pulsed river plume. *Journal of Geophysical Research: Oceans*, *114*(C2). doi: 10.1029/2008JC005036@10.1002/(ISSN)2169-9291.RISE1

Nash, J. D., & Moum, J. N. (2005, sep). River plumes as a source of large-amplitude internal waves in the coastal ocean. *Nature*, *437*(7057), 400–403. doi: 10.1038/nature03936

Pan, J., & Jay, D. A. (2009, jan). Dynamic characteristics and horizontal transports of internal solitons generated at the Columbia River plume front. *Continental Shelf Research*, *29*(1), 252–262. doi: 10.1016/j.csr.2008.01.002

Pietrzak, J., Kranenburg, C., & Abraham, G. (1990, apr). Resonant internal waves in fluid flow. *Nature*, *344*(6269), 844–847. doi: 10.1038/344844a0

Pietrzak, J., & Labeur, R. J. (2004, jul). Trapped internal waves over undular topography in a partially mixed estuary. *Ocean Dynamics*, *54*(3-4), 315–323. doi: 10.1007/s10236-003-0081-4

Rijnsburger, S., Flores, R. P., Pietrzak, J. D., Horner-Devine, A. R., & Souza, A. J. (2018, aug). The Influence of Tide and Wind on the Propagation of Fronts in a Shallow River Plume. *Journal of Geophysical Research: Oceans*, *123*(8), 5426–5442. doi: 10.1029/2017JC013422

Rijnsburger, S., Flores, R. P., Pietrzak, J. D., Horner-Devine, A. R., Souza, A. J., Jones, N., & Lamb, K. (2019b). Observations of internal waves generated by a frictional river plume. (In preparation)

Rijnsburger, S., Flores, R. P., Pietrzak, J. D., Zijl, F., Horner-Devine, A. R., & Souza, A. J. (2019a). The evolution and interaction of multiple tidal plume fronts released into a strong tidal cross flow, the Rhine River plume. (In preparation)

Schijf, J., & Schönfled, J. (1953). *Theoretical considerations on the motion of salt and fresh water.* IAHR.

Simpson, J. H., Bos, W. G., Schirmer, F., Souza, A. J., Rippeth, T. P., Jones, S. E., & Hydes, D. (1993). Periodic stratification in the Rhine ROFI in the North Sea. *Oceanologica Acta*, *16*(1), 23–32.

Souza, A., & Simpson, J. (1996, jul). The modification of tidal ellipses by stratification in the Rhine ROFI. *Continental Shelf Research*, *16*(8), 997–1007. doi: 10.1016/0278-4343(95)00042-9

Souza, A. J., & Simpson, J. H. (1997, aug). Controls on stratification in the Rhine ROFI system. *Journal of Marine Systems*, *12*(1-4), 311–323. doi: 10.1016/S0924-7963(96)00105-4

Staquet, C., & Sommeria, J. (2002, jan). I NTERNAL G RAVITY W AVES : From Instabilities to Turbulence. *Annual Review of Fluid Mechanics*, *34*(1), 559–593. doi: 10.1146/annurev.fluid.34.090601.130953

Stastna, M., & Lamb, K. G. (2002, sep). Large fully nonlinear internal solitary waves: The effect of background current. *Physics of Fluids*, *14*(9), 2987–2999. doi: 10.1063/1.1496510

Sutherland, B. R. (2010). *Internal Gravity Waves*. Cambridge University Press.

Tisseur, F., & Meerbergen, K. (2001, jan). The Quadratic Eigenvalue Problem. *SIAM Review*, *43*(2), 235–286. doi: 10.1137/S0036144500381988

Visser, A., Souza, A., Hessner, K., & Simpson, J. (1994). The effect of stratification on tidal current profiles in a region of fresh-water influence. *Oceanologica Acta*, *17*(4), 369–381.

A

Combination between MSc Applied Mathematics and MSc Civil Engineering

This thesis is a combination between the thesis projects of MSc Applied Mathematics (WI5005) and MSc Civil Engineering (CIE5060-09). The total study load of this thesis is 60 ECTS. This is divided in a part for Applied Mathematics only (20 ECTS), a part specific for Civil Engineering (18 ECTS) and an overlap of 22 ECTS. This sums up to 42 ECTS for Applied Mathematics and 40 ECTS for Civil Engineering, which is the normal study load of the separate projects. Based on this division the chapters of this thesis have been divided to be part for a certain study or not. This is indicated at the bottom of each page inside the chapters and in table A.1 an overview is given.

As the chapters about the derivation and sensitivity of the variable bed KdV model (chapter 5, 6 and 9) have to do with the mathematical background of the problem, these chapters are for Applied Mathematics only. Deriving the KdV model and writing it down clearly was time consuming and has cost approximately a third of all time spent on the thesis. Chapters 4, 8 and 11 have to do with the specific dynamics of the Rhine ROFI: the Delft3D model and field data. To understand this field data the TGE fitting procedure has been developed; this can be found in chapter 7 (method) and 12 (results). Therefore these five chapters are part of the Civil Engineering project only. Modifying the Delft3D model and writing all Matlab scripts to process the Delft3D and field data into the final plots presented in this report has cost a lot of time. This has also cost approximately a third of all time spent. The chapters left are connecting the research parts from Applied Mathematics and Civil Engineering and are therefore part of both projects. In total the work executed on both sides matches the division of ECTS as mentioned earlier.

Chapter		MSc AM	MSc CE
1.	Introduction	x	x
2.	Background	x	x
3.	Introduction to the methods used	x	x
4.	Setup of the Delft3D model		x
5.	Derivation of the variable bed KdV model	x	
6.	Solutions to the variable bed KdV model	x	
7.	TGE fitting procedure		x
8.	Delft3D model results		x
9.	Sensitivity of the variable bed KdV model	x	
10.	Applicability of the KdV model in the Rhine ROFI	x	x
11.	Environmental variation of internal waves		x
12.	Results for observed wave events		x
14.	Conclusions and recommendations	x	x
13.	Discussion	x	x

Table A.1: Division of chapters between MSc Applied Mathematics (AM) and MSc Civil Engineering (CE).

B

KdV calculations

In this appendix the calculations corresponding to the derivation of the KdV equation in chapter 5 are given.

Calculation for the simplified continuity equation

The simplified continuity equation can be derived using equations (5.2) and (5.1). Start by expanding the derivative of (5.1)

$$\frac{\partial \rho}{\partial t} + \rho \frac{\partial u}{\partial x} + \rho \frac{\partial w}{\partial z} + u \frac{\partial \rho}{\partial x} + w \frac{\partial \rho}{\partial z} = 0, \tag{B.1}$$

using equation (5.2)

$$\Rightarrow \rho \frac{\partial u}{\partial x} + \rho \frac{\partial w}{\partial z} = 0, \tag{B.2}$$

and finally divide by ρ

$$\frac{\partial u}{\partial x} + \frac{\partial w}{\partial z} = 0. \tag{B.3}$$

Calculation for checking the density definition

In equation (5.54) the scaling of the density was defined. In this paragraph will be shown that this definition satisfies equation (5.2). Start by expanding the total derivative of ρ

$$\frac{d\rho}{dt} = \frac{\partial \rho}{\partial t} + u \frac{\partial \rho}{\partial x} + w \frac{\partial \rho}{\partial z}, \tag{B.4}$$

apply the density split of equation (5.13) to the variables

$$= \frac{\partial \rho_0(Z)}{\partial t} + u \frac{\partial \rho_0(Z)}{\partial x} + w \frac{\partial \rho_0(Z)}{\partial z}, \tag{B.5}$$

expanding the derivatives using the chain rule, where ρ_0' is the derivative of ρ_0

$$= \rho_0' \left[-\frac{\partial \zeta}{\partial t} - u \frac{\partial \zeta}{\partial x} + w \left(1 - \frac{\partial \zeta}{\partial z} \right) \right], \tag{B.6}$$

collecting terms for the total derivative

$$= \rho_0' \left[-\frac{d\zeta}{dt} + w \right], \tag{B.7}$$

and using equation (5.82)

$$= 0. \tag{B.8}$$

This shows that (5.2) is indeed satisfied with this choice for the density.

Calculation for the scaling

In section 5.1.1 transformations are given for internal waves and in 5.2 the non-dimensional scaling is given. These will be applied to the system of equations (5.3), (5.4) and (5.5) and the corresponding boundary conditions (5.6)-(5.8). Starting from equation (5.4), where the derivative from the pressure to $\hat{x}$ is being calculated and the transformation and scaling are carried out

$$\begin{aligned} \bar{\rho}(1+\sigma\hat{\rho}_0)\left[\frac{\sigma g h_0}{\lambda}\left(\frac{\partial \hat{U}}{\partial \hat{t}} + \frac{a}{h_0}\frac{\partial \hat{u}'}{\partial \hat{t}}\right)\right. \\ + \frac{\sigma g h_0}{\lambda}\left(\hat{U} + \frac{a}{h_0}\hat{u}'\right)\left(\frac{\partial \hat{U}}{\partial \hat{x}} + \frac{a}{h_0}\frac{\partial \hat{u}'}{\partial \hat{x}} + \frac{\lambda}{l}\frac{\partial \hat{U}}{\partial \hat{X}} + \frac{\lambda}{l}\frac{a}{h_0}\frac{\partial \hat{u}'}{\partial \hat{X}}\right) \\ \left. + \frac{\sigma g h_0}{\lambda}\left(\frac{\lambda}{l}\hat{W} + \frac{a}{h_0}\hat{w}'\right)\left(\frac{\partial \hat{U}}{\partial \hat{z}} + \frac{a}{h_0}\frac{\partial \hat{u}'}{\partial \hat{z}}\right)\right] = -\frac{ag\Delta\rho}{\lambda}\frac{\partial \hat{q}}{\partial \hat{x}} - \frac{ag\Delta\rho}{l}\frac{\partial \hat{q}}{\partial \hat{X}}, \end{aligned} \tag{B.9}$$

divide both sides by $\bar{\rho}\frac{\sigma g h_0}{\lambda}$

$$\begin{aligned} \Rightarrow (1+\sigma\hat{\rho}_0)\left[\left(\frac{\partial \hat{U}}{\partial \hat{t}} + \frac{a}{h_0}\frac{\partial \hat{u}'}{\partial \hat{t}}\right)\right. \\ + \left(\hat{U} + \frac{a}{h_0}\hat{u}'\right)\left(\frac{\partial \hat{U}}{\partial \hat{x}} + \frac{a}{h_0}\frac{\partial \hat{u}'}{\partial \hat{x}} + \frac{\lambda}{l}\frac{\partial \hat{U}}{\partial \hat{X}} + \frac{\lambda}{l}\frac{a}{h_0}\frac{\partial \hat{u}'}{\partial \hat{X}}\right) \\ \left. + \left(\frac{\lambda}{l}\hat{W} + \frac{a}{h_0}\hat{w}'\right)\left(\frac{\partial \hat{U}}{\partial \hat{z}} + \frac{a}{h_0}\frac{\partial \hat{u}'}{\partial \hat{z}}\right)\right] + \frac{a}{h_0}\frac{\partial \hat{q}}{\partial \hat{x}} + \frac{a}{h_0}\frac{\lambda}{l}\frac{\partial \hat{q}}{\partial \hat{X}} = 0. \end{aligned} \tag{B.10}$$

Next, investigate the vertical momentum equation (5.5), where also the derivative from the pressure to $\hat{z}$ is being calculated and the transformation and scaling are performed

$$\begin{aligned} \bar{\rho}(1+\sigma\hat{\rho}_0)\left[\sigma g\frac{h_0^2}{\lambda^2}\left(\frac{\lambda}{l}\frac{\partial \hat{W}}{\partial \hat{t}} + \frac{a}{h_0}\frac{\partial \hat{w}'}{\partial \hat{t}}\right)\right. \\ + \sigma g\frac{h_0^2}{\lambda^2}\left(\hat{U} + \frac{a}{h_0}\hat{u}'\right)\left(\frac{\lambda}{l}\frac{\partial \hat{W}}{\partial \hat{x}} + \frac{a}{h_0}\frac{\partial \hat{w}'}{\partial \hat{x}} + \left(\frac{\lambda}{l}\right)^2\frac{\partial \hat{W}}{\partial \hat{X}} + \frac{\lambda}{l}\frac{a}{h_0}\frac{\partial \hat{w}'}{\partial \hat{X}}\right) \\ \left. + \sigma g\frac{h_0^2}{\lambda^2}\left(\frac{\lambda}{l}\hat{W} + \frac{a}{h_0}\hat{w}'\right)\left(\frac{\lambda}{l}\frac{\partial \hat{W}}{\partial \hat{z}} + \frac{a}{h_0}\frac{\partial \hat{w}'}{\partial \hat{z}}\right)\right] = \bar{\rho}g + \bar{\rho}\sigma g\hat{\rho}_0(\hat{z}) - \Delta\rho g\frac{a}{h_0}\frac{\partial \hat{q}}{\partial \hat{z}} \\ - g\bar{\rho}(1+\sigma\hat{\rho}_0(\hat{Z})), \end{aligned} \tag{B.11}$$

divide the equation by $\bar{\rho}\sigma g$

$$\begin{aligned} \Rightarrow \frac{h_0^2}{\lambda^2}(1+\sigma\hat{\rho}_0)\left[\left(\frac{\lambda}{l}\frac{\partial \hat{W}}{\partial \hat{t}} + \frac{a}{h_0}\frac{\partial \hat{w}'}{\partial \hat{t}}\right)\right. \\ + \left(\hat{U} + \frac{a}{h_0}\hat{u}'\right)\left(\frac{\lambda}{l}\frac{\partial \hat{W}}{\partial \hat{x}} + \frac{a}{h_0}\frac{\partial \hat{w}'}{\partial \hat{x}} + \left(\frac{\lambda}{l}\right)^2\frac{\partial \hat{W}}{\partial \hat{X}} + \frac{\lambda}{l}\frac{a}{h_0}\frac{\partial \hat{w}'}{\partial \hat{X}}\right) \\ \left. + \left(\frac{\lambda}{l}\hat{W} + \frac{a}{h_0}\hat{w}'\right)\left(\frac{\lambda}{l}\frac{\partial \hat{W}}{\partial \hat{z}} + \frac{a}{h_0}\frac{\partial \hat{w}'}{\partial \hat{z}}\right)\right] + \frac{a}{h_0}\frac{\partial \hat{q}}{\partial \hat{z}} - \hat{\rho}_0(\hat{z}) + \hat{\rho}_0(\hat{Z}) = 0. \end{aligned} \tag{B.12}$$

Now take the continuity equation (5.3)

$$\frac{\sqrt{\sigma g h_0}}{\lambda}\left(\frac{\partial \hat{U}}{\partial \hat{x}}+\frac{a}{h_0}\frac{\partial \hat{u}'}{\partial \hat{x}}+\frac{\lambda}{l}\frac{\partial \hat{U}}{\partial \hat{X}}+\frac{\lambda}{l}\frac{a}{h_0}\frac{\partial \hat{u}'}{\partial \hat{X}}\right)+\frac{\sqrt{\sigma g h_0}}{h_0}\frac{h_0}{\lambda}\left(\frac{\lambda}{l}\frac{\partial \hat{W}}{\partial \hat{z}}+\frac{a}{h_0}\frac{\partial \hat{w}'}{\partial \hat{z}}\right)=0, \tag{B.13}$$

and divide by $\frac{\sqrt{\sigma g h_0}}{\lambda}$

$$\Rightarrow\left(\frac{\partial \hat{U}}{\partial \hat{x}}+\frac{a}{h_0}\frac{\partial \hat{u}'}{\partial \hat{x}}+\frac{\lambda}{l}\frac{\partial \hat{U}}{\partial \hat{X}}+\frac{\lambda}{l}\frac{a}{h_0}\frac{\partial \hat{u}'}{\partial \hat{X}}\right)+\frac{\lambda}{l}\frac{\partial \hat{W}}{\partial \hat{z}}+\frac{a}{h_0}\frac{\partial \hat{w}'}{\partial \hat{z}}=0. \tag{B.14}$$

The boundary conditions also need to be transformed, the first one (5.8)

$$\sqrt{\sigma g h_0}\frac{h_0}{\lambda}\left(\frac{\lambda}{l}\hat{W}+\frac{a}{h_0}\hat{w}'\right)=-\sqrt{\sigma g h_0}\frac{h_1}{\lambda}\frac{\lambda}{l}\left(\hat{U}+\frac{a}{h_0}\hat{u}'\right)\frac{\partial \hat{h}'}{\partial \hat{X}}\bigg|_{h_0\hat{z}=-h_0-h_1\hat{h}'}, \tag{B.15}$$

divide this by $\sqrt{\sigma g h_0}\frac{h_0}{\lambda}$

$$\Rightarrow\left(\frac{\lambda}{l}\hat{W}+\frac{a}{h_0}\hat{w}'\right)=-\frac{h_1}{h_0}\frac{\lambda}{l}\left(\hat{U}+\frac{a}{h_0}\hat{u}'\right)\frac{\partial \hat{h}'}{\partial \hat{X}}\bigg|_{\hat{z}=-1-\frac{h_1}{h_0}\hat{h}'}. \tag{B.16}$$

The condition for the pressure at the free surface (5.7) reads

$$-\bar{\rho}g h_0\hat{z}+\bar{\rho}\sigma g h_0\int_{\hat{z}}^{0}\hat{\rho}_0(z')dz'+agA\rho\hat{q}=0|_{h_0\hat{z}=a\hat{\xi}}, \tag{B.17}$$

enter the value of the vertical position

$$\Rightarrow\bar{\rho}g h_0\frac{a}{h_0}\hat{\xi}-\bar{\rho}\sigma g h_0\int_{\frac{a}{h_0}\hat{\xi}}^{0}\hat{\rho}_0(z')dz'=agA\rho\hat{q}|_{\hat{z}=\frac{a}{h_0}\hat{\xi}}, \tag{B.18}$$

divide by $\bar{\rho}g h_0$

$$\Rightarrow\frac{a}{h_0}\hat{\xi}-\sigma\int_{\frac{a}{h_0}\hat{\xi}}^{0}\hat{\rho}_0(z')dz'=\frac{a}{h_0}\sigma\hat{q}\bigg|_{\hat{z}=\frac{a}{h_0}\hat{\xi}}. \tag{B.19}$$

Finally consider the free surface condition (5.6)

$$\sqrt{\sigma g h_0}\frac{h_0}{\lambda}\left(\frac{\lambda}{l}\hat{W}+\frac{a}{h_0}\hat{w}'\right)=\sqrt{\sigma g h_0}\frac{a}{\lambda}\frac{\partial \hat{\xi}}{\partial \hat{t}}+\frac{\sqrt{\sigma g h_0}}{\lambda}\left(\hat{U}+\frac{a}{h_0}\hat{u}'\right)\left(a\frac{\partial \hat{\xi}}{\partial \hat{x}}+a\frac{\lambda}{l}\frac{\partial \hat{\xi}}{\partial \hat{X}}\right)\bigg|_{h_0\hat{z}=a\hat{\xi}}, \tag{B.20}$$

divide by $\sqrt{\sigma g h_0}\frac{h_0}{\lambda}$

$$\Rightarrow\frac{\lambda}{l}\hat{W}+\frac{a}{h_0}\hat{w}'=\frac{a}{h_0}\frac{\partial \hat{\xi}}{\partial \hat{t}}+\left(\hat{U}+\frac{a}{h_0}\hat{u}'\right)\left(\frac{a}{h_0}\frac{\partial \hat{\xi}}{\partial \hat{x}}+\frac{a}{h_0}\frac{\lambda}{l}\frac{\partial \hat{\xi}}{\partial \hat{X}}\right)\bigg|_{\hat{z}=\frac{a}{h_0}\hat{\xi}}. \tag{B.21}$$

Analysis of the scaling parameters, shows that four small parameters are found in the derived equations above. The definition of these parameters ε, δ, μ and γ are stated in (5.60)-(5.63). If these are substituted in the equations, the set of equations in (5.64)-(5.69) is obtained.

Calculation for relating ε and δ

The transformation described in equations (5.70)-(5.74), can be applied to the system of equations. This transformation removes δ from the equations, such that only one small wave variable is left ε. For equation (5.64) this yields to

$$(1+\sigma\rho_0^*)\left[\frac{\sqrt{\varepsilon}}{\delta}\left(\frac{\partial U^*}{\partial t^*}+\varepsilon\frac{\partial u'^*}{\partial t^*}\right)+\frac{\sqrt{\varepsilon}}{\delta}(U^*+\varepsilon u'^*)\left(\frac{\partial U^*}{\partial x^*}+\varepsilon\frac{\partial u'^*}{\partial x^*}+\mu\frac{\partial U^*}{\partial X^*}+\mu\varepsilon\frac{\partial u'^*}{\partial X^*}\right)\right.$$
$$\left.+\frac{\sqrt{\varepsilon}}{\delta}(\mu W^*+\varepsilon w'^*)\left(\frac{\partial U^*}{\partial z^*}+\varepsilon\frac{\partial u'^*}{\partial z^*}\right)\right]+\frac{\sqrt{\varepsilon}}{\delta}\left(\varepsilon\frac{\partial q^*}{\partial x^*}+\varepsilon\mu\frac{\partial q^*}{\partial X^*}\right)=0, \tag{B.22}$$

divide both sides by $\frac{\sqrt{\varepsilon}}{\delta}$

$$\Rightarrow(1+\sigma\rho_0^*)\left[\left(\frac{\partial U^*}{\partial \hat{t}}+\varepsilon\frac{\partial u'^*}{\partial t^*}\right)+(U^*+\varepsilon u'^*)\left(\frac{\partial U^*}{\partial x^*}+\varepsilon\frac{\partial u^*}{\partial x^*}+\mu\frac{\partial U^*}{\partial X^*}+\mu\varepsilon\frac{\partial u'^*}{\partial X^*}\right)\right.$$
$$\left.+(\mu W^*+\varepsilon w'^*)\left(\frac{\partial U^*}{\partial z^*}+\varepsilon\frac{\partial u'^*}{\partial z^*}\right)\right]+\varepsilon\frac{\partial q^*}{\partial x^*}+\varepsilon\mu\frac{\partial q^*}{\partial X^*}=0. \tag{B.23}$$

(B.24)

Investigate the vertical momentum equation (5.65)

$$\delta^2(1+\sigma\rho_0^*)\left[\left(\frac{\sqrt{\varepsilon}}{\delta}\right)^2\left(\mu\frac{\partial W^*}{\partial t^*}+\varepsilon\frac{\partial w'^*}{\partial t^*}\right)+(U^*+\varepsilon u'^*)\left(\frac{\sqrt{\varepsilon}}{\delta}\right)^2\left(\mu\frac{\partial W^*}{\partial x^*}+\varepsilon\frac{\partial w'^*}{\partial x^*}+\mu^2\frac{\partial W^*}{\partial X^*}+\varepsilon\mu\frac{\partial w'^*}{\partial X^*}\right)\right.$$
$$\left.+\varepsilon\left(\frac{\sqrt{\varepsilon}}{\delta}\right)^2(\mu W^*+\varepsilon w'^*)\left(\mu\frac{\partial W^*}{\partial z^*}+\varepsilon\frac{\partial w'^*}{\partial z^*}\right)\right]+\varepsilon\frac{\partial q^*}{\partial z^*}-\rho_0^*(z^*)+\rho_0^*(y^*)=0, \tag{B.25}$$

recalculate the appearance of ε and δ in the equation

$$\Rightarrow\varepsilon(1+\sigma\rho_0^*)\left[\left(\mu\frac{\partial W^*}{\partial t^*}+\varepsilon\frac{\partial w'^*}{\partial t^*}\right)+(U^*+\varepsilon u'^*)\left(\mu\frac{\partial W^*}{\partial x^*}+\varepsilon\frac{\partial w'^*}{\partial x^*}+\mu^2\frac{\partial W^*}{\partial X^*}+\varepsilon\mu\frac{\partial w'^*}{\partial X^*}\right)\right.$$
$$\left.+(\mu W^*+\varepsilon w'^*)\left(\mu\frac{\partial W^*}{\partial z^*}+\varepsilon\frac{\partial w'^*}{\partial z^*}\right)\right]+\varepsilon\frac{\partial q^*}{\partial z^*}-\rho_0^*(z^*)+\rho_0^*(Z^*)=0. \tag{B.26}$$

Consider equation (5.66)

$$\frac{\sqrt{\varepsilon}}{\delta}\left(\frac{\partial U^*}{\partial x^*}+\varepsilon\frac{\partial u'^*}{\partial x^*}+\mu\frac{\partial U^*}{\partial X^*}+\varepsilon\mu\frac{\partial u'^*}{\partial X^*}\right)+\frac{\sqrt{\varepsilon}}{\delta}\left(\mu\frac{\partial W^*}{\partial z^*}+\varepsilon\frac{\partial w'^*}{\partial z^*}\right)=0, \tag{B.27}$$

divide by $\frac{\sqrt{\varepsilon}}{\delta}$

$$\Rightarrow\left(\frac{\partial U^*}{\partial x^*}+\varepsilon\frac{\partial u'^*}{\partial x^*}+\mu\frac{\partial U^*}{\partial X^*}+\varepsilon\mu\frac{\partial u'^*}{\partial X^*}\right)+\mu\frac{\partial W^*}{\partial z^*}+\varepsilon\frac{\partial w'^*}{\partial z^*}=0. \tag{B.28}$$

The bottom boundary condition (5.67) results into

$$-\gamma\mu\frac{\sqrt{\varepsilon}}{\delta}(U^*+\varepsilon u'^*)\frac{\partial h'^*}{\partial X^*}=\frac{\sqrt{\varepsilon}}{\delta}(\mu W^*+\varepsilon w'^*)\Big|_{\hat{z}=-1-\gamma\hat{h}'}, \tag{B.29}$$

which also will be divide by: $\frac{\sqrt{\varepsilon}}{\delta}$

$$\Rightarrow-\gamma\mu(U^*+\varepsilon u'^*)\frac{\partial h'^*}{\partial X^*}=\mu W^*+\varepsilon w'^*|_{z^*=-1-\gamma h'^*}. \tag{B.30}$$

The pressure boundary condition is equal to

$$\varepsilon\xi^* - \sigma\int_{\varepsilon\xi^*}^{0}\rho_0^*(z')dz' = \varepsilon\sigma q^*|_{z^*=\varepsilon\xi^*}. \tag{B.31}$$

Finally the free surface boundary condition (5.69) is equal to

$$\frac{\sqrt{\varepsilon}}{\delta}\varepsilon\frac{\partial\xi^*}{\partial t^*} + (U^* + \varepsilon u'^*)\frac{\sqrt{\varepsilon}}{\delta}\left(\varepsilon\frac{\partial\xi^*}{\partial x^*} + \varepsilon\mu\frac{\partial\xi^*}{\partial X^*}\right) = \frac{\sqrt{\varepsilon}}{\delta}(\mu W^* + \varepsilon w'^*)\Big|_{z^*=\varepsilon\xi^*} \tag{B.32}$$

divde by: $\frac{\sqrt{\varepsilon}}{\delta}$

$$\Rightarrow \varepsilon\frac{\partial\xi^*}{\partial t^*} + (U^* + \varepsilon u'^*)\left(\varepsilon\frac{\partial\xi^*}{\partial x^*} + \varepsilon\mu\frac{\partial\xi^*}{\partial X^*}\right) = \mu W^* + \varepsilon w'^*|_{z^*=\varepsilon\xi^*}. \tag{B.33}$$

Calculation for the transformation to isopycnal coordinates

A transformation is made to isopycnal coordinates. This means that all equations needs to be moved from the $((x, X, z, t)$ to the $(\tilde{x}, \tilde{X}, \tilde{Z}, \tilde{t})$ reference frame. The transformation is given by

$$x = \tilde{x}, \tag{B.34}$$
$$X = \tilde{X}, \tag{B.35}$$
$$z - \varepsilon\zeta(x, z, t) = \tilde{Z}, \tag{B.36}$$
$$t = \tilde{t}. \tag{B.37}$$

Now all functions need to be mapped. In particular all derivatives should be checked.

Consider a arbitrary function f which will be mapped: $f(x, X, z, t) = F(\tilde{x}, \tilde{X}, \tilde{Z}, \tilde{t}) = F(x, X, z-\varepsilon\zeta(x, X, z, t), t)$. Start with the derivative to x

$$\frac{\partial f}{\partial x} = \frac{\partial F}{\partial\tilde{x}}\frac{\partial\tilde{x}}{\partial x} + \frac{\partial F}{\partial\tilde{X}}\frac{\partial\tilde{X}}{\partial x} + \frac{\partial F}{\partial\tilde{Z}}\frac{\partial\tilde{Z}}{\partial x} + \frac{\partial F}{\partial\tilde{t}}\frac{\partial\tilde{t}}{\partial x}, \tag{B.38}$$

using the definition of $\tilde{Z}$

$$= \frac{\partial F}{\partial\tilde{x}} - \varepsilon\frac{\partial F}{\partial\tilde{Z}}\frac{\partial\zeta}{\partial\tilde{x}}. \tag{B.39}$$

Consider the derivative to X

$$\frac{\partial f}{\partial X} = \frac{\partial F}{\partial\tilde{x}}\frac{\partial\tilde{x}}{\partial X} + \frac{\partial F}{\partial\tilde{X}}\frac{\partial\tilde{X}}{\partial X} + \frac{\partial F}{\partial\tilde{Z}}\frac{\partial\tilde{Z}}{\partial X} + \frac{\partial F}{\partial\tilde{t}}\frac{\partial\tilde{t}}{\partial X}, \tag{B.40}$$

using the definition of $\tilde{Z}$

$$= \frac{\partial F}{\partial\tilde{X}} - \varepsilon\frac{\partial F}{\partial\tilde{Z}}\frac{\partial\zeta}{\partial X}. \tag{B.41}$$

Consider the derivative to z

$$\frac{\partial f}{\partial z} = \frac{\partial F}{\partial\tilde{x}}\frac{\partial\tilde{x}}{\partial z} + \frac{\partial F}{\partial\tilde{X}}\frac{\partial\tilde{X}}{\partial z} + \frac{\partial F}{\partial\tilde{Z}}\frac{\partial\tilde{Z}}{\partial z} + \frac{\partial F}{\partial\tilde{t}}\frac{\partial\tilde{t}}{\partial z}, \tag{B.42}$$

also use the definition of $\tilde{Z}$

$$= \frac{\partial F}{\partial\tilde{Z}}\left(1 - \varepsilon\frac{\partial\zeta}{\partial z}\right). \tag{B.43}$$

Consider the derivative to t,

$$\frac{\partial f}{\partial t} = \frac{\partial F}{\partial \tilde{x}}\frac{\partial \tilde{x}}{\partial t} + \frac{\partial F}{\partial \tilde{X}}\frac{\partial \tilde{X}}{\partial t} + \frac{\partial F}{\partial \tilde{Z}}\frac{\partial \tilde{Z}}{\partial t} + \frac{\partial F}{\partial \tilde{t}}\frac{\partial \tilde{t}}{\partial t}, \tag{B.44}$$

using the definition of $\tilde{Z}$

$$= \frac{\partial F}{\partial \tilde{t}} - \varepsilon\frac{\partial F}{\partial \tilde{Z}}\frac{\partial \zeta}{\partial t}. \tag{B.45}$$

Finally the total derivative is checked, note that f is in the original framework and the total velocity $U + \varepsilon u'$ should be used

$$\frac{df}{dt} = \frac{\partial f}{\partial t} + (U + \varepsilon u')\left(\frac{\partial f}{\partial x} + \mu\frac{\partial f}{\partial X}\right) + (\mu W + \varepsilon w')\frac{\partial f}{\partial z}, \tag{B.46}$$

substitute the previous results

$$\begin{aligned} &= \frac{\partial F}{\partial \tilde{t}} - \varepsilon\frac{\partial F}{\partial \tilde{Z}}\frac{\partial \zeta}{\partial t} + (U + \varepsilon u')\left(\frac{\partial F}{\partial \tilde{x}} - \varepsilon\frac{\partial F}{\partial \tilde{Z}}\frac{\partial \zeta}{\partial x} + \mu\frac{\partial F}{\partial \tilde{X}} - \mu\varepsilon\frac{\partial F}{\partial \tilde{Z}}\frac{\partial \zeta}{\partial X}\right) \\ &+ (\mu W + \varepsilon w')\frac{\partial F}{\partial \tilde{Z}}\left(1 - \varepsilon\frac{\partial \zeta}{\partial z}\right), \end{aligned} \tag{B.47}$$

collecting the terms for $\frac{\partial F}{\partial \tilde{Z}}$

$$\begin{aligned} &= \frac{\partial F}{\partial \tilde{t}} + (U + \varepsilon u')\left(\frac{\partial F}{\partial \tilde{x}} + \mu\frac{\partial F}{\partial \tilde{X}}\right) \\ &+ \frac{\partial F}{\partial \tilde{Z}}\left(\mu W + \varepsilon w' - \varepsilon\frac{\partial \zeta}{\partial t} - \varepsilon(U + \varepsilon u')\left(\frac{\partial \zeta}{\partial x} + \mu\frac{\partial \zeta}{\partial X}\right) - \varepsilon(\mu W + \varepsilon w')\frac{\partial \zeta}{\partial z}\right), \end{aligned} \tag{B.48}$$

finally using equation (5.82)

$$= \frac{\partial F}{\partial \tilde{t}} + (U + \varepsilon u')\left(\frac{\partial F}{\partial \tilde{x}} + \mu\frac{\partial F}{\partial \tilde{X}}\right). \tag{B.49}$$

Now define the displacement in the new coordinate system by: $\zeta(x, z, t) = \tilde{\eta}(\tilde{x}, \tilde{Z}, \tilde{t})$ and therefore will be obtained, from (B.39)

$$\frac{\partial \zeta}{\partial x} = \frac{\partial \tilde{\eta}}{\partial \tilde{x}} - \varepsilon\frac{\partial \tilde{\eta}}{\partial \tilde{Z}}\frac{\partial \zeta}{\partial x}, \tag{B.50}$$

rewriting the expression for $\frac{\partial \zeta}{\partial x}$

$$\Rightarrow \frac{\partial \zeta}{\partial x} = \frac{\frac{\partial \tilde{\eta}}{\partial \tilde{x}}}{1 + \varepsilon\frac{\partial \tilde{\eta}}{\partial \tilde{Z}}}. \tag{B.51}$$

For the derivative to X, using (B.41)

$$\frac{\partial \zeta}{\partial X} = \frac{\partial \tilde{\eta}}{\partial \tilde{X}} - \varepsilon\frac{\partial \tilde{\eta}}{\partial \tilde{Z}}\frac{\partial \zeta}{\partial X} \tag{B.52}$$

rewriting the equation in terms of $\frac{\partial \zeta}{\partial X}$

$$\Rightarrow \frac{\partial \zeta}{\partial X} = \frac{\frac{\partial \tilde{\eta}}{\partial \tilde{X}}}{1 + \varepsilon\frac{\partial \eta}{\partial \tilde{Z}}} \tag{B.53}$$

For the derivative to z, using (B.43)

$$\frac{\partial \zeta}{\partial z} = \frac{\partial \tilde{\eta}}{\partial \tilde{Z}}\left(1 - \varepsilon \frac{\partial \zeta}{\partial z}\right), \tag{B.54}$$

rewriting the expression for $\frac{\partial \zeta}{\partial z}$

$$\Rightarrow \frac{\partial \zeta}{\partial z} = \frac{\frac{\partial \tilde{\eta}}{\partial \tilde{Z}}}{1 + \varepsilon \frac{\partial \tilde{\eta}}{\partial \tilde{Z}}}, \tag{B.55}$$

and for the derivative to t, using (B.45)

$$\frac{\partial \zeta}{\partial t} = \frac{\partial \tilde{\eta}}{\partial \tilde{t}} - \varepsilon \frac{\partial \tilde{\eta}}{\partial \tilde{Z}} \frac{\partial \zeta}{\partial t}, \tag{B.56}$$

finally rewriting the expression for $\frac{\partial \zeta}{\partial t}$

$$\Rightarrow \frac{\partial \zeta}{\partial t} = \frac{\frac{\partial \tilde{\eta}}{\partial \tilde{t}}}{1 + \varepsilon \frac{\partial \tilde{\eta}}{\partial \tilde{Z}}}. \tag{B.57}$$

This transformation may now be applied to the system of equations. Starting from equation (5.75):

$$\begin{aligned}(1 + \sigma\tilde{\rho}_0)\left[\left(\frac{\partial \tilde{U}}{\partial \tilde{t}} - \varepsilon \frac{\partial \tilde{U}}{\partial \tilde{Z}} \frac{\partial \zeta}{\partial t} + \varepsilon \frac{\partial \tilde{u}'}{\partial \tilde{t}} - \varepsilon^2 \frac{\partial \tilde{u}'}{\partial \tilde{Z}} \frac{\partial \zeta}{\partial t}\right)\right. \\ + (\tilde{U} + \varepsilon \tilde{u}')\left(\frac{\partial \tilde{U}}{\partial \tilde{x}} - \varepsilon \frac{\partial \tilde{U}}{\partial \tilde{Z}} \frac{\partial \zeta}{\partial x} + \varepsilon \frac{\partial \tilde{u}'}{\partial \tilde{x}} - \varepsilon^2 \frac{\partial \tilde{u}'}{\partial \tilde{Z}} \frac{\partial \zeta}{\partial x} + \mu \frac{\partial \tilde{U}}{\partial \tilde{X}} - \mu\varepsilon \frac{\partial \tilde{U}}{\partial \tilde{Z}} \frac{\partial \zeta}{\partial X} + \mu\varepsilon \frac{\partial \tilde{u}'}{\partial \tilde{X}} - \mu\varepsilon^2 \frac{\partial \tilde{u}'}{\partial \tilde{Z}} \frac{\partial \zeta}{\partial X}\right) \\ \left. + (\mu \tilde{W} + \varepsilon \tilde{w}')\left(\frac{\partial \tilde{U}}{\partial \tilde{Z}} + \varepsilon \frac{\partial \tilde{u}'}{\partial \tilde{Z}}\right)\left(1 - \varepsilon \frac{\partial \zeta}{\partial z}\right)\right] + \varepsilon \frac{\partial \tilde{q}}{\partial \tilde{x}} - \varepsilon^2 \frac{\partial \tilde{q}}{\partial \tilde{Z}} \frac{\partial \zeta}{\partial x} + \varepsilon\mu \frac{\partial \tilde{q}}{\partial \tilde{X}} - \varepsilon^2 \mu \frac{\partial \tilde{q}}{\partial \tilde{Z}} \frac{\partial \zeta}{\partial X} = 0,\end{aligned} \tag{B.58}$$

collecting terms to $\frac{\partial \tilde{U}}{\partial \tilde{Z}} + \varepsilon \frac{\partial \tilde{u}'}{\partial \tilde{Z}}$ and using equation (B.51) and (B.53) results in

$$\begin{aligned}\Rightarrow (1 + \sigma\tilde{\rho}_0)\left[\frac{\partial \tilde{U}}{\partial \tilde{t}} + \varepsilon \frac{\partial \tilde{u}'}{\partial \tilde{t}} + (\tilde{U} + \varepsilon \tilde{u}')\left(\frac{\partial \tilde{U}}{\partial \tilde{x}} + \varepsilon \frac{\partial \tilde{u}'}{\partial \tilde{x}} + \mu \frac{\partial \tilde{U}}{\partial \tilde{X}} + \mu\varepsilon \frac{\partial \tilde{u}'}{\partial \tilde{X}}\right)\right. \\ + \left(\frac{\partial \tilde{U}}{\partial \tilde{Z}} + \varepsilon \frac{\partial \tilde{u}'}{\partial \tilde{Z}}\right)\left(\mu \tilde{W} + \varepsilon \tilde{w}' - \varepsilon \frac{\partial \zeta}{\partial t} - \varepsilon(\tilde{U} + \varepsilon \tilde{u}')\left(\frac{\partial \zeta}{\partial x} + \mu \frac{\partial \zeta}{\partial X}\right) - \varepsilon(\mu \tilde{W} + \varepsilon \tilde{w}')\frac{\partial \zeta}{\partial z}\right)\Bigg] \\ + \varepsilon \frac{\partial \tilde{q}}{\partial \tilde{x}} - \varepsilon^2 \frac{\partial \tilde{q}}{\partial \tilde{Z}} \frac{\frac{\partial \tilde{\eta}}{\partial \tilde{x}}}{1 + \varepsilon \frac{\partial \tilde{\eta}}{\partial \tilde{Z}}} + \varepsilon\mu \frac{\partial \tilde{q}}{\partial \tilde{X}} - \varepsilon^2 \mu \frac{\partial \tilde{q}}{\partial \tilde{Z}} \frac{\frac{\partial \tilde{\eta}}{\partial \tilde{X}}}{1 + \varepsilon \frac{\partial \tilde{\eta}}{\partial \tilde{Z}}} = 0,\end{aligned} \tag{B.59}$$

using equation (5.82)

$$\begin{aligned}\Rightarrow (1 + \sigma\tilde{\rho}_0)\left[\frac{\partial \tilde{U}}{\partial \tilde{t}} + \varepsilon \frac{\partial \tilde{u}'}{\partial \tilde{t}} + (\tilde{U} + \varepsilon \tilde{u}')\left(\frac{\partial \tilde{U}}{\partial \tilde{x}} + \varepsilon \frac{\partial \tilde{u}'}{\partial \tilde{x}} + \mu \frac{\partial \tilde{U}}{\partial \tilde{X}} + \mu\varepsilon \frac{\partial \tilde{u}'}{\partial \tilde{X}}\right)\right] \\ + \varepsilon \frac{\partial \tilde{q}}{\partial \tilde{x}} - \varepsilon^2 \frac{\partial \tilde{q}}{\partial \tilde{Z}} \frac{\frac{\partial \tilde{\eta}}{\partial \tilde{x}}}{1 + \varepsilon \frac{\partial \tilde{\eta}}{\partial \hat{z}}} + \varepsilon\mu \frac{\partial \tilde{q}}{\partial \tilde{X}} - \varepsilon^2 \mu \frac{\partial \tilde{q}}{\partial \tilde{Z}} \frac{\frac{\partial \tilde{\eta}}{\partial \tilde{X}}}{1 + \varepsilon \frac{\partial \tilde{\eta}}{\partial \tilde{Z}}} = 0.\end{aligned} \tag{B.60}$$

note that $\tilde{U}$ is not a function of $\tilde{t}$ and so $\frac{\partial \tilde{U}}{\partial \tilde{t}}$ will equal zero

$$\Rightarrow (1+\sigma\tilde{\rho}_0)\left[\varepsilon\frac{\partial\tilde{u}'}{\partial\tilde{t}}+(\tilde{U}+\varepsilon\tilde{u}')\left(\frac{\partial\tilde{U}}{\partial\tilde{x}}+\varepsilon\frac{\partial\tilde{u}'}{\partial\tilde{x}}+\mu\frac{\partial\tilde{U}}{\partial\tilde{X}}+\mu\varepsilon\frac{\partial\tilde{u}'}{\partial\tilde{X}}\right)\right] +\varepsilon\left(\frac{\partial\tilde{q}}{\partial\tilde{x}}+\mu\frac{\partial\tilde{q}}{\partial\tilde{X}}\right)-\varepsilon^2\frac{\partial\tilde{q}}{\partial\tilde{Z}}\frac{\frac{\partial\tilde{\eta}}{\partial\tilde{x}}+\mu\frac{\partial\tilde{\eta}}{\partial\tilde{X}}}{1+\varepsilon\frac{\partial\tilde{\eta}}{\partial\tilde{z}}}=0. \tag{B.61}$$

Now the transformation will be applied to equation (5.76)

$$\begin{aligned}&\varepsilon(1+\sigma\tilde{\rho}_0)\left[\mu\frac{\partial\tilde{W}}{\partial\tilde{t}}-\varepsilon\mu\frac{\partial\tilde{W}}{\partial\tilde{Z}}\frac{\partial\zeta}{\partial t}+\varepsilon\frac{\partial\tilde{w}'}{\partial\tilde{t}}-\varepsilon^2\frac{\partial\tilde{w}'}{\partial\tilde{Z}}\frac{\partial\zeta}{\partial t}\right.\\ &+(\tilde{U}+\varepsilon\tilde{u}')\left(\mu\frac{\partial\tilde{W}}{\partial\tilde{x}}-\varepsilon\mu\frac{\partial\tilde{W}}{\partial\tilde{Z}}\frac{\partial\zeta}{\partial x}+\varepsilon\frac{\partial\tilde{w}'}{\partial\tilde{x}}-\varepsilon^2\frac{\partial\tilde{w}'}{\partial\tilde{Z}}\frac{\partial\zeta}{\partial x}+\mu^2\frac{\partial\tilde{W}}{\partial\tilde{X}}-\varepsilon\mu^2\frac{\partial\tilde{W}}{\partial\tilde{Z}}\frac{\partial\zeta}{\partial X}+\varepsilon\mu\frac{\partial\tilde{w}'}{\partial\tilde{X}}-\varepsilon^2\mu\frac{\partial\tilde{w}'}{\partial\tilde{Z}}\frac{\partial\zeta}{\partial X}\right)\\ &\left.+(\mu\tilde{W}+\varepsilon\tilde{w}')\left(\mu\frac{\partial\tilde{W}}{\partial\tilde{Z}}+\varepsilon\frac{\partial\tilde{w}'}{\partial\tilde{Z}}\right)\left(1-\varepsilon\frac{\partial\zeta}{\partial z}\right)\right]+\varepsilon\frac{\partial\tilde{q}}{\partial\tilde{Z}}\left(1-\varepsilon\frac{\partial\zeta}{\partial z}\right)+\tilde{\rho}_0(\tilde{Z})-\tilde{\rho}_0(\tilde{Z}+\varepsilon\tilde{\eta})=0,\end{aligned} \tag{B.62}$$

collect the terms of $\mu\frac{\partial\tilde{W}}{\partial\tilde{Z}}+\varepsilon\frac{\partial\tilde{w}'}{\partial\tilde{Z}}$ and use equation (B.55)

$$\begin{aligned}&\Rightarrow\varepsilon(1+\sigma\tilde{\rho}_0)\left[\mu\frac{\partial\tilde{W}}{\partial\tilde{t}}+\varepsilon\frac{\partial\tilde{w}'}{\partial\tilde{t}}+(\tilde{U}+\varepsilon\tilde{u}')\left(\mu\frac{\partial\tilde{W}}{\partial\tilde{x}}+\varepsilon\frac{\partial\tilde{w}'}{\partial\tilde{x}}+\mu^2\frac{\partial\tilde{W}}{\partial\tilde{X}}+\varepsilon\mu\frac{\partial\tilde{w}'}{\partial\tilde{X}}\right)\right.\\ &\left.+\left(\mu\frac{\partial\tilde{W}}{\partial\tilde{Z}}+\varepsilon\frac{\partial\tilde{w}'}{\partial\tilde{Z}}\right)\left(\mu\tilde{W}+\varepsilon\tilde{w}'-\varepsilon\frac{\partial\zeta}{\partial t}-\varepsilon(\tilde{U}+\varepsilon\tilde{u}')\left(\frac{\partial\zeta}{\partial x}+\mu\frac{\partial\zeta}{\partial X}\right)-\varepsilon(\mu\tilde{W}+\varepsilon\tilde{w}')\frac{\partial\zeta}{\partial z}\right)\right]\\ &+\varepsilon\frac{\partial\tilde{q}}{\partial\tilde{Z}}\left(1-\frac{\varepsilon\frac{\partial\tilde{\eta}}{\partial\tilde{Z}}}{1+\varepsilon\frac{\partial\tilde{\eta}}{\partial\tilde{z}}}\right)+\tilde{\rho}_0(\tilde{Z})-\tilde{\rho}_0(\tilde{Z}+\varepsilon\tilde{\eta})=0,\end{aligned} \tag{B.63}$$

following equation (5.82) the second line of the equation can be removed

$$\Rightarrow\varepsilon(1+\sigma\tilde{\rho}_0)\left[\mu\frac{\partial\tilde{W}}{\partial\tilde{t}}+\varepsilon\frac{\partial\tilde{w}'}{\partial\tilde{t}}+(\tilde{U}+\varepsilon\tilde{u}')\left(\mu\frac{\partial\tilde{W}}{\partial\tilde{x}}+\varepsilon\frac{\partial\tilde{w}'}{\partial\tilde{x}}+\mu^2\frac{\partial\tilde{W}}{\partial\tilde{X}}+\varepsilon\mu\frac{\partial\tilde{w}'}{\partial\tilde{X}}\right)\right] +\varepsilon\frac{\partial\tilde{q}}{\partial\tilde{Z}}\frac{1}{1+\varepsilon\frac{\partial\tilde{\eta}}{\partial\tilde{z}}}+\tilde{\rho}_0(\tilde{Z})-\tilde{\rho}_0(\tilde{Z}+\varepsilon\tilde{\eta})=0. \tag{B.64}$$

Also the continuity equation should be transformed

$$\begin{aligned}&\frac{\partial\tilde{U}}{\partial\tilde{x}}-\varepsilon\frac{\partial\tilde{U}}{\partial\tilde{Z}}\frac{\partial\zeta}{\partial x}+\varepsilon\frac{\partial\tilde{u}'}{\partial\tilde{x}}-\varepsilon^2\frac{\partial\tilde{u}'}{\partial\tilde{Z}}\frac{\partial\zeta}{\partial x}+\mu\frac{\partial\tilde{U}}{\partial\tilde{X}}-\varepsilon\mu\frac{\partial\tilde{U}}{\partial\tilde{Z}}\frac{\partial\zeta}{\partial X}\\ &+\varepsilon\mu\frac{\partial\tilde{u}'}{\partial\tilde{X}}-\varepsilon^2\mu\frac{\partial\tilde{u}'}{\partial\tilde{Z}}\frac{\partial\zeta}{\partial X}+\left(\mu\frac{\partial\tilde{W}}{\partial\tilde{Z}}+\varepsilon\frac{\partial\tilde{w}'}{\partial\tilde{Z}}\right)\left(1-\varepsilon\frac{\partial\zeta}{\partial z}\right)=0,\end{aligned} \tag{B.65}$$

using equation (B.51), (B.55) and (B.53)

$$\begin{aligned}&\Rightarrow\frac{\partial\tilde{U}}{\partial\tilde{x}}+\varepsilon\frac{\partial\tilde{u}'}{\partial\tilde{x}}+\mu\frac{\partial\tilde{U}}{\partial\tilde{X}}+\varepsilon\mu\frac{\partial\tilde{u}'}{\partial\tilde{X}}+\mu\frac{\partial\tilde{W}}{\partial\tilde{Z}}+\varepsilon\frac{\partial\tilde{w}'}{\partial\tilde{Z}}\\ &-\varepsilon\frac{\partial\tilde{U}}{\partial\tilde{Z}}\frac{\frac{\partial\tilde{\eta}}{\partial\tilde{x}}+\mu\frac{\partial\tilde{\eta}}{\partial\tilde{X}}}{1+\varepsilon\frac{\partial\tilde{\eta}}{\partial\tilde{z}}}-\varepsilon^2\frac{\partial\tilde{u}'}{\partial\tilde{Z}}\frac{\frac{\partial\tilde{\eta}}{\partial\tilde{x}}+\mu\frac{\partial\tilde{\eta}}{\partial\tilde{X}}}{1+\varepsilon\frac{\partial\tilde{\eta}}{\partial\tilde{z}}}-\varepsilon\left(\mu\frac{\partial\tilde{W}}{\partial\tilde{Z}}+\varepsilon\frac{\partial\tilde{w}'}{\partial\tilde{Z}}\right)\frac{\frac{\partial\tilde{\eta}}{\partial\tilde{Z}}}{1+\varepsilon\frac{\partial\tilde{\eta}}{\partial\tilde{z}}}=0,\end{aligned} \tag{B.66}$$

rearrange the different terms in the equation

$$\Rightarrow \frac{\partial \tilde{U}}{\partial \tilde{x}} + \varepsilon\frac{\partial \tilde{u}'}{\partial \tilde{x}} + \mu\frac{\partial \tilde{U}}{\partial \tilde{X}} + \varepsilon\mu\frac{\partial \tilde{u}'}{\partial \tilde{X}} + \mu\frac{\partial \tilde{W}}{\partial \tilde{Z}} + \varepsilon\frac{\partial \tilde{w}'}{\partial \tilde{Z}}$$
$$-\frac{\varepsilon}{1+\varepsilon\frac{\partial \tilde{\eta}}{\partial \tilde{Z}}}\left[\left(\frac{\partial \tilde{U}}{\partial \tilde{Z}} + \varepsilon\frac{\partial \tilde{u}'}{\partial \tilde{Z}}\right)\left(\frac{\partial \tilde{\eta}}{\partial \tilde{x}} + \mu\frac{\partial \tilde{\eta}}{\partial \tilde{X}}\right) + \left(\mu\frac{\partial \tilde{W}}{\partial \tilde{Z}} + \varepsilon\frac{\partial \tilde{w}'}{\partial \tilde{Z}}\right)\frac{\partial \tilde{\eta}}{\partial \tilde{Z}}\right] = 0. \quad \text{(B.67)}$$

The bottom boundary condition (5.78) is equivalent to

$$\mu W + \varepsilon w' = -\gamma\mu(U + \varepsilon u')\frac{\partial h'}{\partial X}\bigg|_{z=-1-\gamma h'} = -\gamma\frac{dh'}{dt}\bigg|_{z=-1-\gamma h'}, \quad \text{(B.68)}$$

as (5.82) can also be evaluated at $z = -1 - \gamma h'$, this yields to

$$\varepsilon\frac{d\zeta}{dt} = -\gamma\frac{dh'}{dt}\bigg|_{z=-1-\gamma h'} \quad \text{(B.69)}$$

by integration this equals

$$\varepsilon\zeta = -\gamma h'|_{z=-1-\gamma h'}. \quad \text{(B.70)}$$

Note that no integration constant is given, as on x_0 the time averaged value of both ζ and h' are equal to zero, see (5.11) and (5.26). Next this expression can be transformed to the new coordinate system

$$\varepsilon\tilde{\eta} = -\gamma\tilde{h}'\big|_{\tilde{Z}=-1-\gamma h'-\varepsilon\zeta(x,-1-\gamma h',t)}, \quad \text{(B.71)}$$

using (B.70) this can be simplified to

$$\varepsilon\tilde{\eta} = -\gamma\tilde{h}'\big|_{\tilde{Z}=-1}. \quad \text{(B.72)}$$

The pressure boundary condition is in the new coordinate equals

$$\varepsilon\tilde{\eta} + \sigma\int_0^{\varepsilon\tilde{\eta}}\tilde{\rho}_0(z')dz' = \varepsilon\sigma\tilde{q}|_{\tilde{Z}=0}. \quad \text{(B.73)}$$

Converting expression (5.82) to the new coordinate system (using (B.49)) results in

$$\mu\tilde{W} + \varepsilon\tilde{w}' = \varepsilon\frac{\partial \tilde{\eta}}{\partial \tilde{t}} + \varepsilon(\tilde{U} + \varepsilon\tilde{u}')\left(\frac{\partial \tilde{\eta}}{\partial \tilde{x}} + \mu\frac{\partial \tilde{\eta}}{\partial \tilde{X}}\right), \quad \text{(B.74)}$$

which automatically satisfies the free boundary condition (5.80).

Reducing the number of equations and variables

For obtaining the first equation, the following procedure is followed

$$\frac{\partial}{\partial Z}(5.91) - \frac{\partial}{\partial x}\left[(5.92)\left(1+\varepsilon\frac{\partial \eta}{\partial Z}\right)\right] - \mu\frac{\partial}{\partial X}\left[(5.92)\left(1+\varepsilon\frac{\partial \eta}{\partial Z}\right)\right] + \frac{\partial}{\partial Z}\left[(5.92)\varepsilon\left(\frac{\partial \eta}{\partial x} + \mu\frac{\partial \eta}{\partial X}\right)\right] = 0, \quad \text{(B.75)}$$

which yields to

$$\begin{aligned}
&\frac{\partial}{\partial Z}\left\{(1+\sigma\rho_0)\left[\varepsilon\frac{\partial u'}{\partial t}+(U+\varepsilon u')\left(\frac{\partial U}{\partial x}+\varepsilon\frac{\partial u'}{\partial x}+\mu\frac{\partial U}{\partial X}+\varepsilon\mu\frac{\partial u'}{\partial X}\right)\right]\right\}\\
&\quad+\varepsilon\frac{\partial^2 q}{\partial x\partial Z}+\varepsilon\mu\frac{\partial^2 q}{\partial X\partial Z}-\varepsilon^2\frac{\partial}{\partial Z}\left(\frac{\frac{\partial\eta}{\partial x}+\mu\frac{\partial\eta}{\partial X}}{1+\varepsilon\frac{\partial\eta}{\partial Z}}\frac{\partial q}{\partial Z}\right)\\
&-\frac{\partial}{\partial x}\left\{\varepsilon(1+\sigma\rho_0)\left[\mu\frac{\partial W}{\partial t}+\varepsilon\frac{\partial w'}{\partial t}+(U+\varepsilon u')\left(\mu\frac{\partial W}{\partial x}+\varepsilon\frac{\partial w'}{\partial x}+\mu^2\frac{\partial W}{\partial X}+\varepsilon\mu\frac{\partial w'}{\partial X}\right)\right]\left(1+\varepsilon\frac{\partial\eta}{\partial Z}\right)\right\}\\
&\quad-\varepsilon\frac{\partial^2 q}{\partial Z\partial x}-\frac{\partial}{\partial x}\left[(\rho_0(Z)-\rho_0(Z+\varepsilon\eta))\left(1+\varepsilon\frac{\partial\eta}{\partial Z}\right)\right]\\
&-\mu\frac{\partial}{\partial X}\left\{\varepsilon(1+\sigma\rho_0)\left[\mu\frac{\partial W}{\partial t}+\varepsilon\frac{\partial w'}{\partial t}+(U+\varepsilon u')\left(\mu\frac{\partial W}{\partial x}+\varepsilon\frac{\partial w'}{\partial x}+\mu^2\frac{\partial W}{\partial X}+\varepsilon\mu\frac{\partial w'}{\partial X}\right)\right]\left(1+\varepsilon\frac{\partial\eta}{\partial Z}\right)\right\}\\
&\quad-\varepsilon\mu\frac{\partial^2 q}{\partial Z\partial X}-\mu\frac{\partial}{\partial X}\left[(\rho_0(Z)-\rho_0(Z+\varepsilon\eta))\left(1+\varepsilon\frac{\partial\eta}{\partial Z}\right)\right]\\
&+\frac{\partial}{\partial Z}\left\{\varepsilon^2(1+\sigma\rho_0)\left[\mu\frac{\partial W}{\partial t}+\varepsilon\frac{\partial w'}{\partial t}+(U+\varepsilon u')\left(\mu\frac{\partial W}{\partial x}+\varepsilon\frac{\partial w'}{\partial x}+\mu^2\frac{\partial W}{\partial X}+\varepsilon\mu\frac{\partial w'}{\partial X}\right)\right]\left[\frac{\partial\eta}{\partial x}+\mu\frac{\partial\eta}{\partial X}\right]\right\}\\
&\quad+\varepsilon^2\frac{\partial}{\partial Z}\left(\frac{\frac{\partial\eta}{\partial x}+\mu\frac{\partial\eta}{\partial X}}{1+\varepsilon\frac{\partial\eta}{\partial Z}}\frac{\partial q}{\partial Z}\right)+\varepsilon\frac{\partial}{\partial Z}\left[(\rho_0(Z)-\rho_0(Z+\varepsilon\eta))\left(\frac{\partial\eta}{\partial x}+\mu\frac{\partial\eta}{\partial X}\right)\right]=0,
\end{aligned}\tag{B.76}$$

expanding some derivatives and cancelling the terms containing q, results into

$$\begin{aligned}
&\Rightarrow\frac{\partial}{\partial Z}\left\{(1+\sigma\rho_0)\left[\varepsilon\frac{\partial u'}{\partial t}+(U+\varepsilon u')\left(\frac{\partial U}{\partial x}+\varepsilon\frac{\partial u'}{\partial x}+\mu\frac{\partial U}{\partial X}+\varepsilon\mu\frac{\partial u'}{\partial X}\right)\right]\right\}\\
&-\left\{\frac{\partial}{\partial x}\varepsilon(1+\sigma\rho_0)\left[\mu\frac{\partial W}{\partial t}+\varepsilon\frac{\partial w'}{\partial t}+(U+\varepsilon u')\left(\mu\frac{\partial W}{\partial x}+\varepsilon\frac{\partial w'}{\partial x}+\mu^2\frac{\partial W}{\partial X}+\varepsilon\mu\frac{\partial w'}{\partial X}\right)\right]\right\}\left(1+\varepsilon\frac{\partial\eta}{\partial Z}\right)\\
&\quad-\varepsilon^2(1+\sigma\rho_0)\left[\mu\frac{\partial W}{\partial t}+\varepsilon\frac{\partial w'}{\partial t}+(U+\varepsilon u')\left(\mu\frac{\partial W}{\partial x}+\varepsilon\frac{\partial w'}{\partial x}+\mu^2\frac{\partial W}{\partial X}+\varepsilon\mu\frac{\partial w'}{\partial X}\right)\right]\frac{\partial^2\eta}{\partial Z\partial x}\\
&-\left\{\mu\frac{\partial}{\partial X}\varepsilon(1+\sigma\rho_0)\left[\mu\frac{\partial W}{\partial t}+\varepsilon\frac{\partial w'}{\partial t}+(U+\varepsilon u')\left(\mu\frac{\partial W}{\partial x}+\varepsilon\frac{\partial w'}{\partial x}+\mu^2\frac{\partial W}{\partial X}+\varepsilon\mu\frac{\partial w'}{\partial X}\right)\right]\right\}\left(1+\varepsilon\frac{\partial\eta}{\partial Z}\right)\\
&\quad-\varepsilon^2\mu(1+\sigma\rho_0)\left[\mu\frac{\partial W}{\partial t}+\varepsilon\frac{\partial w'}{\partial t}+(U+\varepsilon u')\left(\mu\frac{\partial W}{\partial x}+\varepsilon\frac{\partial w'}{\partial x}+\mu^2\frac{\partial W}{\partial X}+\varepsilon\mu\frac{\partial w'}{\partial X}\right)\right]\frac{\partial^2\eta}{\partial Z\partial X}\\
&+\left(\frac{\partial}{\partial Z}\varepsilon^2(1+\sigma\rho_0)\left[\mu\frac{\partial W}{\partial t}+\varepsilon\frac{\partial w'}{\partial t}+(U+\varepsilon u')\left(\mu\frac{\partial W}{\partial x}+\varepsilon\frac{\partial w'}{\partial x}+\mu^2\frac{\partial W}{\partial X}+\varepsilon\mu\frac{\partial w'}{\partial X}\right)\right]\right)\left(\frac{\partial\eta}{\partial x}+\mu\frac{\partial\eta}{\partial X}\right)\\
&\quad+\varepsilon^2(1+\sigma\rho_0)\left[\mu\frac{\partial W}{\partial t}+\varepsilon\frac{\partial w'}{\partial t}+(U+\varepsilon u')\left(\mu\frac{\partial W}{\partial x}+\frac{\partial w'}{\partial x}+\mu^2\frac{\partial W}{\partial X}+\varepsilon\mu\frac{\partial w'}{\partial X}\right)\right]\left(\frac{\partial^2\eta}{\partial x\partial Z}+\mu\frac{\partial^2\eta}{\partial X\partial Z}\right)\\
&\quad+\varepsilon\frac{\partial\rho_0}{\partial Z}\frac{\partial\eta}{\partial x}\left(1+\varepsilon\frac{\partial\eta}{\partial Z}\right)-\varepsilon\left(\rho_0(Z)-\rho_0(Z+\varepsilon\eta)\right)\frac{\partial^2\eta}{\partial Z\partial x}\\
&\quad+\varepsilon\mu\frac{\partial\rho_0}{\partial Z}\frac{\partial\eta}{\partial X}\left(1+\varepsilon\frac{\partial\eta}{\partial Z}\right)-\varepsilon\mu\left(\rho_0(Z)-\rho_0(Z+\varepsilon\eta)\right)\frac{\partial^2\eta}{\partial Z\partial X}\\
&\quad+\varepsilon\left[\frac{\partial\rho_0}{\partial Z}-\frac{\partial\rho_0}{\partial Z}\left(1+\varepsilon\frac{\partial\eta}{\partial Z}\right)\right]\left(\frac{\partial\eta}{\partial x}+\mu\frac{\partial\eta}{\partial X}\right)+\varepsilon\left(\rho_0(Z)-\rho_0(Z+\varepsilon\eta)\right)\left(\frac{\partial^2\eta}{\partial x\partial Z}+\mu\frac{\partial^2\eta}{\partial X\partial Z}\right)=0,
\end{aligned}\tag{B.77}$$

cancelling terms, using (5.94) for simplification

$$\Rightarrow \frac{\partial}{\partial Z}\left\{(1+\sigma\rho_0)\left[\varepsilon\frac{\partial u'}{\partial t}+(U+\varepsilon u')\left(\frac{\partial U}{\partial x}+\varepsilon\frac{\partial u'}{\partial x}+\mu\frac{\partial U}{\partial X}+\varepsilon\mu\frac{\partial u'}{\partial X}\right)\right]\right\}$$
$$-\left\{\left(\frac{\partial}{\partial x}+\mu\frac{\partial}{\partial X}\right)\varepsilon^2(1+\sigma\rho_0)\left[\frac{\partial}{\partial t}+(U+\varepsilon u')\left(\frac{\partial}{\partial x}+\mu\frac{\partial}{\partial X}\right)\right]^2\eta\right\}\left[1+\varepsilon\frac{\partial\eta}{\partial Z}\right]$$
$$+\left\{\frac{\partial}{\partial Z}\varepsilon^3(1+\sigma\rho_0)\left[\frac{\partial}{\partial t}+(U+\varepsilon u')\left(\frac{\partial}{\partial x}+\mu\frac{\partial}{\partial X}\right)\right]^2\eta\right\}\left(\frac{\partial\eta}{\partial x}+\mu\frac{\partial\eta}{\partial X}\right)+\varepsilon\frac{\partial\rho_0}{\partial Z}\left(\frac{\partial\eta}{\partial x}+\mu\frac{\partial\eta}{\partial X}\right)=0. \tag{B.78}$$

The second equation can be simplified using this procedure

$$(5.93)\left(1+\varepsilon\frac{\partial\eta}{\partial Z}\right)=0 \tag{B.79}$$

which gives

$$\left[1+\varepsilon\frac{\partial\eta}{\partial Z}\right]\left(\frac{\partial U}{\partial x}+\varepsilon\frac{\partial u'}{\partial x}+\mu\frac{\partial U}{\partial X}+\varepsilon\mu\frac{\partial u'}{\partial X}\right)+\left[1+\varepsilon\frac{\partial\eta}{\partial Z}\right]\left(\mu\frac{\partial W}{\partial Z}+\varepsilon\frac{\partial w'}{\partial Z}\right)$$
$$-\varepsilon\left(\frac{\partial U}{\partial Z}+\varepsilon\frac{\partial u'}{\partial Z}\right)\left(\frac{\partial\eta}{\partial x}+\mu\frac{\partial\eta}{\partial X}\right)-\varepsilon\left(\mu\frac{\partial W}{\partial Z}+\varepsilon\frac{\partial w'}{\partial Z}\right)\frac{\partial\eta}{\partial Z}=0, \tag{B.80}$$

cancelling terms and using equation (5.94)

$$\left[1+\varepsilon\frac{\partial\eta}{\partial Z}\right]\left(\frac{\partial U}{\partial x}+\varepsilon\frac{\partial u'}{\partial x}+\mu\frac{\partial U}{\partial X}+\varepsilon\mu\frac{\partial u'}{\partial X}\right)$$
$$+\varepsilon\frac{\partial}{\partial Z}\left[\frac{\partial\eta}{\partial t}+(U+\varepsilon u')\left(\frac{\partial\eta}{\partial x}+\mu\frac{\partial\eta}{\partial X}\right)\right]-\varepsilon\left(\frac{\partial U}{\partial Z}+\varepsilon\frac{\partial u'}{\partial Z}\right)\left(\frac{\partial\eta}{\partial x}+\mu\frac{\partial\eta}{\partial X}\right)=0, \tag{B.81}$$

expanding the derivative

$$\left[1+\varepsilon\frac{\partial\eta}{\partial Z}\right]\left(\frac{\partial U}{\partial x}+\varepsilon\frac{\partial u'}{\partial x}+\mu\frac{\partial U}{\partial X}+\varepsilon\mu\frac{\partial u'}{\partial X}\right)$$
$$+\varepsilon\frac{\partial^2\eta}{\partial t\partial Z}+\varepsilon\left(\frac{\partial U}{\partial Z}+\varepsilon\frac{\partial u'}{\partial Z}\right)\left(\frac{\partial\eta}{\partial x}+\mu\frac{\partial\eta}{\partial X}\right)+\varepsilon(U+\varepsilon u')\left(\frac{\partial^2\eta}{\partial x\partial Z}+\mu\frac{\partial^2\eta}{\partial X\partial Z}\right)$$
$$-\varepsilon\left(\frac{\partial U}{\partial Z}+\varepsilon\frac{\partial u'}{\partial Z}\right)\left(\frac{\partial\eta}{\partial x}+\mu\frac{\partial\eta}{\partial X}\right)=0, \tag{B.82}$$

cancelling and collecting terms

$$\left[1+\varepsilon\frac{\partial\eta}{\partial Z}\right]\left(\frac{\partial U}{\partial x}+\varepsilon\frac{\partial u'}{\partial x}+\mu\frac{\partial U}{\partial X}+\varepsilon\mu\frac{\partial u'}{\partial X}\right)+\varepsilon\left[\frac{\partial}{\partial t}+(U+\varepsilon u')\left(\frac{\partial}{\partial x}+\mu\frac{\partial}{\partial X}\right)\right]\frac{\partial\eta}{\partial Z}=0. \tag{B.83}$$

Also one of the boundary conditions need to be transformed, which gives (differentiating equation (5.96) to x and X)

$$\varepsilon\frac{\partial\eta}{\partial x}+\varepsilon\mu\frac{\partial\eta}{\partial X}+\sigma\left(\frac{\partial}{\partial x}+\mu\frac{\partial}{\partial X}\right)\int_0^{\varepsilon\eta}\rho_0(Z')dZ'=\left(\frac{\partial}{\partial x}+\mu\frac{\partial}{\partial X}\right)\varepsilon\sigma q\Big|_{Z=0}, \tag{B.84}$$

calculating the derivatives

$$\Rightarrow\varepsilon\left(\frac{\partial\eta}{\partial x}+\mu\frac{\partial\eta}{\partial X}\right)+\varepsilon\sigma\rho_0(\varepsilon\eta)\left(\frac{\partial\eta}{\partial x}+\mu\frac{\partial\eta}{\partial X}\right)=\varepsilon\sigma\left(\frac{\partial q}{\partial x}+\mu\frac{\partial q}{\partial X}\right)\Big|_{Z=0}, \tag{B.85}$$

collecting terms and divide by σ

$$\Rightarrow \varepsilon\frac{1+\sigma\rho_0(\varepsilon\eta)}{\sigma}\left(\frac{\partial\eta}{\partial x}+\mu\frac{\partial\eta}{\partial X}\right)=\varepsilon\left(\frac{\partial q}{\partial x}+\mu\frac{\partial q}{\partial X}\right)\Big|_{Z=0}, \tag{B.86}$$

apply equation (5.91) to substitute $\frac{\partial q}{\partial x}$

$$\begin{aligned}\Rightarrow \varepsilon\frac{1+\sigma\rho_0(\varepsilon\eta)}{\sigma}\left(\frac{\partial\eta}{\partial x}+\mu\frac{\partial\eta}{\partial X}\right)&=-(1+\sigma\rho_0)\left[\varepsilon\frac{\partial u'}{\partial t}+(U+\varepsilon u')\left(\frac{\partial U}{\partial x}+\varepsilon\frac{\partial u'}{\partial x}+\mu\frac{\partial U}{\partial X}+\mu\varepsilon\frac{\partial u'}{\partial X}\right)\right]\\&\quad+\varepsilon^2\frac{\partial q}{\partial Z}\frac{1}{1+\varepsilon\frac{\partial\eta}{\partial Z}}\left(\frac{\partial\eta}{\partial x}+\mu\frac{\partial\eta}{\partial X}\right)\Big|_{Z=0},\end{aligned} \tag{B.87}$$

using (5.92) to replace $\frac{1}{1+\varepsilon\frac{\partial\eta}{\partial Z}}\frac{\partial q}{\partial Z}$

$$\begin{aligned}\Rightarrow \varepsilon\frac{1+\sigma\rho_0(\varepsilon\eta)}{\sigma}\left(\frac{\partial\eta}{\partial x}+\mu\frac{\partial\eta}{\partial X}\right)&=-(1+\sigma\rho_0)\left[\varepsilon\frac{\partial u'}{\partial t}+(U+\varepsilon u')\left(\frac{\partial U}{\partial x}+\varepsilon\frac{\partial u'}{\partial x}+\mu\frac{\partial U}{\partial X}+\mu\varepsilon\frac{\partial u'}{\partial X}\right)\right]\\&\quad-\varepsilon^3(1+\sigma\rho_0)\left\{\left[\frac{\partial}{\partial t}+(U+\varepsilon u')\left(\frac{\partial}{\partial x}+\mu\frac{\partial}{\partial X}\right)\right]^2\eta\right\}\left(\frac{\partial\eta}{\partial x}+\mu\frac{\partial\eta}{\partial X}\right)\\&\quad-\varepsilon\left(\rho_0(0)-\rho_0(\varepsilon\eta)\right)\left(\frac{\partial\eta}{\partial x}+\mu\frac{\partial\eta}{\partial X}\right)\Big|_{Z=0},\end{aligned} \tag{B.88}$$

rearranging the terms yields

$$\begin{aligned}\Rightarrow \varepsilon\frac{1+\sigma\rho_0(0)}{\sigma}\left(\frac{\partial\eta}{\partial x}+\mu\frac{\partial\eta}{\partial X}\right)&=-(1+\sigma\rho_0)\left[\varepsilon\frac{\partial u'}{\partial t}+(U+\varepsilon u')\left(\frac{\partial U}{\partial x}+\varepsilon\frac{\partial u'}{\partial x}+\mu\frac{\partial U}{\partial X}+\mu\varepsilon\frac{\partial u'}{\partial X}\right)\right]\\&\quad-\varepsilon^3(1+\sigma\rho_0)\left\{\left[\frac{\partial}{\partial t}+(U+\varepsilon u')\left(\frac{\partial}{\partial x}+\mu\frac{\partial}{\partial X}\right)\right]^2\eta\right\}\left(\frac{\partial\eta}{\partial x}+\mu\frac{\partial\eta}{\partial X}\right)\Big|_{Z=0},\end{aligned} \tag{B.89}$$

divide the equation by $\frac{1+\sigma\rho_0(0)}{\sigma}$

$$\begin{aligned}\Rightarrow \varepsilon\left(\frac{\partial\eta}{\partial x}+\mu\frac{\partial\eta}{\partial X}\right)&=-\sigma\left[\varepsilon\frac{\partial u'}{\partial t}+(U+\varepsilon u')\left(\frac{\partial U}{\partial x}+\varepsilon\frac{\partial u'}{\partial x}+\mu\frac{\partial U}{\partial X}+\mu\varepsilon\frac{\partial u'}{\partial X}\right)\right]\\&\quad-\varepsilon^3\sigma\left\{\left[\frac{\partial}{\partial t}+(U+\varepsilon u')\left(\frac{\partial}{\partial x}+\mu\frac{\partial}{\partial X}\right)\right]^2\eta\right\}\left(\frac{\partial\eta}{\partial x}+\mu\frac{\partial\eta}{\partial X}\right)\Big|_{Z=0}.\end{aligned} \tag{B.90}$$

The other boundary condition (5.95) remains unchanged.

Reducing number of equations and variables in the approximated case

Equation (5.212)-(5.213) can be combined into one equation containing $\eta'^{(0)}$ only. Start from equation (5.213)

$$\frac{\partial u'^{(0)}}{\partial x}=-\frac{\partial^2\eta'^{(0)}}{\partial t\partial Z}-U_0\frac{\partial^2\eta'^{(0)}}{\partial x\partial Z}, \tag{B.91}$$

calculate the derivative to t

$$\Rightarrow \frac{\partial^2 u'^{(0)}}{\partial t\partial x}=-\frac{\partial^3\eta'^{(0)}}{\partial t^2\partial Z}-U_0\frac{\partial^3\eta'^{(0)}}{\partial t\partial x\partial Z}. \tag{B.92}$$

Also the derivative to x can be calculated

$$\Rightarrow \frac{\partial^2 u'^{(0)}}{\partial x^2} = -\frac{\partial^3 \eta'^{(0)}}{\partial x \partial t \partial Z} - U_0 \frac{\partial^3 \eta'^{(0)}}{\partial x^2 \partial Z}. \tag{B.93}$$

The derivative to x from equation (5.212) can be taken, which yields

$$\frac{\partial}{\partial Z}\left(-\frac{\partial^2 u'^{(0)}}{\partial x \partial t} + U_0 \frac{\partial^2 u'^{(0)}}{\partial x^2}\right) + \frac{\partial \rho_0}{\partial Z}\frac{\partial^2 \eta'^{(0)}}{\partial x^2} = 0, \tag{B.94}$$

now the previous calculated derivatives of $u'^{(0)}$ can be substituted in the equation

$$\Rightarrow \frac{\partial}{\partial Z}\left(\frac{\partial^3 \eta'^{(0)}}{\partial t^2 \partial Z} + 2U_0 \frac{\partial^3 \eta'^{(0)}}{\partial t \partial x \partial Z} + U_0^2 \frac{\partial^3 \eta'^{(0)}}{\partial x^2 \partial Z}\right) - \frac{\partial \rho_0}{\partial Z}\frac{\partial^2 \eta'^{(0)}}{\partial x^2} = 0. \tag{B.95}$$

Moving reference frame without background shear flow

Equation (5.216) without shear flow equals

$$\frac{\partial^4 \eta'^{(0)}}{\partial t^2 \partial Z^2} - \frac{\partial \rho_0}{\partial Z}\frac{\partial^2 \eta'^{(0)}}{\partial x^2} = 0. \tag{B.96}$$

The method of separation of variables will be applied to this equation. Solutions of the following product form will be attempted

$$\eta'^{(0)}(x, Z, t) = A(x, t)\Phi(Z). \tag{B.97}$$

Now this definition will be used in the governing equation

$$\frac{\partial^2 A}{\partial t^2}\frac{\partial^2 \Phi}{\partial Z^2} - \frac{\partial \rho_0}{\partial Z}\frac{\partial^2 A}{\partial x^2}\Phi = 0, \tag{B.98}$$

rearrange the terms in the equation and divide the equation by $\frac{\partial^2 A}{\partial x^2}\frac{\partial^2 \Phi}{\partial Z^2}$

$$\Rightarrow \frac{\frac{\partial^2 A}{\partial t^2}}{\frac{\partial^2 A}{\partial x^2}} = \frac{\partial \rho_0}{\partial Z}\frac{\Phi}{\frac{\partial^2 \Phi}{\partial Z^2}} = c_0^2, \tag{B.99}$$

which shows that the equation is indeed separable with a constant c_0^2.

The equation needed to solve for the vertical structure will be

$$c_0^2 \frac{\partial^2 \Phi}{\partial Z^2} + \frac{\partial \rho_0}{\partial Z}\Phi = 0, \tag{B.100}$$

which is the Taylor-Goldstein equation in the long-wave limit in the Boussinesq approximation without shear flow. The equation is subject to the boundary conditions

$$\Phi = 0|_{Z=0}, \tag{B.101}$$

$$\Phi = 0|_{Z=-1}. \tag{B.102}$$

The equation for A in the horizontal and time domain is equal to

$$\frac{\partial^2 A}{\partial t^2} - c_0^2 \frac{\partial^2 A}{\partial x^2} = 0. \tag{B.103}$$

This equation is the linear wave equations and has solutions of the form

$$A(x, t) = f(x + c_0 t) + g(x - c_0 t). \tag{B.104}$$

Moving reference frame with background shear flow

The same approach of finding a solution will be applied to the case with a background shear flow present. First the derivative to Z will be extended in equation (5.216)

$$\frac{\partial^4\eta'^{(0)}}{\partial t^2\partial Z^2}-\frac{\partial\rho_0}{\partial Z}\frac{\partial^2\eta'^{(0)}}{\partial x^2}+2\frac{\partial U_0}{\partial Z}\frac{\partial^3\eta'^{(0)}}{\partial t\partial x\partial Z}+2U_0\frac{\partial^4\eta'^{(0)}}{\partial t\partial x\partial Z^2}+2U_0\frac{\partial U_0}{\partial Z}\frac{\partial^3\eta'^{(0)}}{\partial x^2\partial Z}+U_0^2\frac{\partial^4\eta'^{(0)}}{\partial x^2\partial Z^2}=0 \quad \text{(B.105)}$$

In this case also solutions of the form will be searched for

$$\eta'^{(0)}(x,Z,t)=A(x,t)\Phi(Z). \quad \text{(B.106)}$$

Now substitute this definition in the equation

$$\frac{\partial^2A}{\partial t^2}\frac{\partial^2\Phi}{\partial Z^2}-\frac{\partial\rho_0}{\partial Z}\frac{\partial^2A}{\partial x^2}\Phi+2\frac{\partial U_0}{\partial Z}\frac{\partial^2A}{\partial t\partial x}\frac{\partial\Phi}{\partial Z}+2U_0\frac{\partial^2A}{\partial t\partial x}\frac{\partial^2\Phi}{\partial Z^2}+2U_0\frac{\partial U_0}{\partial Z}\frac{\partial^2A}{\partial x^2}\frac{\partial\Phi}{\partial Z}+U_0^2\frac{\partial^2A}{\partial x^2}\frac{\partial^2\Phi}{\partial Z^2}=0, \quad \text{(B.107)}$$

divide the equation by $\frac{\partial^2A}{\partial x^2}\frac{\partial^2\Phi}{\partial Z^2}$

$$\Rightarrow \frac{\frac{\partial^2A}{\partial t^2}}{\frac{\partial^2A}{\partial x^2}}-\frac{\partial\rho_0}{\partial Z}\frac{\Phi}{\frac{\partial^2\Phi}{\partial Z^2}}+2\frac{\partial U_0}{\partial Z}\frac{\frac{\partial^2A}{\partial t\partial x}}{\frac{\partial^2A}{\partial x^2}}\frac{\frac{\partial\Phi}{\partial Z}}{\frac{\partial^2\Phi}{\partial Z^2}}+2U_0\frac{\frac{\partial^2A}{\partial t\partial x}}{\frac{\partial^2A}{\partial x^2}}+2U_0\frac{\partial U_0}{\partial Z}\frac{\frac{\partial\Phi}{\partial Z}}{\frac{\partial^2\Phi}{\partial Z^2}}+U_0^2=0, \quad \text{(B.108)}$$

now reorder the terms in the equation such that one part is dependent on x and t only, one part on Z only and one on still on x, Z and t

$$\Rightarrow \underbrace{\frac{\frac{\partial^2A}{\partial t^2}}{\frac{\partial^2A}{\partial x^2}}}_{\text{depends on: }(x,t)}\underbrace{-\frac{\partial\rho_0}{\partial Z}\frac{\Phi}{\frac{\partial^2\Phi}{\partial Z^2}}+2U_0\frac{\partial U_0}{\partial Z}\frac{\frac{\partial\Phi}{\partial Z}}{\frac{\partial^2\Phi}{\partial Z^2}}+U_0^2}_{\text{depends on: }(Z)}+\underbrace{\left(2\frac{\partial U_0}{\partial Z}\frac{\frac{\partial\Phi}{\partial Z}}{\frac{\partial^2\Phi}{\partial Z^2}}+2U_0\right)\frac{\frac{\partial^2A}{\partial t\partial x}}{\frac{\partial^2A}{\partial x^2}}}_{\text{depends on :}(x,Z,t)}=0. \quad \text{(B.109)}$$

This equation is not directly separable as (B.99). To see that this equation is indeed separable first an extra observation need to made. Therefore take the derivative to x and Z of this equations, which results in

$$\underbrace{\frac{\partial}{\partial Z}\left(2\frac{\partial U_0}{\partial Z}\frac{\frac{\partial\Phi}{\partial Z}}{\frac{\partial^2\Phi}{\partial Z^2}}+2U_0\right)}_{\text{depends on: }(Z)}\frac{\partial}{\partial x}\underbrace{\left(\frac{\frac{\partial^2A}{\partial t\partial x}}{\frac{\partial^2A}{\partial x^2}}\right)}_{\text{depends on: }(x,t)}=0. \quad \text{(B.110)}$$

This implies that or the term depending on Z is constant or the term depending on x and t is constant. Assume that the second ((x,t) term) is constant, then the separation of variables can be made with the constant c_0^2

$$\underbrace{\frac{\frac{\partial^2A}{\partial t^2}}{\frac{\partial^2A}{\partial x^2}}}_{\text{depends on: }(x,t)}=\underbrace{\frac{\partial\rho_0}{\partial Z}\frac{\Phi}{\frac{\partial^2\Phi}{\partial Z^2}}-2U_0\frac{\partial U_0}{\partial Z}\frac{\frac{\partial\Phi}{\partial Z}}{\frac{\partial^2\Phi}{\partial Z^2}}-U_0^2-\left(2\frac{\partial U_0}{\partial Z}\frac{\frac{\partial\Phi}{\partial Z}}{\frac{\partial^2\Phi}{\partial Z^2}}+2U_0\right)}_{\text{depends on: }(Z)}\underbrace{\frac{\frac{\partial^2A}{\partial t\partial x}}{\frac{\partial^2A}{\partial x^2}}}_{\text{constant}}=c_0^2. \quad \text{(B.111)}$$

The equation needed to solve for $A(x,t)$ becomes

$$\frac{\partial^2A}{\partial t^2}-c_0^2\frac{\partial^2A}{\partial x^2}=0. \quad \text{(B.112)}$$

Which implies solutions traveling with speed c_0

$$A(x,t) = f(x + c_0 t) + g(x - c_0 t). \tag{B.113}$$

For now only will be focused on the right going waves, then can be obtained

$$\frac{\frac{\partial^2 A}{\partial t \partial x}}{\frac{\partial^2 A}{\partial x^2}} = \frac{-c_0 g''(x - ct)}{g''(x - ct)} = -c_0, \tag{B.114}$$

which shows that this expression is indeed a constant. This can be used to derive the equation for the vertical structure

$$\frac{\partial \rho_0}{\partial Z}\frac{\Phi}{\frac{\partial^2 \Phi}{\partial Z^2}} - 2U_0\frac{\partial U_0}{\partial Z}\frac{\frac{\partial \Phi}{\partial Z}}{\frac{\partial^2 \Phi}{\partial Z^2}} - U_0^2 + c_0\left(2\frac{\partial U_0}{\partial Z}\frac{\frac{\partial \Phi}{\partial Z}}{\frac{\partial^2 \Phi}{\partial Z^2}} + 2U_0\right) = c_0^2, \tag{B.115}$$

multiply the equation with $-\frac{\partial^2 \Phi}{\partial Z^2}$

$$\Rightarrow 2(U_0 - c_0)\frac{\partial U}{\partial Z}\frac{\partial \Phi}{\partial Z} + (U_0 - c_0)^2\frac{\partial^2 \Phi}{\partial Z^2} - \frac{\partial \rho_0}{\partial Z}\Phi = 0, \tag{B.116}$$

group the derivatives

$$\frac{\partial}{\partial Z}\left[(U_0 - c_0)^2\frac{\partial \Phi}{\partial Z}\right] - \frac{\partial \rho_0}{\partial Z}\Phi = 0, \tag{B.117}$$

which is the Taylor-Goldstein equation in the long-wave limit in the Boussinesq approximation with shear flow. This system is subject to the boundary conditions

$$\Phi = 0|_{Z=0}, \tag{B.118}$$

$$\Phi = 0|_{Z=-1}. \tag{B.119}$$

Transformation to a moving reference frame

Here a transformation to the new coordinates ξ and τ will be made. First the partial derivatives for this transformation, (5.220) and (5.221), are given

$$\frac{\partial}{\partial t} = -c_0\frac{\partial}{\partial \xi} + \varepsilon\frac{\partial}{\partial \tau} \tag{B.120}$$

$$\frac{\partial}{\partial x} = \frac{\partial}{\partial \xi} \tag{B.121}$$

Start the transformation for equation (5.103)

$$\begin{aligned}
&\frac{\partial}{\partial Z}\left\{(1 + \varepsilon^2\hat{\sigma}\rho_0)\left[-\varepsilon c_0\frac{\partial u'}{\partial \xi} + \varepsilon^2\frac{\partial u'}{\partial \tau} + (U + \varepsilon u')\left(\frac{\partial U}{\partial \xi} + \varepsilon\frac{\partial u'}{\partial \xi} + \varepsilon^2\hat{\mu}\frac{\partial U}{\partial X} + \varepsilon^3\hat{\mu}\frac{\partial u'}{\partial X}\right)\right]\right\} \\
&-\varepsilon^2\left(\frac{\partial}{\partial \xi} + \varepsilon^2\hat{\mu}\frac{\partial}{\partial X}\right)\left\{(1 + \varepsilon^2\hat{\sigma}\rho_0)\left[-c_0\frac{\partial}{\partial \xi} + \varepsilon\frac{\partial}{\partial \tau} + (U + \varepsilon u')\left(\frac{\partial}{\partial \xi} + \varepsilon^2\hat{\mu}\frac{\partial}{\partial X}\right)\right]^2(\hat{\gamma}\bar{\eta} + \eta')\right\} \\
&\cdot\left[1 + \varepsilon\hat{\gamma}\frac{\partial \bar{\eta}}{\partial Z} + \varepsilon\frac{\partial \eta'}{\partial Z}\right] + \varepsilon^3\frac{\partial}{\partial Z}\left\{(1 + \varepsilon^2\hat{\sigma}\rho_0)\left[-c_0\frac{\partial}{\partial \xi} + \varepsilon\frac{\partial}{\partial \tau} + (U + \varepsilon u')\left(\frac{\partial}{\partial \xi} + \varepsilon^2\hat{\mu}\frac{\partial}{\partial X}\right)\right]^2(\hat{\gamma}\bar{\eta} + \eta')\right\} \\
&\cdot\left(\hat{\gamma}\frac{\partial \bar{\eta}}{\partial \xi} + \frac{\partial \eta'}{\partial \xi} + \varepsilon^2\hat{\mu}\hat{\gamma}\frac{\partial \bar{\eta}}{\partial X} + \varepsilon^2\hat{\mu}\frac{\partial \eta'}{\partial X}\right) + \varepsilon\frac{\partial \rho_0}{\partial Z}\left(\hat{\gamma}\frac{\partial \bar{\eta}}{\partial \xi} + \frac{\partial \eta'}{\partial \xi} + \varepsilon^2\hat{\mu}\hat{\gamma}\frac{\partial \bar{\eta}}{\partial X} + \varepsilon^2\hat{\mu}\frac{\partial \eta'}{\partial X}\right) = 0,
\end{aligned} \tag{B.122}$$

rearrange the terms in the equation, such that all small terms (order ε^2 or higher) are on the right-hand side:

$$\Rightarrow \frac{\partial}{\partial Z}\left[(U+\varepsilon u')\frac{\partial U}{\partial \xi}+\varepsilon(U-c_0)\frac{\partial u'}{\partial \xi}\right]+\varepsilon\frac{\partial \rho_0}{\partial Z}\left(\hat{\gamma}\frac{\partial \bar{\eta}}{\partial \xi}+\frac{\partial \eta'}{\partial \xi}\right)=F, \tag{B.123}$$

where F is given by

$$\begin{aligned}F=&-\frac{\partial}{\partial Z}\left\{\varepsilon^2\frac{\partial u'}{\partial \tau}+\varepsilon^2 u'\frac{\partial u'}{\partial \xi}+(U+\varepsilon u')\left(\varepsilon^2\hat{\mu}\frac{\partial U}{\partial X}+\varepsilon^3\hat{\mu}\frac{\partial u'}{\partial X}\right)\right.\\&\left.-\varepsilon^2\hat{\sigma}\rho_0\left[-\varepsilon c_0\frac{\partial u'}{\partial \xi}+\varepsilon^2\frac{\partial u'}{\partial \tau}+(U+\varepsilon u')\left(\frac{\partial U}{\partial \xi}+\varepsilon\frac{\partial u'}{\partial \xi}+\varepsilon^2\hat{\mu}\frac{\partial U}{\partial X}+\varepsilon^3\hat{\mu}\frac{\partial u'}{\partial X}\right)\right]\right\}\\&+\varepsilon^2\left[1+\varepsilon\hat{\gamma}\frac{\partial \bar{\eta}}{\partial Z}+\varepsilon\frac{\partial \eta'}{\partial Z}\right]\left(\frac{\partial}{\partial \xi}+\varepsilon^2\hat{\mu}\frac{\partial}{\partial X}\right)\left[(1+\varepsilon^2\hat{\sigma}\rho_0)H\right]\\&-\varepsilon^3\left(\hat{\gamma}\frac{\partial \bar{\eta}}{\partial \xi}+\frac{\partial \eta'}{\partial \xi}+\varepsilon^2\hat{\mu}\hat{\gamma}\frac{\partial \bar{\eta}}{\partial X}+\varepsilon^2\hat{\mu}\frac{\partial \eta'}{\partial X}\right)\frac{\partial}{\partial Z}\left[(1+\varepsilon^2\hat{\sigma}\rho_0)H\right]-\varepsilon^3\hat{\mu}\frac{\partial \rho_0}{\partial Z}\left(\hat{\gamma}\frac{\partial \bar{\eta}}{\partial X}+\frac{\partial \eta'}{\partial X}\right),\end{aligned} \tag{B.124}$$

and where H is equal to

$$H=\left[(U-c_0)\frac{\partial}{\partial \xi}+\varepsilon^2\hat{\mu}U\frac{\partial}{\partial X}+\varepsilon\frac{\partial}{\partial \tau}+\varepsilon u'\left(\frac{\partial}{\partial \xi}+\varepsilon^2\hat{\mu}\frac{\partial}{\partial X}\right)\right]^2(\hat{\gamma}\bar{\eta}+\eta'). \tag{B.125}$$

The transformation of equation (5.104) equals

$$\begin{aligned}&\left[1+\hat{\gamma}\varepsilon\frac{\partial \bar{\eta}}{\partial Z}+\varepsilon\frac{\partial \eta'}{\partial Z}\right]\left(\frac{\partial U}{\partial \xi}+\varepsilon\frac{\partial u'}{\partial \xi}+\varepsilon^2\hat{\mu}\frac{\partial U}{\partial X}+\varepsilon^3\hat{\mu}\frac{\partial u'}{\partial X}\right)\\&+\varepsilon\left[-c_0\frac{\partial}{\partial \xi}+\varepsilon\frac{\partial}{\partial \tau}+(U+\varepsilon u')\left(\frac{\partial}{\partial \xi}+\varepsilon^2\hat{\mu}\frac{\partial}{\partial X}\right)\right]\left(\hat{\gamma}\frac{\partial \bar{\eta}}{\partial Z}+\frac{\partial \eta'}{\partial Z}\right)=0,\end{aligned} \tag{B.126}$$

move all small terms ($\mathcal{O}\left(\varepsilon^2\right)$ and higher) to the right-hand side:

$$\Rightarrow\left[1+\hat{\gamma}\varepsilon\frac{\partial \bar{\eta}}{\partial Z}+\varepsilon\frac{\partial \eta'}{\partial Z}\right]\frac{\partial U}{\partial \xi}+\varepsilon\frac{\partial u'}{\partial \xi}+\varepsilon(U-c_0)\left(\frac{\partial^2(\hat{\gamma}\bar{\eta}+\eta')}{\partial \xi\partial Z}\right)=G. \tag{B.127}$$

where G is equals

$$\begin{aligned}G=&-\left[1+\hat{\gamma}\varepsilon\frac{\partial \bar{\eta}}{\partial Z}+\varepsilon\frac{\partial \eta'}{\partial Z}\right]\left(\varepsilon^2\hat{\mu}\frac{\partial U}{\partial X}+\varepsilon^3\hat{\mu}\frac{\partial u'}{\partial X}\right)-\varepsilon^2\frac{\partial}{\partial \xi}\left(u'\frac{\partial(\hat{\gamma}\bar{\eta}+\eta')}{\partial Z}\right)\\&-\varepsilon^2\frac{\partial^2(\hat{\gamma}\bar{\eta}+\eta')}{\partial \tau\partial Z}-\varepsilon^3\hat{\mu}(U+\varepsilon u')\frac{\partial^2(\hat{\gamma}\bar{\eta}+\eta')}{\partial X\partial Z}.\end{aligned} \tag{B.128}$$

Apply the transformation to the surface boundary condition yields

$$\begin{aligned}&-\varepsilon^2\hat{\sigma}\left[-\varepsilon c_0\frac{\partial u'}{\partial \xi}+\varepsilon^2\frac{\partial u'}{\partial \tau}+(U+\varepsilon u')\left(\frac{\partial U}{\partial \xi}+\varepsilon\frac{\partial u'}{\partial \xi}\right.\right.\\&\left.\left.+\varepsilon^2\hat{\mu}\frac{\partial U}{\partial X}+\varepsilon^3\hat{\mu}\frac{\partial u'}{\partial X}\right)\right]-\varepsilon^5\hat{\sigma}\left[-c_0\frac{\partial}{\partial \xi}+\varepsilon\frac{\partial}{\partial \tau}\right.\\&\left.+(U+\varepsilon u')\left(\frac{\partial}{\partial \xi}+\mu\frac{\partial}{\partial X}\right)\right]^2(\hat{\gamma}\bar{\eta}+\eta')\\&\cdot\left(\hat{\gamma}\frac{\partial \bar{\eta}}{\partial \xi}+\frac{\partial \eta'}{\partial \xi}+\varepsilon^2\hat{\mu}\hat{\gamma}\frac{\partial \bar{\eta}}{\partial X}+\varepsilon^2\hat{\mu}\frac{\partial \eta'}{\partial X}\right)=\varepsilon\left(\hat{\gamma}\frac{\partial \bar{\eta}}{\partial \xi}+\frac{\partial \eta'}{\partial \xi}+\varepsilon^2\hat{\mu}\hat{\gamma}\frac{\partial \bar{\eta}}{\partial X}+\varepsilon^2\hat{\mu}\frac{\partial \eta'}{\partial X}\right)\Big|_{Z=0},\end{aligned} \tag{B.129}$$

divide the equation by ε and put only the leading order terms at the left-hand side

$$\Rightarrow \hat{\gamma}\frac{\partial \bar{\eta}}{\partial \xi} + \frac{\partial \eta'}{\partial \xi} = -\varepsilon^2\hat{\gamma}\hat{\mu}\frac{\partial \bar{\eta}}{\partial X} - \varepsilon^2\hat{\mu}\frac{\partial \eta'}{\partial X} - \varepsilon\hat{\sigma}(U+\varepsilon u')\frac{\partial U}{\partial \xi} - \varepsilon^2\hat{\sigma}(U-c_0)\frac{\partial u'}{\partial \xi} + \varepsilon\hat{\sigma}H_1\Big|_{Z=0}, \tag{B.130}$$

where

$$H_1 = -\varepsilon^2\frac{\partial u'}{\partial \tau} - \varepsilon^2 u'\frac{\partial u'}{\partial \xi} - (U+\varepsilon u')\left(\varepsilon^2\hat{\mu}\frac{\partial U}{\partial X} + \varepsilon^3\hat{\mu}\frac{\partial u'}{\partial X}\right) - \varepsilon^3\left(\hat{\gamma}\frac{\partial \bar{\eta}}{\partial \xi} + \frac{\partial \eta'}{\partial \xi} + \varepsilon^2\hat{\mu}\hat{\gamma}\frac{\partial \bar{\eta}}{\partial X} + \varepsilon^2\hat{\mu}\frac{\partial \eta'}{\partial X}\right)H. \tag{B.131}$$

The other boundary conditions remains the same and equals

$$\hat{\gamma}\bar{\eta} + \eta' = -\hat{\gamma}h'|_{Z=-1}. \tag{B.132}$$

Solving the leading order asymptotic expansion

In (5.230)-(5.233) the system of equations for the first order was given. The governing equation can be separated using equation (5.234), which leads towards

$$\frac{\partial A}{\partial \xi}\left[\frac{\partial}{\partial Z}\left((U_0-c_0)^2\frac{\partial \Phi}{\partial Z}\right) - \frac{\partial \rho_0}{\partial Z}\Phi\right] = 0. \tag{B.133}$$

To satisfy this equation, there are two options or the first part or the second part should equal zero. When the first part equals zero, the solution to A will be constant in space. Note that $\eta'^{(0)}$ is a disturbance quantity, which means that the time averaged is zero. This implies that the only satisfying solution is the trivial zero solution. Therefore the other options is the one to solve (with the corresponding boundary conditions)

$$\frac{\partial}{\partial Z}\left((U_0-c_0)^2\frac{\partial \Phi}{\partial Z}\right) - \frac{\partial \rho_0}{\partial Z}\Phi = 0, \tag{B.134}$$

$$\Phi = 0|_{Z=0}, \tag{B.135}$$

$$\Phi = 0|_{Z=-1}. \tag{B.136}$$

This system is equal to the previous obtained system for the approximated case.

Based on equation (5.231) evaluated at the leading order the disturbance velocity can be determined

$$\frac{\partial u'^{(0)}}{\partial \xi} = -(U_0-c_0)\frac{\partial A}{\partial \xi}\frac{\partial \Phi}{\partial Z}, \tag{B.137}$$

integrate both sides to ξ

$$\Rightarrow u'^{(0)} = -(U_0-c_0)A\frac{\partial \Phi}{\partial Z} + C, \tag{B.138}$$

since $u'^{(0)}$ is a disturbance quantity the time averaged should equal zero and therefore $C = 0$

$$\Rightarrow u'^{(0)} = -(U_0-c_0)A\frac{\partial \Phi}{\partial Z}. \tag{B.139}$$

Calculation for Green's formula

Using Green's formula a compatibility condition can be found, (Haberman, 2014). Start by expanding the linear operators

$$\int_{-h}^{0}\left(L\frac{\partial \eta}{\partial \xi}\right)\Phi - (L\Phi)\frac{\partial \eta}{\partial \xi}\,dZ = \int_{-h}^{0}\left[\frac{\partial}{\partial Z}\left((U-c_0)^2\frac{\partial^2 \eta}{\partial Z \partial \xi}\right) - \frac{\partial \rho_0}{\partial Z}\frac{\partial \eta}{\partial \xi}\right]\Phi - \left[\frac{\partial}{\partial Z}\left((U-c_0)^2\frac{\partial \Phi}{\partial Z}\right) - \frac{\partial \rho_0}{\partial Z}\Phi\right]\frac{\partial \eta}{\partial \xi}\,dZ, \tag{B.140}$$

expand the multiplication between the brackets and note that the term $N^2\Phi\frac{\partial\eta}{\partial\xi}$ will vanish

$$= \int_{-h}^{0} \frac{\partial}{\partial Z}\left((U-c_0)^2\frac{\partial^2\eta}{\partial Z\partial\xi}\right)\Phi - \frac{\partial}{\partial Z}\left((U-c_0)^2\frac{\partial\Phi}{\partial Z}\right)\frac{\partial\eta}{\partial\xi}\,dZ, \tag{B.141}$$

expanding the derivatives to Z

$$= \int_{-h}^{0} \left[\frac{\partial}{\partial Z}(U-c_0)^2\frac{\partial^2\eta}{\partial Z\partial\xi}\right]\Phi + \left[(U-c_0)^2\frac{\partial^3\eta}{\partial\xi\partial Z^2}\right]\Phi - \frac{\partial}{\partial Z}\left[(U-c_0)^2\right]\frac{\partial\Phi}{\partial Z}\frac{\partial\eta}{\partial\xi}$$
$$- (U-c_0)^2\frac{\partial^2\Phi}{\partial Z^2}\frac{\partial\eta}{\partial\xi}dZ, \tag{B.142}$$

next the terms are collect for $(U-c_0)^2$

$$= \int_{-h}^{0} \frac{\partial}{\partial Z}\left[(U-c_0)^2\right]\left[\frac{\partial^2\eta}{\partial Z\partial\xi}\Phi - \frac{\partial\Phi}{\partial Z}\frac{\partial\eta}{\partial\xi}\right] + (U-c_0)^2\left[\frac{\partial^3\eta}{\partial\xi\partial Z^2}\Phi - \frac{\partial^2\Phi}{\partial Z^2}\frac{\partial\eta}{\partial\xi}\right]\,dZ, \tag{B.143}$$

the derivative to Z can be extracted from the last term

$$= \int_{-h}^{0} \frac{\partial}{\partial Z}\left[(U-c_0)^2\right]\left[\frac{\partial^2\eta}{\partial Z\partial\xi}\Phi - \frac{\partial\Phi}{\partial Z}\frac{\partial\eta}{\partial\xi}\right] + (U-c_0)^2\frac{\partial}{\partial Z}\left[\frac{\partial^2\eta}{\partial Z\partial\xi}\Phi - \frac{\partial\Phi}{\partial Z}\frac{\partial\eta}{\partial\xi}\right]\,dZ, \tag{B.144}$$

now the derivate to Z can be rewritten as

$$= \int_{-h}^{0} \frac{\partial}{\partial Z}\left\{\left[(U-c_0)^2\right]\left[\frac{\partial^2\eta}{\partial Z\partial\xi}\Phi - \frac{\partial\Phi}{\partial Z}\frac{\partial\eta}{\partial\xi}\right]\right\}\,dZ, \tag{B.145}$$

by the fundamental theorem of calculus, this simplifies to

$$= (U-c_0)^2\left[\frac{\partial^2\eta}{\partial Z\partial\xi}\Phi - \frac{\partial\Phi}{\partial Z}\frac{\partial\eta}{\partial\xi}\right]\Bigg|_{Z=-h}^{0}, \tag{B.146}$$

which can be rewritten as

$$= (U-c_0)^2\left[\frac{\partial^2\eta}{\partial Z\partial\xi}\Phi - \frac{\partial\Phi}{\partial Z}\frac{\partial\eta}{\partial\xi}\right]\Bigg|_{Z=0} - (U-c_0)^2\left[\frac{\partial^2\eta}{\partial Z\partial\xi}\Phi - \frac{\partial\Phi}{\partial Z}\frac{\partial\eta}{\partial\xi}\right]\Bigg|_{Z=-h}. \tag{B.147}$$

Calculation for the compatibility condition

Before that the compatibility condition is determined, the integral value of different parts of M will be investigated. Start using integration by parts on the first part

$$\int_{-1}^{0}\left[\frac{\partial}{\partial Z}\left\{\frac{\partial u'^{(0)}}{\partial\tau} + u'^{(0)}\frac{\partial u'^{(0)}}{\partial\xi}\right\}\right]\Phi\,dZ = \left\{\frac{\partial u'^{(0)}}{\partial\tau} + u'^{(0)}\frac{\partial u'^{(0)}}{\partial\xi}\right\}\Phi\Bigg|_{Z=-1}^{0},$$
$$- \int_{-1}^{0}\left[\frac{\partial u'^{(0)}}{\partial\tau} + u'^{(0)}\frac{\partial u'^{(0)}}{\partial\xi}\right]\frac{\partial\Phi}{\partial Z}\,dZ, \tag{B.148}$$

note that $\Phi = 0$ on the boundaries and therefore

$$= -\int_{-1}^{0}\left[\frac{\partial u'^{(0)}}{\partial\tau} + u'^{(0)}\frac{\partial u'^{(0)}}{\partial\xi}\right]\frac{\partial\Phi}{\partial Z}\,dZ, \tag{B.149}$$

use the solution of $u'^{(0)}$ (5.239)

$$= \int_{-1}^{0} (U_0 - c_0) \frac{\partial A}{\partial \tau} \left(\frac{\partial \Phi}{\partial Z} \right)^2 - (U_0 - c_0)^2 A \frac{\partial A}{\partial \xi} \left(\frac{\partial \Phi}{\partial Z} \right)^3 \, dZ, \tag{B.150}$$

take the terms of A outside the integral

$$= \frac{\partial A}{\partial \tau} \int_{-1}^{0} (U_0 - c_0) \left(\frac{\partial \Phi}{\partial Z} \right)^2 \, dZ - A \frac{\partial A}{\partial \xi} \int_{-1}^{0} (U_0 - c_0)^2 \left(\frac{\partial \Phi}{\partial Z} \right)^3 \, dZ. \tag{B.151}$$

The solution of $\eta'^{(0)}$ from (5.234) can be used to evaluate the second part of M

$$- \int_{-1}^{0} \left[\frac{\partial}{\partial \xi} \left[(U_0 - c_0) \frac{\partial}{\partial \xi} \right]^2 \eta'^{(0)} \right] \Phi \, dZ = - \int_{-1}^{0} (U_0 - c_0)^2 \frac{\partial^3 A}{\partial \xi^3} \Phi^2 \, dZ, \tag{B.152}$$

as A is independent of Z this part can be put in front of the integral

$$= - \frac{\partial^3 A}{\partial \xi^3} \int_{-1}^{0} (U_0 - c_0)^2 \Phi^2 \, dZ. \tag{B.153}$$

Finally the third and last part of M is considered

$$- \int_{-1}^{0} \frac{\partial}{\partial Z} \left[(U_0 - c_0) \left(\frac{\partial}{\partial \xi} \left(u'^{(0)} \frac{\partial \eta'^{(0)}}{\partial Z} \right) + \hat{\gamma} \frac{\partial u'^{(0)}}{\partial \xi} \frac{\partial \bar{\eta}^{(0)}}{\partial Z} + \frac{\partial^2 \eta'^{(0)}}{\partial \tau \partial Z} \right) \right] \Phi \, dZ, \tag{B.154}$$

start by applying integration by parts

$$\begin{aligned} &= -(U_0 - c_0) \left(\frac{\partial}{\partial \xi} \left(u'^{(0)} \frac{\partial \eta'^{(0)}}{\partial Z} \right) + \hat{\gamma} \frac{\partial u'^{(0)}}{\partial \xi} \frac{\partial \bar{\eta}^{(0)}}{\partial Z} + \frac{\partial^2 \eta'^{(0)}}{\partial \tau \partial Z} \right) \Phi \Big|_{Z=-1}^{0} \\ &+ \int_{-1}^{0} \left[(U_0 - c_0) \left(\frac{\partial}{\partial \xi} \left(u'^{(0)} \frac{\partial \eta'^{(0)}}{\partial Z} \right) + \hat{\gamma} \frac{\partial u'^{(0)}}{\partial \xi} \frac{\partial \bar{\eta}^{(0)}}{\partial Z} + \frac{\partial^2 \eta'^{(0)}}{\partial \tau \partial Z} \right) \right] \frac{\partial \Phi}{\partial Z} \, dZ, \end{aligned} \tag{B.155}$$

use the solution of $\eta'^{(0)}$ (5.234) and $u'^{(0)}$ (5.239),

$$= \int_{-1}^{0} -2(U_0 - c_0)^2 A \frac{\partial A}{\partial \xi} \left(\frac{\partial \Phi}{\partial Z} \right)^3 - \hat{\gamma} (U_0 - c_0)^2 \frac{\partial A}{\partial \xi} \left(\frac{\partial \Phi}{\partial Z} \right)^2 \frac{\partial \bar{\eta}^{(0)}}{\partial Z} + (U_0 - c_0) \frac{\partial A}{\partial \tau} \left(\frac{\partial \Phi}{\partial Z} \right)^2 \, dZ, \tag{B.156}$$

write the parts independent of Z in front of the integral

$$= -2A \frac{\partial A}{\partial \xi} \int_{-1}^{0} (U_0 - c_0)^2 \left(\frac{\partial \Phi}{\partial Z} \right)^3 \, dZ - \hat{\gamma} \frac{\partial A}{\partial \xi} \int_{-1}^{0} (U_0 - c_0)^2 \left(\frac{\partial \Phi}{\partial Z} \right)^2 \frac{\partial \bar{\eta}^{(0)}}{\partial Z} \, dZ + \frac{\partial A}{\partial \tau} \int_{-1}^{0} (U_0 - c_0) \left(\frac{\partial \Phi}{\partial Z} \right)^2 \, dZ. \tag{B.157}$$

Using the left-hand side of equation (5.253), first note that the second part is zero since (5.252) and use (5.251)

$$\int_{-1}^{0} \left(L \frac{\partial \eta'^{(1)}}{\partial \xi} \right) \Phi - (L\Phi) \frac{\partial \eta'^{(1)}}{\partial \xi} dZ = \int_{-1}^{0} M \Phi \, dZ, \tag{B.158}$$

apply the definition of M

$$= \int_{-1}^{0} \left[\frac{\partial}{\partial Z} \left\{ \frac{\partial u'^{(0)}}{\partial \tau} + u'^{(0)} \frac{\partial u'^{(0)}}{\partial \xi} \right\} - \frac{\partial}{\partial \xi} \left[(U_0 - c_0) \frac{\partial}{\partial \xi} \right]^2 \eta'^{(0)} \right.$$
$$\left. - \frac{\partial}{\partial Z} \left\{ (U_0 - c_0) \left(\frac{\partial}{\partial \xi} \left(u'^{(0)} \frac{\partial \eta'^{(0)}}{\partial Z} \right) + \frac{\partial^2 \eta'^{(0)}}{\partial \tau \partial Z} \right) \right\} \right] \Phi \, dZ, \tag{B.159}$$

using equation (B.151), (B.153) and (B.157) this is equal to

$$= 2 \frac{\partial A}{\partial \tau} \int_{-1}^{0} (U_0 - c_0) \left(\frac{\partial \Phi}{\partial Z} \right)^2 dZ - 3A \frac{\partial A}{\partial \xi} \int_{-1}^{0} (U_0 - c_0)^2 \left(\frac{\partial \Phi}{\partial Z} \right)^3 dZ$$
$$- \frac{\partial^3 A}{\partial \xi^3} \int_{-1}^{0} (U_0 - c_0)^2 \Phi^2 \, dZ - \hat{\gamma} \frac{\partial A}{\partial \xi} \int_{-1}^{0} (U_0 - c_0)^2 \left(\frac{\partial \Phi}{\partial Z} \right)^2 \frac{\partial \bar{\eta}^{(0)}}{\partial Z} \, dZ. \tag{B.160}$$

When this result is combined with equation (5.253) a compatibility condition is found, which is a KdV equation adjusted for a sloping bed. This equation is given by

$$\frac{\partial A}{\partial \tau} + c_h \frac{\partial A}{\partial \xi} + \alpha_1 A \frac{\partial A}{\partial \xi} + \beta_1 \frac{\partial^3 A}{\partial \xi^3} = 0, \tag{B.161}$$

where the constants are given by

$$c_h = \frac{\hat{\gamma}}{2} \frac{\int_{-1}^{0} (c_0 - U_0)^2 \left(\frac{\partial \Phi}{\partial Z} \right)^2 \frac{\partial \bar{\eta}^{(0)}}{\partial Z} \, dZ}{\int_{-1}^{0} (c_0 - U_0) \left(\frac{\partial \Phi}{\partial Z} \right)^2 dZ}, \tag{B.162}$$

$$\alpha_1 = \frac{3}{2} \frac{\int_{-1}^{0} (c_0 - U_0)^2 \left(\frac{\partial \Phi}{\partial Z} \right)^3 dZ}{\int_{-1}^{0} (c_0 - U_0) \left(\frac{\partial \Phi}{\partial Z} \right)^2 dZ}, \tag{B.163}$$

$$\beta_1 = \frac{1}{2} \frac{\int_{-1}^{0} (c_0 - U_0)^2 \Phi^2 \, dZ}{\int_{-1}^{0} (c_0 - U_0) \left(\frac{\partial \Phi}{\partial Z} \right)^2 dZ}. \tag{B.164}$$

C

KdV solution calculations

In the following sections the calculations for the solution of the KdV equation are given. This as detail of the solution derivation as presented in chapter 6.

C.1. Analytical calculations for the Taylor-Goldstein equation

The solution of Taylor-Goldstein equation will first being calculated for two cases where an analytic answer can obtained. After that the QEP approach will be discussed.

Two-layer system without shear flow

The two-layer system described in section 6.1.1 will be solved. A sketch of this situation is shown in figure C.1. The density (in full dimensional form) is given by the following function

$$\rho = \rho_2 - (\rho_2 - \rho_1)H\left(z + h_1\right), \tag{C.1}$$

where H is the Heaviside function. Furthermore there will be no shear flow present in the system, in other words

$$U(z) = 0. \tag{C.2}$$

The expression for the density (C.1) can be transformed and scaled such that it is in the form of equation

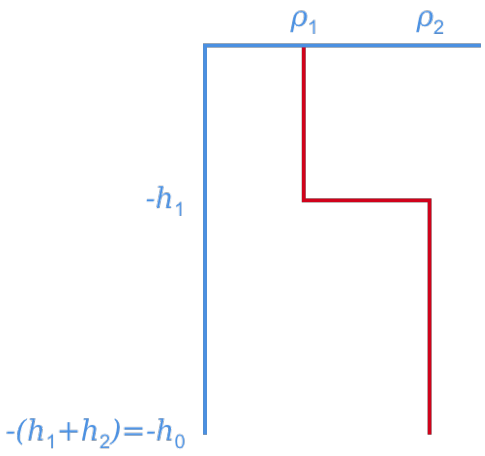

Figure C.1: Density structure in a two-layer system

(5.39). Start by making the first term equal to the mean density

$$\rho = \frac{\rho_1 + \rho_2}{2} + \frac{\rho_2 - \rho_1}{2} - (\rho_2 - \rho_1)H(z + h_1). \tag{C.3}$$

Combine the terms with the density difference and use the definition of the Boussinesq parameter (5.31). This leads to

$$\rho = \bar{\rho}\left[1 + \sigma\left(\frac{1}{2} - H(z + h_1)\right)\right]. \tag{C.4}$$

Here the relevant constants are defined as

$$\bar{\rho} = \frac{\rho_1 + \rho_2}{2}, \tag{C.5}$$

$$\sigma = \frac{\rho_2 - \rho_1}{\bar{\rho}}. \tag{C.6}$$

This implies that ρ_0 as the scaled density variation is given by

$$\rho_0 = \frac{1}{2} - H\left(Z + \frac{h_1}{h_0}\right). \tag{C.7}$$

This expression for ρ_0 can now be used in equation (6.1), which results in

$$c_0^2 \frac{\partial^2 \Phi}{\partial Z^2} + \delta\left(Z + \frac{h_1}{h_0}\right)\Phi = 0. \tag{C.8}$$

The solution can be determined on two interiors: $-\frac{h_1}{h_0} < Z < 0$ (I) and $-1 < Z- < \frac{h_1}{h_0}$ (II). At the pycnocline ($Z = -\frac{h_1}{h_0}$) the solution is assumed to be continuous. This can be accomplished by requiring that the limit of Φ when Z tends to $-\frac{h_1}{h_0}$ from below is the same as the limit from above. This can be expressed in the following condition

$$\Phi|_{Z=-h_1/h_0^+} = \Phi|_{Z=-h_1/h_0^-}. \tag{C.9}$$

In each interior the governing equation is given by, from (C.8),

$$c_0^2 \frac{\partial^2 \Phi}{\partial Z^2} = 0. \tag{C.10}$$

The general solution to this problem is equal to, where i can be I or II depending on the interior of interest

$$\Phi^i = A^i + B^i Z. \tag{C.11}$$

Applying the top boundary (6.2) to the first interior yields

$$A^I = 0, \tag{C.12}$$

and using the bottom boundary (6.3) for the second part will give

$$A^{II} = B^{II}. \tag{C.13}$$

The solutions for both interiors are now given by

$$\Phi^I = B^I Z, \tag{C.14}$$

$$\Phi^{II} = B^{II}(Z + 1). \tag{C.15}$$

Using the continuity condition around the pycnocline (C.9) with these solutions, will give

$$-B^I \frac{h_1}{h_0} = B^{II}\left(1 - \frac{h_1}{h_0}\right), \tag{C.16}$$

divide by $-\frac{h_1}{h_0}\left(1 - \frac{h_1}{h_0}\right)$ and define a new constant C

$$\Rightarrow \frac{B^I}{1 - \frac{h_1}{h_0}} = \frac{B^{II}}{-\frac{h_1}{h_0}} =: C. \tag{C.17}$$

Using this definition of C, the solutions for the two interiors equals

$$\Phi^I = C\left(1 - \frac{h_1}{h_0}\right)Z, \tag{C.18}$$

$$\Phi^{II} = C\frac{h_1}{h_0}(1 - Z). \tag{C.19}$$

Next integrate equation (6.1) around the pycnocline

$$\int_{-h_1/h_0-\varepsilon}^{-h_1/h_0+\varepsilon} c_0^2 \frac{\partial^2 \Phi}{\partial Z^2} + \delta\left(Z + h_1/h_0\right)\Phi dZ = 0, \tag{C.20}$$

where $\varepsilon > 0$. Calculating the integral value, where the delta peak will give just one value of Φ, yields

$$\Rightarrow c_0^2 \left.\frac{\partial \Phi}{\partial Z}\right|_{Z=-h_1/h_0-\varepsilon}^{-h_1/h_0+\varepsilon} + \Phi|_{Z=-h_1/h_0} = 0, \tag{C.21}$$

using the solutions for both interiors and evaluate at $-\frac{h_1}{h_0}$ (note that ε drops out of the equation and the limited can also dropped)

$$\Rightarrow c_0^2\left[C\left(1 - \frac{h_1}{h_0}\right) + C\frac{h_1}{h_0}\right] - C\left(1 - \frac{h_1}{h_0}\right)\frac{h_1}{h_0} = 0, \tag{C.22}$$

reorder the terms in the equation, giving

$$\Rightarrow C\left[c_0^2 - \left(1 - \frac{h_1}{h_0}\right)\frac{h_1}{h_0}\right] = 0. \tag{C.23}$$

From this points there are two options. The first is $C = 0$, which will give the not interesting trivial solution. The other option, where the relation between the layer depths is used, is given by

$$\Rightarrow c_0^2 = \left(1 - \frac{h_1}{h_0}\right)\frac{h_1}{h_0} = \frac{h_1 h_2}{h_0^2}, \tag{C.24}$$

take the square root of the expression yields

$$\Rightarrow c_0^{\pm} = \pm\sqrt{\frac{h_1 h_2}{h_0^2}}. \tag{C.25}$$

As referenced earlier only the right-going waves are of interest, so from now on only the positive eigenvalue will be considered.

The eigenfunction will be normalized, such that (6.4) holds. The maximum of the function is at the pycnocline (see the piecewise solution in (C.18) and (C.19)), C is therefore equal to

$$C = \frac{1}{-\frac{h_1}{h_0}\left(1-\frac{h_1}{h_0}\right)}. \tag{C.26}$$

The solution for the eigenfunction Φ is now given by

$$\Phi = \begin{cases} -\frac{h_0}{h_1}Z & \text{for } -\frac{h_1}{h_0} \leq Z \leq 0, \\ \frac{h_0}{h_2}(Z+1) & \text{for } -1 \leq Z \leq -\frac{h_1}{h_0}. \end{cases} \tag{C.27}$$

Next the constants for the KdV are evaluated. To simplify the expressions it convenient to define

$$I := 2\int_{-1}^{0} c_0 \left(\frac{\partial \Phi}{\partial Z}\right)^2 dZ. \tag{C.28}$$

Now start evaluating the constants

$$\alpha_1 I = 3\int_{-1}^{0} c_0^2 \left(\frac{\partial \Phi}{\partial Z}\right)^3 dZ, \tag{C.29}$$

split the integral over the two interiors and use the piecewise solutions

$$\alpha_1 I = 3c_0^2\left[\int_{-1}^{-h_1/h_0}\left(\frac{h_0}{h_2}\right)^3 dZ + \int_{-h_1/h_0}^{0}\left(-\frac{h_0}{h_1}\right)^3 dZ\right], \tag{C.30}$$

calculate the integral value

$$\alpha_1 I = 3c_0^2\left[\frac{h_2}{h_0}\frac{h_0^3}{h_2^3} - \frac{h_1}{h_0}\frac{h_0^3}{h_1^3}\right], \tag{C.31}$$

simplify the expression

$$\alpha_1 I = 3c_0^2\left[\frac{h_0^2}{h_2^2} - \frac{h_0^2}{h_1^2}\right], \tag{C.32}$$

combine the two fractions into one fraction

$$\alpha_1 I = 3c_0^2\frac{h_0^2\left(h_1^2 - h_2^2\right)}{h_1^2 h_2^2}. \tag{C.33}$$

The next expression to be evaluated reads

$$\beta_1 I = \int_{-1}^{0} c_0^2 \Phi^2 dZ, \tag{C.34}$$

split the integral and evaluate the function

$$\beta_1 I = c_0^2\left[\int_{-1}^{-h_1/h_0}\frac{h_0^2}{h_2^2}(1+Z)^2 dZ + \int_{-h_1/h_0}^{0}\frac{h_0^2}{h_1^2}Z^2 dZ\right], \tag{C.35}$$

the integrals are equal to

$$\beta_1 I = c_0^2\left[\frac{h_0^2}{h_2^2}\frac{1}{3}\left(\left(1-\frac{h_1}{h_0}\right)^3 - (1-1)^3\right) + \frac{h_0^2}{h_1^2}\frac{1}{3}\left(0^3 - \left(-\frac{h_1}{h_0}\right)^3\right)\right], \tag{C.36}$$

remove all zero's from the equation and simplify the fractions

$$\beta_1 I = \frac{1}{3} c_0^2 \left[\frac{h_2}{h_0} + \frac{h_1}{h_0} \right], \tag{C.37}$$

using that the the two layers sum up to the total water depth

$$\beta_1 I = \frac{1}{3} c_0^2. \tag{C.38}$$

Finally I needs to be calculated, start by the definition

$$I = 2 \int_{-1}^{0} c_0 \left(\frac{\partial \Phi}{\partial Z} \right)^2 dZ, \tag{C.39}$$

again split the integral and use the values from the solution (C.27)

$$I = 2c_0 \left[\int_{-1}^{-h_1/h_0} \left(\frac{h_0}{h_2} \right)^2 dZ + \int_{-h_1/h_0}^{0} \left(-\frac{h_0}{h_1} \right)^2 dZ \right], \tag{C.40}$$

evaluate the integral

$$I = 2c_0 \left[\frac{h_2}{h_0} \frac{h_0^2}{h_2^2} + \frac{h_1}{h_0} \frac{h_0^2}{h_1^2} \right], \tag{C.41}$$

simplify the fractions

$$I = 2c_0 \left[\frac{h_0}{h_2} + \frac{h_0}{h_1} \right], \tag{C.42}$$

combine into one fraction

$$I = 2c_0 \frac{h_0 (h_1 + h_2)}{h_1 h_2}, \tag{C.43}$$

using equation the sum of the two layer depths

$$I = 2c_0 \frac{h_0^2}{h_1 h_2}. \tag{C.44}$$

Now the constants α_1 and β_1 can be evaluated, start by the first one, using (C.33) and (C.44)

$$\alpha_1 = \frac{3}{2} c_0 \frac{h_1^2 - h_2^2}{h_1 h_2}, \tag{C.45}$$

use the sum of the two layer depths

$$\alpha_1 = \frac{3}{2} c_0 \frac{h_1^2 - (h_0 - h_1)^2}{h_1 h_2}, \tag{C.46}$$

expanding the quadratic term will give

$$\alpha_1 = \frac{3}{2} c_0 \frac{h_1^2 - h_0^2 - h_1^2 + 2h_0 h_1}{h_1 h_2}, \tag{C.47}$$

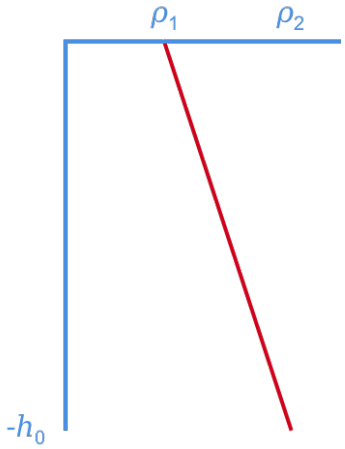

Figure C.2: Density structure in a system with linear stratification

group the terms by h_0

$$\alpha_1 = \frac{3}{2} c_0 \frac{h_0(2h_1 - h_0)}{h_1 h_2}, \tag{C.48}$$

use again the sum of the two layer depths

$$\alpha_1 = \frac{3}{2} c_0 \frac{h_0(h_1 - h_2)}{h_1 h_2}. \tag{C.49}$$

Finally evaluate β_1, using (C.38) and (C.44)

$$\beta_1 = \frac{1}{6} c_0 \frac{h_1 h_2}{h_0^2}. \tag{C.50}$$

Using equations (5.265), (5.267) and (5.268), the full dimensional constants can be obtained

$$C_0 = \sqrt{\sigma g h_0} \sqrt{\frac{h_1 h_2}{h_0^2}} = \sqrt{\frac{\sigma g h_1 h_2}{h_0}}, \tag{C.51}$$

$$\mathrm{A}_1 = \frac{\sqrt{\sigma g h_0}}{h_0} \frac{3}{2} c_0 \frac{h_0(h_1 - h_2)}{h_1 h_2} = \frac{3}{2} C_0 \frac{h_1 - h_2}{h_1 h_2}, \tag{C.52}$$

$$\mathrm{B}_1 = \sqrt{\sigma g h_0} h_0^2 \frac{1}{6} c_0 \frac{h_1 h_2}{h_0^2} = \frac{1}{6} C_0 h_1 h_2. \tag{C.53}$$

Linear stratification without shear flow

In this case the density is described by the following function (in full dimensional form)

$$\rho = \rho_1 - (\rho_2 - \rho_1) \frac{z}{h_0}. \tag{C.54}$$

In figure C.2 a sketch of the system is given.

The formula for the density can now also be written similar to (5.39). Start by bringing the mean density at front

$$\rho = \frac{\rho_1 + \rho_2}{2} - \frac{\rho_2 - \rho_1}{2} - (\rho_2 - \rho_1) \frac{z}{h_0}. \tag{C.55}$$

Now group the density difference of the second and third term and use the definition of the Boussinesq parameter (5.31)

$$\rho = \bar{\rho}\left[1 + \sigma\left(-\frac{1}{2} - \frac{z}{h_0}\right)\right]. \tag{C.56}$$

The definition of $\bar{\rho}$ is here the same as for the two-layer system. Now the scaled density variation can be obtained

$$\rho_0 = -\frac{1}{2} - Z. \tag{C.57}$$

Using this definition the corresponding derivative equals

$$\frac{\partial \rho_0}{\partial Z} = -1. \tag{C.58}$$

The equation to solve is now given by

$$c_0^2 \frac{\partial^2 \Phi}{\partial Z^2} + \Phi = 0, \tag{C.59}$$

subject to the two boundary conditions

$$\Phi = 0|_{Z=0}, \tag{C.60}$$
$$\Phi = 0|_{Z=-1}. \tag{C.61}$$

For this boundary value problem of problem, it is known that the eigenfunctions are given by a series of sine functions, (Haberman, 2014). The solution can be written as

$$\Phi = \sum_{n=1}^{\infty} A^k \sin(n\pi Z), \tag{C.62}$$

where the corresponding eigenvalues are given by

$$c_0^{k,\pm} = \pm\frac{1}{k\pi}. \tag{C.63}$$

Also in this case only the positive modes will be considered, as the left-going waves are not of interest.

Assume that only one certain mode (n) is present in the system then $A^n = -1$ and the other constants are zero. This such that the condition of (6.4) is satisfied. The eigenfunctions are now given by

$$\Phi^n = -\sin(n\pi Z). \tag{C.64}$$

Now the KdV constants can be determined, using the same definition for I as before (C.28). Starting by the first expression

$$\alpha_1^n I^n = 3\int_{-1}^{0} \left(c_0^n\right)^2 \left(\frac{\partial \Phi^n}{\partial Z}\right)^3 dZ, \tag{C.65}$$

evaluate the derivative

$$\alpha_1^n I^n = 3\left(c_0^n\right)^2 (n\pi)^3 \int_{-1}^{0} -\cos^3(n\pi Z) dZ, \tag{C.66}$$

the integral value equals zero and so

$$\alpha_1^n I^n = 0. \tag{C.67}$$

Now the next expression can be evaluated

$$\beta_1^n I^n = \int_{-1}^{0} \left(c_0^n\right)^2 \left(\Phi^n\right)^2 dZ, \tag{C.68}$$

using the value for the eigenfunction

$$\beta_1^n I^n = \left(c_0^n\right)^2 \int_{-1}^{0} \sin^2(n\pi Z) dZ, \tag{C.69}$$

the integral value equals $\frac{1}{2}$ and so

$$\beta_1^n I^n = \frac{1}{2}\left(c_0^n\right)^2. \tag{C.70}$$

Finally evaluate I^n for each eigenfunction, start by using the definition

$$I^n = 2\int_{-1}^{0} c_0^n \left(\frac{\partial \Phi^n}{\partial Z}\right)^2 dZ, \tag{C.71}$$

evaluate the derivative of the eigenfunction

$$I^n = 2c_0^n (n\pi)^2 \int_{-1}^{0} \cos^2(n\pi Z) dZ, \tag{C.72}$$

the integral value is equal to $\frac{1}{2}$, and using the value of c_0^n can be obtained that

$$I^n = \frac{1}{c_0^n}. \tag{C.73}$$

The KdV constants can now being obtained from the previous evaluations. For α_1 using (C.67) and (C.73)

$$\alpha_1^n = 0, \tag{C.74}$$

and next use (C.70) in combination with (C.73)

$$\beta_1^n = \frac{1}{2}\left(c_0^n\right)^3. \tag{C.75}$$

Finally the full-dimensional equation is obtained using (5.265), (5.267) and (5.268)

$$C_0^n = \frac{\sqrt{\sigma g h_0}}{n\pi}, \tag{C.76}$$

$$\mathrm{A}_1^n = 0, \tag{C.77}$$

$$\mathrm{B}_1^n = \sqrt{\sigma g h_0} h_0^2 \frac{1}{2}\left(c_0^n\right)^3 = \frac{1}{2}\frac{h_0}{\sigma g}\left(C_0^n\right)^3. \tag{C.78}$$

C.2. Numerical calculations for the Taylor-Goldstein equation

The TGE will be solved numerically using the QEP approach. Here the discretization and setup of the matrix-vector problem will be discussed.

Rewriting problem (6.1), where first U_m is introduced yields

$$\frac{\partial}{\partial Z}\left([(U_0 - U_m) - (c_0 - U_m)]^2 \frac{\partial \Phi}{\partial Z}\right) - \frac{\partial \rho_0}{\partial Z}\Phi = 0, \tag{C.79}$$

calculate the derivative

$$\Rightarrow [(U_0 - U_m) - (c_0 - U_m)]^2 \frac{\partial^2 \Phi}{\partial Z^2} + 2[(U_0 - U_m) - (c_0 - U_m)] \frac{\partial U_0}{\partial Z} \frac{\partial \Phi}{\partial Z} - \frac{\partial \rho_0}{\partial Z} \Phi = 0, \tag{C.80}$$

expand the squared parts of the equation

$$\begin{aligned} \Rightarrow (c_0 - U_m))^2 \frac{\partial^2 \Phi}{\partial Z^2} - (c_0 - U_m) 2(U_0 - U_m) \frac{\partial^2 \Phi}{\partial Z^2} - 2(c_0 - U_m) \frac{\partial U_0}{\partial Z} \frac{\partial \Phi}{\partial Z} \\ + (U_0 - U_m)^2 \frac{\partial^2 \Phi}{\partial Z^2} + 2(U_0 - U_m) \frac{\partial U_0}{\partial Z} \frac{\partial \Phi}{\partial Z} - \frac{\partial \rho_0}{\partial Z} \Phi = 0. \end{aligned} \tag{C.81}$$

Let N be the number of unknowns in the interior and denote these locations by Z_i. Z_0 and Z_{N+1} will be the locations of the boundaries. On an equidistant grid, the locations of the grid points are given by

$$Z_i = -1 + \frac{i}{N+1}. \tag{C.82}$$

Sometimes the midpoint of the grid cell needs to be used to determine the value of the derivatives. That location is given by

$$Z_{i+\frac{1}{2}} = \frac{Z_{i+1} + Z_i}{2}. \tag{C.83}$$

The size of a specific grid cell is given by

$$\Delta Z_i = Z_i - Z_{i-1}. \tag{C.84}$$

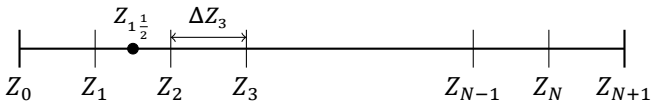

Figure C.3: Computational grid

The discrete vector representing the function Φ is defined as

$$\Phi' = \begin{bmatrix} \Phi(Z_1) \\ \Phi(Z_2) \\ \vdots \\ \Phi(Z_N) \end{bmatrix}. \tag{C.85}$$

Equation (C.81) can now discretized, where the eigenvalue is defined as

$$\lambda = c_0 - U_m. \tag{C.86}$$

The discrete equation is given by

$$\lambda^2 A_2 \Phi' + \lambda C_1 A_2 \Phi' + \lambda C_2 A_1 \Phi' + K_1 A_2 \Phi' + K_2 A_1 \Phi' + K_3 \Phi' = 0, \tag{C.87}$$

where the discrete operators (matrices) are now introduced for each term. First the operators for the differentials of Φ are given. For the second order derivative central differences will be used, so A_2 will be given by equation

$$A_2 := \begin{bmatrix} -(\mu_{1,2} + \mu_{2,1}) & \mu_{2,1} & & & \\ \mu_{2,3} & -(\mu_{2,3} + \mu_{3,2}) & \mu_{3,2} & & \\ & \ddots & \ddots & \ddots & \\ & & \mu_{N,N+1} & -(\mu_{N,N+1} + \mu_{N+1,N}) & \end{bmatrix}. \tag{C.88}$$

In this matrix the variable $\mu_{i,j}$ is defined as

$$\mu_{i,j} := \frac{2}{\Delta Z_i(\Delta Z_i + \Delta Z_j)}. \tag{C.89}$$

The first order derivative will be approximated with central differences, therefore matrix A_1 is given by

$$A_1 := \begin{bmatrix} 0 & \nu_1 & & \\ -\nu_2 & 0 & \nu_2 & \\ & \ddots & \ddots & \ddots \\ & & -\nu_N & 0 \end{bmatrix}, \tag{C.90}$$

where ν_i in this matrix is defined as

$$\nu_i := \frac{1}{\Delta Z_i + \Delta Z_{i+1}}. \tag{C.91}$$

Next all terms in equation (C.87) will be discussed. The first term has only the squared eigenvalue in front of the second order partial derivative. The second term is multiplied by $2(U_0 - U_m)$ and so the discrete version should be multiplied by

$$C_1 = -2\begin{bmatrix} U_0(Z_1) - U_m & & & \\ & U_0(Z_2) - U_m & & \\ & & \ddots & \\ & & & U_0(Z_N) - U_m \end{bmatrix}. \tag{C.92}$$

The third term is a first order derivative multiplied by $2\frac{\partial U_0}{\partial Z}$ the discrete version is than given by: $C_2 A_1$ where

$$C_2 = -2\begin{bmatrix} \frac{\partial U_0}{\partial Z}(Z_1) & & & \\ & \frac{\partial U_0}{\partial Z}(Z_2) & & \\ & & \ddots & \\ & & & \frac{\partial U_0}{\partial Z}(Z_N) \end{bmatrix}. \tag{C.93}$$

The fourth term is the second order derivative of Φ times $(U_0 - U_m)^2$ so K_1 is given by

$$K_1 = \begin{bmatrix} (U_0(Z_1) - U_m)^2 & & & \\ & (U_0(Z_2) - U_m)^2 & & \\ & & \ddots & \\ & & & (U_0(Z_N) - U_m)^2 \end{bmatrix}. \tag{C.94}$$

The next term is $2(U_0 - U_m)\frac{\partial U_0}{\partial Z}\frac{\partial \Phi}{\partial Z}$. The discrete version is equivalent to $K_2 A_1$ and so

$$K_2 = 2\begin{bmatrix} (U_0(Z_1) - U_m)\frac{\partial U_0}{\partial Z}(Z_1) & & & \\ & (U_0(Z_2) - U_m)\frac{\partial U_0}{\partial Z}(Z_2) & & \\ & & \ddots & \\ & & & (U_0(Z_N) - U_m)\frac{\partial U_0}{\partial Z}(Z_N) \end{bmatrix}. \tag{C.95}$$

The sixth and last term is the value of the density derivative and is given by

$$K_3 = -\begin{bmatrix} \frac{\partial \rho_0}{\partial Z}(Z_1) & & & \\ & \frac{\partial \rho_0}{\partial Z}(Z_2) & & \\ & & \ddots & \\ & & & \frac{\partial \rho_0}{\partial Z}(Z_N) \end{bmatrix}. \tag{C.96}$$

Combining the different matrices of (C.87) yields

$$\left(\lambda^2 M + \lambda C + K\right)\Phi' = 0, \tag{C.97}$$

where the matrices are given by

$$M = A_2, \tag{C.98}$$
$$C = C_1 A_2 + C_2 A_1, \tag{C.99}$$
$$K = K_1 A_2 + K_2 A_1 + K_3. \tag{C.100}$$

C.3. Numerical calculations for determining the KdV constants

Note that Φ is known on all points Z_i for $0 \leq i \leq N+1$, and also c_0 is now known. U_0 and $\frac{\partial U_0}{\partial Z}$ are analytic functions or can be interpolated based on the available dataset. This means that these values can be evaluated at every point.

To determine the constants three values need to be evaluated: $\alpha_1 I$, $\beta_1 I$ and I, for the definition of I see (C.28). The first expression is defined as

$$\alpha_1 I = 3\int_{-1}^{0} (c_0 - U_0)^2 \left(\frac{\partial \Phi}{\partial Z}\right)^3 dZ, \tag{C.101}$$

using the midpoint rule for numerical integration, this yields

$$\alpha_1 I = 3\sum_{i=0}^{N} \Delta Z_{i+1} \left[c_0 - U_0\left(Z_{i+\frac{1}{2}}\right)\right]^2 \left[\frac{\partial \Phi}{\partial Z}\left(Z_{i+\frac{1}{2}}\right)\right]^3, \tag{C.102}$$

use a central difference approximation for the derivative of Φ

$$\alpha_1 I = 3\sum_{i=0}^{N} \Delta Z_{i+1} \left[c_0 - U_0\left(Z_{i+\frac{1}{2}}\right)\right]^2 \left[\frac{\Phi(Z_{i+1}) - \Phi(Z_i)}{\Delta Z_{i+1}}\right]^3. \tag{C.103}$$

Start by using the definition of $\beta_1 I$

$$\beta_1 I = \int_{-1}^{0} (c_0 - U_0)^2 \Phi^2 dZ, \tag{C.104}$$

apply the trapezoidal rule for integration

$$\beta_1 I = \left[\frac{\Delta Z_1}{2}(c_0 - U_0(Z_0))^2 \Phi(Z_0) + \frac{\Delta Z_{N+1}}{2}(c_0 - U_0(Z_{N+1}))^2 \Phi(Z_{N+1}) + \sum_{i=1}^{N} \frac{\Delta Z_{i+1} + \Delta Z_i}{2}(c_0 - U_0(Z_i))^2 (\Phi(Z_i))^2\right], \tag{C.105}$$

note that the boundary values of Φ are zero, so the equation reduces to

$$\beta_1 I = \sum_{i=1}^{N} \frac{\Delta Z_{i+1} + \Delta Z_i}{2}(c_0 - U_0(Z_i))^2 (\Phi(Z_i))^2. \tag{C.106}$$

Next approximate the value of I

$$I = 2\int_{-1}^{0} (c_0 - U_0)\left(\frac{\partial \Phi}{\partial Z}\right)^2 dZ, \tag{C.107}$$

approximate the integral, using the midpoint rule

$$I = 2\sum_{i=0}^{N} \Delta Z_{i+1}\left[c_0 - U_0\left(Z_{i+\frac{1}{2}}\right)\right]\left[\frac{\partial \Phi}{\partial Z}\left(Z_{i+\frac{1}{2}}\right)\right]^2, \tag{C.108}$$

approximate the derivative with a central difference, yields

$$I = 2\sum_{i=0}^{N} \Delta Z_{i+1}\left[c_0 - U_0\left(Z_{i+\frac{1}{2}}\right)\right]\left[\frac{\Phi(Z_{i+1}) - \Phi(Z_i)}{\Delta Z_{i+1}}\right]^2. \tag{C.109}$$

Finally approximate $c_h I$

$$c_h I = \hat{\gamma}\int_{-1}^{0} (c_0 - U_0)^2 \left(\frac{\partial \Phi}{\partial Z}\right)^2 \left(-h\frac{\partial g}{\partial Z}\right) dZ, \tag{C.110}$$

using the midpoint rule for integration

$$c_h I = \hat{\gamma}\sum_{i=0}^{N} \Delta Z_{i+1}\left[c_0 - U_0\left(Z_{i+\frac{1}{2}}\right)\right]^2\left[\frac{\partial \Phi}{\partial Z}\left(Z_{i+\frac{1}{2}}\right)\right]^2\left[-h\frac{\partial g}{\partial Z}\left(Z_{i+\frac{1}{2}}\right)\right], \tag{C.111}$$

approximate the derivative with a central difference, yields

$$c_h I = \hat{\gamma}\sum_{i=0}^{N} \Delta Z_{i+1}\left[c_0 - U_0\left(Z_{i+\frac{1}{2}}\right)\right]^2\left[\frac{\Phi(Z_{i+1}) - \Phi(Z_i)}{\Delta Z_{i+1}}\right]^2\left[h\frac{g(Z_i) - g(Z_{i+1})}{\Delta Z_{i+1}}\right]. \tag{C.112}$$

With these three results, the constants α_1, β_1 and c_h can be easily obtained. The full dimensional version of this constants can now be determined using the relations from (5.265)-(5.268).

D

Delft3D model run validation

The results from the new model runs is checked against the reference model and the measurement data from Rijnsburger et al. (2019a).

In figures D.1 and D.2 is shown that the sea surface height in all new model runs (with 48 layers) is equal to the reference model. This means that the model offset (relative to the measurements) is the same in this new cases. This difference is on average 0.2 [m] for both stations and the maximum difference is approximately 0.5 [m]. The order of magnitude of the different models for the salinity one meter below the surface is equal to the measurements. The models with four grids show a better timing of the density jumps (when the river plume is passing the observation points) than the model with only three grids. It can also be seen that the results of the 4 grid model with 48 layers and $\Delta t = 0.8$ [min] is closest to the reference run. The salinity at $2.5 - 3$ [m] below the surface shows a good agreement between the models and the measurement data. Near the bed the salinity structure of the measurements is followed by all models, but there a constant offset of about 2 [psu] is found. From this analysis no conclusion could be drawn which model performs better compared to the measurements.

At neap tide the salinity and velocity is given in figure D.3 for station M12 and in D.4 for M18. It could be seen that the salinity has a more smooth behavior in the models with 48 layers. The salinity offset as observed earlier near the bottom can also be found here. In the alongshore velocity of the measurements and the models the tidal signal can clearly be obtained. The magnitude of this flow has in all cases a maximum of 1.0 [m/s]. The cross-shore velocity for the M18 station shows in all cases approximately the same flow structure and magnitude. The magnitude of this velocity in the four grid models is in better agreement with the measurements, as the magnitude in the three grid model is smaller. At M12 the structure of the cross-shore velocity in the three grid model is different to the other model runs and the measurements. The four grid models and the measurements have most of the time opposite directed velocities in the water column, while the three grids have longer periods where the flow is in the same direction. The velocity structure of the models with $\Delta t = 0.8$ [min] are closest to what was observed in the measurements. Therefore the four grid model with 48 layers and the smallest time step is considered as the best model available.

During spring tide (figure D.4 and D.6) the water columns are well-mixed during low waters. This while the measurements show a small density variation. In the results of the three grid model at M12 a massive fresh bulb is passing at day 269. This bulb is not visible in any other model and the measurements. The models with a time step of only 0.8 [min] are less mixed and have a higher salt content in the bottom layer, when compared to the other two models. This means, that the models with a small time step are in better agreement with the measurements. At M18 the effect of the ROFI is not clearly visible in any of the models, while the measurements of the surface layer show a plume passing most of the tidal cycles. The alongshore velocity at both locations shows a good agreement with the measurements, the reference model and all models with 48 layers. For M12 the cross-shore velocity in the models is not as strong as obtained from the measurements. The flow pattern in the results from three grids is strange compared to the other results. The structure of a cross-shore flow with opposite directed layers

Figure unavailable until publication of Rijnsburger, et al. (2019a)

Figure D.1: Sea surface height and salinity at multiple depths - M12 (mbs = meters below surface).

Figure unavailable until publication of Rijnsburger, et al. (2019a)

Figure D.2: Sea surface height and salinity at multiple depths - M18 (mbs = meters below surface).

Figure unavailable until publication of Rijnsburger, et al. (2019a)

Figure D.3: Salinity and velocity comparison at neap tide - M12 (a-c: measurements; d-f: reference model; g-i: 3 grids, 48 layers; j-l: 4 grids, 48 layers, $\Delta t = 2$; m-o: 4 grids, 48 layers, $\Delta t = 0.8$).

Figure unavailable until publication of Rijnsburger, et al. (2019a)

Figure D.4: Salinity and velocity comparison at neap tide - M18 (a-c: measurements; d-f: reference model; g-i: 3 grids, 48 layers; j-l: 4 grids, 48 layers, $\Delta t = 2$; m-o: 4 grids, 48 layers, $\Delta t = 0.8$).

is best obtained in the model with four grids, 48 layers and $\Delta t = 0.8$ [min]. At M18 the magnitude of the cross-shore flow is of the same order for all models as in the measurements. The flow pattern also differs, where the two-layer split is best obtained in the latest model.

In figure D.7 the surface salinity and velocity of the reference model and the new model runs are given for multiple times on September, 28th. The velocity at most points is in the same order of magnitude and more or less in the same direction. The three grid model shows a completely different result for the surface salinity compared to the other models. The plume is fresher in this case and less detail can be obtained in the structure of the Rhine ROFI. When the models with four grids are compared with each other, no clear difference can be found.

In all three new model runs the basic properties of the Rhine ROFI are captured. When compared to the measurements the model with four grids and $\Delta t = 0.8$ [min] shows the best agreement. As the vertical structure is better resolved in the model with 48 layers this model is chosen to use in further analysis.

Figure unavailable until publication of Rijnsburger, et al. (2019a)

Figure D.5: Salinity and velocity comparison at spring tide - M12 (a-c: measurements; d-f: reference model; g-i: 3 grids, 48 layers; j-l: 4 grids, 48 layers, $\Delta t = 2$; m-o: 4 grids, 48 layers, $\Delta t = 0.8$).

Figure unavailable until publication of Rijnsburger, et al. (2019a)

Figure D.6: Salinity and velocity comparison at spring tide - M18 (a-c: measurements; d-f: reference model; g-i: 3 grids, 48 layers; j-l: 4 grids, 48 layers, $\Delta t = 2$; m-o: 4 grids, 48 layers, $\Delta t = 0.8$).

Figure unavailable until publication of Rijnsburger, et al. (2019a)

Figure D.7: Surface salinity and velocity comparison.

E

Additional figures

E.1. Figures belonging to 8. Delft3D model results

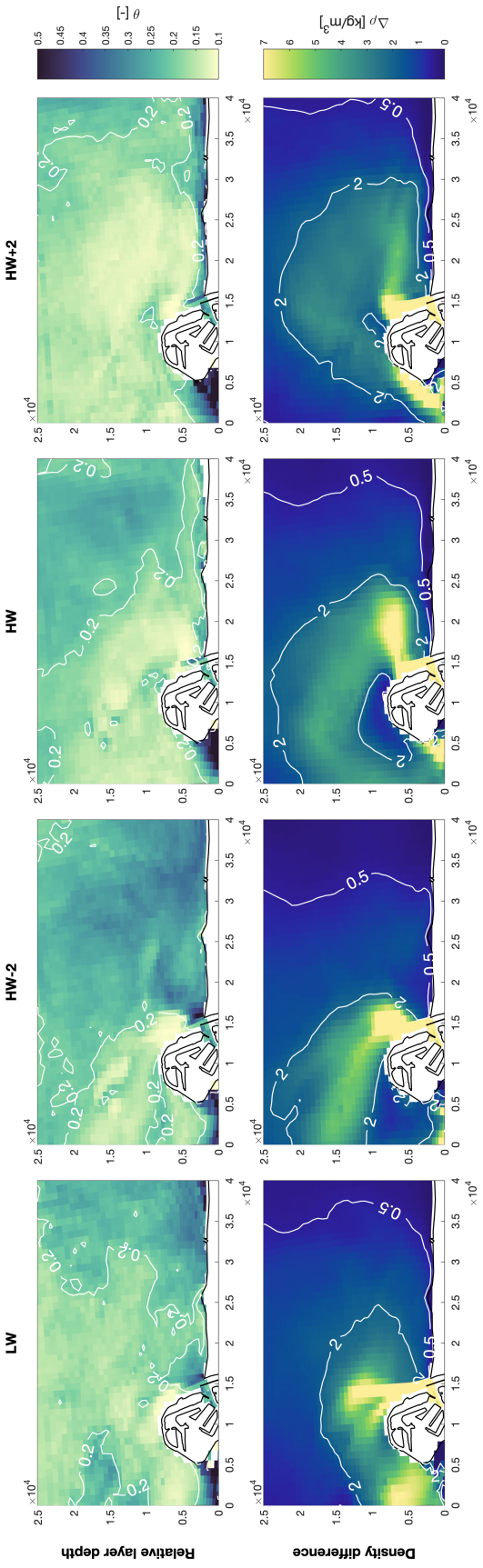

Figure E.1: Mean value of relative layer depth and density difference for multiple M_2 tidal stages (July, 10th - August, 8th).

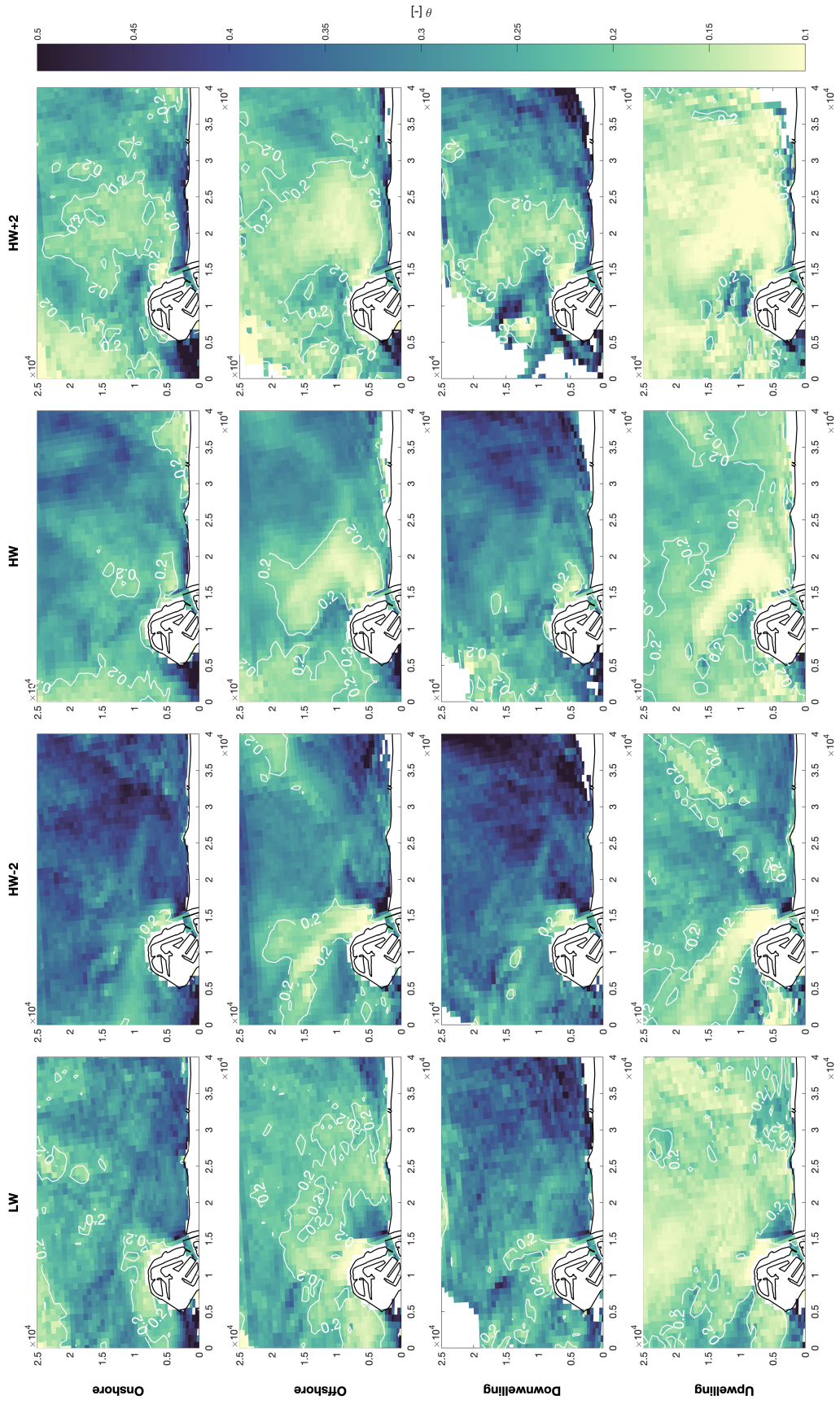

Figure E.2: Mean value of relative layer depth for multiple M_2 tidal stages for multiple wind directions.

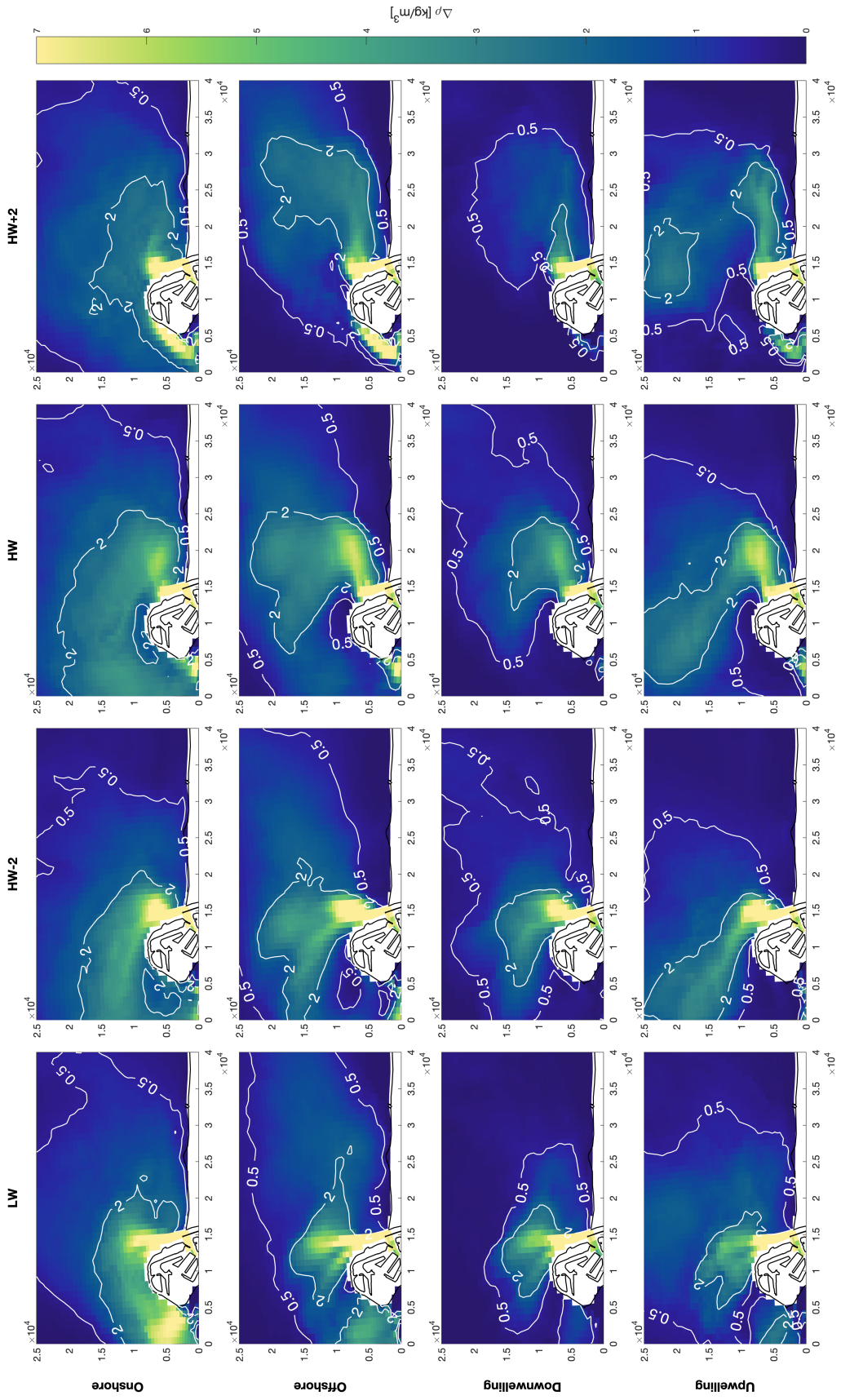

Figure E.3: Mean value of density difference for multiple M_2 tidal stages for multiple wind directions.

E.2. Figures belonging to 11. Environmental variation of internal waves

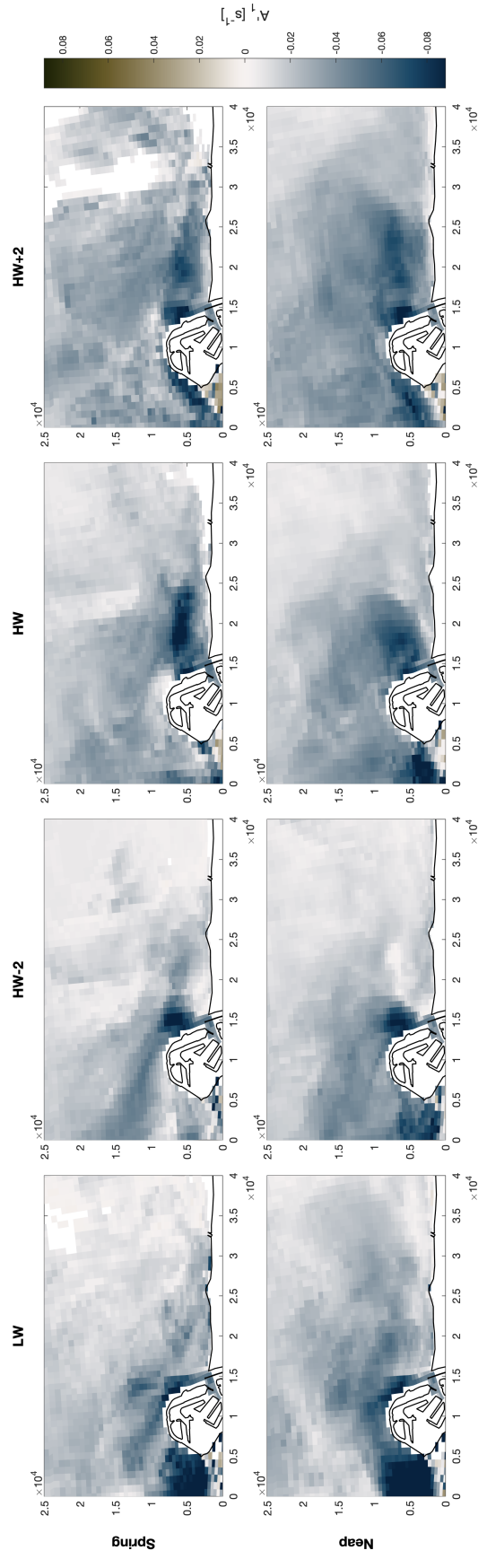

Figure E.4: Mean value of A'_1 without shear-flow for multiple M_2 tidal stages during spring and neap tide.

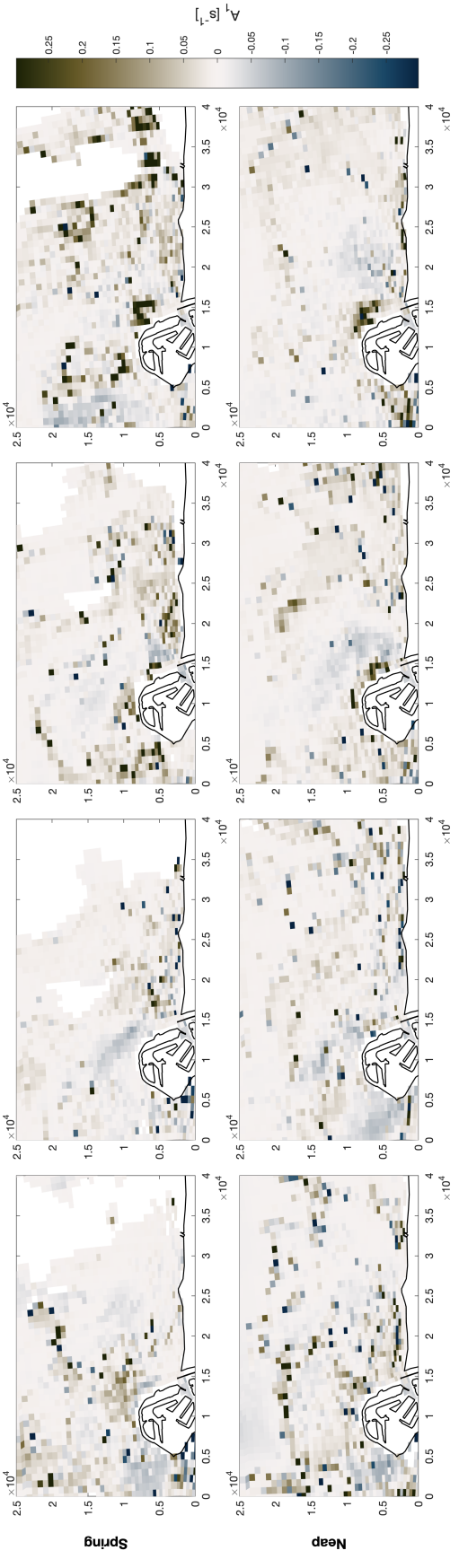

Figure E.5: Mean value of A_1 with shear-flow in the flow direction of the upper layer for multiple M_2 tidal stages during spring and neap tide.

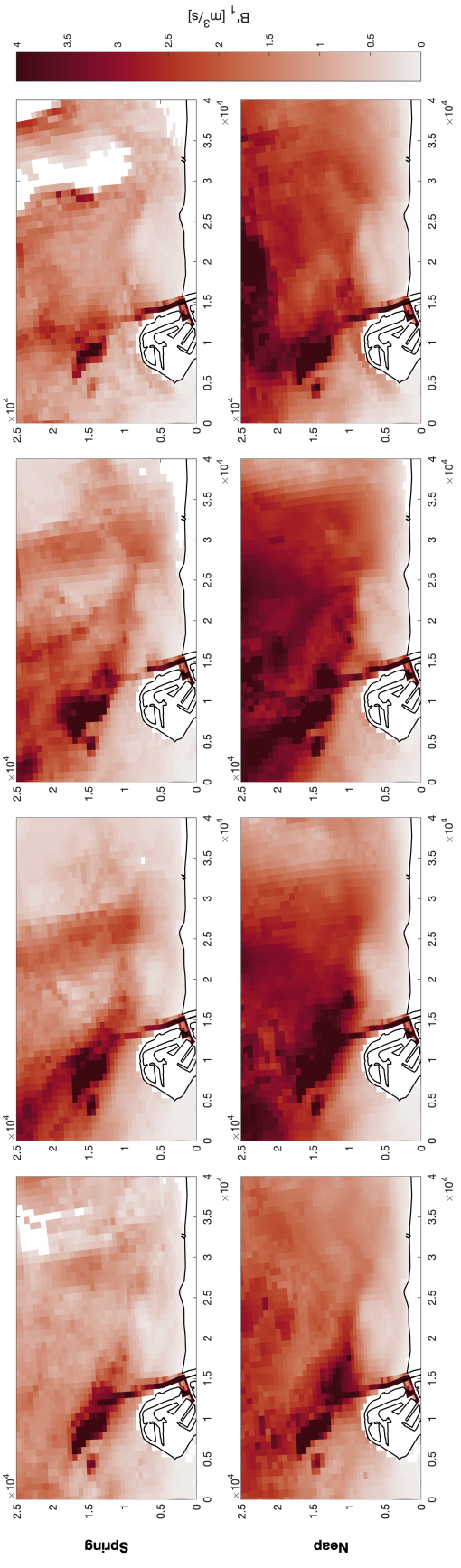

Figure E.6: Mean value of B_1' without shear-flow for multiple M_2 tidal stages during spring and neap tide.

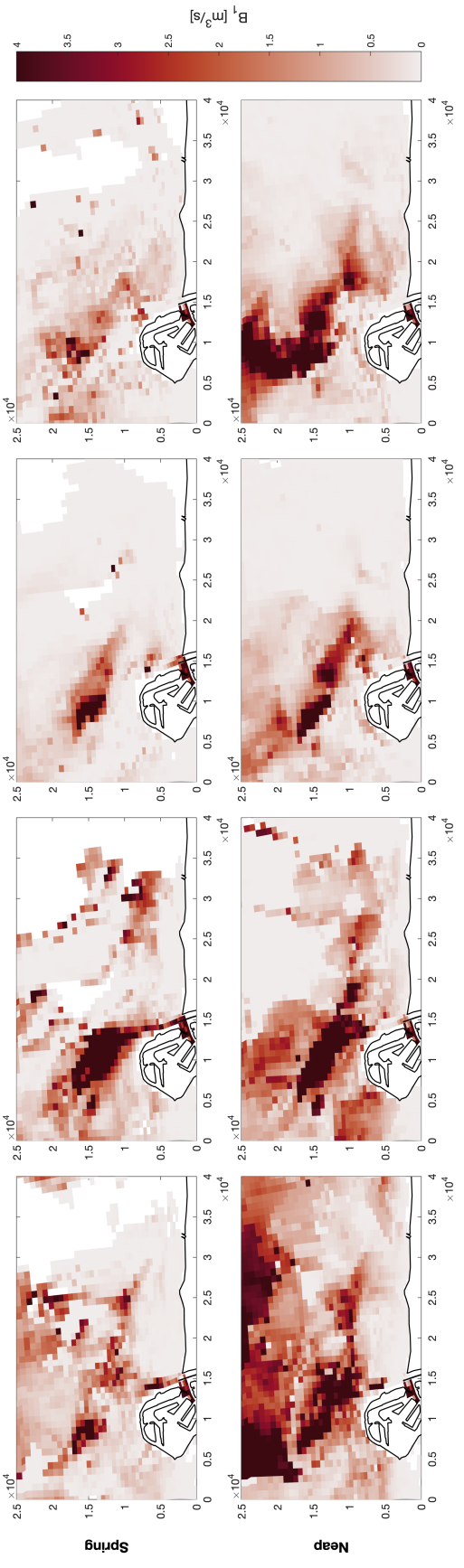

Figure E.7: Mean value of B_1 with shear-flow in the flow direction of the upper layer for multiple M_2 tidal stages during spring and neap tide.

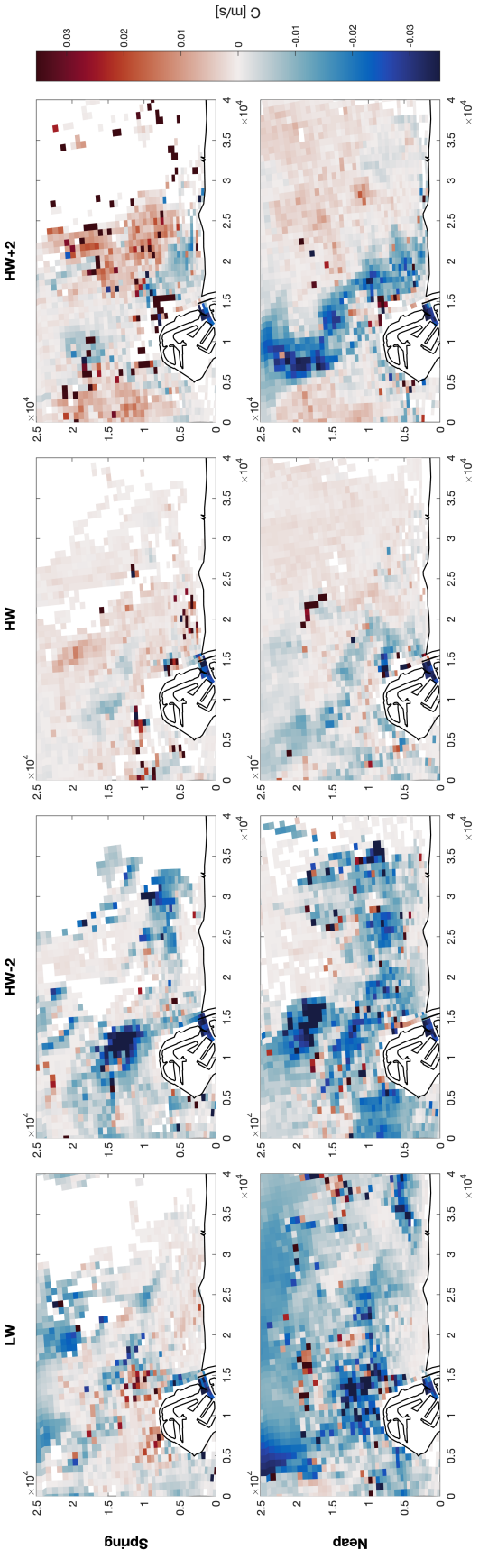

Figure E.8: Mean value of the traveling wave velocity C with shear-flow in the flow direction of the upper layer for multiple M_2 tidal stages during spring and neap tide.

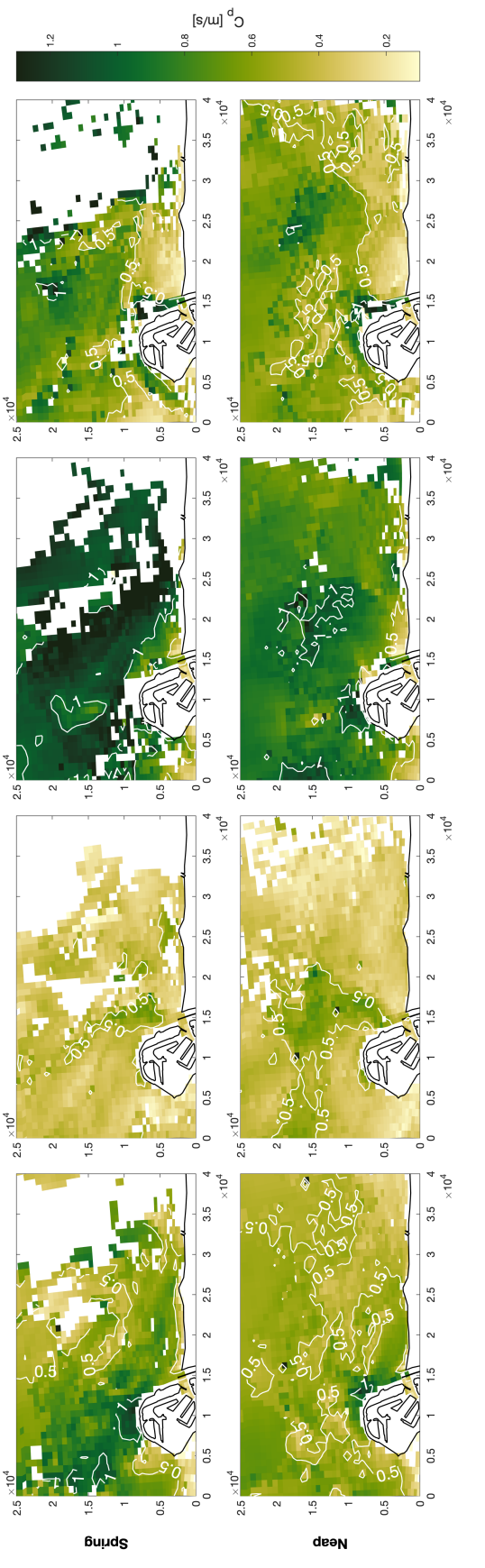

Figure E.9: Mean value of the total propagation speed C_p with shear-flow in the flow direction of the upper layer for multiple M_2 tidal stages during spring and neap tide.

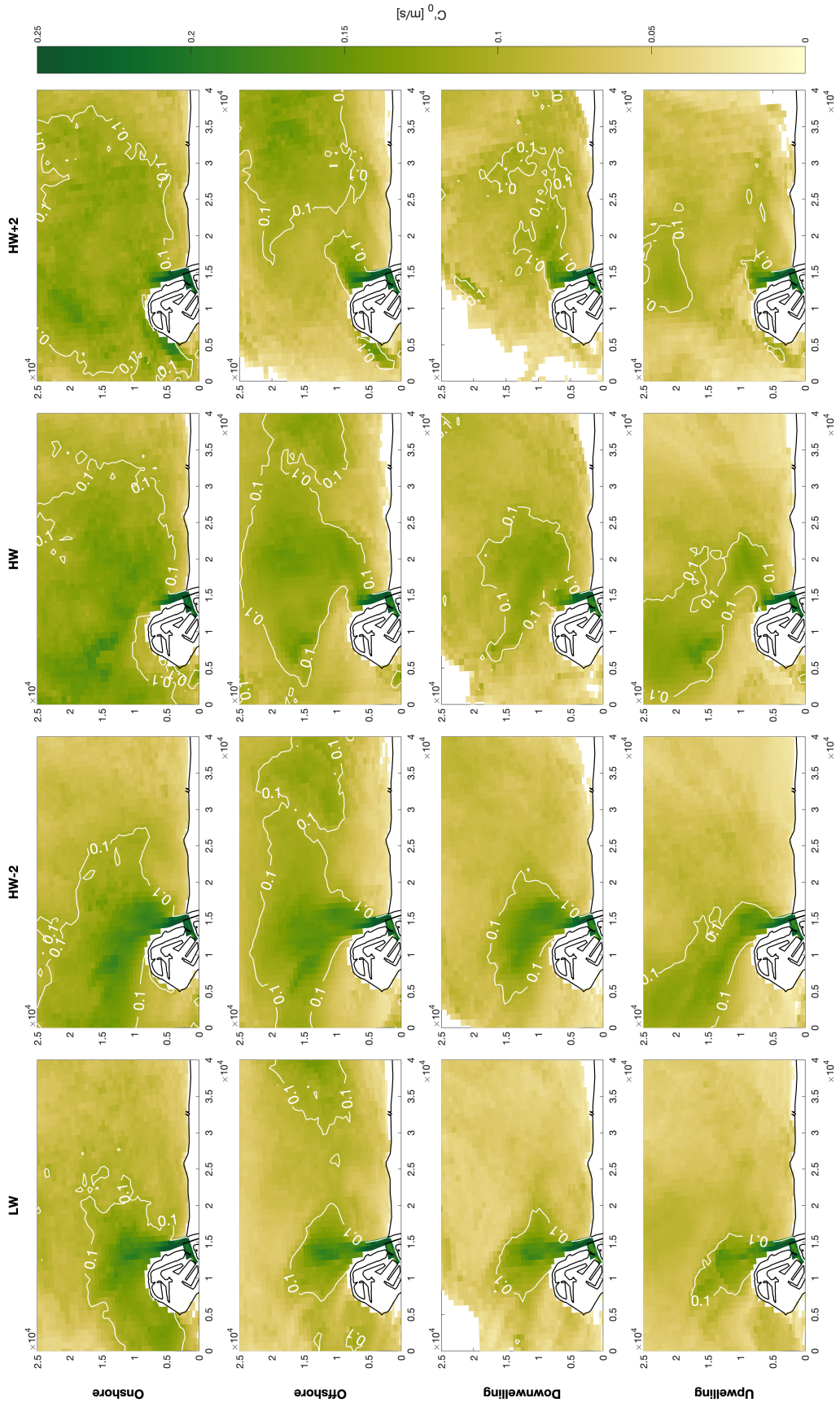

Figure E.10: Mean value of c_0' without shear-flow for multiple M_2 tidal stages for multiple wind directions.

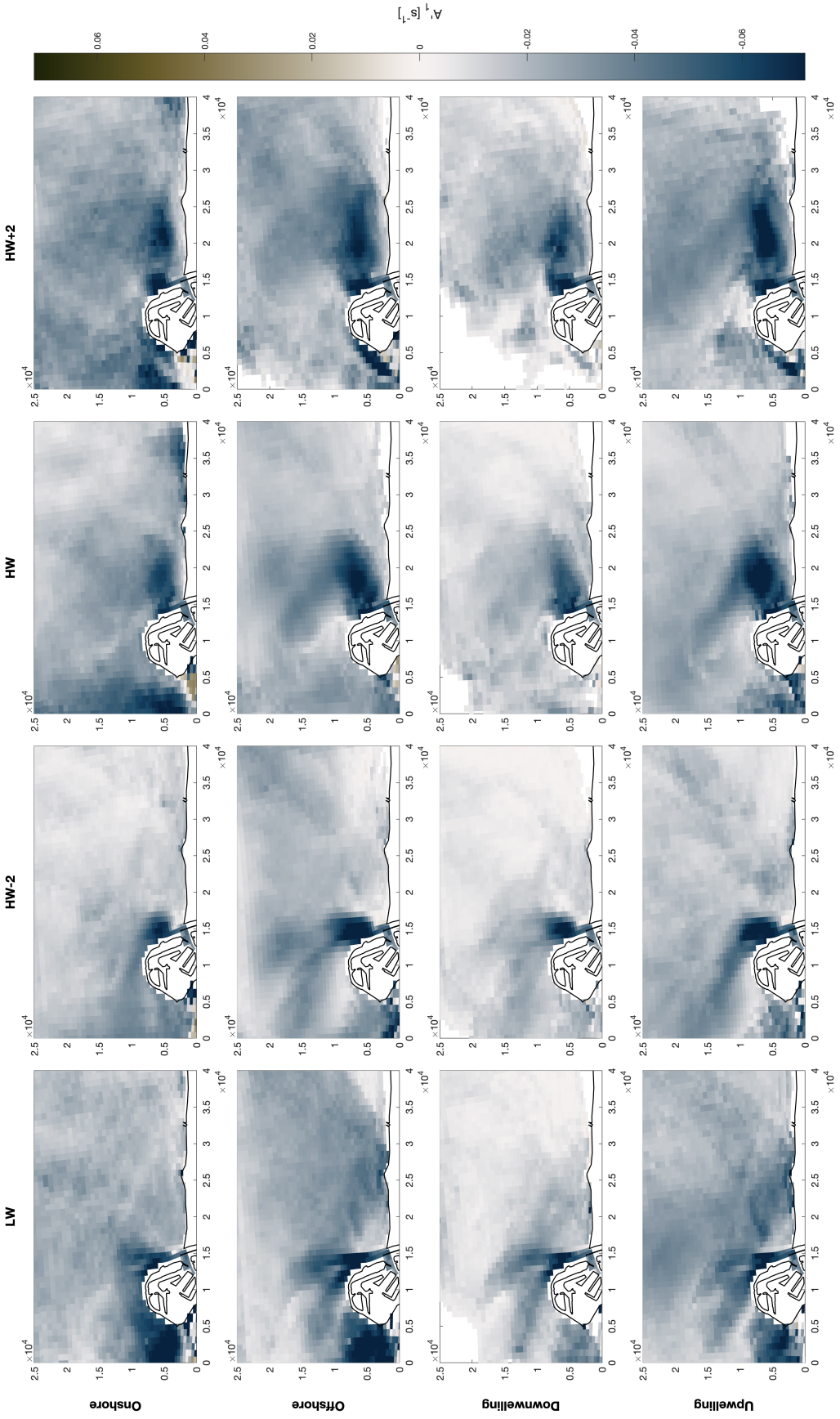

Figure E.11: Mean value of A_1' without shear-flow for multiple M_2 tidal stages for multiple wind directions.

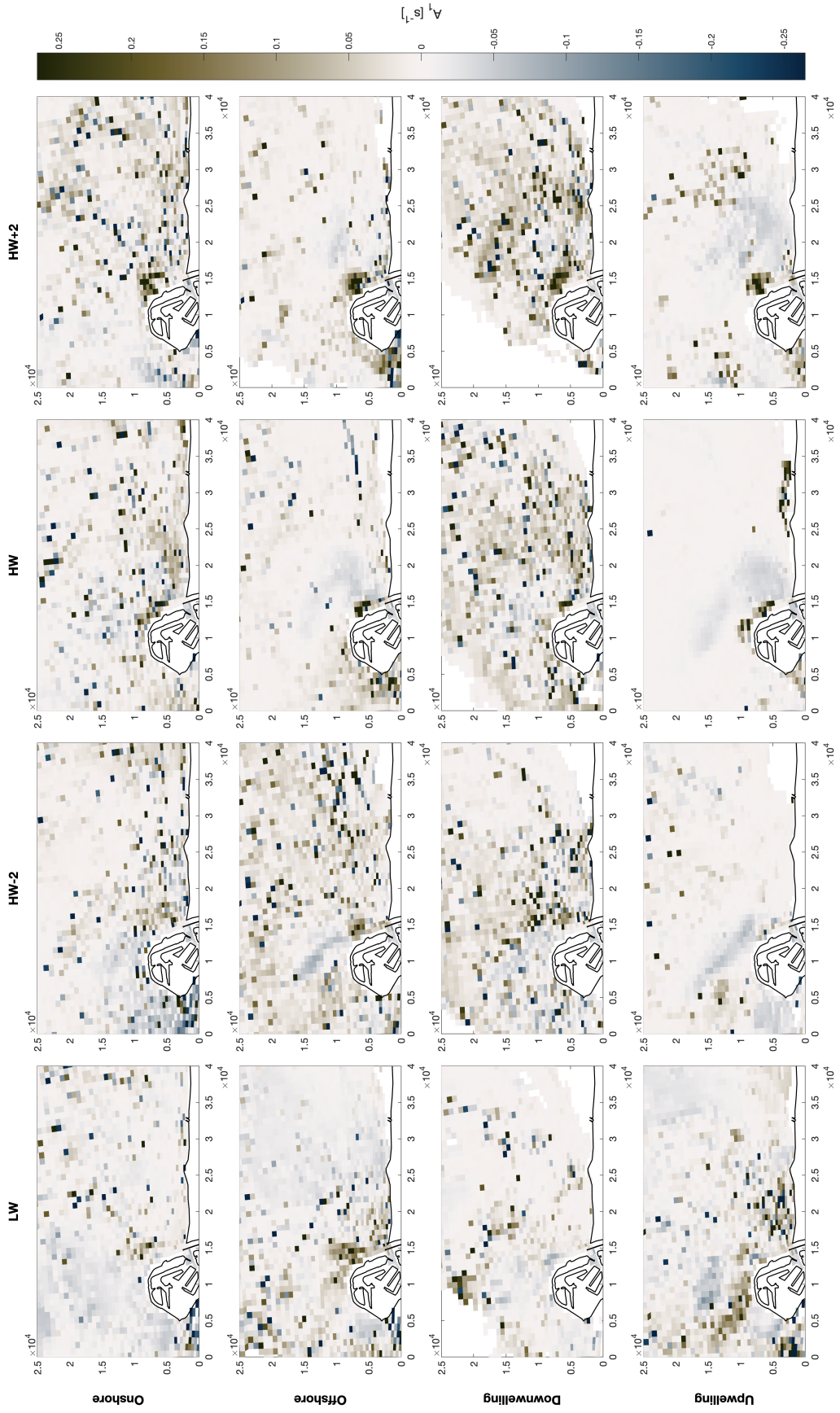

Figure E.12: Mean value of A_1 with shear-flow in the flow direction of the upper layer for multiple M_2 tidal stages for multiple wind directions.

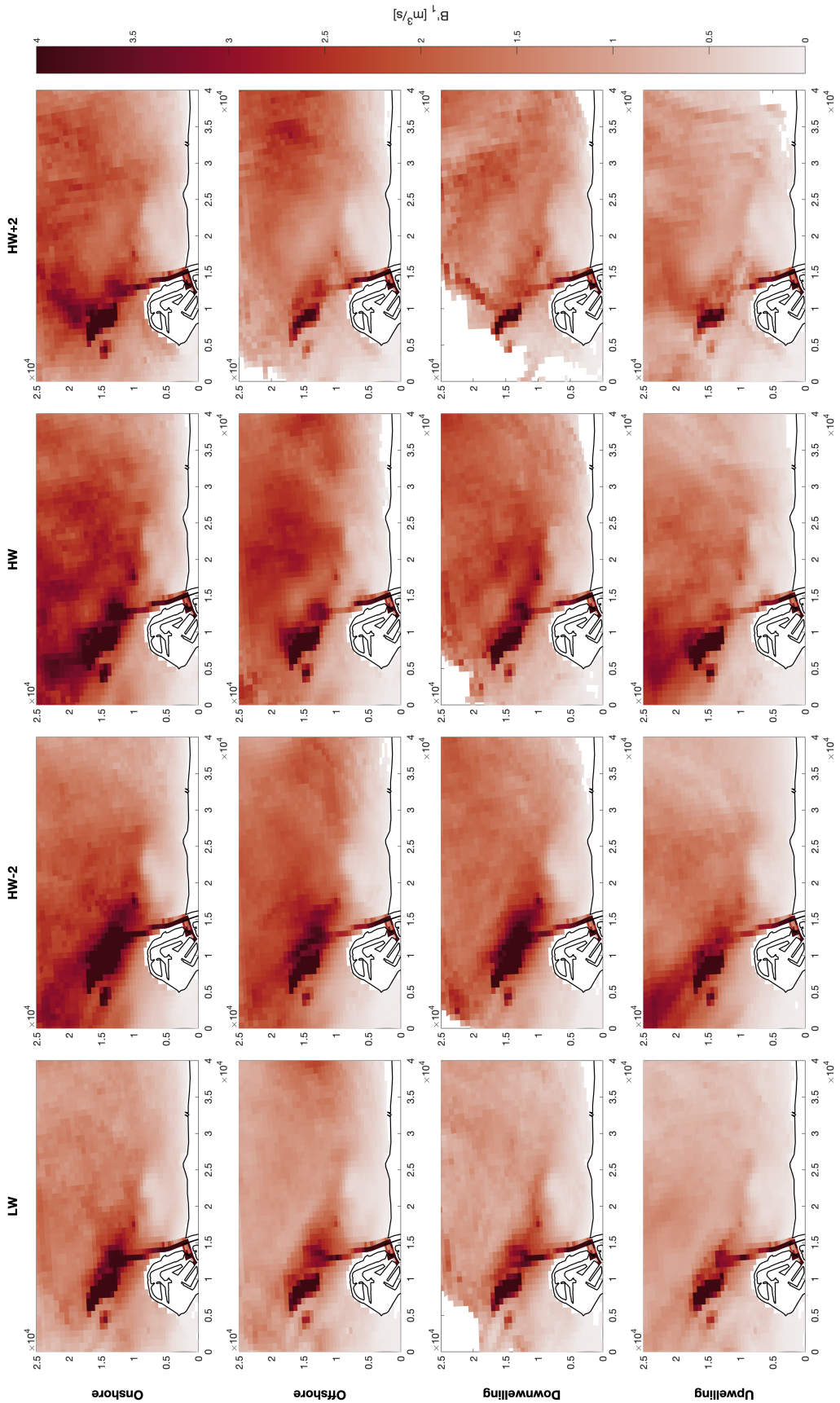

Figure E.13: Mean value of B_1' without shear-flow for multiple M_2 tidal stages for multiple wind directions.

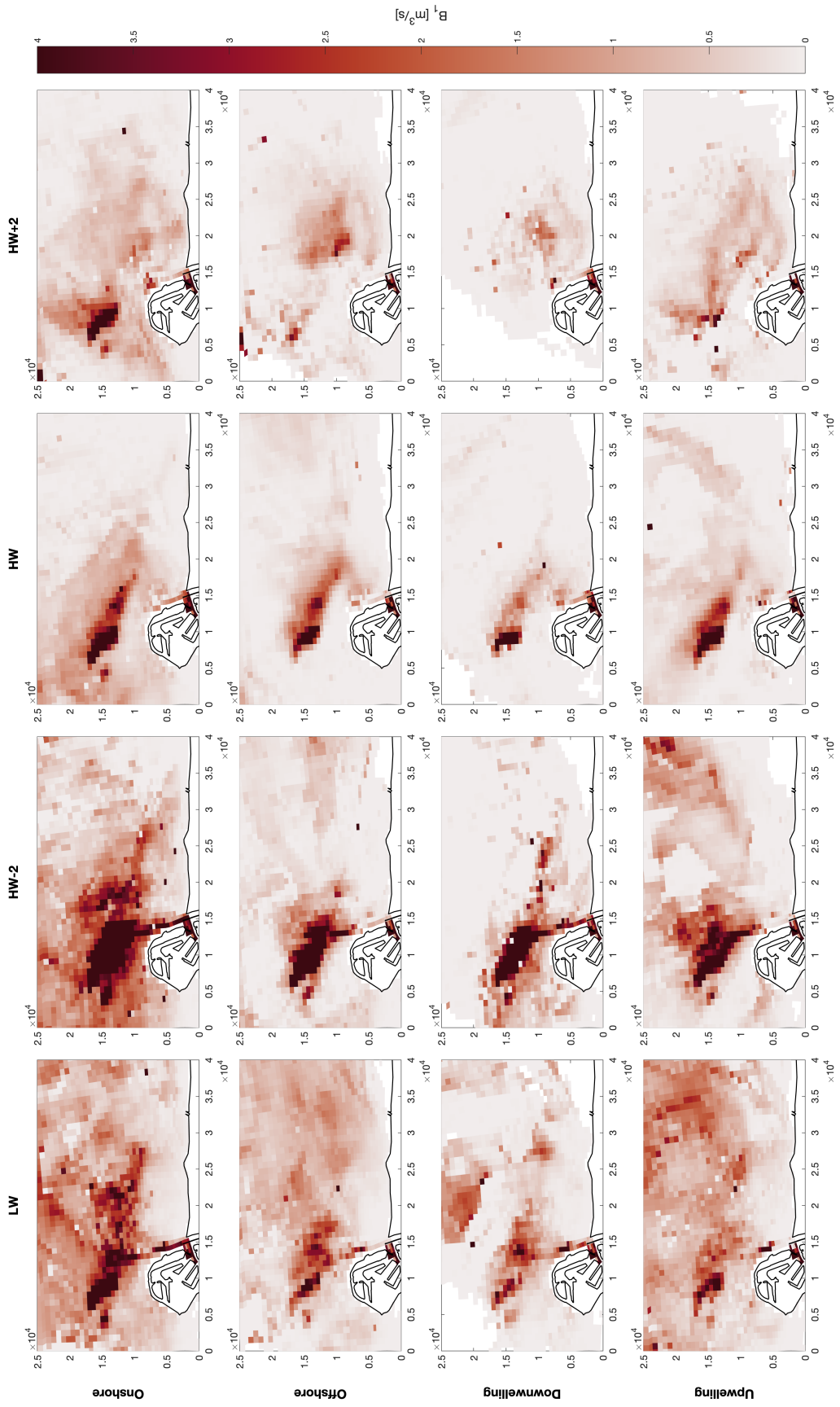

Figure E.14: Mean value of B_1 with shear-flow in the flow direction of the upper layer for multiple M_2 tidal stages for multiple wind directions.

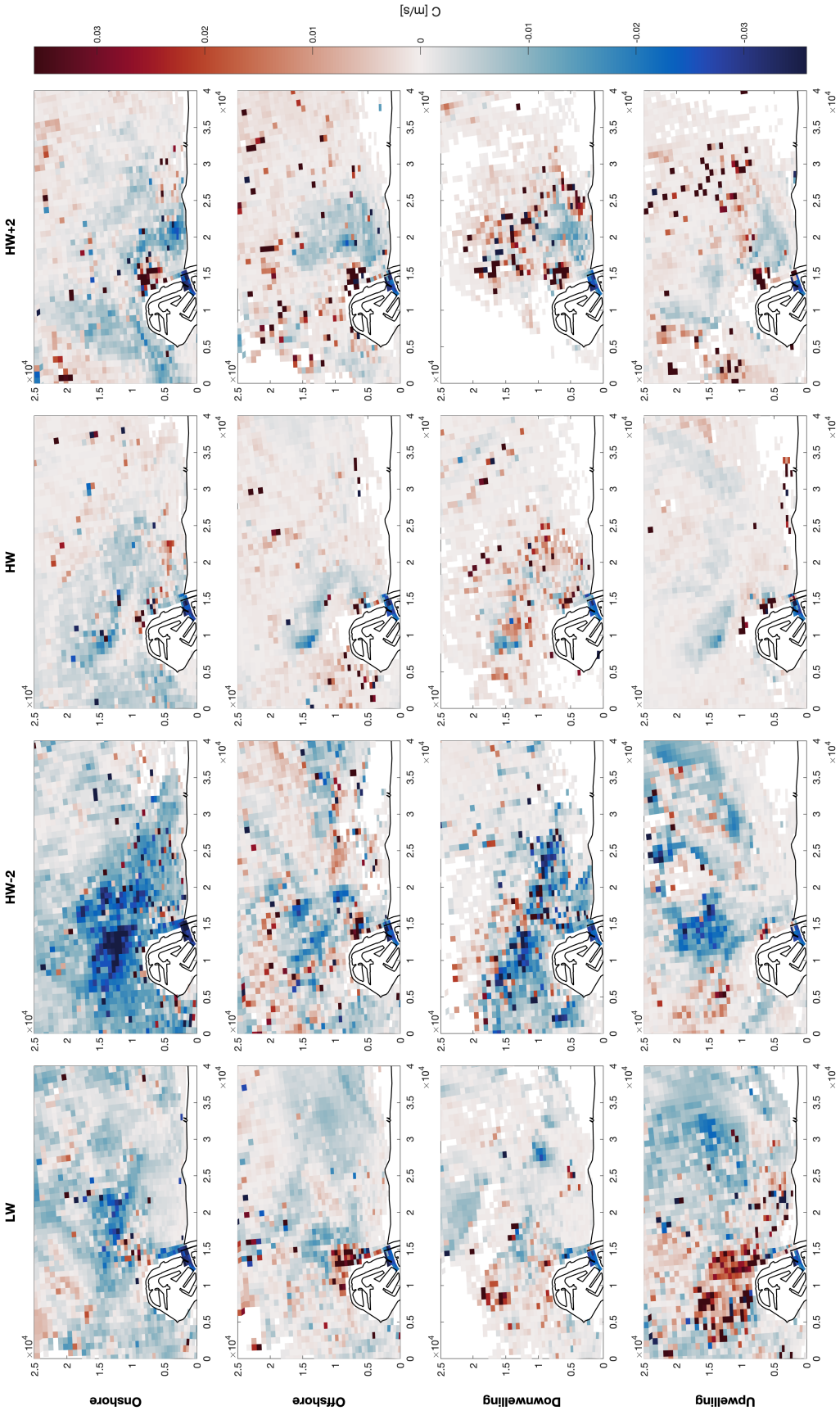

Figure E.15: Mean value of traveling wave velocity C with shear-flow in the flow direction of the upper layer for multiple M_2 tidal stages for multiple wind directions.

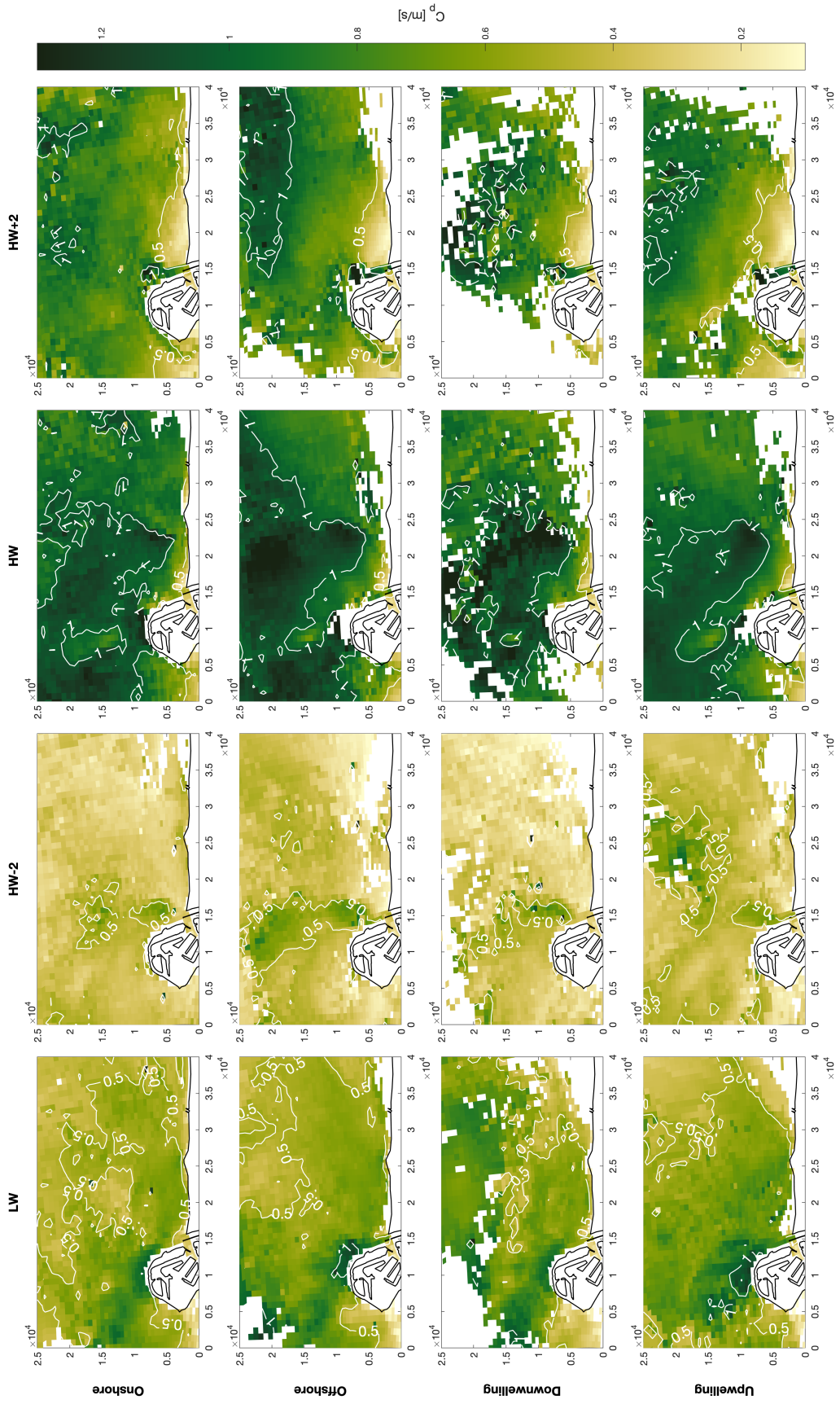

Figure E.16: Mean value of the total propagation speed C_p with shear-flow in the flow direction of the upper layer for multiple M_2 tidal stages for multiple wind directions.